NUMERICAL MODELING OF HYDRAULIC FRACTURE PROPAGATION USING THERMO-HYDRO-MECHANICAL ANALYSIS WITH BRITTLE DAMAGE MODEL BY FINITE ELEMENT METHOD

A Dissertation

by

KYOUNG SUK MIN

Submitted to the Office of Graduate Studies of
Texas A&M University
in partial fulfillment of the requirements for the degree of

DOCTOR OF PHILOSOPHY

Chair of Committee,	Ahmad Ghassemi
Committee Members,	Stephen A. Holditch
	Jerome J. Schubert
	Amine Benzerga
Head of Department,	A. Daniel Hill

August 2013

Major Subject: Petroleum Engineering

ABSTRACT

Better understanding and control of crack growth direction during hydraulic fracturing are essential for enhancing productivity of geothermal and petroleum reservoirs. Structural analysis of fracture propagation and impact on fluid flow is a challenging issue because of the complexity of rock properties and physical aspects of rock failure and fracture growth. Realistic interpretation of the complex interactions between rock deformation, fluid flow, heat transfer, and fracture propagation induced by fluid injection is important for fracture network design. In this work, numerical models are developed to simulate rock failure and hydraulic fracture propagation. The influences of rock deformation, fluid flow, and heat transfer on fracturing processes are studied using a coupled thermo-hydro-mechanical (THM) analysis.

The models are used to simulate microscopic and macroscopic fracture behaviors of laboratory-scale uniaxial and triaxial experiments on rock using an elastic/brittle damage model considering a stochastic heterogeneity distribution. The constitutive modeling by the energy release rate-based damage evolution allows characterizing brittle rock failure and strength degradation. This approach is then used to simulate the sequential process of heterogeneous rock failures from the initiation of microcracks to the growth of macrocracks. The hydraulic fracturing path, especially for fractures emanating from inclined wellbores and closed natural fractures, often involves mixed mode fracture propagation. Especially, when the fracture is inclined in a 3D stress field, the propagation cannot be modeled using 2D fracture models. Hence, 2D/3D mixed-

modes fracture growth from an initially embedded circular crack is studied using the damage mechanics approach implemented in a finite element method.

As a practical problem, hydraulic fracturing stimulation often involves fluid pressure change caused by injected fracturing fluid, fluid leakoff, and fracture propagation with brittle rock behavior and stress heterogeneities. In this dissertation, hydraulic fracture propagation is simulated using a coupled fluid flow/diffusion and rock deformation analysis. Later THM analysis is also carried out. The hydraulic forces in extended fractures are solved using a lubrication equation. Using a new moving-boundary element partition methodology (EPM), fracture propagation through heterogeneous media is predicted simply and efficiently. The method allows coupling fluid flow and rock deformation, and fracture propagation using the lubrication equation to solve for the fluid pressure through newly propagating crack paths.

Using the proposed model, the 2D/3D hydraulic fracturing simulations are performed to investigate the role of material and rock heterogeneity. Furthermore, in geothermal and petroleum reservoir design, engineers can take advantage of thermal fracturing that occurs when heat transfers between injected flow and the rock matrix to create reservoir permeability. These thermal stresses are calculated using coupled THM analysis and their influence on crack propagation during reservoir stimulation are investigated using damage mechanics and thermal loading algorithms for newly fractured surfaces.

DEDICATION

To my lovely wife and parents who encouraged me in this study over a number of years for their unconditional love and support

ACKNOWLEDGEMENTS

I gratefully thank my advisor, Dr. Ahmad Ghassemi, for his support and guidance during the course of my research. He gave me the opportunity to pursue a Ph.D. program in petroleum engineering, when I decided to transfer from mechanical engineering. He encouraged me to pursue my research in the field of computational geomechanics.

I would like to express my sincere appreciation to my committee members, Dr. Holditch, Dr. Schubert and Dr. Benzerga for their support and valuable discussions. In addition, I want to thank my friends for their help, discussion and exciting moments during this long journey.

I gratefully acknowledge the financial support from the U.S. Department of Energy for EGS Component R&D/ Stimulation Prediction Models.

Finally, I am forever indebted to my wife, Sae Young Lee, my parents and my sisters for their support and continuous encouragement.

NOMENCLATURE

a_i	Shape parameter for Weibull function
A	Cross-sectional area
A_D	Damaged cross-sectional area
A_f	Fracture plane area
$\overline{A}$	Effective cross-sectional area
B	Skempton coefficient
$\mathbf{B}_\mathrm{j}$	Geometry matrix
c_F	Cohesive strength
c^T	Thermal diffusivity coefficient
C_{ijkl}	Elastic stiffness tensor
C^f	Fluid diffusion coefficient
C_t	Specific heat capacity
D	Damage variable
$\mathbf{D}_m$	Material stiffness matrix
E	Young's modulus
E'	Effective Young's modulus
F_i^1	Equivalent nodal force at node i of element 1
$\mathbf{F}_u$	External applied loads
$g(\varepsilon)$	Softening function for damage evolution law
G	Shear modulus

h_i	Heat transfer in rock matrix
I_s, I_t, I_θ	Stress invariants
J	Jacobian matrix
k	Permeability
k_m	Rock matrix permeability
k^T	Thermal conductivity
K	Bulk modulus
K_s	Bulk modulus of solid matrix
K_f	Bulk modulus of fluid
$\mathbf{K}_e$	Element stiffness matrix
l_{adv}	Increment crack length
$l_{\max}$	Maximum increment crack length
m	random variables by Weibull function
m_i	Scale parameter for Weibull function
M	Biot modulus
nf	Total number of fracture elements
N_j	Shape function vector
p	Pore pressure
p'	Mean effective stress
p_f	Fluid pressure in fracture
Pc	Confining pressure
q'	Mean deviatoric stress

q_i	Fluid flow in rock matrix
q_{inj}	Injection rate of fracturing fluid
q_l	Leakoff rate
Q_i	Volumetric fluid injection rate
Re	Reynolds number
s	Softening parameter for damage evolution law
S_H	Maximum horizontal far-field stress
S_h	Minimum horizontal far-field stress
S_v	Vertical far-field stress
t	Time
t_s	Time step
t_{inj}	Injection time
T	Temperature
T_0	Initial temperature
u_{ij}	Displacement tensor
$\overline{u}$	Average flow velocity in fracture
$\tilde{U}_e$	Elastic strain energy per unit volume
$U_{\max}$	Maximum strain energy concentration at crack tip
$U_{\min}$	Minimum strain energy required to advance a crack tip
U_{tip}	Strain energy accumulated at crack tip
v_l	Leakoff fluid velocity
V_{ed}	Damaged element volume

V_d	Total volume of damaged elements
V_f	Fracture volume
V_i	Injected fluid volume
V_l	Leakoff volume
V_r	Representative volume
w_f	Fracture aperture
Y	Driving force for the growth of damage
$\tilde{Y}_e$	Spatial average of damage energy release rate
$\tilde{Y}_{e0}$	Initial value of damage energy release rate
α	Biot's constant
α_p^T	Volumetric thermal expansion coefficient of pore space
α_{ij}^T	Volumetric thermal expansion coefficient tensor
α_m	Volumetric thermal expansion coefficient of solid
α_f	Volumetric thermal expansion coefficient of fluid
β	Thermal expansion coefficients
δ_{ij}	Kronecker delta
ε	Strain
ε_{ij}	Strain tensor
ε_1	Maximum principal strain
ε_3	Minimum principal strain

ε_f	Average error of fluid pressure distribution during iteration
ε_{inj}	Injection efficiency
$\varepsilon_{c1}, \varepsilon_{c2}$	Maximum compressive strains
$\varepsilon_{c1r}, \varepsilon_{c2r}$	Residual compressive strains
ε_t	Maximum tensile strain
ε_{tr}	Residual tensile strain
ε_v	Volumetric strain
$\overline{\varepsilon}$	Current equivalent strain
θ_t	Parameter for time discretization
θ_p	Propagation angle at crack tip
λ, μ_L	Lamé's constants
μ	Fluid viscosity
μ_f	Fracturing fluid viscosity
ρ	Mass density
ρ_f	Mass density of fracturing fluid
ν	Poisson ratio
ν_u	Undrained poisson ratio
σ_{ij}	Stress tensor
σ_{eff}	Effective stress
σ_1	Maximum principal stress

σ_3	Minimum principal stress
σ_{c1}, σ_{c2}	Compressive strengths
σ_T	Tensile strength
σ_{nf}	Normal effective stress
τ_f	Shear effective stress
τ_{xy}	Shear stresses
φ	Energy dissipation rate
ϕ	Porosity
ϕ_f	Friction angle
ζ	Variation of the fluid content
χ	Empirical velocity index for crack increment law
ψ	Free energy density
ω	Convergence parameter for iteration method

TABLE OF CONTENTS

Page

LIST OF FIGURES

Page

LIST OF TABLES

Page

1. INTRODUCTION

Since hydraulic fracturing was introduced around the 1930's (Grebe and Stoesser 1935), the hydraulic fracturing technique has been actively used in unconventional reservoir and enhanced geothermal system (EGS) developments because the treatment is essential for enhancing productivity by increasing fracture connectivity. To design successful fracture networks, understanding of complex interactions of rock deformation, fluid flow and heat exchanges on fracture propagation is very important. However, several existing geomechanical challenges, such as extremely low permeability, uncertainty of rock properties, and complexity of brittle fracture growth, complicate design. Practically, a hydraulic fracturing process involves complex physical phenomena of multiphase fluid flow, conductive and convective heat transfer, and highly discontinuous fracture growth in complex forms. Thus, when the fluid induced fracturing is modeled via a numerical method, the hydraulic fracturing process is used to simplify to the continuous hydraulic pressurization through injection induced fracturing path.

But the most difficult aspect of the hydraulic fracturing simulation is how to describe the simultaneous phenomena of the complex physical interactions of fluid flow and rock deformation in a porous reservoir, because spatial and temporal variation of reservoir stresses by fluid injection increases the numerical difficulties while solving the coupled processes. The presence of fractures qualitatively changes the fluid flow that is mainly through these fracture networks in the rock mass, and the fluid flow will be

focused on the small aperture areas of the fractures (Stephansson et al. 1996; Wang and Narasimhan 1985).

In addition, the rock mass is generally heterogeneous material, composed of grains, pores, crystals, minerals, and various scales of natural cracks (Hoek and Brown 1990; Jaeger et al. 2007), so that the reservoir heterogeneity could make tortuous and un-predictable fracture growth, Therefore, numerical challenge is how to handle the coupled processes by applying appropriate numerical models. Correct numerical interpretation and analysis of the failure mechanism of heterogeneous rock mass, discontinuous fracture propagation in complex forms, and impact on fluid flow are key points to develop the reliable hydraulic fracturing simulator.

1.1 Problems and methodologies

In recent years, interest in fully coupled hydraulic fracturing simulation has increased. However, this is a very challenging problem to deal with because of the coupled behavior of rock deformation, fluid flow, and heat transfer under various stress regimes. Previously several 2D, pseudo-3D, and planar-3D hydraulic fracturing simulators based on linear-elastic facture mechanics (LEFM) have been developed; these simulators work well only when the geometry of the fracture is simply confined to a single plane such as the Khristianovich-Geertsma-DeKlerk (KGD) model (Geertsma and Klerk 1969; Khristianovic and Zheltov 1955) and the Perkins-Kern-Nordgren (PKN) model (Nordgren 1972; Perkins and Kern 1961). The PKN model is applicable to long fractures, which have limited height and elliptical vertical cross-section, while the KGD

model is used for short fracture where plane strain assumptions are applicable to horizontal sections and width calculation is height independent. However, stimulation of petroleum and geothermal reservoirs usually involves hydraulically induced multiple fractures that complicate the fracturing treatments by tortuosity and early fracture closure by interaction of fracture networks (Min et al. 2011; Yamamoto et al. 2000). In practical problems, the rupture paths are variable and depend on material deformation properties, material strength, and rock heterogeneity, which critically influence the hydraulic fracture propagation. The fracture geometry is generally non-planar with arbitrary directions and is generated by a nonlinear fracture mechanism.

In addition, fluid flow in fractures complicates the hydraulic fracture propagation under high-pressure condition. So the reservoir stresses vary spatially and temporally in complex combinations among rock deformation, pore pressure, and temperature. The complicated coupled behaviors of rock failure mechanisms, fluid flow in fractures, and complex crack geometry pose extremely difficult numerical challenges for implementing hydraulic fracturing.

Therefore, a simplification procedure for the complicated problem is necessary to develop hydraulic fracturing simulation. In this study, the complex hydraulic fracturing processes were simplified to three coupled processes: rock deformation induced by hydraulic pressurization, fluid flow (fluid pressure) within the fractures caused by fluid injection, and fracture propagation by rock failures. To simulate the coupled processes, the following key factors are considered for hydraulic fracturing design in complex settings:

- First, the nonlinear mechanical behavior of a rock mass is described by elastic/brittle constitutive modeling using continuum damage mechanics (CDM). The failure mechanism of brittle rock is described using a mechanical damage evolution law at the elemental scale within the finite element method. So, at current stage, no rate/time-dependent behaviors such as plasticity are taken into account.
- Second, the heterogeneity of rock mass is considered using spatial distributions of material properties (Young's modulus, strength, and permeability). The spatial distribution curves are described by the Weibull distribution function (Weibull 1939). The random variable approach of the Weibull function is popularly used to represent rock heterogeneity because of its simplicity (Fang and Harrison 2002a; Tang and Hudson 2011; Tang et al. 2002; Wong et al. 2006; Yuan and Harrison 2005) and have been used in stimulation (Lee and Ghassemi 2010).
- Third, the porous rock mass is assumed to be fully saturated with fluid flow governed by Darcy's law, and the reservoir response by the coupled processes of rock deformation, pore pressure, and temperature during hydraulic fracture propagation were described using the fully coupled thermo-hydro-mechanical (THM) analysis under the governance of mass, momentum and energy conservation laws (Noorishad and Tsang 1996).
- Fourth, the fluid flow inside fractures is assumed as incompressible and single phase, with Newtonian flow, so that the hydraulic pressure distribution inside

fractures is solved using the lubrication equation with a no-flow boundary condition at the fracture tip.

- Fifth, the quasi-static crack growth algorithm is developed to describe hydraulic fracture propagation. The Mohr-Coulomb failure criterion with tension cut-off was used to capture shear and tensile crack initiation. A moving-boundary scheme is developed to describe the transition of hydraulic pressure through the fracturing paths.

Consequently, better explanations for fracturing complexity, coupled processes, and shear localized cracking phenomena can be obtained. Results from the numerical simulation provide important information for hydraulic fracturing treatment design and provide several case studies to optimize the hydraulic fracturing treatment.

1.2 Objectives of the study

The major objective of my dissertation is providing numerical interpretation for complicate hydraulic fracturing processes. Introduction and application of design methodology for brittle failure and fracture propagation considering heterogeneity and dilation is one of the primary objectives of this research. Ideally, various constitutive relations suitable for different types of material can be used to give realistic physical interpretation; however the simplified elastic/brittle constitutive model developed here can estimate compressive strength and describes general strain-softening behavior corresponding to the confining pressure. Hence, the brittle failure mechanism of a

heterogeneous rock specimen is studied to provide numerical description and interpretation of rock properties, fracture patterns, and data from rock experiments for reservoir characterization.

Understanding the impact of coupled variations of rock deformation, pore pressure, and temperature during stimulation is important for reservoir development and its long-term performance. The fundamental finite element model (FEM) construction of fully coupled THM analysis with damage mechanics was implemented previously (Lee 2011; Zhou and Ghassemi 2009), and it was extended to hydraulic fracturing and thermal fracturing simulation in this dissertation. In particular, spatial and temporal changes of fluid transport and temperature distribution in porous rock matrix were of interest.

Numerically, discontinuous crack behavior is very challenging to apply to a continuum-based FEM model, because the strong discontinuity leads to solution instability and requires a large-scale matrix solver. So my dissertation is aimed at finding a robust numerical model to characterize complex fracturing behavior in the highly tight reservoirs by using damage/fracture mechanics and a stochastic method to create a successful fracture network. Providing 3D hydraulic fracturing model for laboratory block experiments and applicable to use in larger geological problems is an important objective in order to test the modeling predictions, so fluid-driven fracture propagation is studied and developed using the coupled fluid-flow analysis and rock-deformation analysis in porous media. Fluid flow inside fractures from fluid injection is modeled using a lubrication equation assuming an incompressible viscous fluid inside the

fractures. A necessary crack-tracking algorithm and a moving-boundary scheme were developed to compute fracturing path, aperture, and pressure profiles, which are variable as a function of time.

A secondary thermal fracturing phenomenon is normally observed when cooled fluid is injected to the hot reservoir, especially if the temperature difference between the cold injection and the reservoir temperature is large. This is an especially important consideration for a geothermal reservoir. The thermally induced crack growth may increase well productivity after a significant period of stable injection (Min and Ghassemi 2011). When a cold fracturing fluid is injected into a hot reservoir, the reservoir rock shrinks as the rock cools during the heat exchange, and eventually it triggers thermally induced fracture initiation as residual stress in the reservoir increases. In this dissertation, the secondary thermal fracturing phenomenon was conceptually studied and simulated using the proposed numerical model.

1.3 Outline of the dissertation

In section 1, motivation and objectives of this research were described. Numerical challenges and problems of hydraulic fracture propagation simulation were presented and methodologies of the hydraulic fracturing simulation were proposed.

In section 2, several failure mechanisms by tensile, shear and compaction were reviewed and effects of pore pressure and confining pressure on rock failure were stated. Stochastic approach was introduced to account for various rock heterogeneity compositions. In addition, several existing crack propagation techniques including EDM,

AEM, CZM, XFEM and Mesh-free were reviewed and discussed for possibility of usage in the hydraulic fracture propagation simulation.

In section 3, constitutive relationship for brittle rock failure was developed using the theory of continuum damage mechanics and nonlocal damage model. Elastic-brittle damage evolution law for brittle rock was developed based on the hypothesis of equivalent energy dissipate rate.

In section 4, design methodologies for hydraulic fracture propagation simulation were introduced. Thermo-Hydro-Mechanical analysis was described to compute hydro-mechanical rock responses by injected fracturing fluid. Flow behavior of the injected fracturing fluid in fractures was described using the lubrication theory and fluid leakoff was described using the Darcy flow between fractures and rock matrix. Numerical modeling of hydraulic fracture propagation and moving boundary scheme were developed using element partition methodology.

In section 5, solution strategy for fully coupled processes of fluid flow, rock deformation and fracture propagation was introduced. Numerical implementations of iterative method, leakoff rate, fracture propagation algorithm, and failure analysis were stated. Model verification of pressurized crack and biaxial tension with analytical solutions were presented for 2D simulation. Model verification of pressurized penny shape fracture with analytical solution was examined for 3D simulation.

In section 6, 2D numerical simulation for compression tests of a heterogeneous brittle rock was performed to investigate the suitability of the elastic-brittle damage model. Laboratory-scaled multistage triaxial tests were used to validate the constitutive

modeling of heterogeneous brittle rock. Influences of confining pressure, heterogeneity parameter and mesh size were investigated.

In section 7, 3D numerical simulation for compression test was performed and snapback issue during triaxial compression simulation was examined.

In section 8, mixed mode fracture propagation under different stress regimes by confining pressure variation was investigated. 2D and 3D Wing crack model were used to exam the mixed mode fracture propagation. Transition from tensile dominant to shear dominant failure mechanism was studied.

In section 9, 2D hydraulic fracture propagation in impermeable rock was simulated to investigate wellbore pressure response, aperture changes, and hydraulic fracture initiation and propagation in parallel/deviated perforation cases.

In section 10, 2D hydraulic fracture propagation in permeable rock was simulated. Difference of hydraulic fracturing simulation between homogeneous and heterogeneous reservoir was examined.

In section 11, 3D hydraulic fracturing simulation was developed and validated with laboratory scaled hydraulic fracturing test of Niobrara shale. Influence of block heterogeneity was examined. Effect of fracturing fluid viscosity and sensitivity of the coupled hydraulic fracturing model against material properties were investigated.

In section 12, numerical simulation for 3D thermal fracturing simulation for randomly grown thermally induced fractures from a cooled pre-exist fracture plane was performed using the fully coupled THM analysis with reservoir heterogeneity.

In section 13, summary and conclusions of this research were introduced. Limitations of the proposed numerical models were presented and recommendations for future research were stated.

2. METHODOLOGIES

Developing a numerical model for the hydraulic fracturing process requires clear understanding of the rock failure mechanism, fluid flow in deformable fractures, and numerical modeling for crack propagation. Especially, numerical capability to capture failure modes and fracture propagation by its failure mode is critical for hydraulic fracturing model design. Rock heterogeneity is also an important factor because of its influence on fluid flow and fracture pattern. Numerically, crack paths are very difficult to replicate because of the complexity of mechanical behavior and strong discontinuity of cracks in heterogeneous rock.

To solve for the fracturing problems, different numerical approaches based on the boundary element method (BEM), the finite element method (FEM), and the discrete element method (DEM) can be used for crack propagation, depending on different purposes. However, each method has both cons and pros.

DEM, which uses interaction between bonds of particles, gives good crack-path estimation for the discontinuous aspect of crack propagation. But it requires numerous particles to obtain accurate results, which lead to high computation costs and limit the method to small-scale geological models. Also, especially for fully coupled poroelastic analysis, it is very difficult to model realistic particle geometries and to determine the material parameters required to define mechanical relationships between these “micro-scale” particles, causing significant errors during simulation.

BEM has the advantages of reducing computational model dimensions and generating a simple mesh, compared with FEM and DEM that use a full-domain discretization method (Jing and Hudson 2002). BEM is especially suitable for linear-elastic fracture problems in homogeneous material. BEM formulations can be extended for coupled hydro-mechanical processes (Ghassemi et al. 2001; Pan and Maier 1997). However, when dealing with rock heterogeneity in numerical domains, the BEM may not be a suitable method, because the basic BEM formulation cannot have sufficient sub-domains to represent the material's heterogeneity, in contrast with FEM and DEM. In addition, the BEM is not as efficient as the FEM for simulating nonlinear material behavior such as plasticity and damage evolution, because it requires sub-domain integrals (Jing 2003).

On the other hand, FEM has disadvantages when the discontinuous crack behavior is embedded on a continuum-mechanics-based FEM formulation. When many fracture elements are included, the FEM solution tends to yield an unstable and ill-conditioned state. Despite these disadvantages, FEM is the most popularly used numerical method in the engineering field because of its wide applicability. Particularly, the FEM is efficient for handling of rock heterogeneity, nonlinear material behavior, complex boundary conditions, and dynamic problems (Jing and Hudson 2002).

The FEM method has been used for hydraulic fracturing simulation by several researchers (Boone and Ingraffea 1989; Boone et al. 1991; Carrier and Granet 2012; Sarris and Papanastasious 2011). However, a simple fracture plane has generally been assumed in these simulations. Therefore, one of the major issues is how to represent the

geometrical complexity of dynamic crack propagation in a numerical domain when simulating the fracture growth process.

In this section, several failure mechanisms of brittle rock and influences of pore pressure and confining pressure were investigated. The Weibull distribution function was introduced for rock heterogeneity as a stochastic approach. Existing numerical methods for crack propagation modeling were reviewed and discussed as possible solutions for numerical interpretation of hydraulic fracture propagation.

2.1 Failure mechanisms of brittle rock

Numerical interpretation of rock failure mechanisms is important for several geomechanical problems such as wellbore instability analysis, sand production, reservoir compaction/subsidence and hydraulic fracturing. Especially, predicting failure conditions of heterogeneous rock is useful for prevention of borehole/reservoir collapse. However, rock failure is a very complex process because of anisotropy and heterogeneity, so that the failure mechanism has not been fully discovered yet. Numerically, replicating the rock failure mechanism is still a very challenging issue in rock engineering, so only simplified descriptions of real rock behavior based on convenient mathematical descriptions are available (Fjær et al. 2008).

Typically, rock specimen is tested in the laboratory using uniaxial and triaxial tests to measure mechanical properties of the rock. From these experiments, rock strength, which is a critical parameter for rock failure, is measured. Figure 2.1 is a typical stress/strain curve from a uniaxial compression test. During the rock-failure

process, three regions are generally observed: the elastic region, where elastic rock deformation is reversible; the ductile region, where rock deformation (microcrack growth) is irreversible; and the brittle region, where sudden loss of strength leads to totally irreversible rock deformation (microcrack coalescence and macrocrack growth).

Typically the ductile region is very short, so the deformed behavior can be modeled as a simplified elastic/brittle constitutive relationship. In a triaxial compression test, the compressive rock strength is varied with confining pressure variation, and post-failure behavior also changes accordingly. In this study, the complex failure mechanism is numerically modeled as a simplified stress/strain relationship using CDM, rock heterogeneity, and a crack propagation model with an FEM formulation.

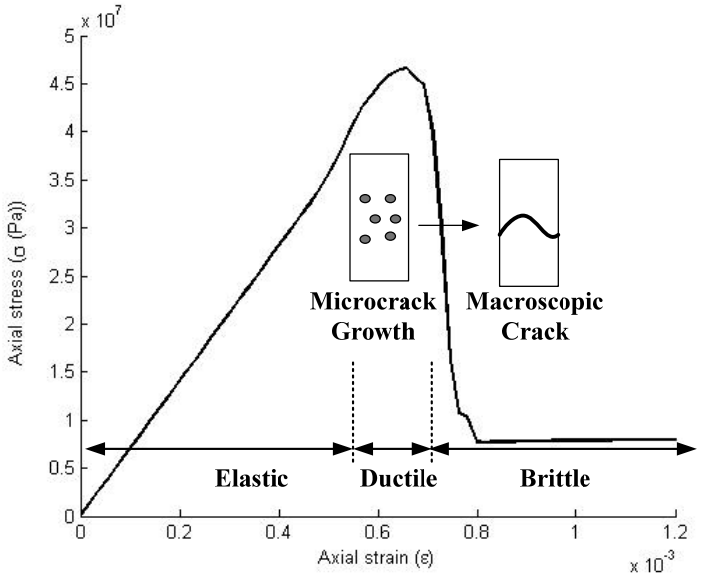

Figure 2.1 Typical stress-strain curve of brittle material from microcrack to macroscopic crack-growth

2.1.1 Fracture modes

Three basic modes of fracture are explained in Figure 2.2. Mode I is a tensile mode: the crack tip is opening; Mode II is an in-plane shear mode: the crack tip is sliding; and Mode III is an anti-plane shear mode: the crack tip is tearing. The tensile mode is the most important and dominant mode in hydraulic fracturing, but the importance of the shear-mode fractures is increasing during hydraulic fracturing treatments in naturally fractured and heterogeneous reservoirs. This is because most fractures are initiated by mixed modes and in practice; there are no single mode fractures because of heterogeneity.

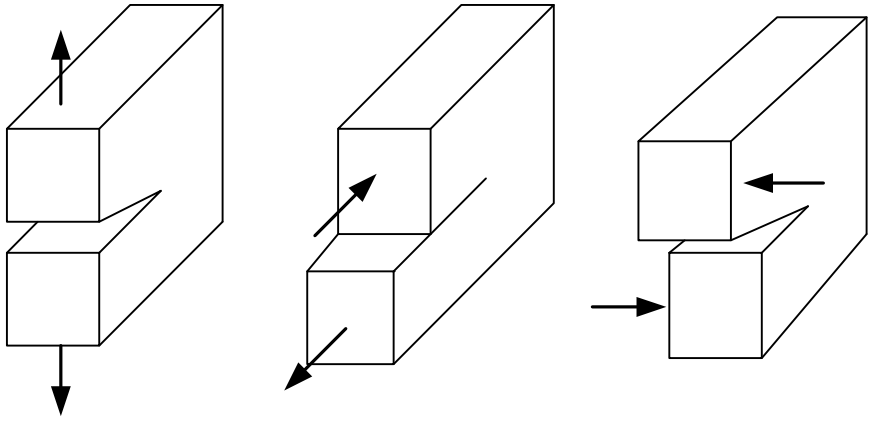

(a) Tensile crack (opening) (b) Shear crack (sliding) (c) Shear crack (tearing)

Figure 2.2 Schematic of fracture modes: (a) Mode I, (b) Mode II, (c) Mode III

2.1.2 Tensile failure

When the effective tensile stress at the crack tip exceeds the critical stress limit called *tensile strength* [Eqn. (2.1)], tensile failure occurs. That is, the tensile crack

initiates when the minimum principal stress, or the maximum tensile stress component during compression, reaches the critical tensile strength of the material. The tensile strength represents the opening mode of fracture toughness. The tensile failure criterion is usually combined with the Mohr-Coulomb failure criterion as a tension cut-off condition as explained in Figure 2.3.

$$\sigma_3 \geq -\sigma_T \,, \tag{2.1}$$

where σ_T is tensile strength of material and σ_3 is the minimum principal stress, which is also the maximum tensile stress.

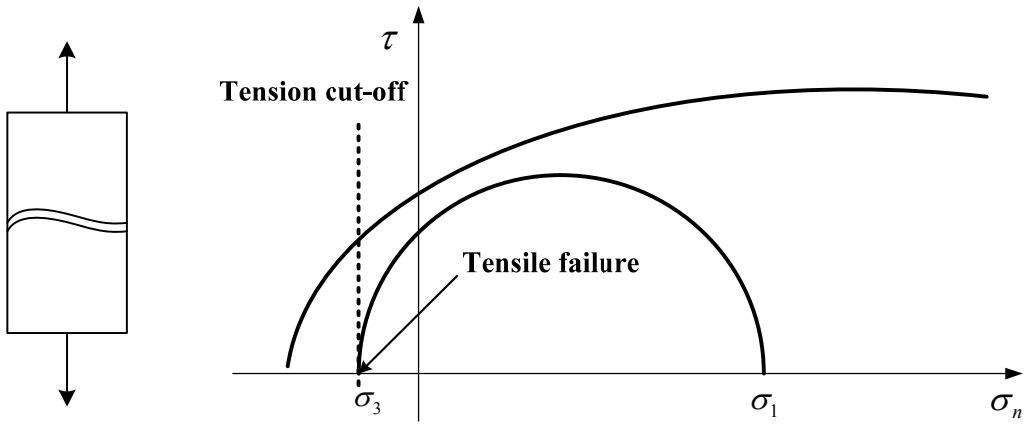

Figure 2.3 Tensile failure with the Mohr-Coulomb failure criterion

2.1.3 Shear failure

When rock is subjected to compressive loading, shear mode failures are commonly observed. In the uniaxial and triaxial tests, shear localized fracturing dominates fracture growth. Generally, a shear crack initiates when effective compressive

stress in the material reaches a specific value, which called *compressive strength*. As explained in Figure 2.4, shear failure occurs along the failure plane when the shear stress increases on the failure plane to a specific value which is a function of the normal stresses in Eqn. (2.2). The Mohr-Coulomb criterion is commonly used to explain this shear localized fracturing behavior; it can predict the angle of the fracture plane and the stress state when the shear failure occurs.

$$\tau_f = c_F + \sigma_{nf} \tan \phi_f \tag{2.2}$$

where τ_f and σ_{nf} are the shear and normal effective stresses on the failure plane respectively, and the cohesion strength c_F and friction angle ϕ_f are rock-strength parameters.

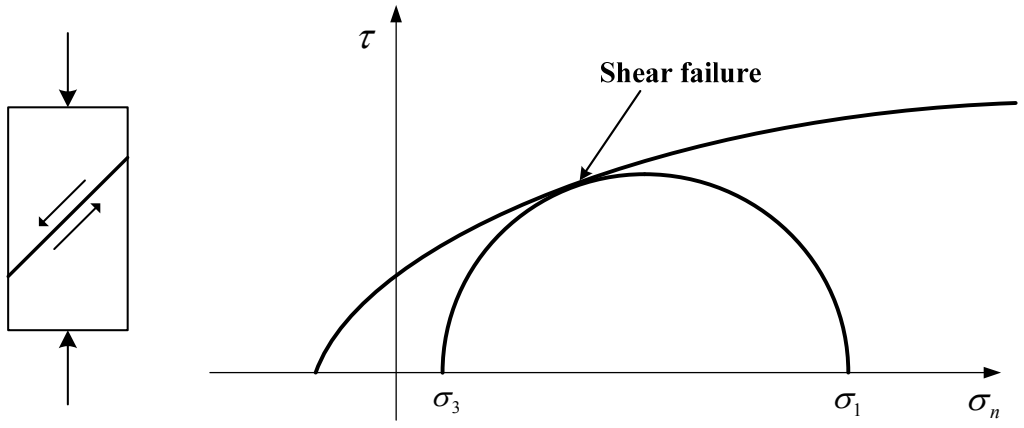

Figure 2.4 Shear failure on the Mohr-Coulomb failure plane

2.1.4 Compaction failure

In highly porous or heterogeneous materials, pore collapse and grain reorientation are normally observed under compaction, as shown in Figure 2.5. The pore collapse might be caused by breaks of grains and then filled into open pore space under pure hydrostatic loading. For instance, when a highly porous chalk is under compaction, the possibility of pore collapse increases because the grain size is much smaller than the pore-space dimension, so that the pore-collapse mechanism becomes the dominating fracture mode in that case (Fjær et al. 2008).

However, microscopically, after compaction failure, shear fracture is initiated by the contact between breaking grains; hence, the pore collapse can be regarded as shear-failure distribution in macroscopic view. Therefore, in this study, the compaction failure mechanism is not considered because of its complexity and uncertainty. And our target is tight reservoirs which have relatively low porosity, so the compaction failure has not effectively happened.

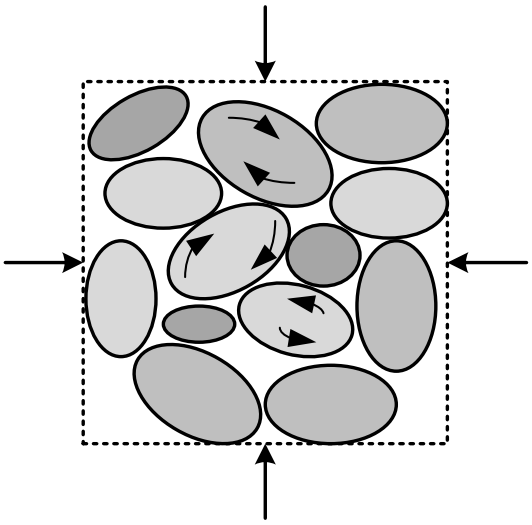

Figure 2.5 Grain reorientation by compaction forces

2.1.5 Pore pressure effect

In porous rock, the pore space is filled with water, oil, or gas under in-situ stresses. The pore fluid may affect the failure of the rock, because the pore pressure is equally acting in all normal directions but not affected by shear stresses (Jaeger et al. 2007). In the Mohr diagram of Figure 2.6, the effect of pore pressure is translated to all the stress circles to the left and close to the failure line for shear and tensile failures. Therefore, increasing pore pressure significantly affects the destabilizing process of a rock and causes the rock to soften.

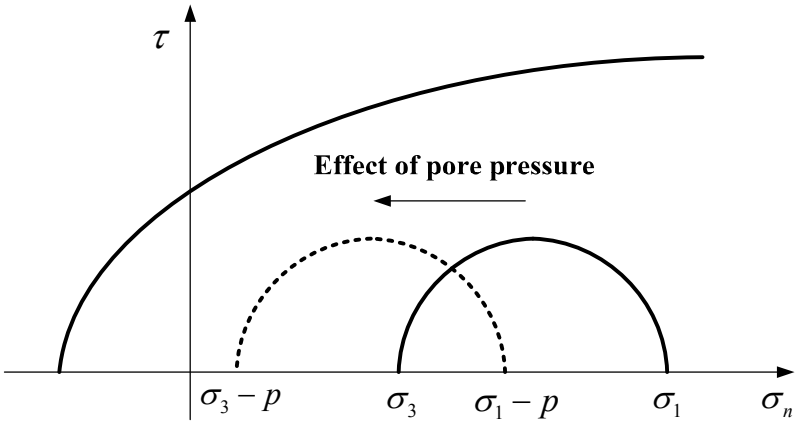

Figure 2.6 Effect of pore pressure on effective stress state

2.1.6 Confining pressure effect

Conventional triaxial tests illustrate that the stress/strain relations of geological materials change as applied confining pressure increases. In Figure 2.7(a), the slope of the stress/strain curve of Rand quartzite is nearly linear elastic, and both the yield strength and the compressive strength increase as the confining stress increases. Complete brittle fracture behavior is found after the yield points regardless of the confining stress variation.

In Figure 2.7(b), a different type of behavior is shown with Carrara marble. As the confining stress increases, more ductile behavior is exhibited. The rock fails by brittle fracture at a low confining zone, transitions from brittle to ductile, and undergoes stress hardening at a high confining zone. The brittle behavior is also seen in other results at various confining stresses (Samieh and Wong 1997). Figure 2.8(a) shows the stress/strain responses of Athabasca oil sand specimens at different confining stresses.

Figure 2.8(b) presents the results of triaxial compression tests on Labiche shale. Except for swollen shale and Carrara marble, the general mechanical behavior of rock is observed as elastic/brittle behavior during triaxial compression tests.

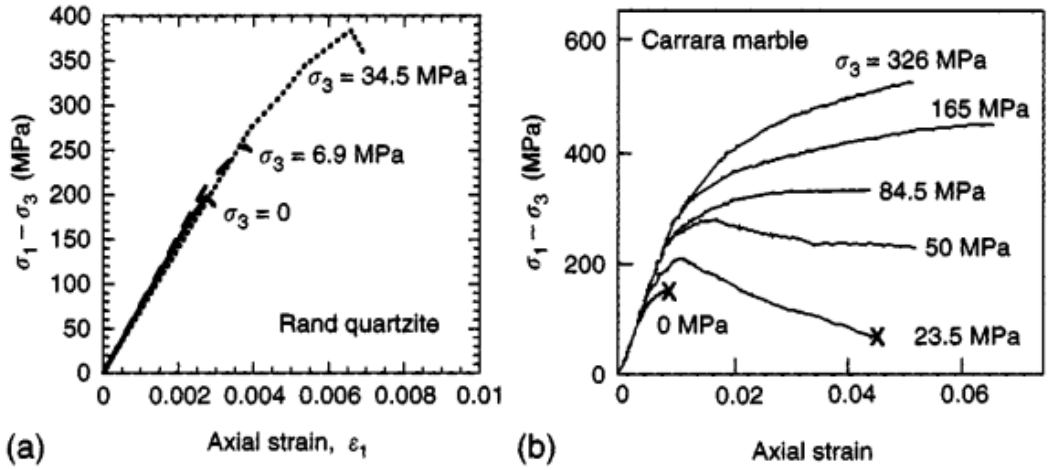

Figure 2.7 Stress/strain curves for (a) Rand quartzite and (b) Carrara marble (Jaeger et al. 2007)

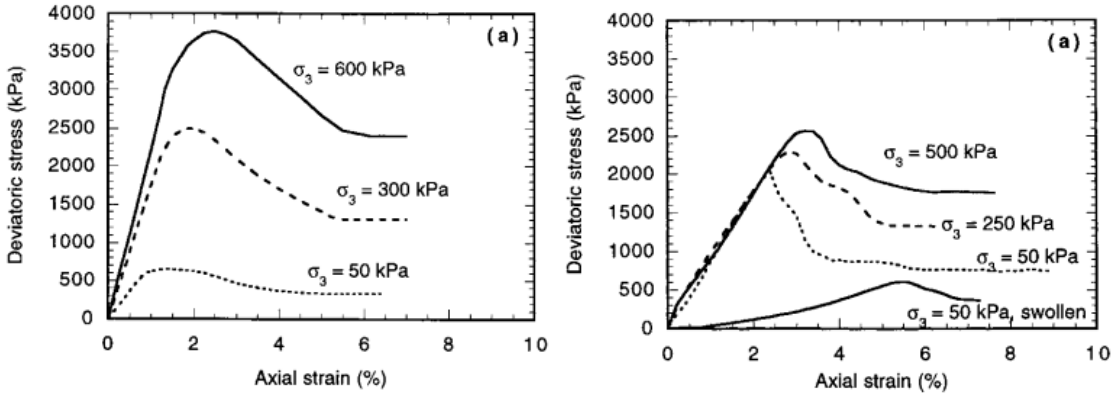

Figure 2.8 Results of drained triaxial compression tests on oil sand and clay shale (Samieh and Wong 1997)

2.1.7 Mohr-Coulomb failure criterion

For capturing the failure of the brittle rock, the simplest and most commonly used criterion is Mohr-Coulomb theory. The Mohr-Coulomb failure criterion is the most general failure criterion for brittle material such as concrete, rock, and soils. The shear stress causing failure across a plane is resisted by the cohesion of the material and the normal stress across the plane. The Mohr-Coulomb criterion is expressed as:

$$\pm\frac{\sigma_3-\sigma_1}{2}=\left[\frac{\sigma_3+\sigma_1}{2}\right]\sin\phi_f+c_F\cdot\cos\phi_f \tag{2.3}$$

where σ_1 and σ_3 are the maximum and minimum principal stresses. ϕ_f and c_F represent the internal friction angle and cohesion strength, respectively. This criterion has the form of an irregular hexagonal cone in a 3D principal stress space.

The principal stress space is obtained in 3D coordinates of the principal stresses, and it is more convenient to use stress invariants to obtain the principal stresses. So the stress invariants (I_s, I_t, I_θ) are defined in Cartesian coordinates:

$$I_s=\frac{1}{\sqrt{3}}\left(\sigma_{xx}+\sigma_{yy}+\sigma_{zz}\right) \tag{2.4}$$

$$I_t=\frac{1}{\sqrt{3}}\sqrt{\left(\sigma_{xx}-\sigma_{yy}\right)^2+\left(\sigma_{yy}-\sigma_{zz}\right)^2+\left(\sigma_{zz}-\sigma_{xx}\right)^2+6\sigma_{xy}^2+6\sigma_{xz}^2+6\sigma_{yz}^2} \tag{2.5}$$

$$I_\theta=\frac{1}{3}\sin^{-1}\left(\frac{-3\sqrt{6}J_3}{I_t^3}\right) \tag{2.6}$$

where

$$J_3=s_xs_ys_z-s_x\sigma_{yz}^2-s_y\sigma_{xz}^2-s_z\sigma_{xy}^2+2\sigma_{xy}\sigma_{xz}\sigma_{yz} \tag{2.7}$$

$$s_x = \frac{\left(2\sigma_{xx} - \sigma_{yy} - \sigma_{zz}\right)}{3} \tag{2.8}$$

Mean effective stress and deviatoric stress are defined as:

$$p' = \frac{1}{\sqrt{3}} s, \text{和} q' = \frac{\sqrt{3}}{\sqrt{2}} t \tag{2.9}$$

The principal stresses are expressed as stress invariants as:

$$\sigma_1 = p' + \frac{2}{3} q' \sin\left(I_\theta - \frac{2\pi}{3}\right) \tag{2.10}$$

$$\sigma_2 = p' + \frac{2}{3} q' \sin I_\theta \tag{2.11}$$

$$\sigma_3 = p' + \frac{2}{3} q' \sin\left(I_\theta + \frac{2\pi}{3}\right) \tag{2.12}$$

Then, the Mohr-Coulomb failure surface is expressed as shown below. The shear strength of rock at failure, τ_f, is given by the Coulomb failure criterion,

$$\tau_f = c_F + \sigma_{nf} \tan \phi_f , \tag{2.13}$$

where τ_f and σ_{nf} are the shear and normal effective stresses on the failure plane respectively. The cohesion strength, c_F , and friction angle, ϕ_f , are rock strength parameters. The Coulomb failure criterion can be rewritten in terms of stress invariants using Mohr's effective stress circle as follows;

$$f = -p' \sin \phi_f + q\left(\frac{\cos I_\theta}{\sqrt{3}} - \frac{\sin I_\theta \sin \phi_f}{3}\right) - c_F \cos \phi_f = 0 \tag{2.14}$$

So for the stress state falls inside of the yield surface, $f < 0$, while it is on the yield surface for $f = 0$, and it is outside the yield surface, $f > 0$. When the effective stress

state is on the yield surface or outside the yield surface, the rock is indicated by shear failure. In addition, to introduce the tensile failure, the maximum tensile strength criterion [Eqn. (2.1)] is combined with Mohr-Coulomb failure criterion as a tension cut-off condition as described in Figure 2.9.

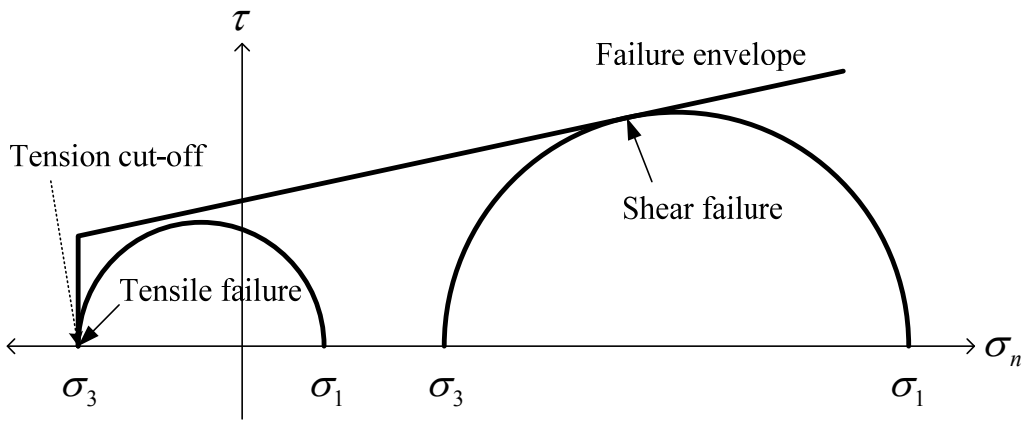

Figure 2.9 Schematic of Mohr-Coulomb failure criterion with tension cut-off

2.2 Rock heterogeneity

Micromechanically, rock is a heterogeneous material that contains lots of different sizes, properties, and types of particle stack. That is, local rock properties may vary by composition and fabrication of the particle stack. Rock heterogeneity leads to various formations of multiple-crack branching during hydraulic fracture propagation. The effect of the rock heterogeneity has been studied experimentally by several researchers (Brace 1961; Fredrich et al. 1990; Mahabadi et al. 2012; Wong et al. 2006), but the effect on strength and deformation has not been well understood. Especially, when the heterogeneity of large geological media is considered, it is almost impossible

to characterize the heterogeneity from field observations. This uncertainty has led to use of a stochastic approach to represent a distribution of material properties and to take into account rock heterogeneity on numerical models.

Characteristics of various micro-defects such as size, strength, and location can be determined by statistical aspects of a random function. The Weibull distribution function is widely used for modeling rock failure because of its simplicity (Fang and Harrison 2002b; Liu et al. 2004; Tang and Hudson 2011; Wong et al. 2006; Yuan and Harrison 2005).

Although failure processes of heterogeneous rock are complex, the stochastic approach can account for a variety of possibilities of rock heterogeneity. However, the stochastic approach cannot explain all different types of rock heterogeneity because each rock has a different form of heterogeneity and each unique statistical model can explain these heterogeneities (Wong et al. 2006). Also, the parameters of the Weibull distribution function are uncertain and highly dependent on the choice of input parameters, so the stochastic model may need to be evaluated on the basis of microstructure analysis and image analysis.

For further improvement, the correlation between Weibull parameters and rock composition must be investigated. This issue is essential for numerical design for rock experiments; however, it is beyond the scope of my study, since lots of uncertainties in rock heterogeneity make it quite difficult.

The Weibull distribution function is used to account for a variety of rock fabric possibilities and has been used by several researchers (Fang and Harrison 2002a; Lee

and Ghassemi 2010; Tang and Hudson 2011; Tang et al. 2002; Yuan and Harrison 2005). The Weibull distribution function is defined by the following probability density function (Weibull 1939):

$$f(m) = \frac{a_i}{m_i}\left(\frac{m}{m_i}\right)^{a_i - 1} \exp\left[-\left(\frac{m}{m_i}\right)^{a_i}\right] \tag{2.15}$$

where m_i, a scale parameter, determines the mean value of the random variable, and a_i, a shape parameter, determines shape of the distribution function. A random variable m for heterogeneity is generated using the Weibull distribution function with parameters m_i and a_i. In Figure 2.10, the effect of a scale parameter showed that the distribution curve was shifted by the scale parameter change. A shape parameter determines the range of the distribution function.

In Figure 2.11(a), the distribution curve becomes narrow when the shape parameter increases. That means the material heterogeneity decreases as the shape parameter increases and until it nears homogeneous material behavior. In Figure 2.11(b), since the scale parameter represents a mean value of the distribution curve, a larger value of m_i indicates a hard, heterogeneous rock, while a smaller m_i indicates a soft heterogeneous rock.

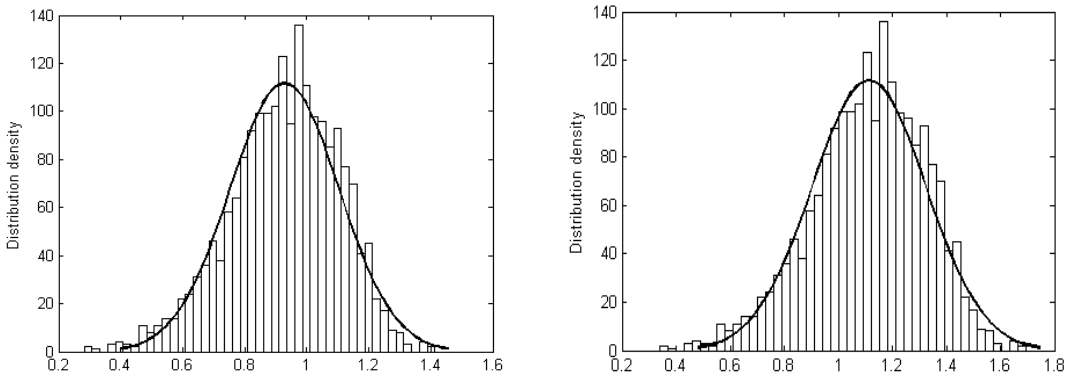

(a) m_i=1, a_i=6 (b) m_i=1.2, a_i=6

Figure 2.10 Distribution curves of random variable *m* by a scale parameter

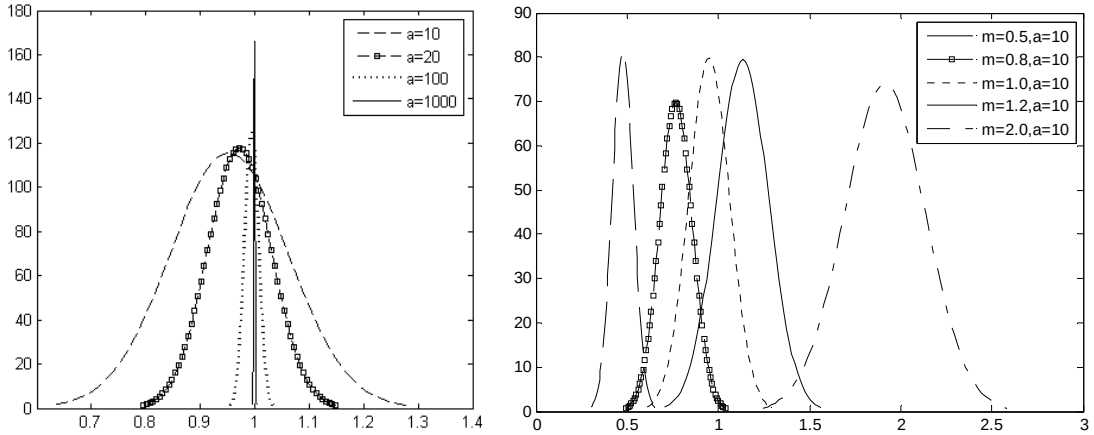

(a) Shape parameter changes (b) Scale parameter changes

Figure 2.11 Distribution curves by Weibull parameter changes

2.3 Numerical methods for crack propagation using FEM

Numerical description of geometrical complexity of crack propagation of brittle fractures is a difficult and challenging issue. Since the crack propagation in geological media is discontinuous, it is very difficult to represent these behaviors in continuum-

based approach. Currently, a number of techniques are available to represent the crack propagation path using FEM. In this section, the element deletion method (EDM), the adaptive element method (AEM), the cohesive zone method (CZM), the cohesive element method (CEM), the extended finite element method (XFEM), and the mesh-free method (MFM) were critically reviewed and discussed about numerical applicability for the hydraulic fracture propagation model.

2.3.1 Element deletion method

The element deletion method (EDM) is widely used for fracture simulation because of its simplicity to represent strong discontinuities in displacement fields (Song et al. 2008; Wulf et al. 1993). In Figure 2.12, elements intersected by the crack path are deleted in order to represent crack propagation. In reality, the element is not deleted during simulation although the stress field in the element is set to zero. EDM was successfully applied to 2D fracture simulation using mesh refinement and a stress/strain softening scheme in LS-DYNA (Hallquist 1998). When a critical strain to failure is reached, the elements are eliminated. However, it is observed the mesh size sensitivity of the local strain which generally increases with finer meshes. To reduce the mesh dependency, the energy dissipation in the softening domain was scaled to the fracture energy. In addition, the element removal could cause overestimated solution. Since the local stress in the failed element is set to zero (i.e. zero material resistance), it causes overestimated crack propagation.

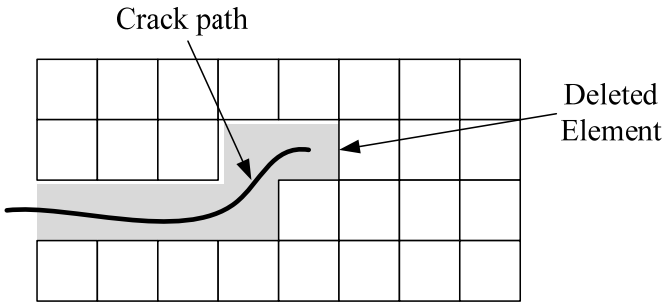

Figure 2.12 Schematic of element deletion method representing the crack path

2.3.2 Adaptive element method

Crack modeling with an adaptive remeshing scheme provides variable routes to track the propagating path in 3D simulation. The elements partitioned by the crack surface are remeshed using the desired element sizes based on the estimated error for a certain prescribed accuracy. Adaptivity around the crack tip is advantageous for crack initiation and stress smoothness, since the crack tip of newly initiated cracks is significantly smaller and it leaves stress singularity at the crack tip (Rabczuk et al. 2007). Among several adaptive element refinement methods, *h*-adaptivity is widely used to obtain a better resolution around the crack front; this refinement around the crack tip could increase accuracy of the results (Devloo et al. 2002; Khoei et al. 2008). In *h*-adaptive strategy, the connectivity of the elements as well as the total number of degrees of freedom may change, while the degree of the shape functions remains the same, so that elements are subdivided into smaller elements when the optimal refinement criterion and an error tolerance are exceeded.

In Figure 2.13, element connectivity with high strain gradients has been changed by a certain refinement ratio such as 1:4 or 1:8. A 1:4 ratio means one element is subdivided into four elements, while 1:8 means one element is subdivided into eight elements. A drawback of the method is that computation cost is very high because node information and the crack front are updated simultaneously at each step.

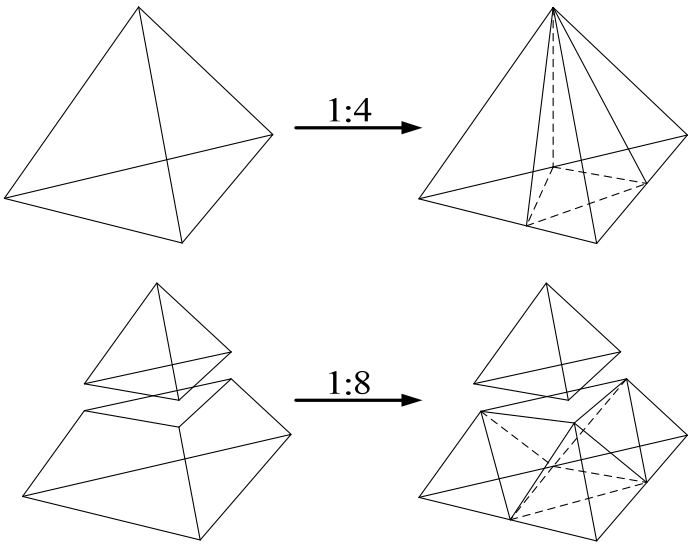

Figure 2.13 Schematic of *h*-adaptive refinement strategy (Loehner 2001)

2.3.3 Cohesive zone method (interelement crack method)

The cohesive zone method (CZM), or the so called interelement crack method, is modeled by implementing a cohesive law between element edges along the crack paths [Figure 2.14]. The cohesive law could be characterized by one of several parameters such as tensile strength, fracture energy, or strain energy. The softening part of the cohesive law can be obtained experimentally. In this approach, a crack grows through

element edges restricted by the cohesive law, providing simple and fast crack trajectories in 2D crack propagation simulation. Two approaches exist for the implementation of this method. One approach assumes that all elements have a cohesive relation at the element edges before the beginning of the crack propagation [Figure 2.14(a)] (Xu and Needleman 2006). Another approach separates only those element edges that are intersected by the crack path assumed as a priori [Figure 2.14(b)]. In this approach, when the criterion is met at the crack tip, the crack path is allowed to separate along the element edges governed by cohesive law (Camacho and Ortiz 1996). CZM has the advantage of simplicity, but for multiple and three-dimensional cracks, the method are not applicable because of geometrical difficulty. Also, crack paths are dependent on the size and shape of the elements.

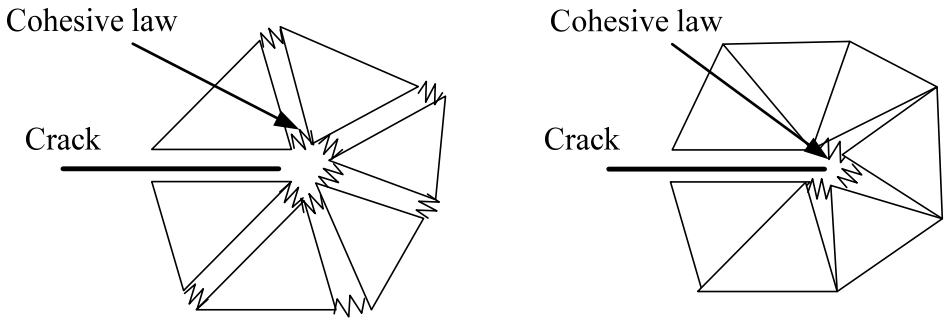

(a) Xu and Needleman (2006) (b) Camacho and Ortiz (1996)

Figure 2.14 Schematic of interelement crack methods (Song et al. 2008)

2.3.4 Cohesive element method

The cohesive element method (CEM) has the advantages of both the EDM and the CZM. The fracture is modeled by an irreversible cohesive law embedded into the cohesive elements [Figure 2.15]. These cohesive elements govern all aspects of the separation and closure of the incipient cracks. In near-tip fields, the surface-separation processes need to be contemplated in the fracture criterion. Those separation processes are modeled by cohesive theories of fracture and cohesive elements (Pandolfi et al. 2000). For example, when the element reaches maximum tensile strength, the element is separated and partitioned through the direction of maximum tensile strength. Along the crack path, certain elements that reach the fracture criterion are governed by a cohesive law. The cohesive law could be characterized by several parameters such as tensile strength, fracture energy, and strain energy. Because crack path grows continuously during simulation, typical elements continue to have the same stiffness. The matrix decreases in softening by the cohesive law, and only the cohesive elements that overlap with the crack path are updated at every time step. In CEM, mesh size should be relatively small in order to represent the proper crack path and stable solution. To avoid mesh dependency, the dissipative energy beyond crack initiation in fracture processing zone is scaled to the fracture energy (Rabczuk et al. 2008).

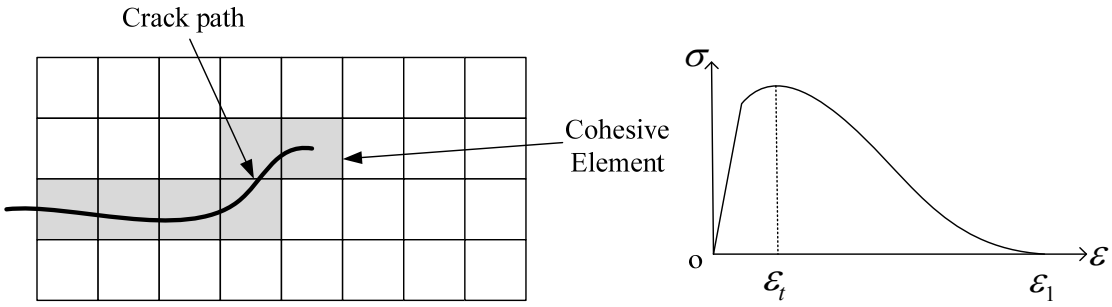

Figure 2.15 Schematic of cohesive element method representing crack path

2.3.5 Extended finite element method

The extended finite element method (XFEM) was introduced to treat arbitrary cracks independent of the mesh and crack growth without remeshing (Belytschko et al. 2001; Zi and Belytschko 2003). The special enrichment functions are applied to the crack path and crack tips. Crack growth takes place where the elements reach maximum tensile strength, specific acoustic emission, or maximum strain energy criteria so that nodes of the elements influenced by the crack path are enriched by a discontinuous function. Enrichment is performed from node to node in a mesh by activating the extra degrees of freedom (DOF). Simply, in near-crack-tip fields, regular DOF is enriched by extra DOFs. A crack that partially cuts an element is enriched by branch functions such as sign and Heaviside functions (Park et al. 2009). The branch functions can represent singular stress behavior at crack tips. The general XFEM form is described as:

$$u^h(x) = \sum_{i \in I} N_i(x) u_i + \sum_{i \in I^*} M_i(x) a_i$$
$$M_i(x) = N_i^*(x) \cdot \psi(x), i \in I^* \tag{2.16}$$

$u^h(x)$: approximated function

$N_i(x)$: standard FE function of node i

u_i : regular DOF of the standard FE at node i

I : set of all nodes in the domain

$M_i(x)$: local enrichment function of node i

a_i : additional DOF of the enrichment at node i

I^* : nodal subset of the enrichment

$N_i^*(x)$: FE shape function by partition of elements

$\psi(x)$: global enrichment function, like sign or Heaviside functions

In this equation, the first term represents the standard FE function, while the second term represents the enrichment function. Therefore, the XFEM is useful for relatively accurate approximation of solutions with non-smooth discontinuities and singularities in small computational domains. However, the disadvantage of the nodal enrichment strategy is that it decreases the sparseness of the resulting matrix because of the added DOF functions (Rabczuk et al. 2007). That means computation time is increased more than in other methods.

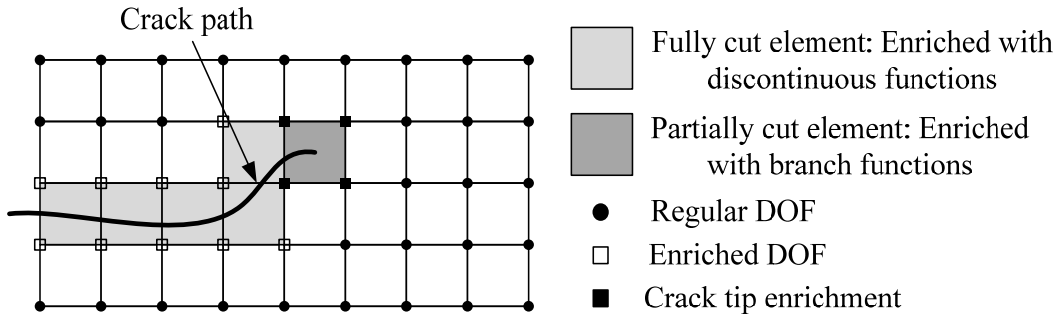

Figure 2.16 Schematic of XFEM using EFM

2.3.6 Mesh-free (meshless) method

Similar to XFEM, the mesh-free method (MM) uses added DOFs to represent crack growth. Using the MM, a crack can simulate in an arbitrary direction and follow more natural crack behavior. The mesh-free method integrates the weak-form overlapping cohesive nodes through the entire domain of influence of a node. In Figure 2.17(b), nodes influenced by the crack path circle are modified by a specific function similar to the enrichment of XFEM.

Modification of the weak form includes the Lagrange multiplier method and the penalty method. Without a mesh, adaptivity is easier to incorporate in the MM than in mesh-based methods (Nguyen et al. 2008). While XFEM and FEM cannot handle highly distorted crack fronts, the MM can provide a smoother stress distribution around the crack fronts. The newly developed MM has not been sufficiently verified, so it requires a large amount of work to develop for application to 3D hydraulic fracturing. Since most meshless shape functions have a nonpolynomial form, the numerical integration of the weak form is very difficult. Moreover, the MM has difficulty implementing 3D crack modeling because of its high computational cost.

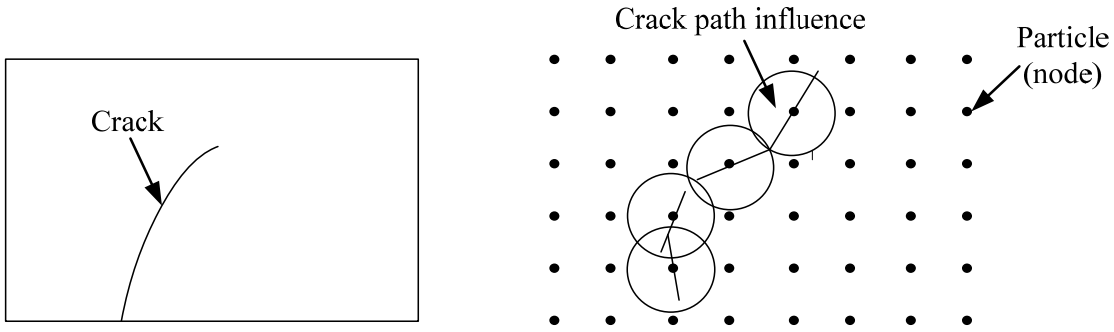

(a) Continuous crack model (b) Discrete crack model by influence circle

Figure 2.17 Schematic of mesh-free method

2.3.7 Summary and discussion

In this section, the numerical methods for crack propagation were reviewed. Major issues are the capability of modeling crack trajectories, stability of the solution, and minimization of computational cost. In addition, the equivalent moving boundary scheme for hydraulic pressurization should be applicable to the method. The element deletion method (EDM) is the simplest method to represent strong discontinuities in displacement fields (Song et al. 2008). In addition, its computational cost is lower because the stiffness matrix and stresses are decayed to zero in a constitutive equation when a certain fracture criterion is met. However, since a relatively large element represents the crack tip on the crack path and gradients of stress-strain fields are increased dramatically in the localization zone, it tends to yield an unstable solution and causes ill-conditioned problems during simulation. So, mesh refinement is required for an accurate solution.

The adaptive element method (ARM) may reduce mesh dependency and provide a more accurate solution. The ARM offers a stable and accurate solution because a finer mesh is applied around the crack tip for solution stability. However, the adaptive scheme is difficult and expensive to apply for 3D crack propagation because the portioned elements by crack surface are adapted at every step of crack propagation. Also, an error could be introduced by element adaptation when a new variable is mapped.

The interelement crack method is similar to the cohesive zone method (CZM), in which the crack grows through the element edges. The element edges are restricted by cohesive law, and the method gives simple and fast crack trajectories in the 2D crack-propagation problem. In CZM, the crack path is initially placed on crack edges, so the method is not suitable for arbitrary crack path growth. Also, the results of the method are very sensitive to the size and shape of the element mesh (Rabczuk et al. 2008). In addition, 3D crack trajectories are not available for the method because it depends on a mesh and has high computational cost.

In the cohesive element method (CEM), a fracture is modeled by recourse to an irreversible cohesive law embedded into the cohesive elements. In near-tip fields, the surface-separation processes need to be considered in the fracture criterion. Those separation processes are modeled by cohesive theories of fracture and cohesive elements (Pandolfi et al. 2000). Because the crack path grows continuously during the simulation, the uncracked part has the same stiffness matrix, and only the cracked part is updated at every time step. Like CZM, the method is also sensitive to the size and shape of the element mesh. At the crack tip, the stress singularity should be carefully treated using

the cohesive stress relationship. Otherwise, it causes an instability problem during simulation.

The extended finite element method (XFEM) was introduced to treat arbitrary cracks, while overcoming mesh dependency and crack growth without remeshing (Belytschko and Black 1999). The general XFEM form includes the standard finite element function and an enrichment function that can explain crack-path influence. The enriched elements on the crack path can produce a smooth stress distribution, and the XFEM has less dependent mesh refinement than the general finite element method. Therefore, the XFEM is useful for the relatively accurate approximation of solutions with non-smooth discontinuities and singularities in small computational domain. However computational costs of the method are higher than other methods because the character of the matrix is sparser. Also, it is difficult to apply 3D equivalent hydraulic pressurization scheme inside of element using the enrichment method, because there are often more than one enrichment term. That means that these additional enrichment functions, including the shape function, should be developed as totally new approximations for 3D hydraulic fracture propagation.

In the mesh-free method (MM), the crack can simulate arbitrarily through the discrete cohesive crack segments. The mesh-free method integrates the weak-form overlapping cohesive nodes through the entire domain of influence of a node. The nodes influenced by the crack path circle are modified by specific functions including the Lagrange multiplier method and the penalty method, similar to the enrichment of XFEM. But the newly developed mesh-free method is not enough to verify and need a

great amount of work to develop for 3D hydraulic fracturing. In addition, because of the nonpolynomial form of most meshless shape functions, the numerical integration of the weak form is very difficult. So the MM has difficulty implementing 3D crack modeling and also has a high computational cost problem.

Consequently, the critical review in this section shows that all methods have both pros and cons in several respects. Considering only numerical applicability for hydraulic fracture propagation, EDM is the simplest method to apply, but its accuracy level is low. MM and XFEM are applicable to use, but both methods require significant time and effort to apply them in 2D/3D hydraulic fracturing simulation. CZM and CEM have recently been used for 2D hydraulic fracturing (Carrier and Granet 2012; Sarris and Papanastasiou 2012), but both methods have a significant restriction on the crack path, since a pre-assigned fracturing path is required. ARM is applicable and benefits from the accuracy of the solution, but high computational cost and difficulty of implementation are restrictions of the method. In addition, all methods must develop an additional moving-boundary scheme to apply correct equivalent hydraulic force to certain nodes detected by crack path.

In this dissertation, we developed new crack propagation model based on element splitting idea and advantages from CEM and XFEM. First, we assumed that crack path can grow in arbitrary direction within existing mesh information, which is similar with XFEM. That means there is no pre-assigned crack path in numerical domain. Second, when each element is identified as a failed element, stress/strain curve of the failed element is softened by a damage evolution law, which is similar with CEM. Third,

the crack path through the inside of elements is expressed without modifying the mesh for simplicity of implementation with low computational effort, which gives huge numerical advantages when we applied a moving-boundary scheme of hydraulic forces as calculating the fracture surface by the element splitting idea. The specific algorithm of the new crack propagation model is explained in Appendix B and C.

3. CONSTITUTIVE MODELING OF BRITTLE ROCK

Various types of mathematical theories such as linear elastic, hyperelastic, plastic, viscoelastic, and viscoplastic are available to describe a realistic constitutive model of material behavior. However, constitutive modeling of realistic behavior of heterogeneous rock is quite difficult using mathematical formulation via numerical methods, because of the largely discontinuous, anisotropic, inhomogeneous and nonelastic behavior of a rock mass (Harrison and Hudson 2000). Failure mechanism and fracture patterns are strongly dependent on the mechanical behavior of rock, so that finding a suitable constitutive model for the rock is an essential part of rock engineering.

In this work, the idealized elastic/brittle constitutive relations of the brittle materials illustrated in Figure 3.1 are used. The idealized elastic/brittle behavior of brittle rock is modeled by employing the elastic/brittle constitutive model using continuum damage mechanics. When brittle rock is under compressive forces, the mechanical behavior of the rock is changed by its confining pressure. Normally, as the confining pressure increases, the brittle rock has larger compressive strength and more ductile behavior, so confining pressure-dependent constitutive relations were developed using compressive-strength data from the experimental results. The constitutive relations needed to be calibrated with experimental results, since realistic strain-softening behavior must be described physically to predict damage and failure mechanisms of brittle materials and capture macroscopic cracking behavior (Bazant 1986; Mazars and Pijaudier-Cabot 1989).

The material degradation of the brittle rock, where a localized, severely damaged zone defines a failure plane in the form of a macrocrack, was macroscopically characterized using the idealized elastic/brittle damage model. The damage variable represents average material degradation and considers various damage types at the micro scale such as nucleation, coalescence, and growth of voids, microcracks, cavities, and other microscopic defects (Budiansky and O'Connell 1976; Lubarda and Krajcinovic 1993; Voyiadjis and Kattan 2009).

The failure mechanism of brittle material is believed to involve growth of microcracks through the interaction of material inhomogeneities and applied stresses. Coalescence of these microcracks leads to macroscopic crack and damaged zone expansion as microcrack population and intensity increase. The brittle behavior is characterized by a sudden drop of the stress/strain curve right after the yield point caused by loss of cohesion, while ductile behavior is characterized by continuous deformation without downward change of the stress/strain curve after the yield point (Mogi 2007).

The initiation and growth of damage variables can be described using CDM (Kachanov 1986). Usually, the critical value of the damage variable is used to decide the macroscopic crack growth. However, an important issue is how a macroscopic crack can be defined and at what amount of damage. Usually, the critical value chosen is in the range of 0.5 to 0.9 (Al-Rub and Darabi 2010; Kachanov 1986; Krajcinovic 1989; Krajcinovic 2000). In principle, CDM can be applied to porous materials weakened by microvoids of all shapes (Krajcinovic 2000).

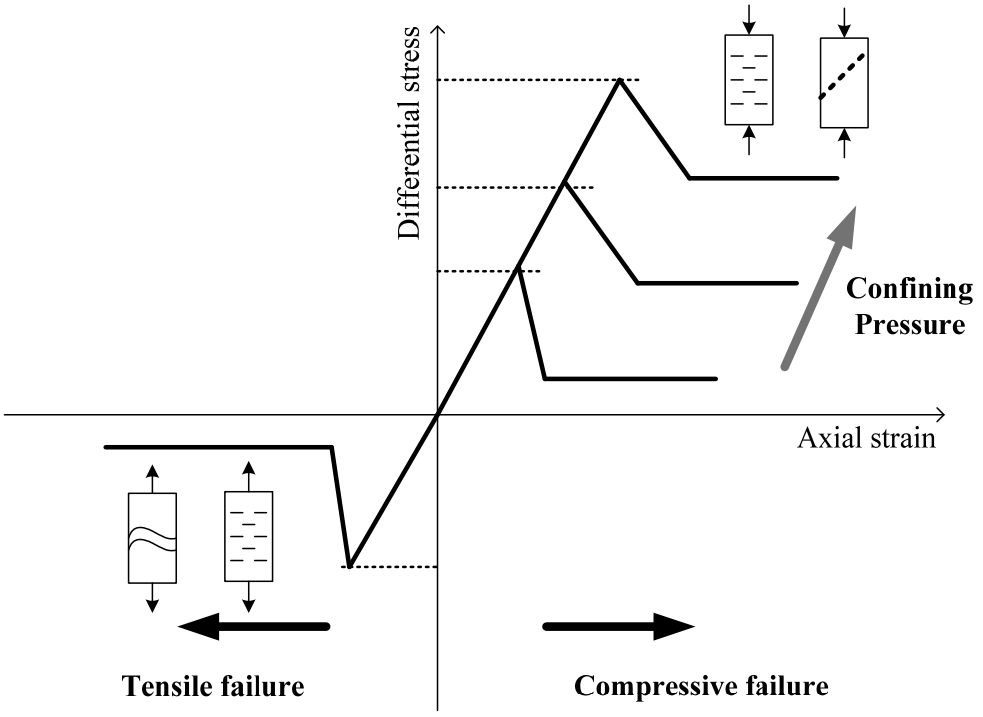

Figure 3.1. Idealized stress/strain behaviors based on compressive and tensile failure corresponding to confining pressure variation

3.1 Continuum damage mechanics

The initial model of CDM was proposed by Kachanov(1958). From a microscopic point of view, breakage of atomic bonds causes damage and crack initiation. The breakage means degradation of material strength, and material strength degradation can be represented by a damage variable. Depending on material behavior (isotropic, transversely isotropic, anisotropic, etc.), a scalar, vector, or tensor damage variable (D, D_{ij}, D_{ijkl}) can be used to describe the isotropic or anisotropic stiffness degradation (Krajcinovic and Fonseka 1981; Voyiadjis and Kattan 2009).

Among the different types of damage variable, the scalar damage variable is frequently used for an isotropic material for simplicity. The assumption of an isotropic damage variable has been found to be effective in predicting local failure in structural components (Lemaitre 1984). The concept of scalar damage parameter and the "effective stress" approach were introduced by Kachanov(1958) and Rabotnov(1969). From the force balance $\sigma A = \sigma_{eff} \overline{A}$, where $\overline{A} = A - A_D$ is the effective area or the undamaged area in the total area A in Figure 3.2 (a)-(b).

$$\sigma = \frac{\overline{A}}{A} \sigma_{eff} \tag{3.1}$$

For an isotropic case, the damage parameter has the same value in all directions, and it can be defined as:

$$D = 1 - \frac{\overline{A}}{A} = \frac{A_D}{A}, \tag{3.2}$$

where A is the total area of the specimen and A_D is the total damaged parts of the area (all microcracks, voids formed) of the specimen in Figure 3.2(a). Propagation and coalescence of the microcracks lead to growth of the damage variable. By substituting Eqn. (3.2) into Eqn. (3.1), the effective stress is expressed as:

$$\sigma_{eff} = \frac{\sigma}{1 - D}, 0 \le D < 1 \tag{3.3}$$

Because the damage model is isotropic, either damaged or undamaged material is still under linear elastic behavior before the strain level reaches breaking point, so the effective stress is governed by the Hooke's law (Kachanov 1986):

$$\sigma_{eff} = E\varepsilon \tag{3.4}$$

Combining Eqn. (3.3) and (3.4), the stress/strain relation is obtained as:

$$\sigma = (1 - D) E \varepsilon \tag{3.5}$$

In CDM, the damage parameter D is considered a macroscopic-state variable that affects stiffness degradation of the material (Kachanov 1986), so that the effective Young's modulus is defined as:

$$E' = (1 - D) E \tag{3.6}$$

The damage evolution equation can be characterized by a function of strain as the simplest method, as described in Figure 3.2(c) (Jirasek 2004; Jirasek and Zimmermann 1998).

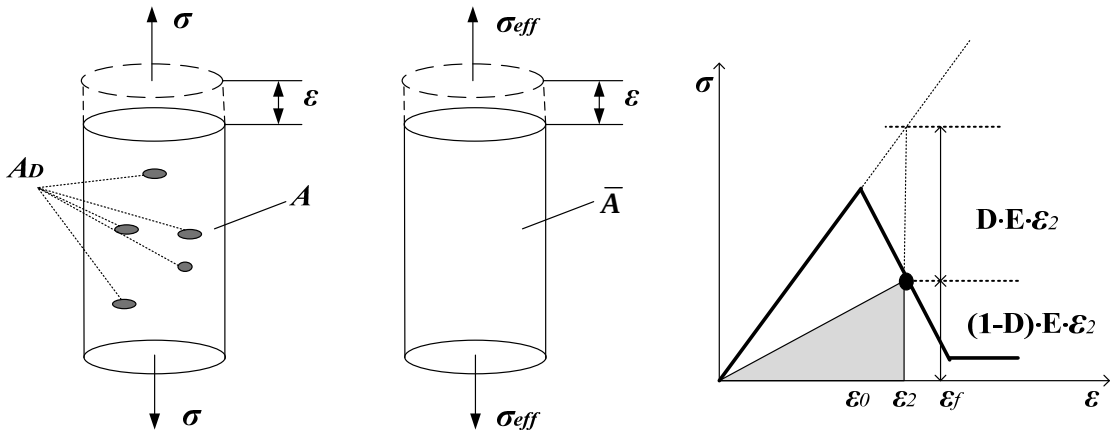

Figure 3.2 (a) Damaged configuration, (b) Effective stress equivalence principle (Kachanov 1986) (c) Linear softening damage evolution (Jirasek and Zimmermann 1998)

3.2 Nonlocal damage model

Local strain-softening phenomena modeled using finite element analysis causes spurious mesh sensitivity due to strain localization in the damaged zone. In order to avoid the strain localization, nonlocal continuum approach was introduced (Erigen and Edelen 1972; Kunin 1968) and the nonlocal theory was extended to the nonlocal damage model by (Bazant and Pijaudier-Cabot 1988; Pijaudier-Cabot and Bazant 1987). The nonlocal damage model is formulated to explain the mesh size effects and prevent instability of strain localization. In the nonlocal theory, the stress is considered as a function of the mean of the strain from a certain representative volume of the material, which plays a central role in the physics of heterogeneous materials to predict their effective properties. The representative volume is defined by a characteristic length. The characteristic length is usually determined by microstructural statistics using image analysis (Graham and Yang 2003). For concrete, the characteristic length can be roughly estimated as 2 to 7 times the maximum aggregation size (Bazant and Pijaudier-Cabot 1988).

The principle idea of the nonlocal damage theory is that the nonlocal damage variable is defined by spatial averaging over the representative volume (Bazant and Pijaudier-Cabot 1988). The spatial averaging form was derived from a thermodynamic approach, and the state of material can be characterized by its free energy density, which is defined as:

$$\rho\psi = \frac{1}{2}\sigma_{ij}\varepsilon_{ij}, \tag{3.7}$$

where ψ is the free energy density, ρ is mass density, and σ_{ij} and ε_{ij} are the stress and strain tensors. From the stress/strain relation for an isotropic damage:

$$\sigma_{ij} = (1 - D) C_{ijkl} \varepsilon_{kl} \tag{3.8}$$

Substituting Eqn. (3.8) into Eqn. (3.7), the following relation is obtained for the specific free energy, $\rho\psi$, per unit volume:

$$\rho\psi = \frac{1-D}{2} \varepsilon_{ij} C_{ijkl} \varepsilon_{kl} \tag{3.9}$$

In Figure 3.2(c), when the material is damaged, the strain energy in the failed zone begins release the stored energy during the failure process, so that the damage variable could be defined by the rate of strain energy dissipation. The energy dissipation rate is expressed as:

$$\varphi = -\frac{\partial(\rho\psi)}{\partial t} = -\frac{\partial(\rho\psi)}{\partial D}\frac{\partial D}{\partial t} = Y\dot{D}\,, \tag{3.10}$$

and the damage energy release rate, which is the driving force for the growth of damage, is defined as (Pijaudier-Cabot and Bazant 1987):

$$Y = -\frac{\partial(\rho\psi)}{\partial D} = \frac{1}{2} \varepsilon_{ij} C_{ijkl} \varepsilon_{kl} \tag{3.11}$$

Based on the nonlocal damage theory (Pijaudier-Cabot and Bazant 1987), the mean value of the damage energy release rate is evaluated over the representative volume. The spatial average of the damage energy release rate over the representative volume is defined as:

$$\tilde{Y}_e = \frac{1}{V_r} \int_V Y \, dV \,, \tag{3.12}$$

where V_r is a representative volume.

3.3 Damage evolution law for brittle rock

Employing an idea from the nonlocal damage theory, the damage energy release rate was evaluated by spatial averaging integral over the damaged volume instead of the representative volume:

$$\tilde{Y}_{ed} = \frac{1}{V_d} \sum \int_{V_{ed}} Y \, dV_{ed} \tag{3.13}$$

where V_d is a total volume of damaged elements and V_{ed} is a damaged element volume. In Figure 3.3, constitutive relationships of the brittle rock are differently described by failure type, so that a threshold value for the damaged release rate is calculated for tensile and shear failure, respectively. Each damage evolution equation for tensile and shear failure can be defined by a function of the damage energy release rate for monotonic damage growth.

The type of softening curve could be obtained from a realistic shape of the stress/strain relationship on the basis of experiments. In this work a linear strain softening, schematically shown in Figure 3.3, was assumed for numerical simplicity. In Figure 3.3, tensile strength (σ_T) and compressive strengths (σ_{c1}, σ_{c2}) by various confining pressures are obtained from experimental data. Based on the material strength information, the material coefficients (ε_t, ε_{tr}, ε_{c1}, ε_{c1r}, ε_{c2}, ε_{c2r}) are determined to control the relationships. In case of a heterogeneous material, the constitutive relationship of each element is varied by employing random variables.

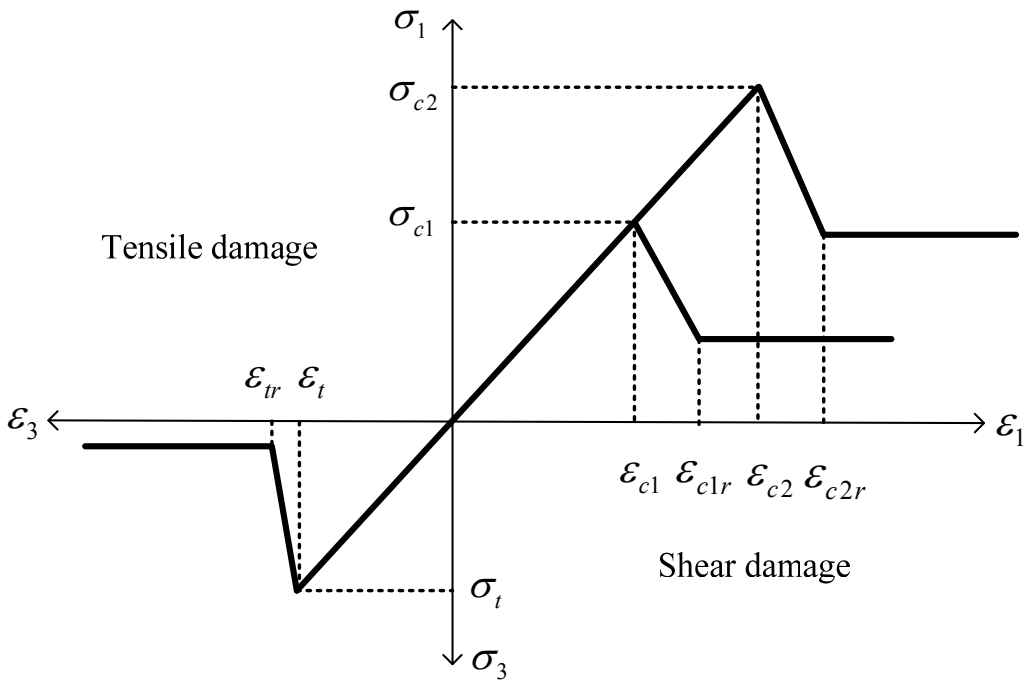

Figure 3.3 Schematic constitutive relationship based on tensile and shear damage

To calculate the damage energy release rate of Eqn. (3.11), the elastic strain energy per unit volume of linear elastic material is used as follows:

$$\tilde{U}_e = \frac{1}{2}\sigma_{ij}\varepsilon_{ij} \tag{3.14}$$

The elastic strain energy per unit volume is rewritten using the stress/strain relation of an isotropic solid, which is described as:

$$\sigma_{ij} = \lambda\delta_{ij}\varepsilon_{kk} + 2\mu_L\varepsilon_{ij} \tag{3.15}$$

where δ_{ij} is the Kronecker delta, and Lamé's constants λ, μ_L are defined as below:

$$\lambda = \frac{\nu E}{(1+\nu)(1-2\nu)}, \mu_L = \frac{E}{2(1+\nu)} \tag{3.16}$$

Then, substituting into Eqn. (3.14), the elastic strain energy per unit volume can be expressed in terms of strains:

$$\tilde{U}_e = \frac{1}{2}\lambda\delta_{ij}\varepsilon_{kk}\varepsilon_{ij} + \mu\varepsilon_{ij}\varepsilon_{ij} \tag{3.17}$$

In this dissertation, the damage dissipated energy rate is assumed to decrease linearly with the principal strain and the damage variable has a different stain softening curve for tensile and shear failure, which are determined by the Mohr-Coulomb failure criterion. The evolution equation of the damage variable is modeled by the damage energy release rate and the softening function, $g(\varepsilon)$ which is determined using:

$$g(\varepsilon) = \begin{cases} 0 & \text{if } \bar{\varepsilon} \le \varepsilon_t \ \ \bar{\varepsilon} \ge \varepsilon_{tr} \\ \dfrac{(s-1)\tilde{Y}_{e0}}{\varepsilon_t - \varepsilon_{tr}} & \text{if } \varepsilon_t < \bar{\varepsilon} < \varepsilon_{tr} \end{cases} \tag{3.18}$$

where ε_t, is the maximum tensile stain, and ε_{tr}, released tensile strain for tensile damage and $\tilde{Y}_{e0}$ is the initial value of damage energy release rate, ε_t is determined by the tensile strength, σ_T, in Figure 3.3, and s is a parameter for strain softening rate, which has $0<s<1$. In Figure 3.4, the softening parameter for the tensile damage is assumed 0.1, while the softening parameter for the shear damage is decided by a confining pressure. We assumed the softening parameter is increasing linearly with the confining pressure. So, the softening parameter for the shear damage is calculated by s=Pc(i)/max(Pc(n))*0.99, where Pc(i) indicates a current confining pressure and max(Pc(n)) represents the maximum confining pressure during triaxial compression tests. If the confining pressure is high, the softening parameter becomes closed to 0.99. That means the stress/stress curve does not softening and the material is nearly perfect

plasticity. When the state of the current equivalent strain, $\bar{\varepsilon}$, is between ε_t and ε_{tr}, the dissipated strain energy is computed by multiplying of the softening function with $\left(\bar{\varepsilon}-\varepsilon_t\right)$. After the equivalent strain is over the softening region ($\bar{\varepsilon} \geq \varepsilon_{tr}$), the damage variable is gradually increased up to 0.99, which is calculated by an equation of $1-s\cdot\tilde{Y}_{e0}/\tilde{U}_e$. The damage evolution law can then be expressed as:

$$D=\begin{cases} 0 & \text{if } \bar{\varepsilon} \leq \varepsilon_t \\ 1-\dfrac{g(\varepsilon)\cdot\left(\bar{\varepsilon}-\varepsilon_t\right)+\tilde{Y}_{e0}}{\tilde{U}_e} & \text{if } \varepsilon_t < \bar{\varepsilon} < \varepsilon_{tr} \\ 1-\dfrac{s\cdot\tilde{Y}_{e0}}{\tilde{U}_e} & \text{if } \bar{\varepsilon} \geq \varepsilon_{tr} \end{cases} \tag{3.19}$$

In cases of shear damage, ε_{c1} and ε_{c2} are used instead of ε_t in Eqn. (3.18) and (3.19). ε_{c1r} and ε_{c2r} are calculated when the shear failure is detected. The shear strains are determined by compressive strength σ_{c1} and σ_{c2}, which are obtained from experimental results for a rock. All these tensile and shear strengths are also varied through the simulation domain (when needed) by employing random variables. Hence, the constitutive relationship of each element could vary by confining pressure, material heterogeneity, and type of failure.

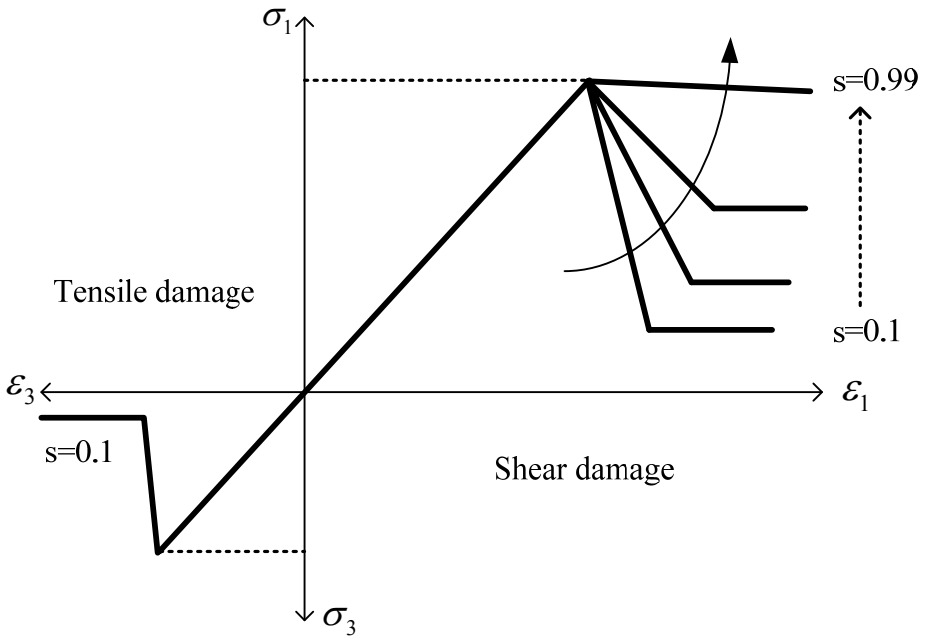

Figure 3.4 Schematic of softening parameter variation by tensile and shear damage

3.4 Conclusions

In this section, an elemental scale constitutive model of the brittle rock is developed using an elastic/brittle damage model. Practical behavior of the brittle rock is largely discontinuous, anisotropic, inhomogeneous, and non-elastic, and it is quite difficult to replicate the realistic behavior of the brittle rock using mathematical formulations or numerical modeling. Therefore, a simplified elastic/brittle constitutive model gives both numerical simplicity and less computational efforts. Damage mechanics can represent the degradation of the rock and discontinuous fracture behavior. When the confining pressure applied to the specimen, the rock requires higher strength and shows more ductility in the stress-strain behaviors. In addition, as the nonlocal damage theory (Pijaudier-Cabot and Bazant 1987) was employed, the simplified

elastic/brittle model could avoid the mesh sensitivity issue. Numerical examples for the mesh dependency problems are shown in section 6 and 7.

4. DESIGN METHODOLOGIES FOR HYDRAULIC FRACTURING

In this section, design methodologies of numerical modeling for the hydraulic fracture propagation simulation are introduced using fluid flow and rock deformation analysis coupled with fracture propagation modeling. First of all, capturing all the key issues for the hydraulic fracturing process is important. The hydraulic fracture propagation process involves fluid injection at high pressure through a perforated borehole into the payzone layer. The injected fluid creates fracture propagation by inducing rock failures. During the hydraulic fracture propagation process, fracturing fluid flow, rock deformation, and fracture propagation interact simultaneously. Hence, the hydraulic fracturing process can be described as a problem of fluid-driven fracture, which is a complex problem because the sequential fracture propagation process is induced by fluid injection. The sequential fluid-driven fracturing processes are briefly described as the injected hydraulic forces are induced by rock deformation; the rock deformation leads the fracture dimensions, including fluid volume and fluid pressure, to change; the fracture pressure distribution induces pore pressure and stress changes around fractures; the stress change at crack tip can lead to local failures in the rock mass. That is, the complex interaction problem of the fluid and solid mechanics, such as non-Newtonian fluid, turbulence flow, leakoff phenomena and geometrical complexity of flow channel (roughness and tortuosity of the fracture network) is involved in the hydraulic fracturing treatment design.

Therefore, coupling the fluid flow through a fracturing path, rock deformation, and fracture propagation is an essential part of the hydraulic fracturing simulation design. In this paper, rock mass was modeled as a fully coupled thermo-poroelastic medium. Rock responses about effective stresses, pore pressure, and temperature were solved via the fully coupled THM model. The governing equations of equilibrium, fluid flow, and heat transfer in the reservoir were employed in a fully coupled manner in an incremental form and implemented in a finite element formulation. Motion of the fluid flow inside fractures was modeled using a lubrication equation, since an important feature of hydraulic fracturing is the existence of pressure gradients inside the fractures.

In addition, numerical description of fracture propagation within the finite element formulation is important for a moving-boundary scheme through a propagated fracturing path. The fracture propagation is modeled using damage mechanics and element partition methodology (EPM) (Huang and Zhang 2010), which provides a numerical algorithm for pressurized fracture surfaces as the cracked element are split virtually during simulation. Finally, the full coupling of the fluid flow and rock deformation analysis is solved simultaneously for the pressure field in the fluid, with the crack opening at each time step.

4.1 Rock response analysis using Thermo-Hydro-Mechanical model

The fully coupled processes involving thermal, hydrologic and mechanical effects have been studied for a nuclear-waste repository in fractured rocks during the early 1980s (Stephansson et al. 1996; Tsang 1987; Tsang 1991; Tsang et al. 2004).

Through the international cooperative DECOVALEX (acronym for DEvelopment of COupled models and their VALidation against Experiments) project, these coupled processes have made significant progress and results have been published in a series of reports and books (Jing et al. 1993; Jing et al. 1995; Jing et al. 1996; Stephansson et al. 1996). Similar coupling procedure operates in the gas/oil recovery industry and geothermal energy development.

The coupled THM process can be extended for chemical effect by the swelling of shale for wellbore stability analysis (Ghassemi and Diek 2003; Ghassemi et al. 2009; Zhou and Ghassemi 2009). The coupled THM process is described using the constitutive relations for the porous matrix, the pore space, and the fluid and heat diffusions within the conservation laws for momentum, mass, and energy. Terzaghi's 1D consolidation theory of soils was proposed for its pore-pressure effect on soil deformation (Terzaghi 1923) and it was extended to linear poroelasticity for elastic porous media considering effective stress change by variations of pore pressure under fluid loading using the isothermal consolidation problem (Biot 1941).

Hooke's law of elasticity with the concept of infinitesimal displacement hypothesis, Darcy's law of flow in porous media, and Fourier's law of heat transfer were adopted. The effective heat transfer concept, which generally assumes that temperature is the same in both rock solids and pore fluid, was also adopted since local heat transfer is rapid enough for equilibrium of temperature, unlike in global heat and fluid diffusion models.

Then, based on the framework of Rice and Cleary formulation (Rice and Cleary 1976) and Kurashige's approach for thermal effects (Kurashige 1989), the thermo-poroelastic model was extended to combined thermal and hydraulic stress for fully-saturated homogeneous rock (McTigue 1986; Palciauskas and Domenico 1982). The deformation processes are considered as quasistatic states, since the inertia effect of rock mass is assumed to be neglected (Li 1998).

4.1.1 Constitutive relations

In deriving the coupled THM equations, the total stress, σ_{ij}, (*tensile positive convention*); pore pressure, p, for compressive positive; and temperature, T, are considered as the coupled variables. The general constitutive equations for fully saturated thermoelastic porous material can be written based on thermodynamics principles as follows (Cleary 1976; Cleary 1977);

$$\varepsilon_{ij} = C_{ijkl}\sigma_{kl} + B_{ij}p + \alpha_{ij}^{T}\delta_{ij}T \tag{4.1}$$

$$\zeta = B_{kl}\sigma_{kl} + \beta p + \alpha_{p}^{T}T \tag{4.2}$$

where σ_{ij} denotes the components of the total stress tensor, ε_{ij} is the strain tensor from the solid displacements, p and T are the pore pressure and temperature, ζ is the variation of the fluid content per unit volume of the porous material, α_{ij}^{T} is the linear thermal expansion coefficient tensor, and α_{p}^{T} is the thermal expansion coefficient of the pore space. The elastic tensors C_{ijkl} and B_{ij} for isotropic materials are described as:

$$C_{ijkl} = \frac{1}{4G}\left(\delta_{ik}\delta_{jl} + \delta_{il}\delta_{kl} - \frac{2}{1+\nu}\delta_{ij}\delta_{kl}\right) \tag{4.3}$$

$$B_{ij} = \frac{3(\nu_u - \nu)}{2GB(1+\nu)(1+\nu_u)}\delta_{ij} \tag{4.4}$$

where B is Skempton's pore pressure coefficient defined as (Skempton 1954):

$$B = \frac{3(\nu_u - \nu)}{\alpha(1-2\nu)(1+\nu_u)} \tag{4.5}$$

$$\beta = \frac{1}{B}\left(\frac{1}{K} - \frac{1}{K_s}\right) - \frac{\phi}{K_f} \tag{4.6}$$

$$K = \frac{2G(1+\nu)}{3(1-2\nu)} \tag{4.7}$$

Kurachige's work introduced an assumption that pores thermally expand while their volume remains the same, so the volumetric thermal expansion coefficient of pore space can be expressed as:

$$\alpha_p^T = \phi\alpha_m \tag{4.8}$$

K and G are bulk and shear moduli, ϕ is the porosity, K_s are the bulk of solid matrix, α is Biot's coefficient, and ν and ν_u are the drained and undrained Poisson's ratio. Rearranging Eqn. (4.1) using above relations and presenting it in a more convenient form,

$$\varepsilon_{ij} = \frac{1}{2G}\left(\sigma_{ij} - \frac{\nu}{1+\nu}\sigma_{kk}\delta_{ij}\right) + \frac{\alpha(1-2\nu)}{2G(1+\nu)}p\delta_{ij} + \frac{\alpha_m}{3}T\delta_{ij} \tag{4.9}$$

where σ_{kk} is the first invariant of the stress tensor:

$$\sigma_{kk} = \frac{2G(1+\nu)}{(1-2\nu)}\varepsilon_{kk} - 3\alpha p - \frac{2G(1+\nu)}{3(1-2\nu)}\alpha_m T \tag{4.10}$$

Eqn. (4.9) can be presented in terms of strain:

$$\sigma_{ij} = 2G\varepsilon_{ij} + \left(K - \frac{2G}{3} \right) \varepsilon_{kk}\delta_{ij} + \alpha p \delta_{ij} + \frac{2G(1+\nu)}{3(1-2\nu)} \alpha_m T \delta_{ij} \tag{4.11}$$

The change of fluid content also can be presented as:

$$\zeta = \frac{3(\nu_u - \nu)}{2GB(1+\nu)(1+\nu_u)} \delta_{ij}\sigma_{ij} + \frac{1}{B}\left(\frac{1}{K} - \frac{1}{K_s} \right) p - \left((\alpha_f - \alpha_m)\phi \right) \Delta T \tag{4.12}$$

Simplifying Eqn. (4.12) by applying Eqn. (1.10) gives the following relationship:

$$\frac{1}{B}\left(\frac{1}{K} - \frac{1}{K_s} \right) = \frac{9(\nu_u - \nu)}{2GB^2(1+\nu)(1+\nu_u)} \tag{4.13}$$

$$\zeta = \frac{3(\nu_u - \nu)}{2GB(1+\nu)(1+\nu_u)} \sigma_{kk} + \frac{1}{B}\left(\frac{1}{K} - \frac{1}{K_s} \right) p - \left((\alpha_m - \alpha_f)\phi \right) \Delta T \tag{4.14}$$

Substituting Skempton's coefficient, B, into the equation above and simplifying Eqn. (4.14), then summarizing from Eqn. (4.11) and (4.16), finally obtains the following constitutive relations:

$$\sigma_{ij} = 2G\varepsilon_{ij} + \left(K - \frac{2G}{3} \right) \varepsilon_{kk}\delta_{ij} + \alpha p \delta_{ij} + K \alpha_m T \delta_{ij} \tag{4.15}$$

$$\zeta = \frac{\alpha(1-2\nu)}{2G(1+\nu)} \left(\sigma_{kk} + \frac{3}{B} p \right) - \left((\alpha_f - \alpha_m)\phi \right) \Delta T \tag{4.16}$$

where α_m and α_f are the thermal expansion coefficients of solid and fluid.

4.1.2 Conservation laws

Three conservation laws are applied for the coupled THM processes. First, a momentum balance or equilibrium equation with no body force assumption is described as:

$$\sigma_{ij,j} = 0 \tag{4.17}$$

Second, to express effective force of the fluxes of fluid, the fluid flow in porous rock was assumed to be governed by Darcy's law with no phase change:

$$q_i = -\frac{k}{\mu} p_{,i} \tag{4.18}$$

The fluid mass balance equation is obtained as:

$$\frac{\partial \zeta}{\partial t} + q_{i,i} = 0 \tag{4.19}$$

Finally, to express the effective force of the heat transfer, the Fourier equation is used for heat transfer.

$$h_i = -k^T T_{,i} \tag{4.20}$$

The energy balance equation is used for an element unit volume (Combarnous and Bories 1975):

$$\frac{\partial \left(\rho C_t T \right)}{\partial t} + h_{i,i} = 0 \tag{4.21}$$

where ρ and C_t are the mass density and specific heat capacity for the bulk material, k is the permeability, μ is the fluid viscosity, and k^T is the thermal conductivity.

4.1.3 Governing equations

The momentum, fluid mass, and energy balance equations can be combined with the above constitutive and transport equations and yield the following field equations. First, substituting these small deformation relationships into Eqn. (4.15):

$$\varepsilon_{ij} = \frac{1}{2}\left(u_{ij} + u_{ji}\right) \tag{4.22}$$

$$\varepsilon_{kk} = u_{kk} \tag{4.23}$$

The deformation field equation is obtained from Eqn. (4.15) and (4.17):

$$Gu_{i,ij} + \frac{G}{1-2\nu}u_{j,ji} - \alpha p_{,i} - \frac{2G\alpha_m\left(1+\nu\right)}{3\left(1-2\nu\right)}T_{,i} = 0 \tag{4.24}$$

Second, for the fluid-diffusivity field equations, differentiating Eqn. (4.11) and (4.23) twice leads to:

$$\sigma_{ii,jj} = 2G\left(\frac{1+\nu}{1-2\nu}\varepsilon_{kk,jj}\right) - 3\alpha p_{,jj} - \frac{1+\nu}{1-2\nu}2G\alpha_m T_{,jj} \tag{4.25}$$

$$\varepsilon_{kk,jj} = u_{ii,jj} \tag{4.26}$$

Differentiating Eqn. (4.24) with respect to x_i, solving for $u_{ii,jj}$ and substituting into Eqn. (4.26) and then into Eqn. (4.25), the compatibility equation can be obtained in terms of stresses:

$$\sigma_{ii,jj} + \frac{2\alpha\left(1-2\nu\right)}{1-\nu}p_{,jj} + \frac{4G\left(1+\nu\right)}{3\left(1-\nu\right)}\alpha_m T_{,jj} = 0 \tag{4.27}$$

Differentiating Eqn. (4.24) with respect to x_j and substituting into Eqn. (4.27), the following equation can be described:

$$\zeta_{,jj} = \frac{\alpha\left(1-2\nu\right)}{2G\left(1+\nu\right)}\left[\left(\frac{3}{B} - \frac{2\alpha\left(1-2\nu\right)}{\left(1-\nu\right)}\right)p_{,jj} - \frac{4G\left(1+\nu\right)}{3\left(1-\nu\right)}\alpha_m T_{,jj}\right] - \gamma_2 \Delta T_{,jj} \tag{4.28}$$

Then, solving for $p_{,jj}$ from Eqn. (4.28) and substituting into Eqn. (4.19), the fluid diffusivity field equation can be obtained as:

$$\dot{\zeta} = C^f \left[\zeta_{,jj} + \left(\frac{2\alpha(1-2\nu)}{3(1-\nu)} - \gamma_2 \right) T_{,jj} \right] \tag{4.29}$$

where, C^f is the fluid diffusion coefficient, which is defined as:

$$C^f = \frac{2kB^2G(1-\nu)(1+\nu_u)^2}{9\mu(1-\nu_u)(\nu_u-\nu)} \tag{4.30}$$

Then, differentiating Eqn. (4.16) with respect to time and substituting into Eqn. (4.19) with Darcy's law [Eqn. (4.18)], and applying the relationships of σ_{kk} and ε_{kk}, the fluid diffusion field equation can be expressed in terms of pore pressure:

$$\dot{p} = M\left[kp_{,jj} - \alpha\dot{\varepsilon}_{kk} + \left(\alpha\alpha_m + (\alpha_f - \alpha_m)\phi \right)\Delta\dot{T} \right] \tag{4.31}$$

where M is the Biot modulus, which is defined as the change of fluid contents as a result of pore pressure variation under constant volumetric strain per unit volume.

$$M = \frac{2G(\nu_u - \nu)}{\alpha^2(1-2\nu)(1-2\nu_u)} \tag{4.32}$$

Finally, for the thermal diffusivity field equation can be obtained from Eqn. (4.20) and (4.21) as:

$$\dot{T} = c^T \nabla^2 T \tag{4.33}$$

where c^T is the thermal diffusivity coefficient for the bulk material.

$$c^T = \frac{k^T}{\rho C_t} \tag{4.34}$$

where ρ and C_t are the mass density and specific heat capacity for the bulk material, and k^T is the thermal conductivity.

Finally, three governing equations (Eqn. (4.29), (4.31), (4.33)) for the coupled THM processes are derived from the momentum, fluid mass, and energy balance equations combined with the constitutive and transport equations above. For convenient forms for the fully coupled Thermo-Hydro-Mechanical model, following governing equations could be written;

$$\left(K+\frac{G}{3}\right)\nabla\left(\nabla\cdot\mathbf{u}\right)+G\nabla^2\mathbf{u}+\mathbf{m}\left(\alpha\nabla p+\gamma_1\nabla T\right)=0 \tag{4.35}$$

$$\alpha\left(\nabla\cdot\dot{\mathbf{u}}\right)+\beta_p\dot{p}-\frac{k}{\mu}\nabla^2 p-\gamma_2\nabla\dot{T}=0 \tag{4.36}$$

$$\dot{T}-c^2\nabla^2 T=0 \tag{4.37}$$

where **u** is displacement vector and $\mathbf{m}=[1,1,1,0,0,0]^{\mathrm{T}}$ for 3D problems. The coefficients in Eqn. (4.35) and (4.36) are defined as following;

$$\beta_p=\frac{\alpha-\phi}{K_s}+\frac{\phi}{K_f} \tag{4.38}$$

$$\gamma_1=K\alpha_m \tag{4.39}$$

$$\gamma_2=\alpha\alpha_m+\left(\alpha_f-\alpha_m\right)\phi \tag{4.40}$$

Then the coupled equations are usually treated by numerical solution techniques using FEM, BEM, FDM, and FVM for practical conditions such as nonlinearity, anisotropy, heterogeneity, and complex geometries (Börgesson et al. 2001; Li 1998; Millard 1996; Noorishad and Tsang 1996; Noorishad et al. 1992; Rutqvist et al. 2001; Schrefler 2001). Among these numerical methods, FEM formulation is popularly used; and previously, the 3D, fully coupled, and nonlinear THM model has been developed

within a finite element formulation using damage mechanics (Lee 2011; Zhou and Ghassemi 2009). Details of the finite element formulation for the fully coupled THM model are described in Appendix A.

4.1.4 Poroelastic parameter changes

Since mechanical behavior of the fully coupled THM model is controlled by damage mechanics. It is necessary to consider the change of the poroelastic parameters such as bulk modulus, Biot's coefficients, and other related parameters (β_p, γ_1, γ_2) and when failure is detected and stress-strain relation is no longer elastic. So, based on the status of the effective stress at a gauss point of an element, type of failure is decided by the Mohr-Coulomb failure criterion with tension cut-off and damage variables are calculated by the damage evolution law proposed in section 3. We used linear 3-node triangular element for 2D simulation and 4-node tetrahedron element for 3D simulation in this dissertation and both triangular and tetrahedron elements have one Gaussian point. So, according to the damage variable at the gauss point of the failed element, the poroelastic parameters are newly calculated. Since the effective Young's modulus is updated by $E' = (1-D)E$, the bulk modulus should be re-calculated by $K = E'/3(1-2\nu)$. In addition, we assumed that Biot's coefficient is changed to 0.99 when the damage variable is over 0.8. By the changes of the bulk modulus and Biot's coefficient, related parameters (β_p, γ_1, γ_2) are updated accordingly.

4.1.5 Time step of the coupling process

The complexity of the THM problem is often attributed to uncertainty of parameter values and unpredictable geometrical complexities of rock fractures with various dimensions under thermal, hydraulic, and mechanical loadings (Jing 2003). Numerically, the coupled THM process is a challenge issue because of wide differences among the three processes in temporal and spatial scales (Tsang et al. 2004). While the thermal effect has relatively longer time and spatial scales, mechanical effect has a shorter time scale. This is because mechanical response can transfer with the speed of elastic waves, and various dimensions of fractures, joints and faults dominated its deformability (Tsang 1991). Also, hydraulic effect is sensitive in both small-scale pore distribution and fracture networks with longer flow and solute transport time. Hence, finding an appropriate value for the time step is a critical aspect of the coupling process. The time increment should be small enough to capture the rock deformation accurately because of the high speed of stress waves in porous rock, however, too small of a time increment is not suitable for the fluid flow and the heat transfer equation as changes from one time step to another would be too small. Therefore, generally the smaller time increment is preferred to use. Moreover, smaller time step requires larger computational costs in time-dependent problems, thus the largest possible time step should be chosen by stability and accuracy analysis.

4.2 Fluid flow analysis in fractures

A common approach to fluid flow analysis in rock fractures is to assume idealized parallel plates separated by a constant aperture. In that approach, as described in Figure 4.1, fracture propagation is driven by injection of an incompressible Newtonian fluid at a constant volumetric injection rate Q_i. The incompressible fluid is described by the Poiseuille (lubrication) equation (Batchelor 1967). The lubrication equation can be used to solve the fluid pressure distribution along the fracture. Fluid flow inside the fracture length depends on the aperture, roughness of the walls, and geometry of fractures. When the aperture is large and the fracture surface is smooth, large bulk flow dominates and Darcy's law is no longer valid. The various laboratory results showed that the assumption of laminar flow in the fractures is valid for Reynolds number less than about 2300 (Witherspoon et al. 1980). The Reynolds number can be defined for fluid flow in the fracture:

$$\mathrm{Re} = \frac{\rho_f \bar{u} w_f}{\mu_f} \tag{4.41}$$

where $\bar{u}$ is an average flow velocity in the fracture, μ_f the fluid viscosity of the fracturing fluid, w_f the fracture aperture, and ρ_f is an density of the fracturing fluid. The lubrication equation for the fluid flow is described as:

$$q = -\frac{w_f^3}{12\mu_f}\frac{\partial p_f}{\partial x} \tag{4.42}$$

Two-dimensional fluid flow in the fracture plane is expressed as:

$$\nabla_2 p_f(x,y,t) = -\frac{12\mu_f}{w_f^3(x,y,t)} q(x,y,t) \tag{4.43}$$

$$\nabla_2 \cdot \left[\frac{w_f^3(x,y,t)}{12\mu_f} \nabla_2 p_f(x,y,t) \right] = -v_l(x,y,t) - Q_i(t)\delta(x-x_i, y-y_i) \tag{4.44}$$

Boundary conditions, $\frac{\partial p_f}{\partial n} = 0$ on ∂A_f

$Q_i(t) = Q_{i0}$ at injection point

where ∇_2 is the two-dimensional divergence operator in the fracture plane, μ_f is the fluid viscosity, v_l is the leakoff fluid from the fracture plane, p_f (x,y,t) is the fluid pressure in the fracture, w_f is the fracture aperture, $Q_i(t)$ is the fluid injection rate, and A_f is area of the fracture plane.

So, the fluid flow inside fractures is governed by the Poiseuille equation. The continuity equation and boundary conditions for the fluid flow in the fracture plane describe the point where the fluid injection rate is equal to the fluid flux at a wellbore and no flow at the crack tip is assumed. This boundary condition is valid when the fracturing fluid is fully filled inside the fracture. That is, there is no fluid lag, defined as an empty zone ahead of the fluid front to the fracturing tip, in the fluid flow analysis. If the fluid lag is included, there is additional unknown of the problem (Garagash and Detournay 2000). Tracking of both the fluid front and the fracturing tip is required to account for the fluid lag, however it is not easy since the fluid lag length is unknown. In addition, the no fluid flux boundary condition is difficult to implement in finite element methods, because an arbitrary constant pressure assumption between the fracturing tip and neighbor is impracticable in the coupling algorithm. Because the pressure level

inside the fracture is unknown, the zero flux boundary condition is not applicable to use in FEM. Therefore, zero pressure boundary condition at the fracturing tip is assumed instead of the zero flux boundary condition. Due to opening mode of fracture by hydraulic pressurization near the fracturing tip, pressure level at this region is near zero so the zero pressure assumption is appropriate and practicable to use in FEM.

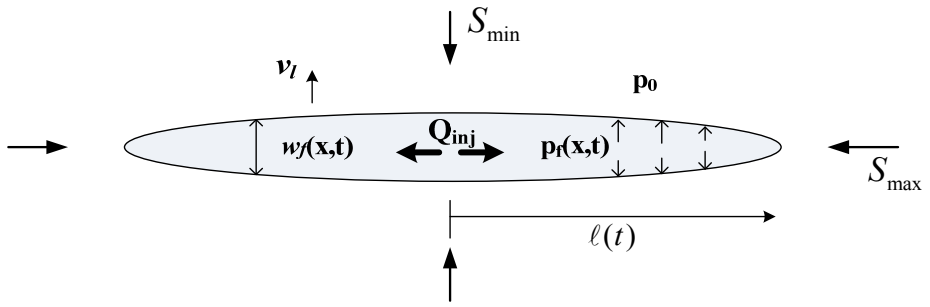

Figure 4.1 The fluid-driven hydraulic fracture propagation process

4.2.1 Fluid leakoff

Leakoff during hydraulic fracturing has been shown to significantly affect fracture growth (Economides and Nolte 2000). The leakoff volume affects the efficiency of the treatment. The injection efficiency, ε_{inj}, can be defined as the volume of fluid in the fracture divided by the total volume of injected fluid. The volume of fluid in the fracture can be defined as the total volume of injected fluid minus the leakoff volume.

$$\varepsilon_{inj} = \frac{V_f}{V_i} = \frac{V_i - V_l}{V_i} \tag{4.45}$$

where V_f is the total volume of the fractures, V_l is the leakoff volume, and V_i is the total injected fluid volume. In this paper, the fluid lost by the injected fluid leaking off into the rock matrix is expressed using Darcy's law:

$$v_l(x,y,t) = -\frac{k_m}{\mu_f}\frac{\partial p(x,y,z,t)}{\partial n} \tag{4.46}$$

where k_m is the rock matrix permeability and n is the normal direction of the fracture plane. The pressure differential between the fracture and the rock matrix and the permeability change of the rock formation are key factors that affect the volume of the leakoff.

4.3 Numerical modeling of fracture propagation

In this dissertation, the fracture propagation model was developed based on three requirements: a possibility to describe continuous crack geometry, a capability to apply a moving-boundary scheme for transition of hydraulic forces through fracturing path, and simplicity of implementation with low computational effort.

To satisfy these requirements, a few guidelines for the fracture propagation model have been established. First, the crack path can only propagate through the inside of elements, as with cohesive element modeling and XFEM. Second, for low computational cost, the crack path should be expressed without modifying the mesh information. No redefinition of the element mesh is required after crack propagation. Third, there is no pre-assigned crack path, which means cracks can grow in arbitrary directions without restriction; this approach puts no limitation on the direction of the

crack propagation. Last, to apply a moving-boundary scheme of hydraulic forces, crack surfaces are assumed inside the cracked element, and the direction of crack propagation is decided by the proportional direction of the maximum principal stress at a fracture tip. Furthermore, a specialized 2D and 3D crack partitioning algorithm was employed to calculate the splitting surface in the cracked element for several scenarios, details in Appendix B.

4.3.1 Comparison of element types

When the fully coupled thermo-hydro-mechanical (THM) analysis is modeled via finite-element methods (FEM), an 8-node quadrilateral element is recommended for use; the 4 corner nodes are used for pore pressures and temperature, while all 8 nodes are used for displacements (Aboustit et al. 1985; Christian 1977). However, in our fracture propagation modeling, the conventional rectangular element mesh is not efficient, because our fracture propagation model assumes that the crack path can grow arbitrarily without redefining mesh information. This approach is hugely beneficial for computational time and simplicity in numerical implementation.

From the standpoint of the fracture propagation approach, if a rectangular mesh is used, the fracture propagation path shows a zig-zag crack band [Figure 4.2(a)]. Moreover, mathematical formulation of the EPM is unavailable and should be developed. Splitting a rectangular element is more complicated than using a triangular element and it may increase computational costs. A triangular mesh [Figure 5.1(b)] clearly represents the arbitrary fracture propagation more flexibly than a rectangular mesh. By the same

token, in the 3D crack propagation problem, a 4-node tetrahedron element has more flexibility to express the arbitrary growth of the 3D crack than an 8-node or 16-node cubic element. We used 3-node triangular and 4-node tetrahedron elements for the fracture propagation model in this project.

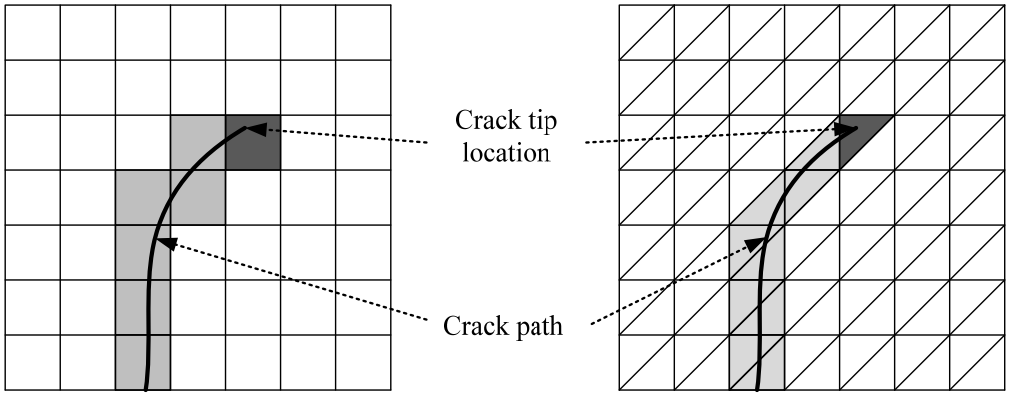

(a) Rectangular element (b) Triangular element

Figure 4.2 Description of fracture path by mesh type (re-drawing from (Bazant and Planas 1997))

4.3.2 Fracture initiation for hydraulic fracturing

Stresses applied to the rock by various loading mechanisms introduce crack nucleation, propagation, interaction, and coalescence, but there is no universally accepted theory for the fracture initiation and propagation. Practically, fractures can be initiated by various failure mechanisms such as tensile, shear and compaction. Among these failure mechanisms, the tensile fracture is dominating failure mechanism in the hydraulic fracture propagation. So, we assumed there is only tensile mode fracture

available at a fracture tip. The fracture initiation criterion is checked at Gaussian point of the crack tip elements. For capturing the hydraulic fracturing failure of the brittle rock, the most commonly used criterion is the maximum tensile strength criterion, defined as:

$$\sigma_3 \geq -\sigma_T, \tag{4.47}$$

where σ_T is a tensile strength of material, and σ_3 is the minimum principal effective stress, which is also the maximum effective tensile stress for poroelastic analysis. So, we checked the fracture initiation criterion at a fracture tip. Once the fracture initiation criterion met, the fracture tip is extended by the fracture propagation algorithm, described in following.

4.3.3 Fracture propagation algorithm

Once the fracture initiation criterion was met at crack tips, the hydraulic fracture is extended with certain length and direction as shown in Figure 4.4. So, tracking the fracture propagation is one of the main issues for hydraulic fracturing simulation. Developing a tracking algorithm for the crack-tip location and path information was necessary to apply correct boundary conditions for fluid pressure inside fractures and for estimating the propagating location of fracture. In order to extend the fracture, crack length criterion for quasi-static crack increments and crack direction criterion for angle of the fracture propagation are required.

First, the crack length criterion is adopted from Paris' law, which is proposed to compute a crack increment by the stress intensity factor under fatigue stress regime (Paris and Erdogan 1963). Usually, the crack tip is assumed to advance in a quasi-static

manner meaning that the crack is propagating at a constant speed in the hydraulic fracture propagation simulation. So every time a crack tip fails, the crack is assumed to advance by a fixed length, but crack should grow at different speeds during various stages because the energy required to propagate the crack could be different at different stages, particularly through heterogeneous materials. So, we adopted the propagation criterion suggested by (Renshaw and Pollard 1994) to extend crack tips at every step. The crack increment is calculated by the energy accumulated at the crack tips.

$$l_{\text{adv}} = l_{\max}\left(\frac{U_{\text{tip}}}{U_{\max}}\right)^{\chi} \tag{4.48}$$

where U_{tip} is the strain energy accumulated at the crack tip, $U_{\max}$ is the maximum stain energy concentration at the crack tip, l_{adv} is an increment crack length, $l_{\max}$ is the maximum increment crack length at any propagation step, and χ is an empirical velocity index. The crack incremental method is a Paris-type law (Paris and Erdogan 1963). Renshaw and Pollard (1994) defined $l_{\max}$ as the initial flaw size, because they assumed the maximum incremental length could be representative of the fracture processing zone (Irwin 1958), which is a nonlinear zone characterized by progressive softening (stress decreases as increasing deformation). Renshaw and Pollard (1994) demonstrated by experimentation that the empirical velocity index of 0.35 yields realistic fracture propagation for the opening mode fractures of brittle rock. However, there is no detail information for the hydraulic fracturing simulation, so that we assumed input parameters by Renshaw and Pollard's crack incremental method. We assumed that $l_{\max}$ is same as a pre-existing crack length and the empirical velocity index is assumed as 0.35. In addition,

U_{max}, the maximum strain energy concentration at the crack tip, is assumed ten times larger than U_{min}, which is the minimum strain energy required to advance the crack tip and defined;

$$U_{\min} = \frac{1}{2}\sigma_T \varepsilon_T = \frac{1}{2E}\sigma_T{}^2 \tag{4.49}$$

where σ_T is the tensile strength of rock, E is Young's modulus.

Second, the fracture propagation angle is assumed to follow the direction of perpendicular to the maximum circumferential tensile stress. It is determined by the normal direction of the maximum tensile stress. Because the fracture propagation induced by hydraulic pressurization is usually attributed to tensile mode opening, the orientation of the failure may simply be determined by the maximum principal stress direction as described in Figure 4.3. The principal angle is computed at the crack tip [Figure 4.4]. The rotation angle, θ_p, is calculated using the normal stresses and the shear stress as follows:

$$\tan\left(2\theta_p\right) = \frac{2\tau_{xy}}{\sigma_x - \sigma_y} \tag{4.50}$$

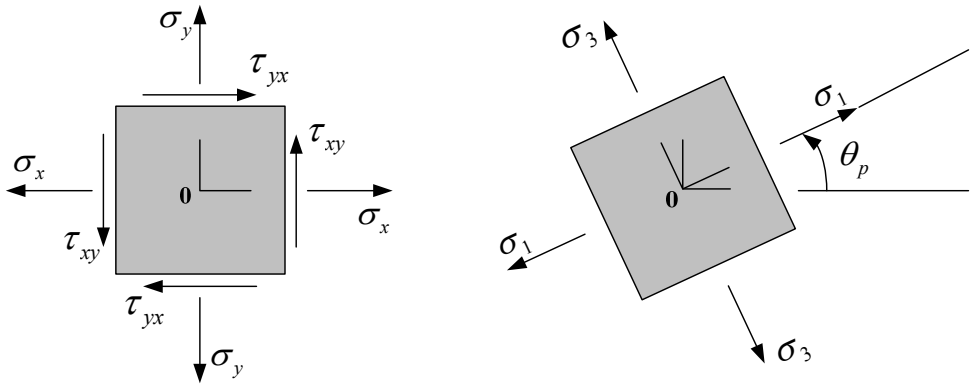

Figure 4.3 Illustration of the maximum principal stress direction

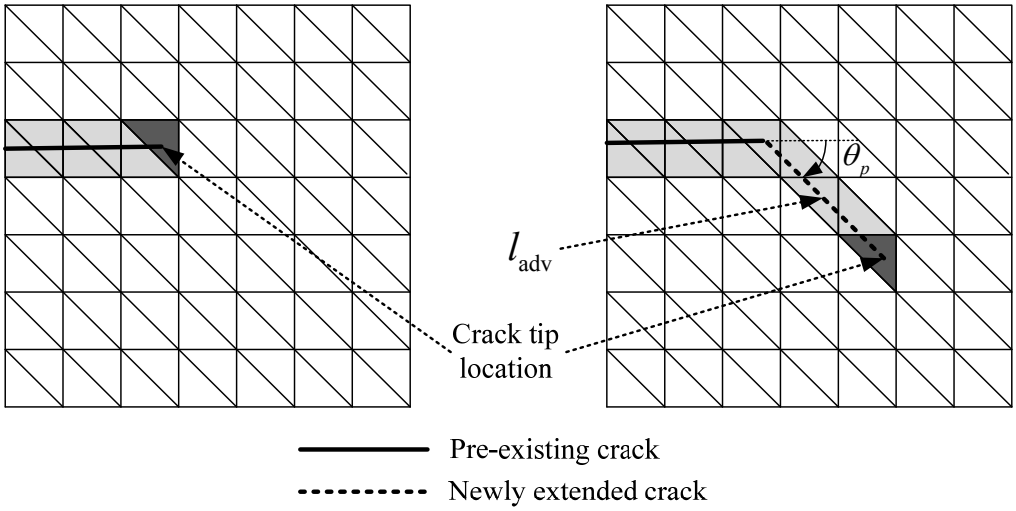

Figure 4.4 Illustration of crack propagation with crack increment and angle

4.3.4 Moving boundary scheme using element partition methodology (EPM)

Another challenging issue for the hydraulic fracture propagation is applying transient boundary conditions on the propagating fracture surfaces at every step. The hydraulic pressure through the updated fracturing path, which is computed by the fluid

flow analysis, must be applied as a boundary condition for the rock deformation analysis. So, a "quasi-static" hydraulic loading algorithm is used to provide the proper boundary conditions for fluid pressure inside fractures. In this approach, when the propagation criterion is satisfied at the crack tip, the fracture geometry is extended by the propagation algorithm and the new crack geometry is calculated by EPM algorithm. Figure 4.5 briefly shows the boundary procedure to transfer from internal fluid pressure distribution to nodal forces. The pre-existing and newly propagated cracks are identified as equivalent crack elements (Zhang and Chen 2008). The major features of the quasi-static hydraulic loading algorithm are identifying the newly extended fracture surface using the intersection points on the edges of the cracked element and applying the resulting nodal forces on the equivalent crack elements. Detail calculation algorithm of the nodal forces in Figure 4.5 is in Appendix B and C.

The EPM is used to compute the fracture areas subjected to the hydraulic pressurization. In this methodology, a crack plane intersecting the existing triangular element is defined using points on the edges of the existing element. When an element is cut by the newly propagated crack plane, the intersection points on the element edges are stored and updated at every time step. The EPM takes advantage of the continuous geometric features in both triangular and tetrahedron elements to construct fracture surfaces when a newly propagated crack path is cut through the triangular element (Huang and Zhang 2010; Zhang and Chen 2008). So the method does not require redefined mesh information during crack propagation, and the total number of degrees of freedom and the dimensions of the general stiffness matrix are not changed. The greatest

advantage of the fixed mesh approach is low computation time and easier to encode for numerical implementation. However, the fixed meshes can lead poor definition of the fracture tips when the mesh size is too big, so that moderate size of the mesh is desired to use the EPM approach. When mesh size is too coarse to represent the fracture tips correctly, special care like the sub-mesh scheme near the fracture tip should be employed to obtain accurate results in the fixed mesh case. However, the sub-mesh scheme is computationally expensive and difficult to implement. Another disadvantage of the fixed mesh approach is resolution issue. This is because fracture elements representing the fracture geometry is too few at the early time, while the fracture elements are too many at the later time. In order to reduce the resolution issue, re-meshing scheme can be employed to make efficient use of computation time by controlling number of elements. Since the re-meshing method has great benefits to save computation time and to reduce the resolution issue, the method is recommended to use for larger scaled problem (i.e. reservoir scaled problem). However, developing the re-meshing scheme is not quite easy. Especially, the 3D re-meshing algorithm may require lots of efforts and mathematical challenges. As a result, we conclude that the fixed mesh approach is more desired than other approaches (sub-mesh, re-meshing), because numerical domains shown in this dissertation is relatively small scale.

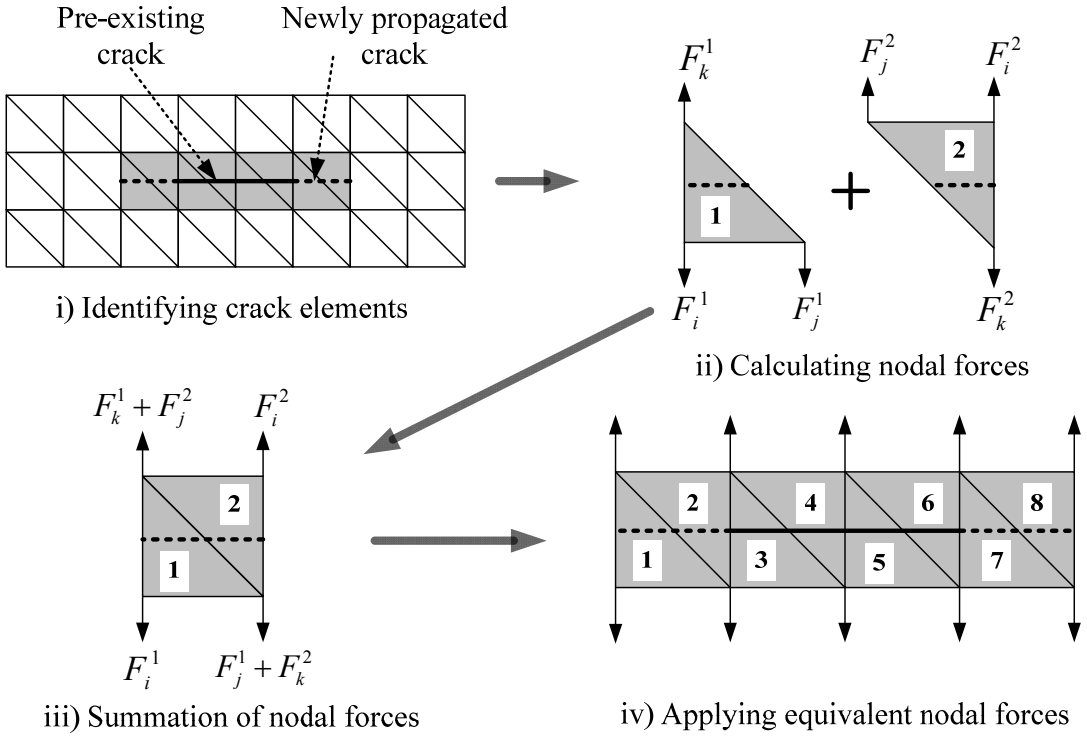

Figure 4.5 Schematic illustration of boundary condition description using EPM

4.4 Discussion and conclusion

Design methodologies for the hydraulic fracture propagation simulation were introduced in this section. In our approach, hydraulic fracturing procedure was modeled using a coupled analysis of fluid flow, rock deformation, and fracture propagation modeling. Three equations the fully coupled THM equations, which are derived from the equilibrium equation for rock deformation; the continuity equation for fluid flow; and heat transfer equation are solved simultaneously in order to capture the hydro-mechanical response of the reservoir by fluid injection. To solve the coupled system of partial differential equations, a fully implicit finite element method is used. The flow analysis for pumped flow was modeled using the lubrication equation to solve for fluid

pressure through newly propagating crack paths. Modeling of the fracture propagation was developed using failure, propagation, and angle criteria.

Fracture propagation is assumed as quasi-static; the original mesh does not change, and crack information is kept updated and recorded independently. In this way, the dimension of the stiffness matrix does not change and no change will be required in the shape functions, so that numerical implementation in the FEM formulation is simple. In addition, a moving-boundary scheme using EPM was used.

The advantage of the proposed fracture propagation is its simplicity and efficiency. Although the solution accuracy is probably lower than some alternative methods such as the adaptive remeshing method (ARM), numerical capability to capture crack paths and its computational efficiency could overcome its drawbacks. In addition, EPM does have some disadvantages. For example, the crack path may not have curvature within one element, although is the method assumes the crack paths are inside the elements, so that the crack path has some mesh dependency. Despite these disadvantages, the advantages of the EPM outweigh its disadvantages, especially for applicability against the hydraulic fracturing simulation.

5. IMPLEMENTATION OF THE HYDRAULIC FRACTURING MODEL

In the previous section, the hydraulic fracturing processes were explained by coupling of these four processes:

i) Hydro-mechanical deformation of the porous rock induced by the fluid pressure is solved using fully coupled THM analysis with an isothermal assumption,

ii) Fluid flow behavior of injected fracturing fluid inside the opened fractures is solved using the lubrication theory with the assumption of Newtonian fluid,

iii) Leakoff rate of the fracturing fluid into the porous rock formation is expressed as a one-dimensional (1D) pressure-dependent flow model using Darcy's law.

iv) Fracture growth and moving boundary conditions are modeled using the propagation algorithm and Element Partition Methodology (EPM).

Most of all, constructing a fully coupled algorithm for these processes is important because all physical behaviors of fluid flow, leakoff, rock deformation, and crack propagation occur simultaneously with fluid injection at high pressure during the hydraulic fracturing treatment. That is, one process would affect the initiation and progress of another and no process can be solved independently. In this section, a solution strategy for the fully coupled processes is presented.

5.1 Solution strategy for fully coupled processes

As mentioned above, the hydraulic fracturing could be defined as a fully coupled fluid-solid interaction problem. Each fluid and solid part is calculated by a separate

solution, so that it is necessary to construct coupling algorithm between the fluid and solid analysis. When constructing the coupling algorithm between two analyses is handled, the consistency of solutions from these analyses remains an important issue. Especially for the hydraulic fracturing problem, the mechanical analysis of fracture opening is coupled with the fluid flow analysis. That is, the fluid pressure obtained from the fluid flow analysis is used to compute the fracture opening in the mechanical analysis. So, the opening amount should be consisted with the amount of injected fluid into the fractures by the mass conservation law. Since the fluid pressure and the fracture opening are calculated by a separate analysis, the iterative method is necessary to introduce to get converged solution between the fluid and solid analysis.

The coupling of the solution scheme for the fluid-driven fracturing problem was studied previously. Numerical modeling of the hydraulic fracturing was studied using mathematical formulation for the fluid-driven fracturing problem of simple planar geometry (Adachi and Detournay 2008; Detournay 2004). The fluid-driven propagation in poroelastic media was simulated using FEM technique and the influence of the poroelastic effects on fracture propagation was studied (Boone and Ingraffea 1989; Boone et al. 1991).

The major difficulty in solving the coupled processes is the non-linear relationship between the fracture opening and the fluid pressure (Adachi and Detournay 2008). Boone and Ingraffea (1990) proposed a partially coupled solution scheme with constant time step (Boone and Ingraffea 1990). Adachi (2008) adopted the Picard iteration method (Picard 1890) to solve the coupled fluid-driven fracturing problem. The

Picard iterative process is useful to get approximation solution using iteration from a given trial solution. Figure 5.1 is a flowchart of the fully coupled iteration process.

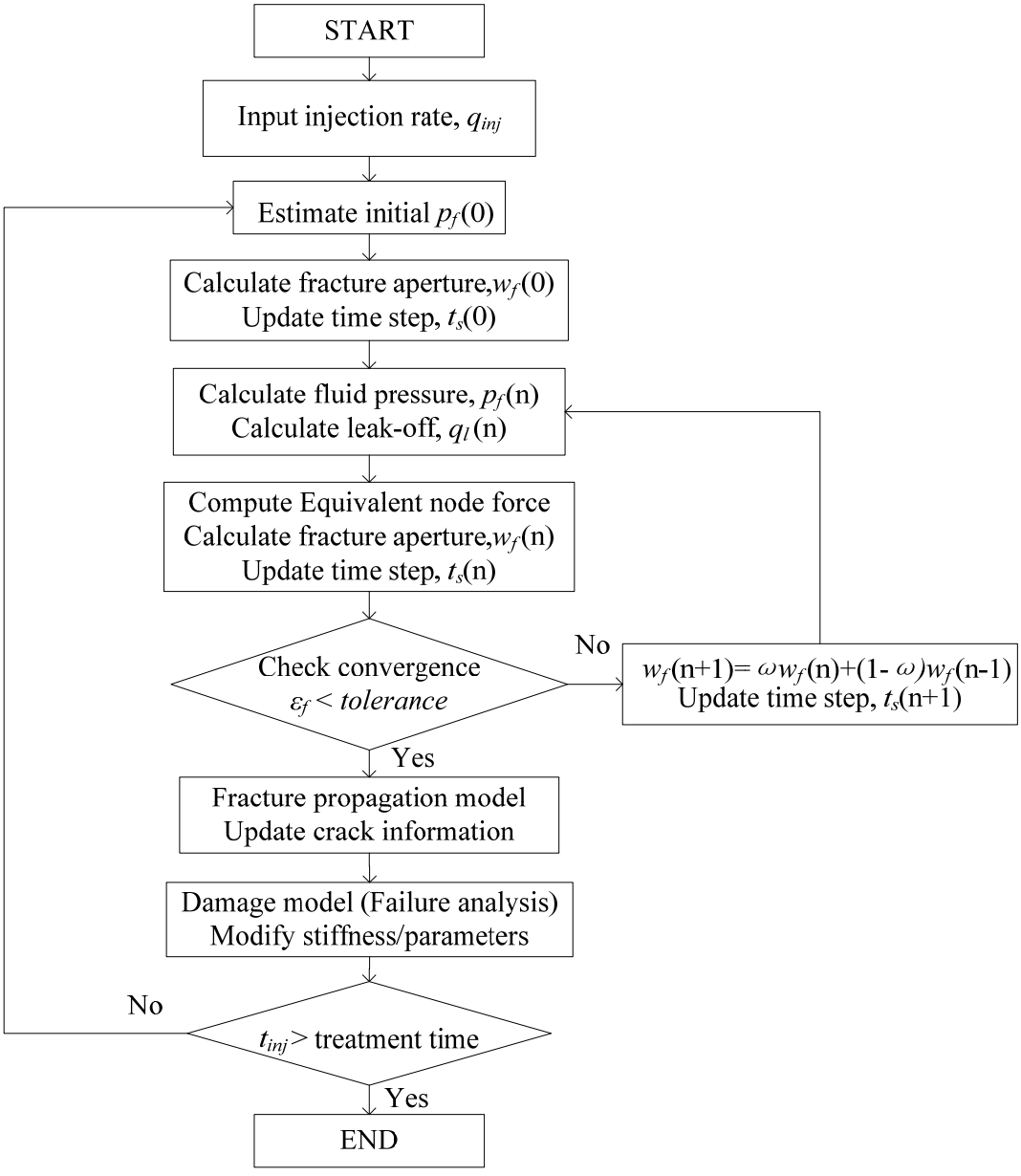

Figure 5.1 Flow chart of the fully coupled solution procedure

5.1.1 Implementation of iterative process

Once a numerical model is constructed with an initial fracture, and input material parameters (E, v, k_m, etc) and necessary boundary conditions (in-situ stresses, Injection rate, etc) are estimated, it is needed to get a converged solution within a given initial fracture geometry before advancing to the next step. We used the iterative method to achieve the converged solution.

The basic procedure of the iterative process is straightforward: i) estimate initial fluid pressure distribution in the fractures, $p_f(0)$ and initial time step for an injection time, $t_s(0)$; ii) solve the coupled poroelastic equation for fracture opening, $w_f(0)$ and update time step, $t_s(0)$ using the total mass balance equation (Eqn. (5.2)) ; iii) solve the fluid flow equation for new fluid pressure inside the fractures, $p_f(\mathrm{n})$ and calculate leakoff rate, $q_l(\mathrm{n})$; iv) solve the poroelastic equation for new fracture opening, $w_f(\mathrm{n})$ and update the time step, $t_s(\mathrm{n})$ using the total mass balance equation (Eqn. (5.2)); v) the convergence of iterations is examined with given tolerance of the average error in the fluid pressure distribution in fractures as described in Eqn. (5.1), if not converged, return to iii) re-solve the fluid flow equation with the newly updated aperture profile and the time step, $w_f(\mathrm{n+1})$ and $t_s(\mathrm{n+1})$. The newly updated aperture profile is computed by $w_f(\mathrm{n+1}) = \omega w_f(\mathrm{n}) + (1-\omega) w_f(\mathrm{n\text{-}1})$, where ω is a convergence parameter, $0< \omega <0.5$, to control extreme changes of the solutions. $t_s(\mathrm{n+1})$ is also calculated based on the newly updated aperture profile using the total mass balance equation (Eqn. (5.2)). If the solution converges within a given tolerance, the iteration process is terminated and the

fracture propagation and failure analysis processes, described in below, are begun to update the crack information (tip location, path).

The convergence of the iteration is determined by the average error in the fluid pressure during the iteration process (Adachi and Detournay 2008; Adachi et al. 2007; Taleghani 2009).

$$\varepsilon_f = \frac{\sum_{i=1}^{NE} \left| p_{f(i)}(\mathrm{n}) - p_{f(i)}(\mathrm{n}-1) \right|}{\sum_{i=1}^{NE} \left| p_{f(i)}(\mathrm{n}) \right|} \leq \text{tolerance} \tag{5.1}$$

where ε_f is an average error of fluid pressure distribution during iteration, $p_f(\mathrm{n})$ is the fluid pressure at the current iteration, and $p_f(\mathrm{n}\text{-}1)$ is the fluid pressure at previous iteration.

5.1.2 Implementation of leakoff rate

The time step in the simulation is calculated from the total mass balance. The total injected fluid volume is a summation of the fracture volume and the fluid leakoff volume. Schematic description of the summation of the leakoff volume is described in Figure 5.2.

$$q_{inj} \cdot t_s = V_f + q_l \cdot t_s \tag{5.2}$$

where t_s is the time step, V_f is the fracture volume, q_{inj} is an injection rate as an input value, and q_l is calculated by summation of the leakoff volume on the fracture surface from Eqn. (4.46). The total leakoff volume is computed by a following equation:

$$\frac{1}{2}q_l = \sum_{i=1}^{nf}\left(-\frac{k_m}{\mu_f}A_f^i\left(p_m^i - p_f^i\right)\right) \tag{5.3}$$

where nf is the number of fracture elements, A_f^i is the area of fracture surface in the fracture element, p_m^i is an average of pore pressure in rock matrix, and p_f^i is an average of fluid pressures in the fracture element. So, we know the fluid injection rate, q_{inj}, the volume of the fractures, V_f, and the leakoff volume, q_l. Then, the time step, t_s, can be obtained from Eqn. (5.2).

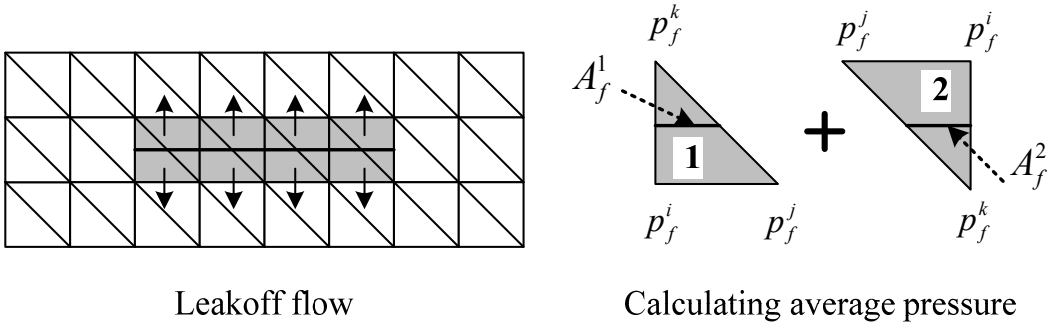

Figure 5.2 Schematic description of leakoff flow and summation

5.1.3 Implementation of fracture propagation algorithm

Before proceeding to the fracture propagation analysis, the crack initiation criterion is examined at the crack tips. If the maximum tensile stress at the crack tip does not meet with the maximum tensile failure criterion, the hydraulic fracturing simulation is terminated and we should change input parameters such as fracturing fluid injection rate or viscosity of the fracturing fluid to increase the hydraulic fracturing. Once the

crack initiation criterion is met, the hydraulic fracture will be extended based on quasi-static crack growth assumption.

In the fracture propagation process, the hydraulic fracture is extended by the propagation angle and the incremental length computed from Eqn. (4.50) and (4.48). And then, fracture elements are identified by the newly extended crack path, and the cutting fracture surfaces are calculated by EPM for equivalent nodal forces of the hydraulic pressurization inside the fracture elements. In this process, the crack path is traced and stored information of the fracture elements at every time step.

One of the advantages of our model is using fixed mesh information for both solid and fluid analysis. That is, it is unnecessary to modify the size of global matrix at every time step, and this feature is beneficial for significant savings of computational cost when a large geological problem is considered. In the fluid-flow analysis, the hydraulic conductivity and pressurization are continuously updated using the crack path information. If the hydraulic fracture is extended, fracture elements are activated in the global matrix. For fluid flow modeling inside the fracture, the fractured elements are considered as fluid networks. As for applying boundary conditions on identified crack tips and injection points, the fluid flow equations are solved in this geometry.

5.1.4 Implementation of failure analysis

Apart from the crack propagation model, intact elements in the rock matrix are examined by the failure criterion to identify failures. Beside with the crack propagation path, the rock is failed when the failure criterion is met. Especially in a heterogeneous

reservoir, the rock failures near the primary fracturing path by the hydraulic pressurization is increasing and the failure events have critical role for the leakoff rate increase. Based on state of the effective stress at the intact element, the M-C failure criterion provides type of failure and can calculate the damage variable by a damage evolution law proposed in section 3. By the calculated damage variable, the effective Young's modulus is calculated by $E' = (1-D)E$. Poroelastic parameters (β_p, γ_1, γ_2) related with bulk modulus and Biot's coefficients updated in the failed elements as described in section 4.

5.1.5 Conclusions and discussions

This section described the fully coupled solution scheme using the Picard iteration method. The fully coupled iterative solution for the fluid-driven fracture propagation problem is difficult to construct, because of the nonlinear relationship of rock deformation and fluid flow in fractures; indeed, all behaviors including rock, fluid, and fracture are part of the dependently coupled problem. Hence, the rock deformation, computed by the fully coupled THM analysis, is iteratively coupled with the fluid flow behavior, which is computed by using the lubrication equation; and the rock/fluid behaviors are coupled with the fracture propagation. Therefore, getting the correct solution is difficult for the complicated, coupled partial differential equations, and the iterative method could give approximate solutions.

When the iterative method is used, it is important to note that the initial guess is critical to get a stable solution with less iteration. The initially given trivial solution and

choice of ω, a convergence parameter, determine how close the solution is to the approximate solution. If the initial guess is too far from the approximate solution, huge iterations are required to get the correct solution.

In addition, the selection of ω, convergence parameter, also affects the convergence of the solution. If the chosen convergence parameter is a high value, sometimes the solution does not converge or lots of iterations are required. However, the value of the convergence parameter depends on the situation of the problem. In our simulation, we used 0.3 ~ 0.4 of the convergence parameter for the 2D hydraulic fracturing problem, while we used 0.05 ~ 0.2 for the 3D hydraulic fracturing problem. So we recommend testing the convergence of the solution before running the whole simulation. Choosing a proper value of the convergence parameter significantly reduces computation cost.

5.2 Model verification

The hydraulic fracture propagation is a complicated and coupled problem of fluid-solid interaction; thus, it is very difficult to find suitable analytical solutions. In the fluid-driven fracture problem, the correct relationship between the fracture aperture and the fluid pressure is important. According to the lubrication theory, the fluid pressure distribution has cubic relationship with the fracture aperture, so that the solution from the lubrication equation is quite sensitive to the fracture aperture value. Hence, to verify the numerical model, the fracture opening and stress near the crack tip are compared

with available analytical solutions using a pressurized, penny-shaped crack problem (Sneddon 1946).

5.2.1 2D pressurized line crack

When the infinitely thin crack is subjected to uniform pressure Δp at the crack surface described in Figure 5.3, the stress and displacement fields are given by the solution with Possion's ratio v and shear modulus G along the x-direction (Sneddon 1946).

$$D_y(x,0^+) = \frac{2\Delta p a(1-\nu)}{G}\sqrt{1-\frac{x^2}{a^2}}, 0 < x < a \tag{5.4}$$

where D_y is a displacement in y-direction, a the half-length of the fracture, and x the computational point within the half length of the fracture. The normal stresses σ_{yy} along the uncracked part of the crack plane are expressed as:

$$\sigma_{yy} = -\frac{\Delta p}{\sqrt{1-\frac{x^2}{a^2}}} - \Delta p, x > a \tag{5.5}$$

The rock material is assumed as a linear elastic material and fracture length is 2 m within a 10-m×10-m rectangular model. The material parameters are set as described in Table 5.1 and uniform pressure, Δp=5 MPa, is applied at the fracture surface as a boundary condition. The uniform triangular mesh is used for the numerical solution, and element size is 0.1-m ×0.1-m each. Figure 5.4 compares the numerical and analytical solutions about the fracture opening and normal stresses near the crack tip under uniform pressurization on the line crack. Therefore, the fracture permeability

estimated by the lubrication equation is validated, since the simulated fracture opening has good agreement with the analytical result in Figure 5.4. However, error increased for the numerical results near the crack tip is, because a uniform mesh was used instead of a fine mesh near the crack tip [Figure 5.4].

Table 5.1 Material parameters for the verification problem

Inputs	Values
Young's Modulus, E (GPa)	37.5
Poisson ratio, υ	0.25
Shear Modulus, G (GPa)	15
Number of Elements	20,000

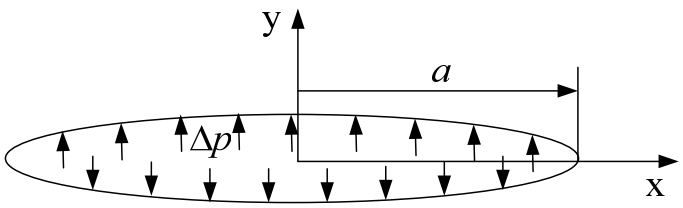

Figure 5.3 Uniformly pressurized crack problem

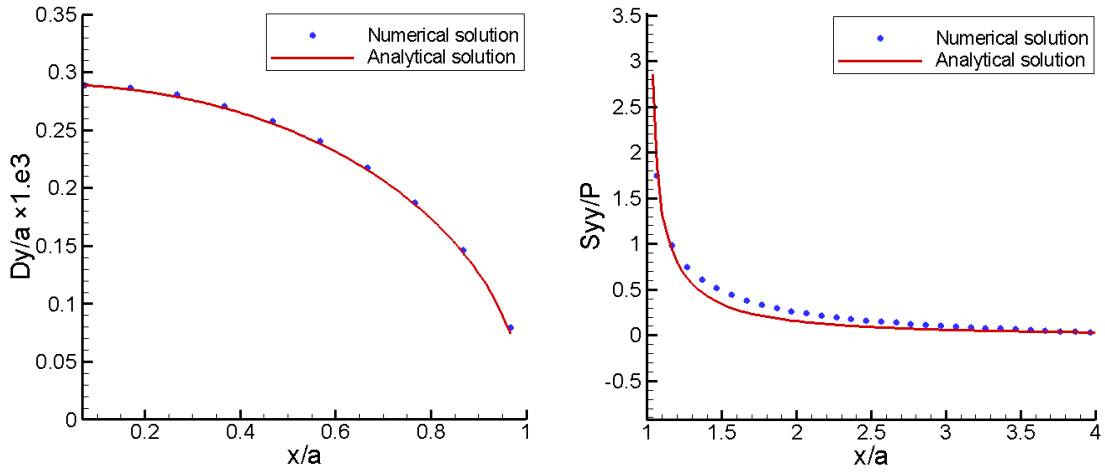

Figure 5.4 Comparison between numerical and analytical solutions for normalized fracture opening and normal stresses distribution

5.2.2 2D biaxial tension

The center-cracked plane problem under uniform biaxial tension (uniform pressure, Δp=5 MPa) is shown in Figure 5.5. Analytical solutions of the fracture opening and the normal stresses σ_{yy} under biaxial tension are same in described in Eqn. (5.4) and (5.5) (Sneddon and Elliott 1946). In Figure 5.6, it is observed that the numerical results have good agreement with the analytical solutions.

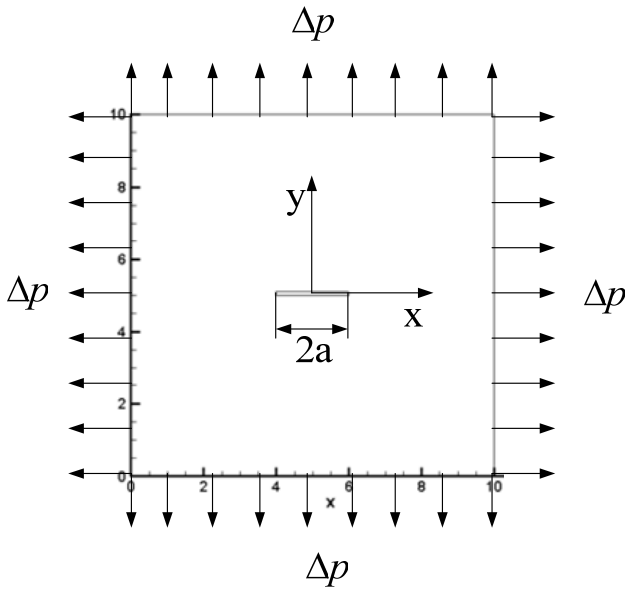

Figure 5.5 Center-cracked plane subjected to equally distributed biaxial tension

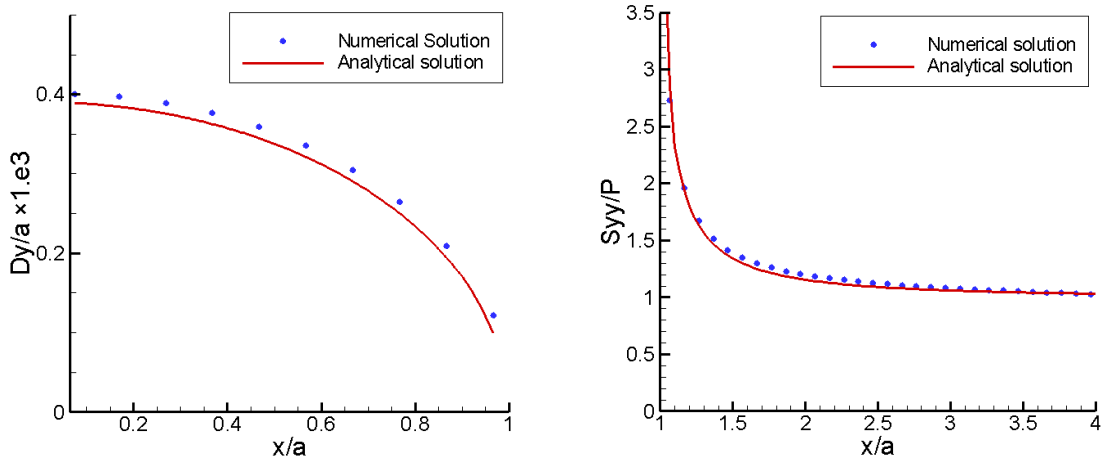

(a) (b)

Figure 5.6 Comparison between numerical and analytical solutions for (a) normalized fracture opening and (a) normal stresses distribution

5.2.3 3D pressurized elliptical crack

For the model verification of the 3D model, the same material properties in Table 5.1 were used, but a circular crack, r=0.4 m, was placed in the center of the 2-m×2-m×2-m cubic model. Uniform pressure Δp=10 MPa was applied on the elliptical crack surface. The model included 16,000 (20×20×40) structurally meshed tetrahedron elements. Same as previous 2D examples, the numerical results of the 3D model are consistent with the analytical solutions in Figure 5.7.

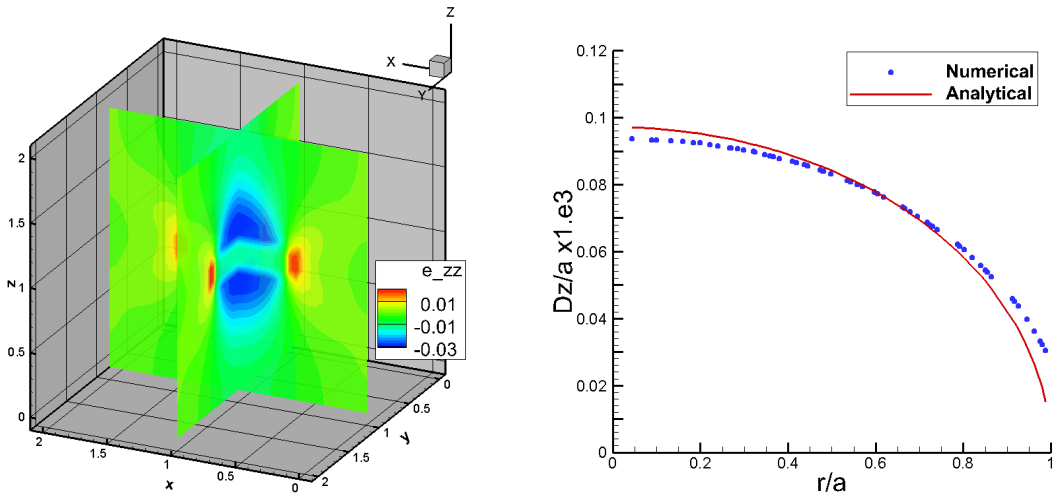

Figure 5.7 Comparison between numerical and analytical solutions for normalized fracture opening of the uniformly pressurized elliptical crack

5.2.4 Conclusions

As we described earlier, verification of the hydraulic fracturing model is a quite challenging issue, since there are no available analytical solutions. Therefore, in order to

validate the numerical hydraulic fracturing model, lab-scaled experiments are frequently used. Validation procedure of the numerical hydraulic fracturing model with the lab-scaled experiments will be discussed in section 11. In this section, we developed the hydraulic fracturing model and the coupled processes of fluid-solid interaction problem were implemented in FEM code. In these coupled processes, relationship between the fracture pressure and the fracture opening is solved by the lubrication equation and the relationship is highly non-linear, so that achieving correct solution of the fracture opening is critical to obtain exact solution of the fracture pressure distribution in the fractures. Otherwise, incorrect solution of fracture opening cause huge numerical error and the solution could not be converged. In this section, the fracture aperture variations under uniform pressurization and biaxial tension were verified with the available analytical solutions. As results, the numerical results have shown good agreement with the analytical solutions in 2D and 3D numerical models [Figure 5.4, Figure 5.6, Figure 5.7].

6. 2D NUMERICAL SIMULATION OF COMPRESSION TESTS

Generally, stresses applied to brittle rock by various loading mechanisms cause crack nucleation, propagation, interaction, and coalescence in different ways. Especially, when the applied forces are compressive, the rupture paths are governed by shale-localized failures. These rupture paths are also variable and depend on material deformation properties and strength and heterogeneity (Hoek and Brown 1990; Jaeger et al. 2007). Characterization of the fracture growth pattern in a brittle and heterogeneous reservoir is a difficult and challenging issue because of the complexity of rock properties and physical aspects of rock failure and fracture. Frequently arbitrary and randomly grown fractures are observed in well stimulation of petroleum and geothermal reservoirs. So numerical modeling of core-sample experiments is useful to investigate the suitability of the damage model of heterogeneous rocks and the numerical core analysis is applicable to use in a larger geological problem.

6.1 Constitutive modeling of heterogeneous rock

The elastic/brittle constitutive model of brittle rock, described in section 3, is used to express the confining-dependent stress/strain relation of core samples. The multistage triaxial tests of Newberry Tuff and Altarock granite core samples performed by (Wang et al. 2012a). The multistage triaxial tests were performed at five different stages of confining pressure to determine the rock properties. In each stage except the last stage, the sample was unloaded when the maximum value of volumetric strain was

observed on the stress-volumetric strain curve. During the last stage, the rock was loaded until complete failure to measure the compressive strength of the rock at the prescribed confining pressure. The confining-dependent stress/strain curves of the Tuff and granite samples are listed in Figure 6.1 and Figure 6.2. Tuff sample appears to be hard, inelastic and brittle, while granite sample shows hard, elastic and brittle. Rock mechanical properties and Mohr-Coulomb parameters (friction angle, cohesion) obtained from the multistage triaxial tests [Table 6.1 and Table 6.2] are used as input parameters for the numerical modeling of the triaxial compression tests. The heterogeneity of the rock was characterized using the Weibull distribution function.

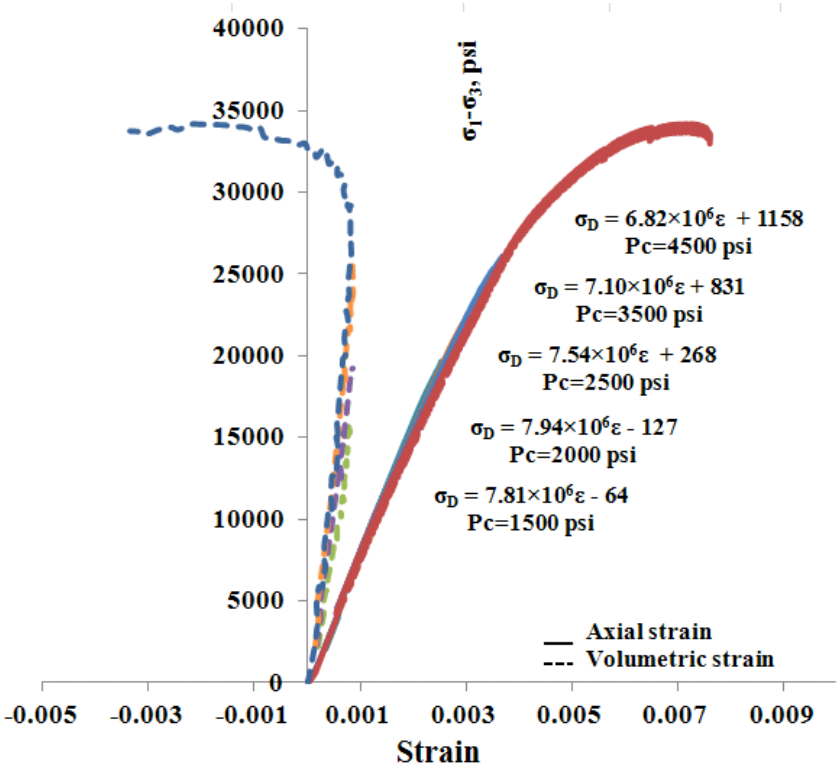

Figure 6.1 Stress-strain relations of Tuff after multi-stage triaxial test (Wang et al. 2012a)

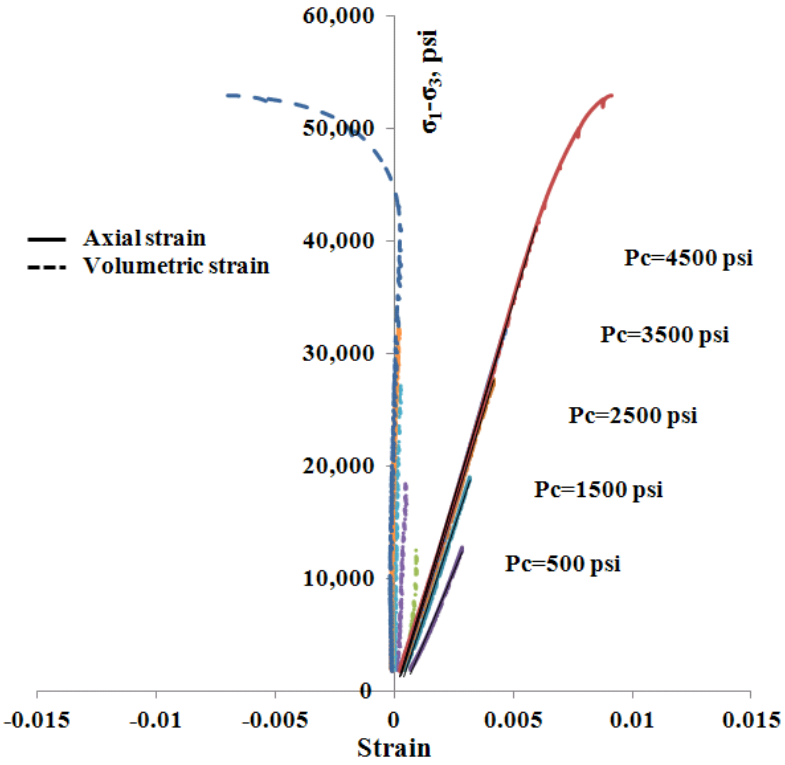

Figure 6.2 Stress-strain relations of granite after multi-stage triaxial test (Wang et al. 2012a)

6.1.1 Laboratory multistage triaxial test of Tuff and granite

Laboratory experiments on rock specimens give general stress/strain curves under different confining pressures [Figure 6.1 and Figure 6.2]. The data used in this work came from triaxial laboratory experiments that provided input data of Young's modulus, Poisson's ratio, estimated compressive strength, uniaxial compressive strength, friction angle, and cohesion, all of which were incorporated into our numerical model. Relationships between petrophysical, mechanical and failure properties are important in reservoir development problems including wellbore stability and hydraulic fracturing.

Table 6.1 Multistage triaxial test data of Tuff (Wang et al. 2012a)

Pc, psi	1500 (10.34 MPa)	2000 (13.79 MPa)	2500 (17.24 MPa)	3500 (24.14 MPa)	4500 (31.03 MPa)
Compressive strength, psi	24,380 (168.14 MPa)	26,758 (184.53 MPa)	29,135 (200.93 MPa)	33,890 (233.72 MPa)	38,645 (266.52 MPa)
E, psi	7,807,493 (53.84 GPa)	7,940,565 (54.76 GPa)	7,544,256 (52.03 GPa)	7,099,090 (48.96 GPa)	6,822,836 (47.04 GPa)
Possion ratio, υ	0.32	0.34	0.37	0.39	0.41
UCS, psi	12,818 (88.38 MPa)				
Friction angle	40.7				
Cohesion, c_F (psi)	3,955 (27.27 MPa)				
Inclination angle of failure plane, β	65.4°				

Table 6.2 Multistage triaxial test data of granite (Wang et al. 2012a)

Pc, psi	500 (3.45 MPa)	1500 (10.34 MPa)	2500 (17.24 MPa)	3500 (24.14 MPa)	4500 (31.03 MPa)
Compressive strength, psi	15873 (109.47 MPa)	24,080 (166.07 MPa)	35,024 (241.54 MPa)	40,827 (281.56 MPa)	52,875 (364.65 MPa)
E, psi	4,996,970 (34.46 GPa)	6,165,314 (42.52 GPa)	6,741,385 (46.49 GPa)	6,918,957 (47.72 GPa)	6,998,963 (48.27 GPa)
Possion ratio, υ	0.37	0.43	0.47	0.47	0.46
UCS, psi	11,246.59 (77.56 MPa)				
Friction angle	55.3				
Cohesion, c_F (psi)	1,756.36 (12.11 MPa)				
Inclination angle of failure plane, β	72.7°				

6.1.2 Heterogeneity of Tuff and granite samples

Petrographic analyses are conducted to describe rock textures, classify and determine the relative amounts of mineral constituents, to identify minerals, and to detect evidence of mineral alteration (Wang et al. 2012a). The identification of mineral

constituents and determination of texture and micro-structural features allows the recognition of rock properties that may influence the mechanical properties of the rock.

According to the petrographic analysis, the tested Tuff specimen has an aphanitic fine-grained texture (Wang et al. 2012a). In Figure 6.3, the images of Tuff show a heterogeneous rock containing different types of grains and various minerals. The Tuff mainly consists of two types of minerals and may have rock properties in brittle with fine-grained crystals. In addition, grain size, grain shape, texture and structure were randomly distributed. All these heterogeneity factors could affect fracture pattern creation. Effective rock properties are a function of rock composition and properties of the components.

The description of petrographic images in Figure 6.4 is about the granite sample and thin section of the granite is composed of course-grained quartz, hornblende, plagioclase, biotite, and muscovite minerals with grain sizes ranging from 0.1 to 0.35 μm. The quartz, feldspar, and biotite are dispersed with various sizes.

As explained in section 2, in order to represent the rock heterogeneity into a numerical domain. Random variables generated by Weibull distribution function are distributed to material strength and Young's modulus as multiplying the random variables at Gaussian point in an element. So, in the finite-element (FEM) formulation, the microscopic heterogeneity can be described only at the elemental scale. Therefore, further improvement, would require the correlation of Weibull parameters with rock composition from mineralogical and textural characterization. This is an important issue

for the practical modeling of rock samples; however, the issue would require extensive rock mechanical and petrological analysis and is beyond the scope of this dissertation.

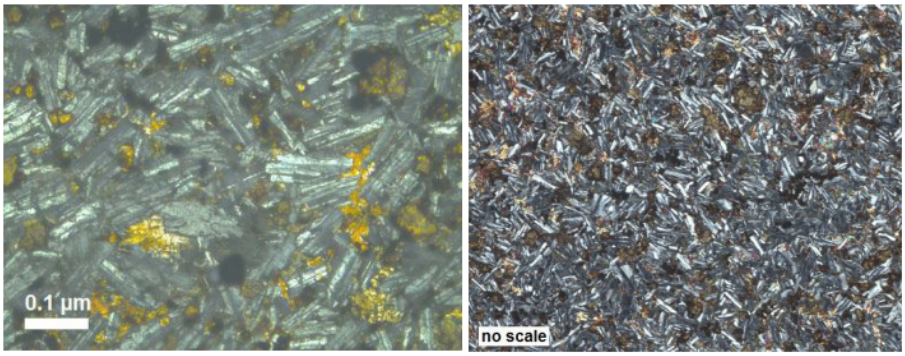

Figure 6.3 Petrographic images of Tuff rock from Newberry (Wang et al. 2012a)

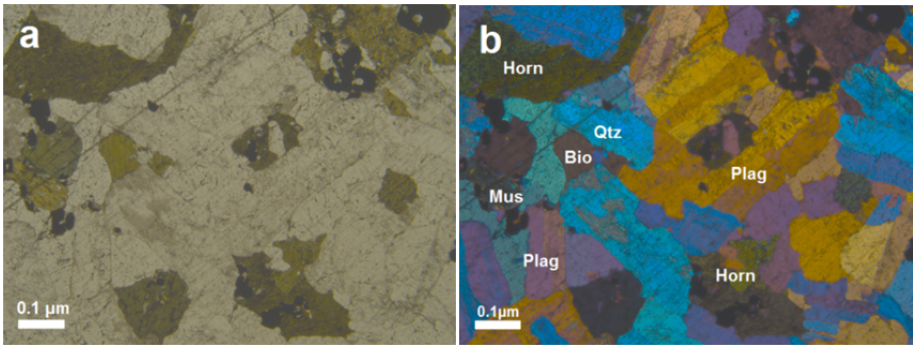

Figure 6.4 Petrographic images of AltaRock granite by (Wang et al. 2012a)

6.2 2D numerical modeling for triaxial tests

Two-dimensional numerical domain and 10,000 uniformly meshed triangular elements were used for triaxial compression [Figure 6.5(b)]. 2D plane strain is used to approximate an axial section through an axi-symmetric triaxial test specimen. This plane strain approximation is commonly taken by other researchers (Fang and Harrison 2002a;

Tang et al. 2000; Wang et al. 2000; Yuan and Harrison 2005). In order to express the fracture pattern of the rock specimen, the 2D plane strain approximation is suitable since 2D axi-symmetric model cannot represent a fracture pattern throughout the specimen. Ultimately 3D numerical model might be the best for the triaxial compression tests, however the 3D simulation still requires huge computational costs despite of recent development of computational capacity and lots of mathematical and numerical difficulties such as uncertainty of heterogeneity effect by three-dimensional micromechanical grains, and highly non-linear and anisotropic mathematical formation are remaining to develop 3D model. Therefore, numerically efficient 2D plane strain model is preferred to use in this research and development of suitable 3D numerical model remains for future improvement.

Material parameters and input parameters are stated in Table 6.3. Boundary conditions of the compression test are that the bottom surface of the specimen was restricted in the y-direction, and force was applied on the top surface of the specimen using the same displacement increment as in an experimental test, and confining pressure was applied to both sides [Figure 6.5(a)]. For heterogeneity characterization, we used random variables generated by Weibull distribution function, since it gives wide possibilities. In order to obtain approximate values of Weibull parameters, few pre-tests are performed. For example, if three cases of m_1=0.5, 1.0, 3.0 were simulated, we can estimate appropriate values of Weibull parameters.

For Tuff sample, we obtained m_1=0.9, a_1=10 for stiffness distribution, and m_2=0.9, a_2=15 for strength distribution. For granite sample, m_1=0.8, a_1=10 for stiffness

distribution, and m_2=0.9, a_2=10 for strength distribution were estimated. In Figure 6.5(c), average value of stiffness is about 51 GPa, which shows that stiffness was distributed to each element by random variables. Darker colored elements represent higher stiffness, while lighter colored elements represent lower stiffness.

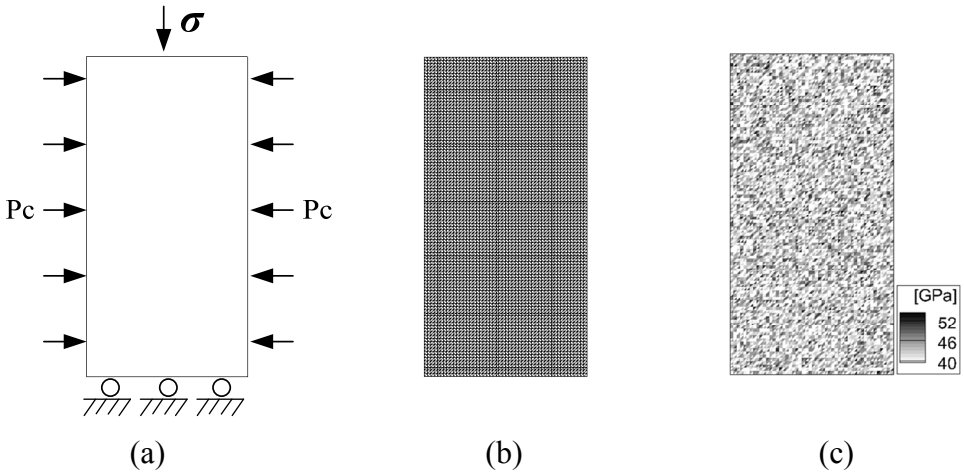

Figure 6.5 Numerical simulation model for triaxial compression tests (a) Boundary conditions, (b) Mesh (NE=10,000), (c) Heterogeneity index

Table 6.3 Material parameters and input parameters for 2D triaxial

Inputs	Values
Element type	Triangular
Young's Modulus, GPa	53.84 (Initial)
Poisson ratio	0.32 (Initial)
Num. of elements	10,000
Size of element	0.02
Aspect ratio (D:H)	1:2
Cut-off strength, MPa	15
Incremental displacement	0.1e-3
Weibull parameters	m_1=0.9, a_1=10 for stiffness (Tuff) m_2=0.9, a_2=15 for strength (Tuff) m_1=0.8, a_1=10 for stiffness (granite) m_2=0.9, a_2=10 for strength (granite)

6.3 Numerical simulation for Tuff at Pc=15 MPa

The simulation result of Tuff sample about the fracture process at 15 MPa confining pressure is shown in Figure 6.7. The results show that local failure events initiate at random locations and gradually propagate, and then the localized failure tends to concentrate on the weaker elements of the rock specimen. The strain localization leads to shear plane development by irreversible friction. After the shear plane takes place, the fracture surface slips and more failure is concentrated on the fracture plane.

In Figure 6.7, Region I is a reversible elastic zone behaving elastically; that is, the deformation is instantaneously reversed to its initial point when the forces are removed. Region II is an irreversible inelastic zone, which means the deformation could not reverse to its initial point when the forces were removed. In Region II, the rock was dilated by heterogeneous microcrack growth. Region III is a brittle fracture zone, which means sudden loss of strength happened across the fracture plane. In Region III, the deformation becomes totally irrecoverable. The fracture plane is formed when shear, compression, and tension forces break molecular bonds. As a result, the compressive forces lead to lots of microcrack growth in Region II, and then combined compressive/tensile macroscopic failures are observed in Region III (Jaeger et al. 2007).

In Figure 6.6(a), initiation of microcracks was detected at an early stage and dilation occurred simultaneously with the microcrack growth. Then the accumulation of microcrack events hikes before reaching its peak stress. When the fracture plane was formed, both tensile and shear damages were found near the fracture plane. This is because slippage related to the shearing behavior caused tensile failures near the

localized shear-fracture plane. Therefore, both tensile and shear failures occurred during the triaxial compression test, and the combined failures triggered the fracture initiation and propagation.

In Figure 6.6(b), the numerical result was compared with the experimental multistage triaxial result, tested at Pc=17.24 MPa. It shows general agreement between two results. Specifically, at the early stage, the strain curve has good agreement with the experiment, while at later stages the experiment's results have more inelastic behavior than the numerical result. The numerical result has less inelastic behavior than the experiment's because the volcanic Tuff sample shows hardening behavior and our constitutive model was developed based on the elastic/brittle assumption. However, the volumetric strain curve has somewhat similar behavior in both the simulation and the experiment even though the discrepancy of axial strain curves.

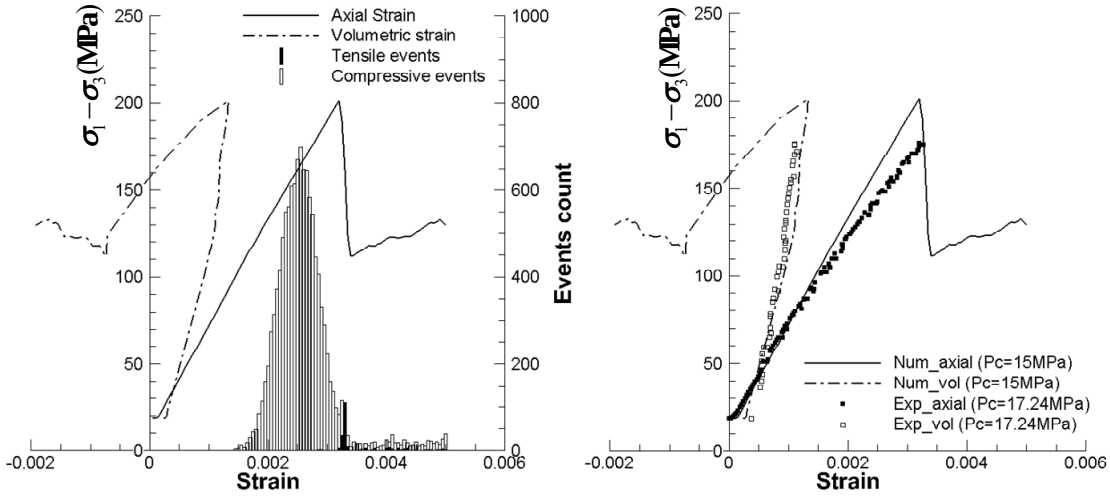

Figure 6.6 (a) Failure events detection during fracture process at Pc=15 MPa
(b) Comparison of numerical with experimental result

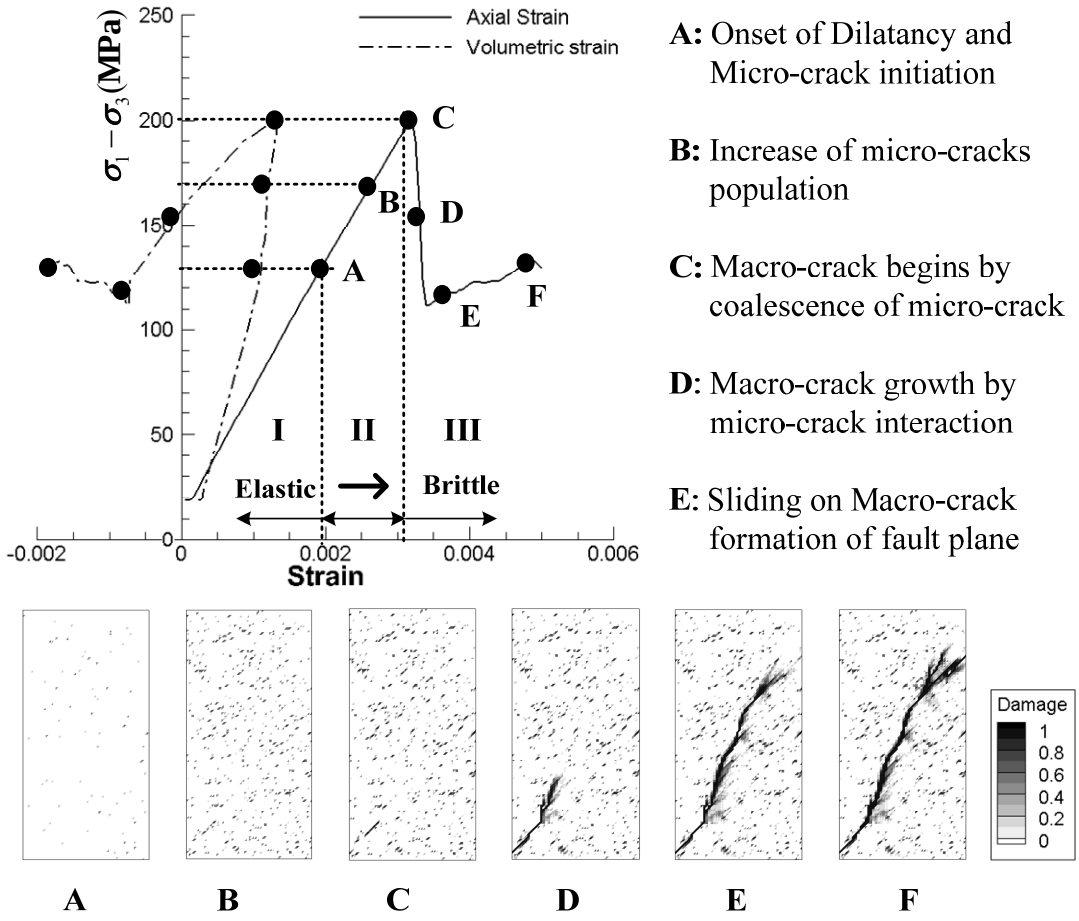

Figure 6.7 Axial and volumetric strain curve at Pc=15 MPa and micro/macro crack growth of brittle fractures in heterogeneous rock

6.3.1 Stress-strain relations of Tuff by confining pressure

In this section, the influence of confining pressure was studied. As discussed in section 2, the stress-strain relations of a rock were highly affected by the confining pressure. Similarly, fracture patterns are also influenced by the confining pressure variation. Under uniaxial compression (i.e. no confinement), a rock tends to by failed by

somewhat irregular longitudinal splitting, while with a moderate amount of confining pressure, the longitudinal fracturing is suppressed and clearly defined plane of fracture is formed through the rock specimen (Jaeger et al. 2007). The fracture plane is characterized by shearing displacement (i.e. shear fracture) and typically inclined at an angle less than 45° from the axial direction. If the confining pressure is increased highly and the rock becomes fully ductile, small shear fractures, accompanied by plastic deformation of the individual rock grains, are observed (Jaeger et al. 2007).

Numerical results show that both the stress-strain relations and the fracture pattern were affected by the confining pressure variation in Figure 6.8 and Figure 6.9. As peak strength increases, absorbed fracture energy increases during the fracturing process. Inclination angles of the fracture plane were varied by the confining pressure. As increasing confinement, the inclination angle of the fracture plane is about 45°. Furthermore, the angle of dilation depends on the confining pressure and the angle of dilation of the higher confinement case has a larger angle than other cases.

In cases of higher confinement, more damaged events were detected and the damaged events could lead to more dilation during the failure process. This is because the angle of dilation is controlled by an amount of plastic volumetric strain developed during fracture shearing. In Figure 6.9, we observed that the fracture pattern after the multistage triaxial simulation has brittle fracturing patterns. Based on the study of confining pressure, the peak strength of the brittle rock undergoing deviatoric loading is highly affected by the confining pressure. The peak strength and shear dilation have strong effects on the fracture pattern.

In Figure 6.18, a fracture pattern of Tuff sample was observed at an angle of 62° after the multistage triaxial compression test at Pc=4500psi (≈31MPa). From the front and side view [Figure 6.18(b)], small fractures are observed along the rock sample. However, a fracture pattern from the numerical simulation at Pc=30MPa [Figure 6.9] shows clearly formed fracture plane at an angle of 45°. This is because the stress-strain relation of numerical simulations at Pc=30MPa [Figure 6.8] has elastic-brittle behavior; on the other hand the stress-strain relation of experimental results has ductile behavior. Hence, the fracture patterns from numerical results are somewhat disagreement with the experimental results when high confining pressure is applied. However, the multi-stage triaxial test is not a good experiment to characterize the fracture pattern variation by the confining pressure, since micro-fractures could be formed due to multi-loading/unloading during the multi-stage test.

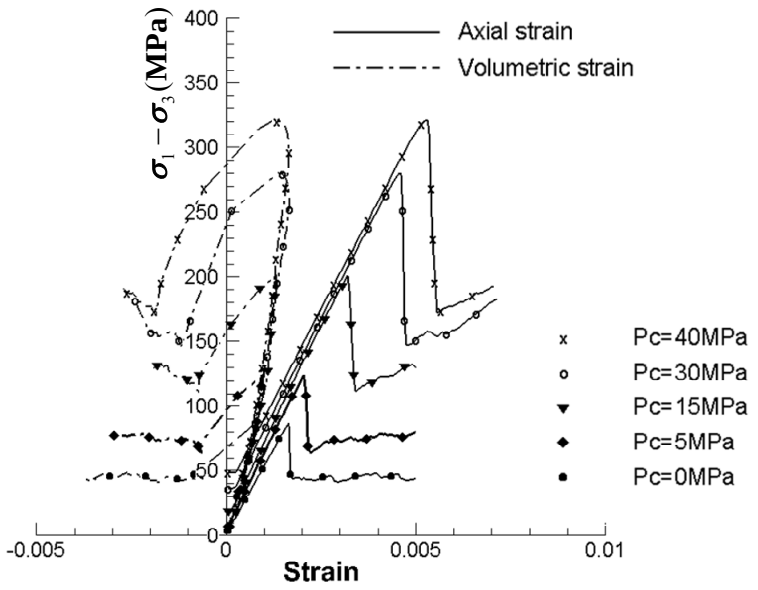

Figure 6.8 Stress/strain relations of Tuff by various confining pressure

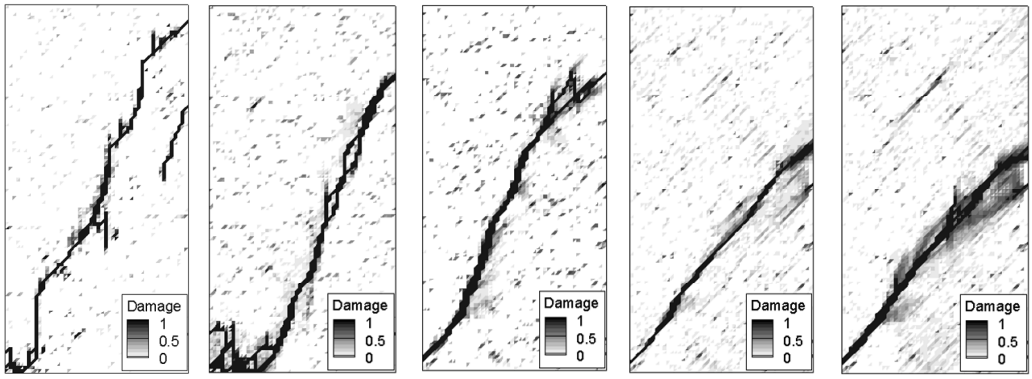

Figure 6.9 Fracture patterns of Tuff by various confining pressure at NE=10,000

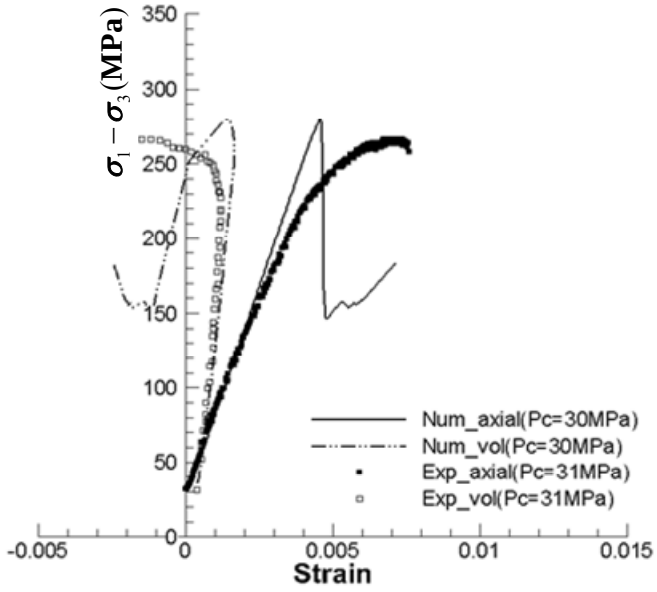

Figure 6.10 Stress-strain relation of Tuff at Pc=30 MPa compared with experimental result (Pc=31MPa)

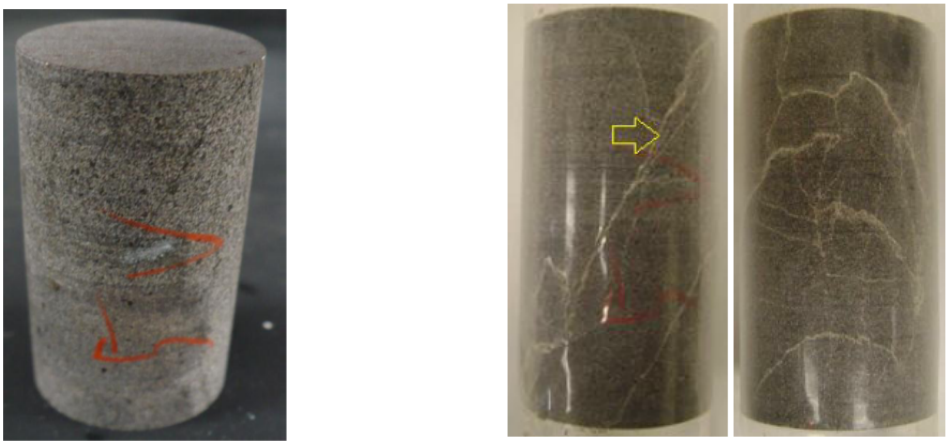

(a) Before multistage tests (b) After multistage test from side and front

Figure 6.11 Fracture pattern of Tuff rock before and after multistage triaxial test (Wang et al. 2012b)

6.4 Numerical simulations for granite at Pc=25 MPa

The simulation result of granite sample about the fracture process at 25 MPa confining pressure is shown in Figure 6.12. Similar with previous Tuff example, compressive failures were mostly observed and accumulated at random locations. While the fracture plane was formed, small amount of tensile failures are observed during the shear fracturing process [Figure 6.12 (a)]. The stress-strain relation of the granite sample shows less inelastic behavior before complete failure and brittle behavior when the rock is completely failed. These small inelastic and brittle behaviors are good agreement with the experimental results [Figure 6.12 (b)]. The granite sample shows less ductile behavior than the Tuff sample [Figure 6.6(b)]. So, it is found that the elastic-brittle constitutive assumption is suitable for the granite rock sample than the Tuff sample.

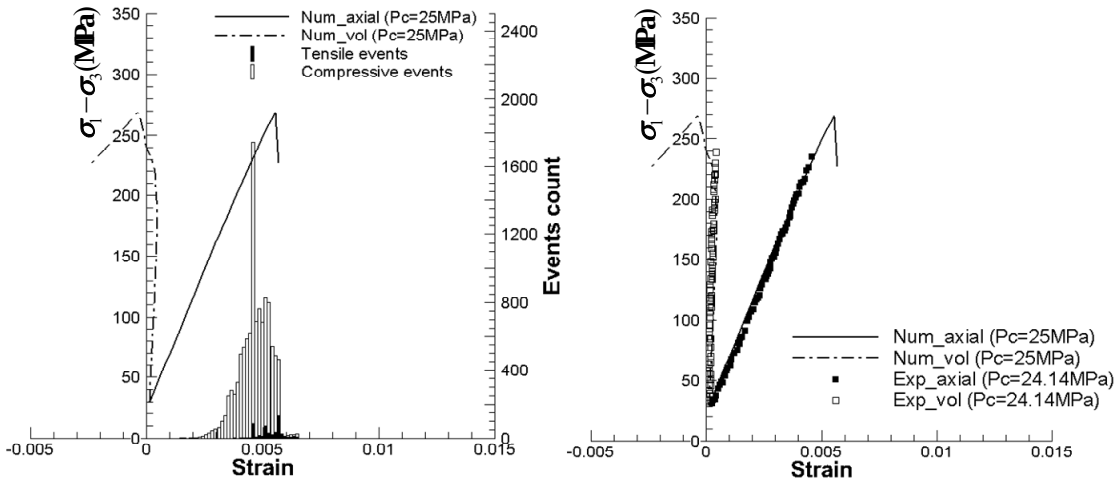

Figure 6.12 (a) Failure events detection during fracture process at Pc=25 MPa
(b) Comparison of numerical with experimental result

6.4.1 Stress-strain relations of granite by confining pressure

As discussed earlier, the confining pressure is critically influencing the stress-strain relations and fracture patterns of a rock. Numerical results show that the stress-strain relations and the fracture pattern were affected by the confining pressure variation in Figure 6.13 and Figure 6.14. The fracture patterns of the granite sample show irrelevant results than the Tuff cases. Under uniaxial compression, somewhat longitudinal splitting fractures were found and clearly formed fracture planes were observed under various confinements. In Figure 6.16, a fracture pattern of granite sample was observed at an angle of 72° after the multistage triaxial compression test at Pc=4500psi (≈31MPa). However, observed fracture pattern from the numerical simulation at Pc=32MPa was inclined at an angle of 50°. This is because a formation of rock heterogeneity is also a critical factor for the fracture plane forming. As mentioned

above, the characterization of the rock heterogeneity is an important issue for the practical modeling of rock samples, but this issue is beyond the scope of this dissertation, because it requires extensive research about micro-mechanical structures of the rock.

In Figure 6.15, the stress-strain relation of the numerical result (Pc=32MPa) and the experiments result (Pc=31.03MPa), which is the last stage of the multi-stage triaxial test was compared until complete failure. General behavior of axial and volumetric strains is almost similar in both numerical and experimental results. The experimental results show high volumetric changes when the complete failure occurred.

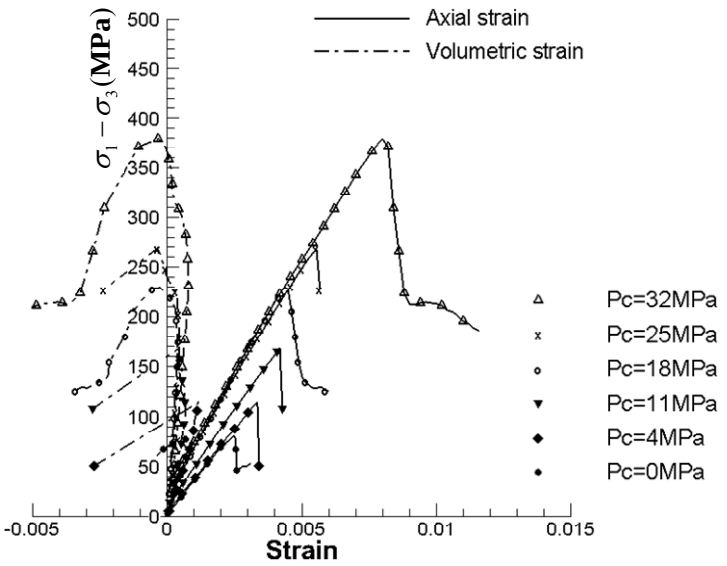

Figure 6.13 Stress/strain relations of granite by various confining pressures

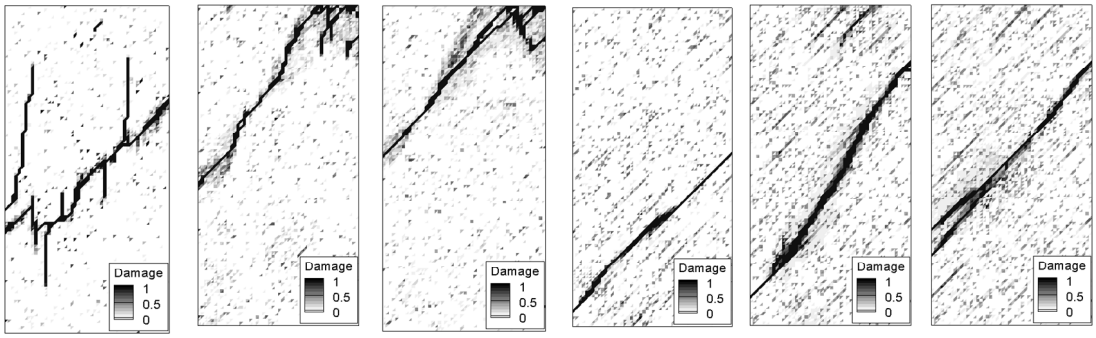

(a) Pc=0MPa (b) Pc=4MPa (c) Pc=11MPa (d) Pc=18MPa (e) Pc=25MPa (f) Pc=32MPa

Figure 6.14 Fracture patterns of granite by various confining pressure

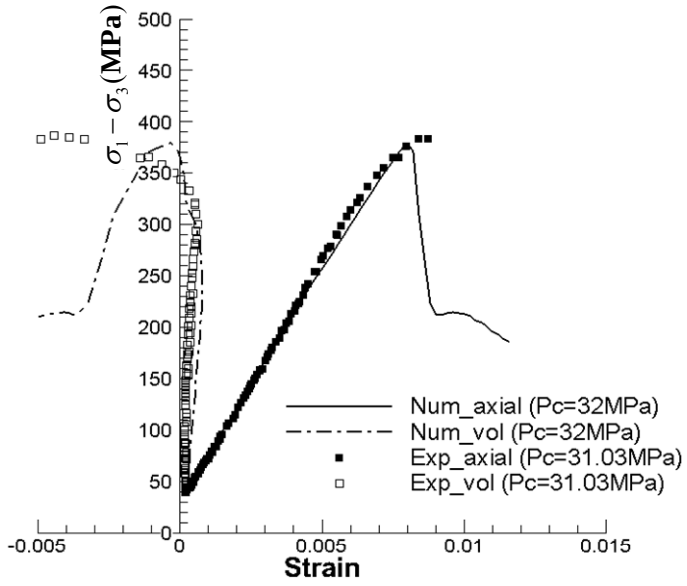

Figure 6.15 Stress-strain relation of granite at Pc=32 MPa compared with experimental result (Pc=31MPa)

(a) Before multistage tests

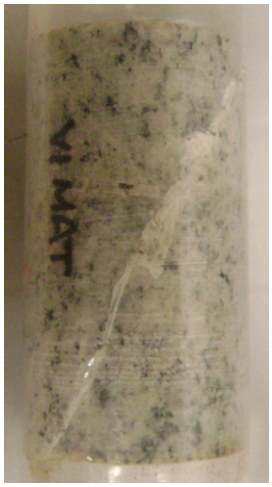

(b) After multistage test from side

Figure 6.16 Fracture pattern of granite before and after multistage triaxial test (Wang et al. 2012b)

6.5 Numerical study for influence of heterogeneity parameter

Because most rocks are brittle and heterogeneous, heterogeneity commonly causes multiple and randomly distributed crack propagation. The brittle rock is composed of different sizes of micrograins and different distributions of micro-defects, so that correct representation of rock heterogeneity is a key factor of the numerical core analysis. However, a large part of the material properties of rock is uncertain, and it is very difficult to characterize the mechanical behavior of the heterogeneous rock in both microscopic and macroscopic views.

In this study, the Weibull distribution function was used to characterize the rock heterogeneity. The Weibull function is commonly used in rock engineering (Fang and Harrison 2002b; Tang and Hudson 2011), although the approach cannot be a perfectly

suitable method to characterize the rock heterogeneity because its randomly generated variables cannot exactly represent texture, orientation, and shape of micrograins.

However, the Weilbull distribution function may be the easiest method for generating heterogeneous properties of rock, and it is also easy to implement in an FEM formulation (Fang and Harrison 2002a; Tang and Hudson 2011; Tang et al. 2002; Wong et al. 2006; Yuan and Harrison 2005). So far, no numerical method can express the complicated mineralogy and microstructures of the brittle rock perfectly, so the heterogeneity study in this section could give valuable interpretation of rock heterogeneity effects on the fracture pattern. This section discusses the simulated influence of the Weibull shape parameters on stiffness and strength distributions using numerical simulations of Tuff samples.

6.5.1 Stiffness mean value parameter effect

Figure 6.18 shows different fracture patterns by controlling of Weibull parameter for average value of stiffness distribution curve. In this simulation, lower value of m_1 means the mean value of Young's modulus of rock becomes smaller, but strength of rock specimen was not changed, because it was determined by confining pressure from experimental data in our numerical model. In this section, influence of different mean values on stiffness distribution was tested without strength variation, because we generally assumed that stiffness variation does not mean corresponding change of material strength. Figure 6.17 shows that case of m_1=1.5 has higher compressive strength than other cases. In addition, as we discussed, fracture patterns are depend on

distribution curve of random variable which means we cannot control the specific location of weaker or stronger elements. In case of m_1=0.5, fracture plane was mostly observed at upper of the specimen, while other cases have clearly inclined fracture plane. In addition, we applied same loading condition of Δd=0.1e-3, so that upper of the rock sample could be failed earlier when a rock is weaker (m_1=0.5). This is because relatively large loading condition was applied on the weaker rock sample and the high stress concentration near loading points, where a top surface of the rock sample, lead shear failures near the top surface. From observation of, both dilation angle and peak strength were influenced by the value of Weibull parameter change.

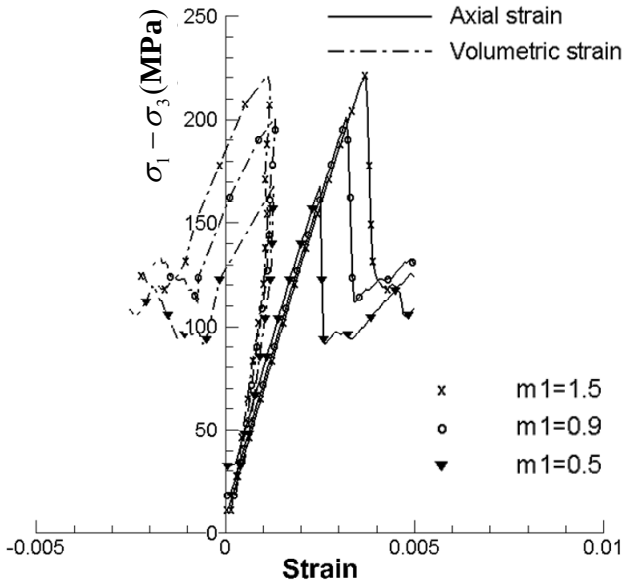

Figure 6.17 Stress/strain curve by stiffness mean value parameter change

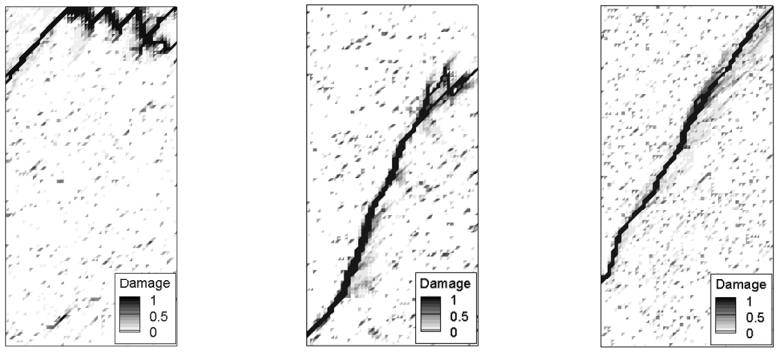

(a) m1= 0.5 (b) m1= 0.9 (c) m1= 1.5

Figure 6.18 Fracture patterns by changing the stiffness mean value (left to right: softer rock to stiffer rock)

6.5.2 Stiffness shape parameter effect

In this section, a shape parameter effect of the stiffness distribution was simulated with values of a_1=5, 10, 20, 100. In Figure 2.11, a larger value of a_1 means more homogeneity and narrow distribution, while a lower value of a_1 means more heterogeneity and wider distribution. Figure 6.19 and Figure 6.20 show effects of the shape variation of the stiffness distribution on the fracture patterns. According to the simulation results, the influence of the stiffness shape parameter wasn't significant because two sets of Weibull parameters were used to represent the rock heterogeneity in our model. One was used for the grain-size distribution, while the other was used for the micro-defects distribution.

As explained earlier, we assumed that the stiffness variation did not correspond with any change of the material strength, so that the combination of the two sets has strong randomicity on the fracture patterns. That is, the distribution of the micro-defects more significantly influenced the material heterogeneity. However, the stiffness shape

parameter could influence crack initiation and its patterns. In Figure 6.20, as the shape parameter increases, the fracture plane becomes more clearly formed, since larger shape parameter represents more homogeneous distribution. On the other hand, more randomly distributed crack growth was found when the stiffness shape parameter was small (a_1=5), which means the matrix was more heterogeneous.

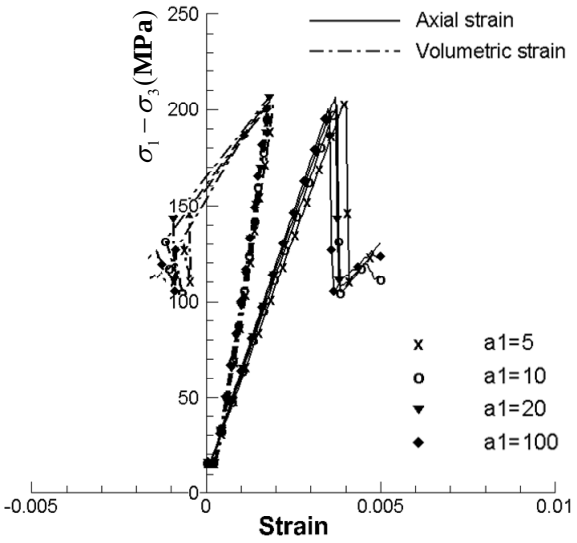

Figure 6.19 Stress/strain curve by stiffness shape parameter change

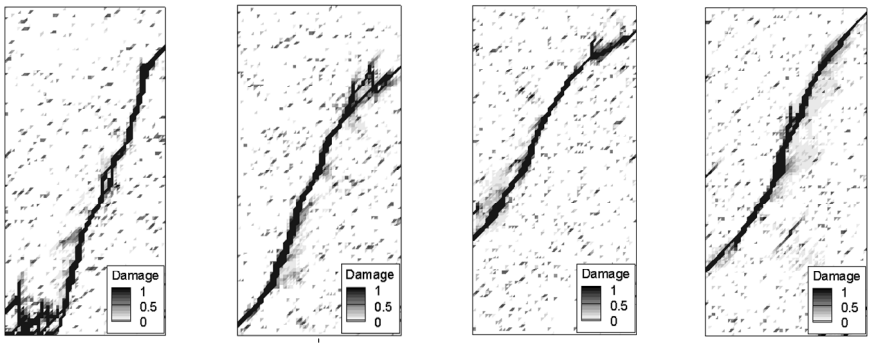

(a) a1= 5 (b) a1= 10 (c) a1= 20 (d) a1= 100

Figure 6.20 Fracture patterns by stiffness shape parameter change

6.5.3 Strength mean value parameter effect

Similar with previous section, mean values of strength distribution were changed accordingly and simulated in Figure 6.21. Based on material strength estimation from numerical results, Weibull parameter change on mean value of strength distribution has strong influence the material strength. It is better to compare the numerical estimation with experimental results, but it is very difficult to use same heterogeneity conditions in experimental test. In every case, fracture plane was fully ruptured through the specimen. Although dip angle and fracture pattern is different, this difference is not critical issue here because rock property has a lot of uncertainty and complexity. Due to these uncertainty and complexity of rock mechanics, it is hard to estimate fracturing phenomena of brittle heterogeneous rock.

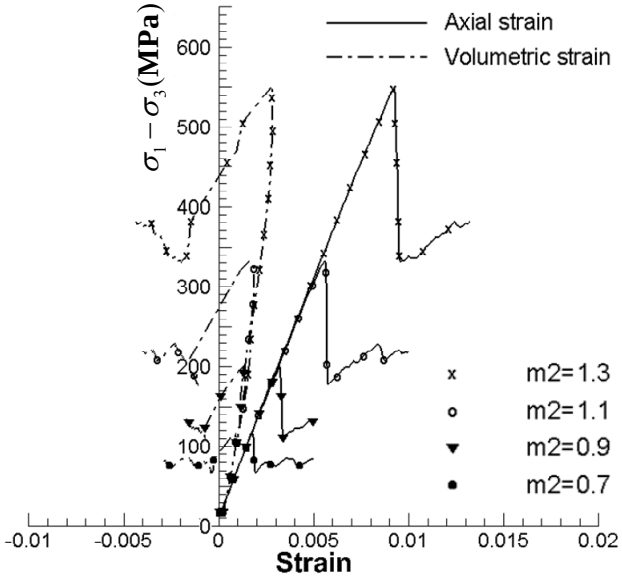

Figure 6.21 Stress/strain curve by strength mean value parameter change

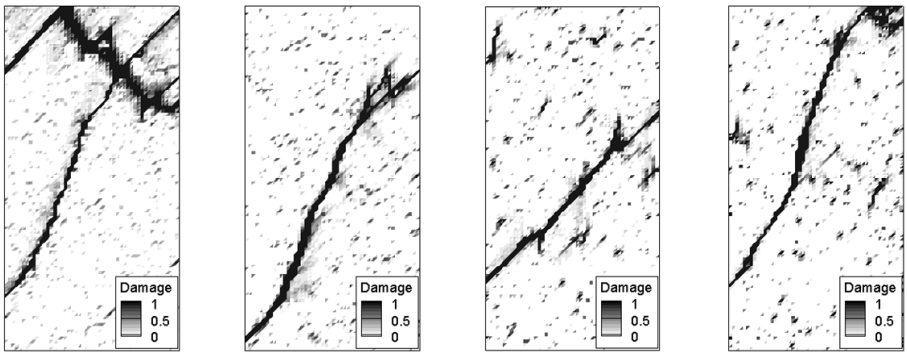

(a) m2= 0.7 (b) m2= 0.9 (c) m2= 1.1 (d) m2= 1.3

Figure 6.22 Fracture patterns by strength mean value parameter change

6.5.4 Strength shape parameter effect

In this section, the effect of the shape parameter on the strength distribution was simulated and discussed with values of a_2=5, 15, 30, 100. Figure 6.23 shows that the strength shape parameters of a_2=15, 30, 100 indicated a similar compressive strength, while the strength shape parameter of a_2=5 has a much lower compressive strength than other cases. As mentioned earlier, a lower Weibull parameter means that the rock has more heterogeneity. That is, the strength shape parameter change has a strong influence on the material strength. In Figure 6.23, fracture planes were formed differently through the fully ruptured path in the specimens. Because every case has different formations of heterogeneity, the fracture patterns are strongly influenced by the heterogeneity formation.

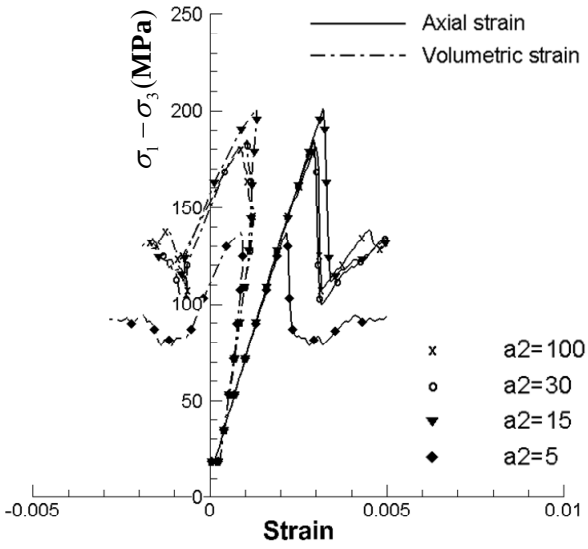

Figure 6.23 Stress/strain curve by strength scale parameter change

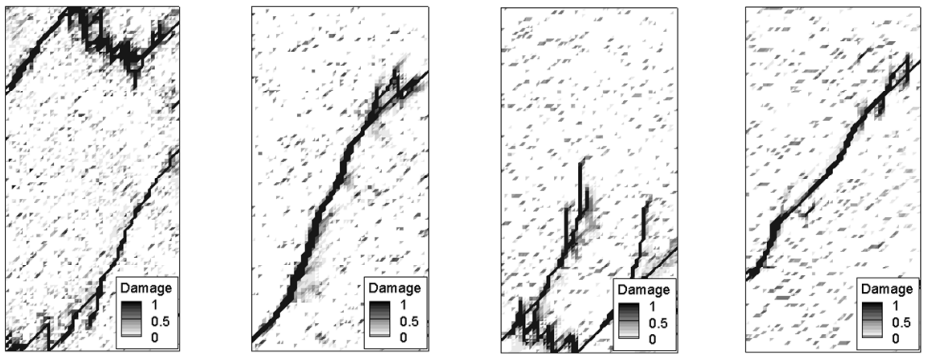

(a) a2= 5 (b) a2= 15 (c) a2= 30 (d) a2= 100

Figure 6.24 Fracture patterns by strength shape parameter change

6.6 Numerical simulation for mesh size effects

In this section, three different sizes of mesh (0.01, 0.02, 0.04) were used for the multistage triaxial simulation [Figure 6.25]. For rock heterogeneity, Weibull parameters of m_1=0.9, a_1=10 for stiffness distribution and m_2=0.9, a_2=15 for strength distribution

were used to generate random variables; this allowed us to apply similar heterogeneity density to the numerical models. Table 6.4 and Figure 6.26 compare compressive strengths estimated by the numerical simulations, and the simulation results show that the estimated strengths generally match well with the experiments. However, the coarse mesh case shows some discrepancy in the high confinement tests, while the intermediate mesh size of 0.02 gives better estimates than other mesh cases.

In Figure 6.27, multiple and unconfined fractures were initiated and propagated during the triaxial compression test. When the confinement increased, the fracture patterns formed with less inclination angle. According to the simulation results, the finer mesh case can capture multiple crack growths; however, computational costs might be exponentially increased. The coarse mesh case shows inaccurate fracture patterns in Figure 6.29. Especially, at the high confinement cases, fracture patterns are significantly different from other mesh cases. Also, estimated compressive strength has larger errors.

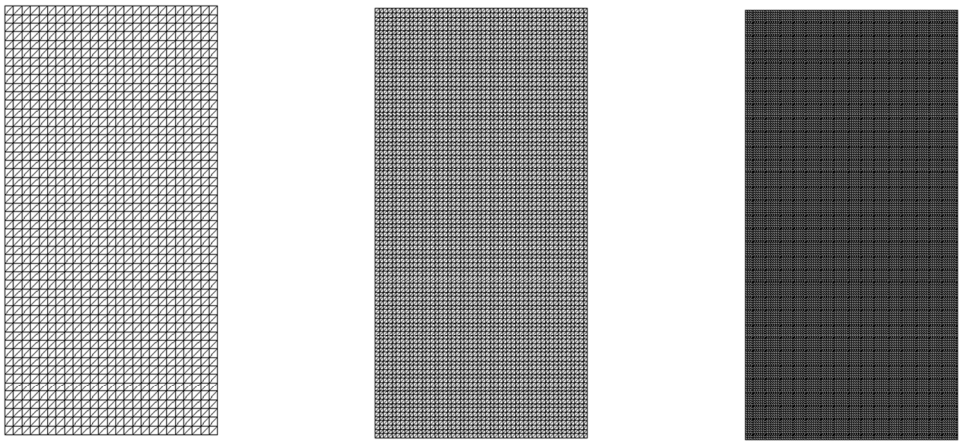

(a) size=0.04(NE=2,500) (b) size=0.02(NE=10,000) (c) size=0.01(NE=40,000)

Figure 6.25 Numerical models with different mesh sizes

Table 6.4. Comparison of experiment and simulations of Tuff samples

Confining Pressure (Unit=MPa)	0	5	15	30	40
Multistage Triaxial tests	88.4	126.9	190.3	261.6	309.2
NE=40,000 (size=0.01)	84.9	107.3	197.5	263.4	339.2
error(%)	4.12	18.27	3.65	0.68	8.84
NE=10,000 (size=0.02)	86.6	124.1	201.1	279.9	321.2
error(%)	2.08	2.26	5.37	6.54	3.74
NE=2,500 (size=0.04)	87.7	132.1	202.9	339.2	385.1
error(%)	0.8	3.94	6.21	22.9	19.7

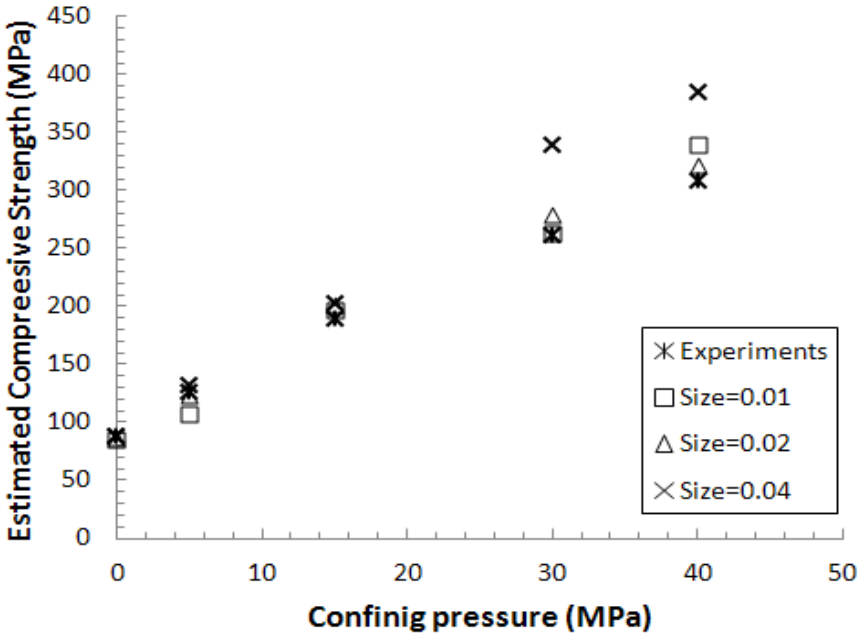

Figure 6.26 Comparison of estimated compressive strength by different mesh size

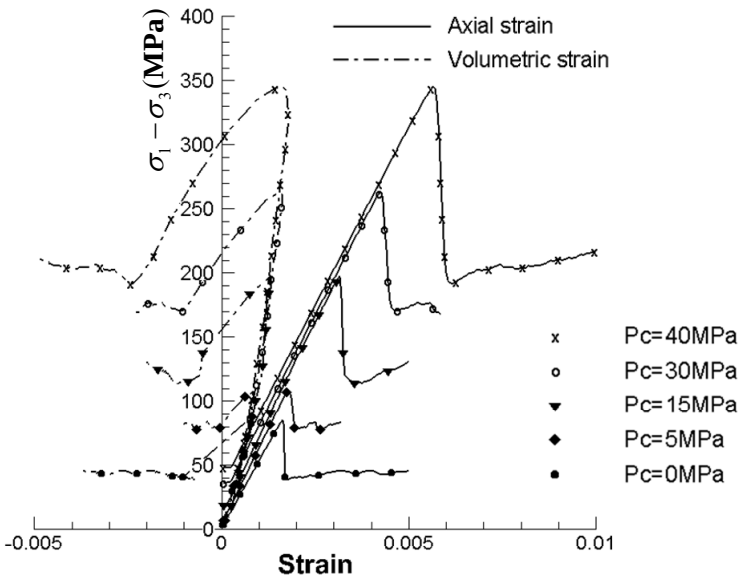

Figure 6.27 Stress/strain curve by various confining pressure at NE=40,000 (size=0.01)

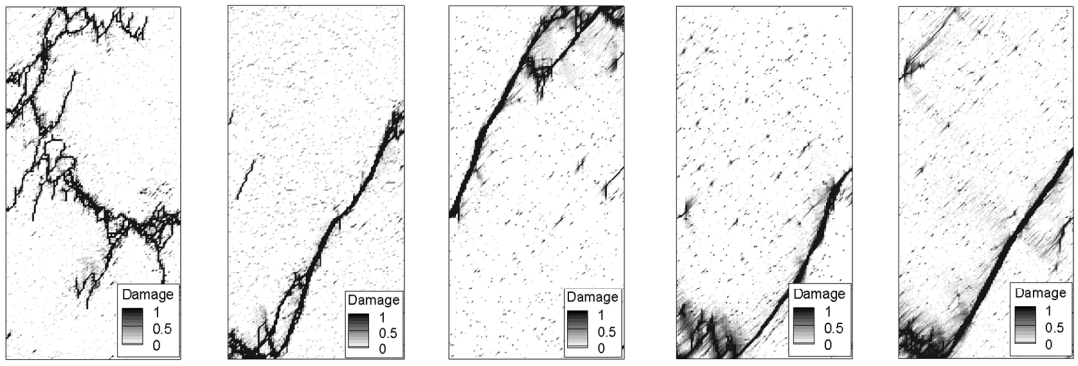

(a)Pc=0MPa (b)Pc=5MPa (c)Pc=15MPa (d)Pc=30MPa (e)Pc=40MPa

Figure 6.28 Fracture patterns by various confining pressure at NE=40,000 (size=0.01)

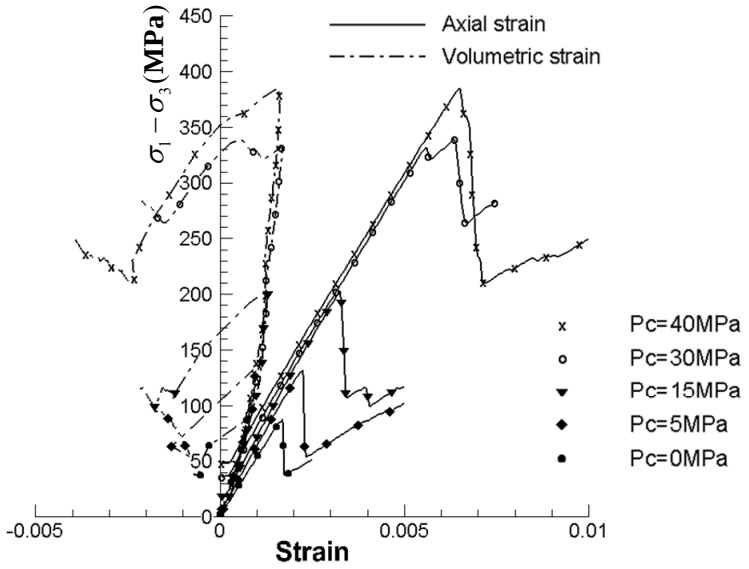

Figure 6.29 Stress/strain curve by various confining pressure at NE=2,500 (size=0.04)

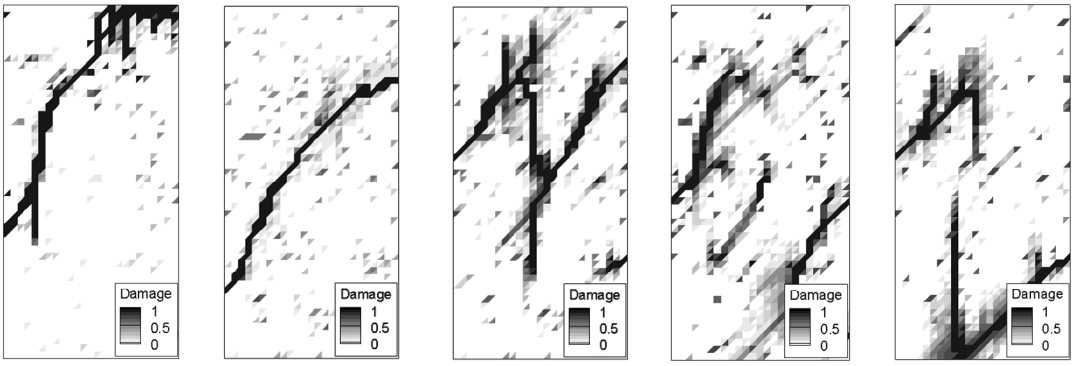

(a)Pc=0MPa (b)Pc=5MPa (c)Pc=15MPa (d)Pc=30MPa (e)Pc=40MPa

Figure 6.30 Fracture patterns by various confining pressure at NE=2,500 (size=0.04)

6.6.1 Mesh dependency issue

Mesh dependency is significant in FEM analysis. A stress-strain relation predicted in finite-element analysis usually depends on the mesh density. The mesh

dependency may increase significant errors during analysis of practical problems (Pande et al. 1990). Thus, reducing mesh dependency is a critical issue in both numerical and practical aspects. In order to reduce the mesh effect, the hypothesis of equivalent energy dissipates rate was proposed and the dissipate energy based constitutive model was developed in section 3. In this constitutive modeling, it is generally assumed that the energy dissipation rate required to initiate/propagate cracks should be similar regardless of finite element size. That is, initial amount of fracture energy and the energy dissipation rate per unit volume for crack initiation/propagation should be consistent in different finite element sizes. So, required fracture energy for bigger element size (NE=2500) should be four times higher than intermediate element size (NE=10000) and sixteen times higher than smallest element size (NE=40000). Also, the energy dissipation rate should be assigned same value regardless of finite element size to maintain the similar softening part of stress-strain curve to keep the fracture energy constant during crack propagation. During the triaxial compression simulation, elastic energy stored by mechanical deformation is computed at each element and the energy dissipation rate is assigned based on the confining pressure, as explained in section 3. Hence, the constitutive relation of each element is governed by the elastic energy variation. When same loading and boundary conditions are applied, the stress-strain relations of three cases (NE=2500, 10000, 40000) show similar behaviors [Figure 6.31], because the fracture energy kept constant.

Based on this hypothesis, the damage model based on energy dissipation rate could be a possible solution for the mesh dependency problem. In the Figure 6.31, strain-

stress curves of the three different mesh sizes show similar behavior. That means total amount of dissipated energy of the three different mesh cases are similar and it indicates less mesh dependency solutions. Consequently, the mesh sensitivity issue has been successfully reduced in numerical analysis; however fracture patterns of the three different mesh cases show different patterns [Figure 6.32]. This is because the fracture patterns are strongly related with distribution of the rock heterogeneity. In our method, the rock heterogeneity does not consist in the three different mesh cases, so that different fracture patterns are obtained in the different mesh cases. In addition, as mentioned earlier, in order to obtain proper fracture pattern and approximated compressive strength, coarse mesh case are not recommended and intermediate finite element size is recommended based on calculation of error estimation and computational cost.

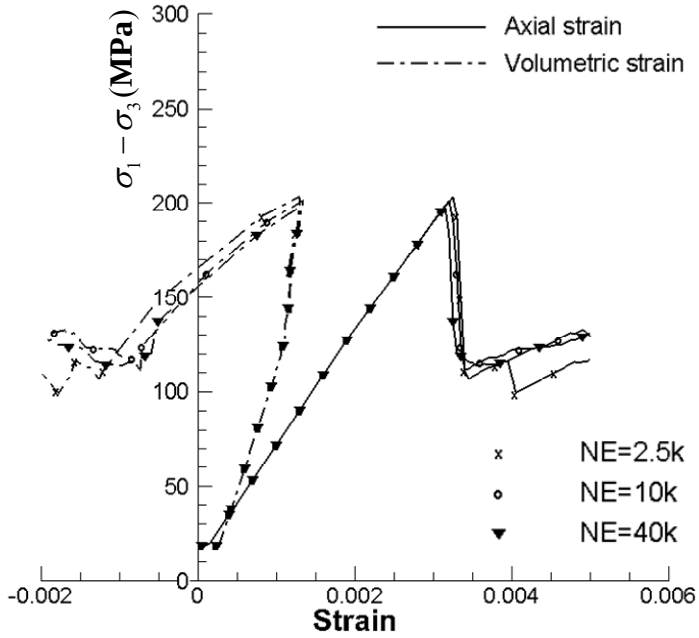

Figure 6.31 Stress-strain behavior at Pc=15 MPa with different element size.

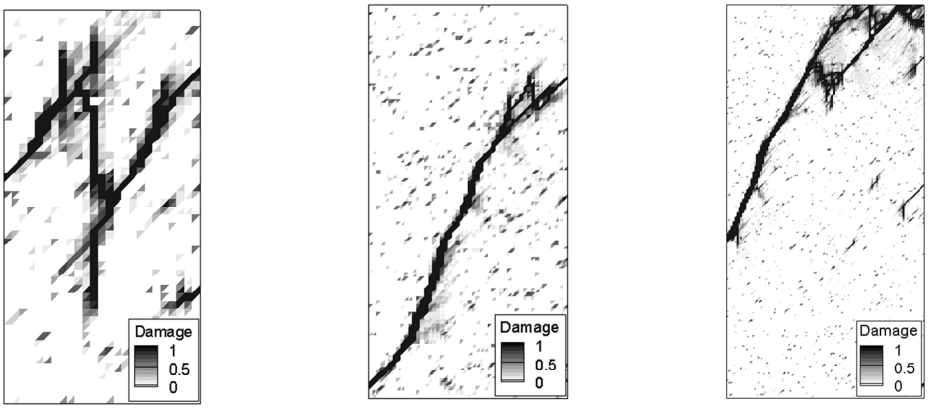

(a) size=0.04(NE=2,500) (b) size=0.02(NE=10,000) (c) size=0.01(NE=40,000)

Figure 6.32 Fracture pattern at Pc=15 MPa with different element size.

6.7 Limitation and future improvement

The elastic/brittle constitutive model of the brittle rock was developed and simulated to study the influence of confining pressure through calibration with the multistage triaxial experiments. The numerical results show a reasonable approximation for the stress-strain relations and fractured behavior with core samples after the triaxial test. The elastic-brittle constitutive assumption is suitable for material behavior of the granite sample, but not for the Tuff sample, because, as confining pressure increases, material behavior of the Tuff becomes more ductile, and the fracture plane may be affected by the material behavior. Our present model does not include the plastic hardening deformation, so the stress-strain relation did not perfectly match laboratory experiment results [Figure 6.10]. Thus, to consider the ductile behavior, we should introduce plasticity to our model, along with an additional damage variable that could represent the plastic hardening behavior (Pijaudier-Cabot and Bazant 1987).

6.8 Conclusion

In this section, the brittle failure mechanism of heterogeneous rock was studied using continuum damage mechanics within an FEM formulation. Also, rock was fractured in mixed modes which require complex criteria for predicting failure, but theoretical approaches were not sufficient to do it. Thus, the simplified constitutive relations were used to estimate compressive strength and general strain-softening behavior corresponding with confining pressure, although it could be ideal to use different constitutive relations for different types of material to give a more realistic physical interpretation. Hence, for simplicity of numerical implementation, an isotropic damage variable was used to represent stiffness degradation and crack initiation/propagation. In addition, three basic types of mechanical state transition processes—reversible elastic, irreversible inelastic, and irreversible friction—were generally explained [Figure 6.7].

The mesh-dependency problem is a critical issue in FEM analysis; a rate theory for how equivalent energy dissipates was proposed in this paper. As a result, generally good agreement was shown in Figure 6.31. A design methodology was shown to predict the strength and dilation for a simplified brittle failure mechanism of heterogeneous rock. For further improvement for a realistic numerical model, predicting practical rock properties is a critical and challenging issue.

To include rock properties into the numerical model, many influencing parameters should be considered. First, specific information of volume fractions and

specific properties of each composed rock including mineral, porosity, and saturation configuration are required. Second, internal structure and texture information regarding rock geometry, which includes grain size and shape, internal surface, and arrangement of components, are necessary. Third, interface and bonding properties including cementation, grain boundary effects, and interface contact effects should also be considered. Fourth, thermodynamic conditions including pressure, stress field, and temperature are necessary to include. In addition, investigations of anisotropy behavior of rock are required to construct a strong correlation of rock heterogeneity with structural/textural properties and physical properties.

7. 3D NUMERICAL SIMULATION OF COMPRESSION TEST

In this section, uniaxial compression test was used to study brittle fracture phenomena in a heterogeneous rock. When compressive forces are applied to the brittle rock, the fracturing patterns are complex, and replicating the shear localized fracturing patterns is challenging using numerical methods, especially for the three-dimensional simulation. The shear-faulting phenomenon depends on many parameters such as strength, heterogeneity, initial flaws, composition pattern, and grain size of rock. Because of the model's complexity, rather than attempting to consider grain size in numerical simulations, a probability distribution function was used to characterize the strength of fine- and coarse-grained rock in this study.

The heterogeneity of brittle rock was characterized by the Weibull distribution function (Weibull 1951), which was chosen for its flexibility. Random values generated by Weibull distribution function were applied to both stiffness and compressive strength to represent the heterogeneous character of the rock. In this study, Weibull distribution parameters, m_1=1, a_1=5 for stiffness distribution and m_2=1, a_2=4 for strength distribution are used to characterize rock heterogeneity. The cylindrical specimen of rock with a size ratio of 2:1 and material properties in Table 7.1 were used in this simulation. The numerical domain for the uniaxial compression test is described in Figure 7.1. We used 57,153 uniform tetrahedron elements and applied displacement loading on the top surface of the cylindrical specimen. Boundary condition was that the bottom surface of the specimen was restricted in the z-direction, and the axial force was

loaded on the top surface of the cylindrical specimen using displacement increments of $\Delta d=3.55\times10^{-3}$. Heterogeneous distribution of element stiffness was applied to each element by random variables with an average stiffness value of 73.5GPa [Figure 7.1]. Lighter-colored elements represent weaker rock, while darker colored elements represent stronger.

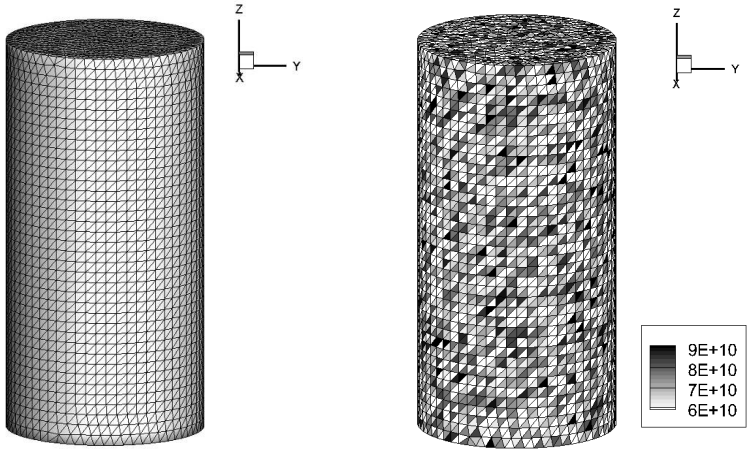

Figure 7.1 Numerical model and heterogeneity index (Unit=Pa)

Table 7.1 Material properties and input parameters for 3D uniaxial

Inputs	Values
Element type	Tetrahedron
Young's Modulus, GPa	73.5 GPa
Poisson ratio	0.32
Num. of elements	57,153
Size of element	0.05
Aspect ratio (D:H)	1:2
Tensile strength, MPa	15-30
Incremental displacement	0.1e-3
Weibull parameters	m_1=1, a_1=5 for stiffness m_2=1, a_2=4 for strength

7.1 Numerical simulation of uniaxial compression

When rock heterogeneities were applied on both the stiffness and compressive strength of each element, fully penetrated cracking was found [Figure 7.2]. Because the rock specimen was modeled as very brittle material, fully ruptured fracturing occurred in a very short period (Steps 175-195). Multiple failures were initiated at Step 175 when the total applied displacement on the top surface was $\Delta d=6.21\times10^{-1}$. Also, we can see very broad and spotted damage propagation due to the rock heterogeneity [Figure 7.3]. The rock specimen is more damaged near the fracture plane after contact and shear faulting fully ruptured fracturing of the specimen. Figure 7.2 shows damage propagation with deformation over the step, so that the part with more deformation in the damaged zone is clearly visible.

In Figure 7.4, the maximum principal stress is mostly focused in the damaged zone and strain localization follows crack element propagation. According to the uniaxial compression simulation, the compressive failure of brittle rock predominated at the earlier period of rock fracture. The compressive stress led to shear faulting of the brittle rock after that, and the shear faulting dominated mostly during the fracture propagation.

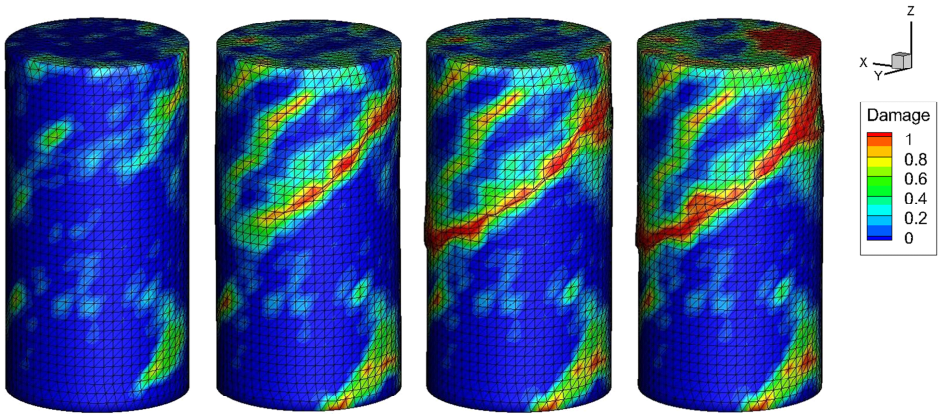

Figure 7.2 Damage propagation along steps with deformation (step= 175,185, 190, 200)

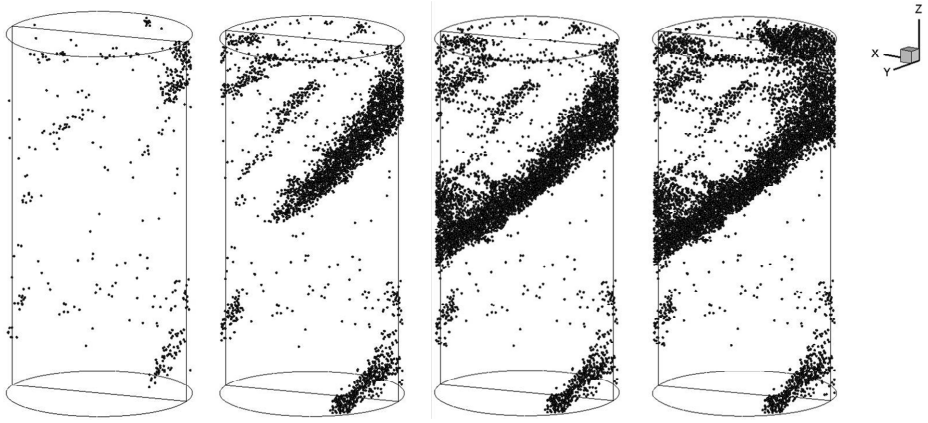

Figure 7.3 Damage events during uniaxial compression (step= 175,185, 190, 200)

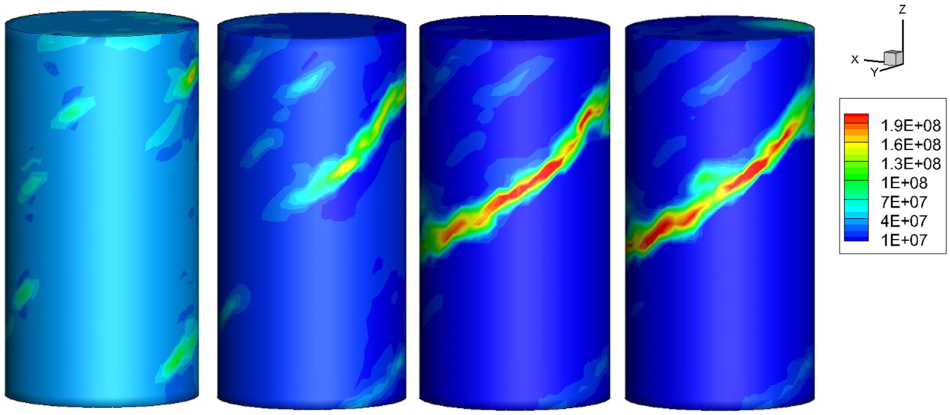

Figure 7.4 Principal stress propagation (Unit=Pa) (step= 175,185, 190, 200)

7.2 Snapback issue during triaxial compression

In this section, 3D numerical simulations were performed for triaxial compression test. Numerical model is same as previous 3D uniaxial simulation and material properties [Table 7.2] were used. When confinement is applied to the rock specimen, snapback issue is found Figure 7.5 and Figure 7.6]. From the numerical results, it is observed that fully ruptured fracture plane is successfully formed through the rock specimen. However, stress-strain curves show snapback behavior during crack propagation [Figure 7.5 and Figure 7.6].

The snapback behavior occurs for brittle materials when more fracture energy dissipated than the stored elastic energy during crack propagation. In the case of brittle materials, crack propagation causes sudden drop of the load and it could lead unstable response of stress-strain relation. The instability of mechanical behavior represents the snapback phenomenon. The snapback issue is normally caused by numerical destabilization, because more energy is dissipated than it actually should (Bazant and Planas 1997). The snapback issue does not occur in 2D triaxial simulation, while only 3D triaxial simulation shows the snapback issue. This is because more energy is dissipated during crack propagation in the 3D triaxial simulation. Since we used scalar relation between the normal stress and strain for 3D constitutive modeling, the scalar degradation model could not represent the compressive failures in triaxial phenomenon, in which failure is triggered by lateral expansion and shear slip on inclined mircroplanes.

Therefore, in order to consider the triaxial variation of elemental degradation model, tensor type of damage model is recommended and the tensor damage model

might be a solution of the numerical destabilization by the snapback phenomenon. However the tensor type of damage modeling is requiring complex mathematical formulation and high computational efforts. So, this issue is out of scope of our research and development of the tensor damage model is remaining for future improvement.

Table 7.2 Material properties and input parameters for 3D tiaxial

Inputs	Values
Young's Modulus, GPa	53.84 ~54.76 Gpa
Poisson ratio	0.32~0.34
Tensile strength, MPa	15-30
Incremental displacement	0.1e-3
Confining pressure, Pc	5MPa, 15MPa
Weibull parameters	m_1=1, a_1=9 for stiffness m_2=0.9, a_2=10 for strength

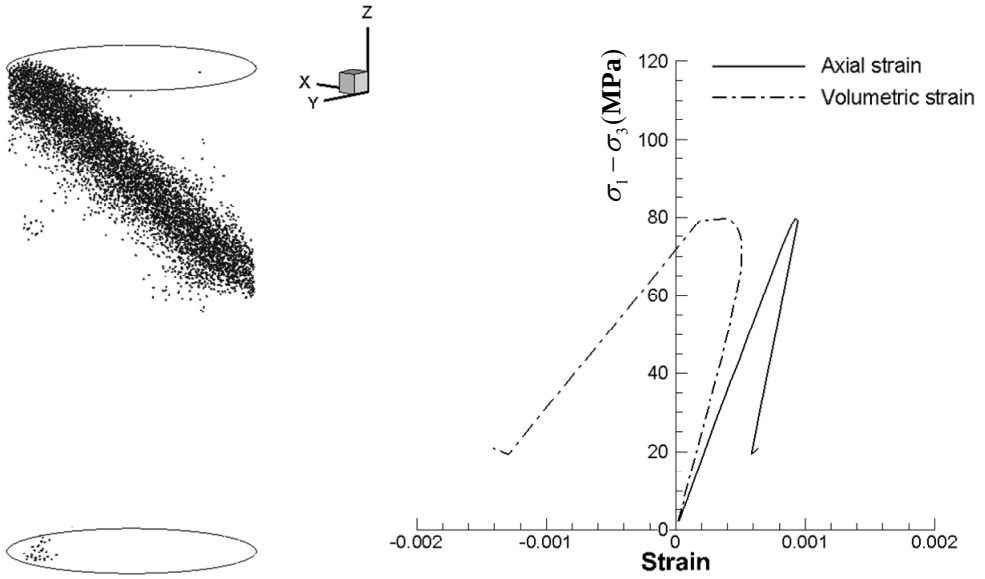

Figure 7.5 Plot of damage events and stress-strain curves of snapback at Pc=5MPa

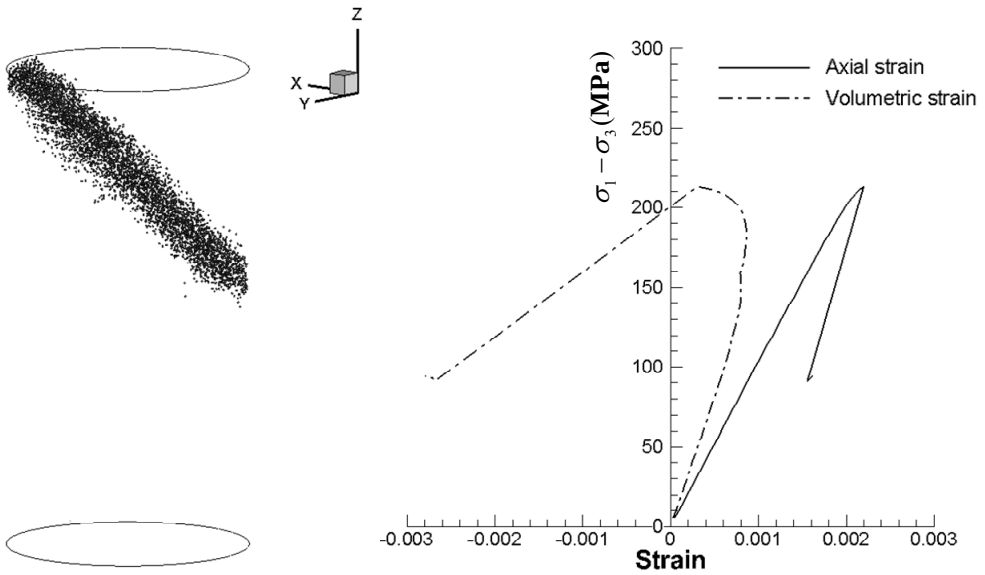

Figure 7.6 Plot of damage events and stress-strain curves of snapback at Pc=15MPa

7.3 Conclusion

In this section, 3D uniaxial and triaxial compression tests were simulated using the elemental degradation model using continuum damage mechanics. The scalar damage variable was used to represent stiffness degradation and crack propagation. According to the numerical results, it is clearly seen that process of fracture propagation through the rock specimen. The snapback phenomenon was found from the 3D triaxial simulation. The numerical instability might be caused by the scalar constitutive modeling of mechanical degradation.

From the numerical simulations, rock heterogeneity is an important factor for forming of fracture propagation, since existing microcrack and grain size could affect on rupture paths through the brittle rock specimen. Also, the brittle rock is composed by several size of micro-grain which has different stiffness, so that accuracy of representing

rock heterogeneity is key factor of numerical simulation of the rock fracturing. However, most of all, large part of material properties of rock is uncertain, so that it is very difficult to characterize mechanical behavior of heterogeneous rock in both microscopic and macroscopic view. In this study, the Weibull distribution function was chosen due to its flexibility, although the Weibull distribution is not perfectly for representing rock heterogeneity.

8. NUMERICAL SIMULATION FOR MIXED FRACTURE PROPAGATION

Hydraulic fracturing paths, especially for fractures emanating from inclined wellbores and closed natural fractures, often involve mixed models of Mode I, Mode II, and Mode III fracture patterns. When an embedded inclined fracture is subjected to compression, the fracture tips are restrained by the surrounding materials so that it does not propagate as predicted by a single-mode fracture (Min et al. 2011). In this section, two- and three-dimensional mixed-modes fracture growths from an initially embedded crack were studied using damage mechanics implemented within a finite element method (FEM). Especially, simulation of three-dimensional fracture propagation is complex as it often simultaneously involves all three fracture modes over a contour. Whereas in a 2D case, the zone of interest is only a point (fracture tips), in a 3D case, the fracture tip is a closed boundary, making development of a fracture criterion for predicting propagation at different points along its edges difficult.

8.1 Wing-crack model

In this section, two-dimensional and three-dimensional wing crack growths were studied under compressive forces. As shown in Figure 8.2, the extension of secondary cracks in the brittle rock forms by mixed mode fracture. In 2D crack growth, the wing cracks (tensile fracture) grow towards the direction of maximum compression, while the secondary cracks (shear fracture) grow by sliding toward the lateral direction of the maximum compressive force due to the transverse shear localization. *Primary cracks*,

describing of the wing crack, are originated from points of highest tension stress. *Secondary cracks*, describing of the shear fractures, are originated from points of compressive stress concentration. After the tensile stress concentration initiates the primary cracks, the compressive stresses originated from the sliding of the upper and lower areas of the pre-existing crack, and the shear concentration leads to growth of the secondary cracks opposite the primary cracks. Sequential growths of the primary and secondary cracks were observed in experimental tests (Bobet and Einstein 1998; Lajtai 1973; Wong and Einstein 2009).

Practically, 3D crack growth mechanism is more complicated. As shown in Figure 8.2, the primary cracks are originated from upper and lower areas of the pre-existing plane. By the compressive stress concentration, the secondary cracks are growing on the opposite side of the contact surface by Mode II conditions and the additional secondary crack could grow in the lateral direction due to Mode III conditions. In Figure 8.3 and Figure 8.4, the mixed modes of fracture propagation have been observed in experimental modeling (Bieniawski 1967; Bobet and Einstein 1998; Dyskin AV 2003; Germanovich and Dyskin 2000; Sagong 2001). The experimental observations show tensile and shear crack growth in compression. The shear crack growth in compression is difficult to observe during the experiments, especially for Mode III, because the tensile mode, not the shear mode, is the dominant fracture mechanism in compression. However, when the confining pressure is high, as occurs when the rock is deep underground, the shear modes cracks may be the dominant fracture mechanism.

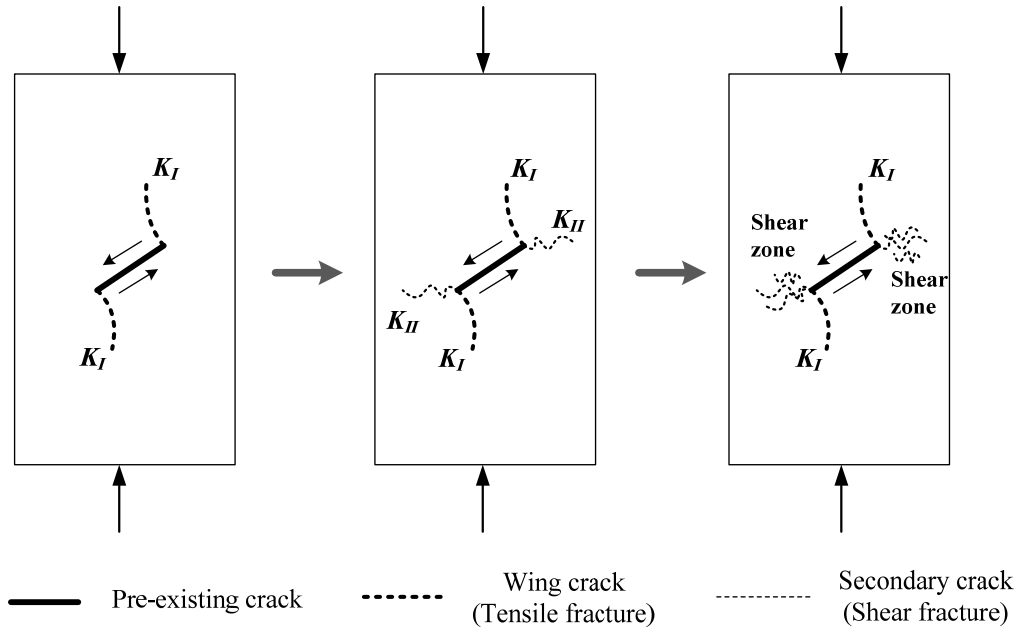

Figure 8.1 Evolution of 2D wing crack fractures from a pre-existing crack by (Mixed mode of $K_I + K_{II}$)

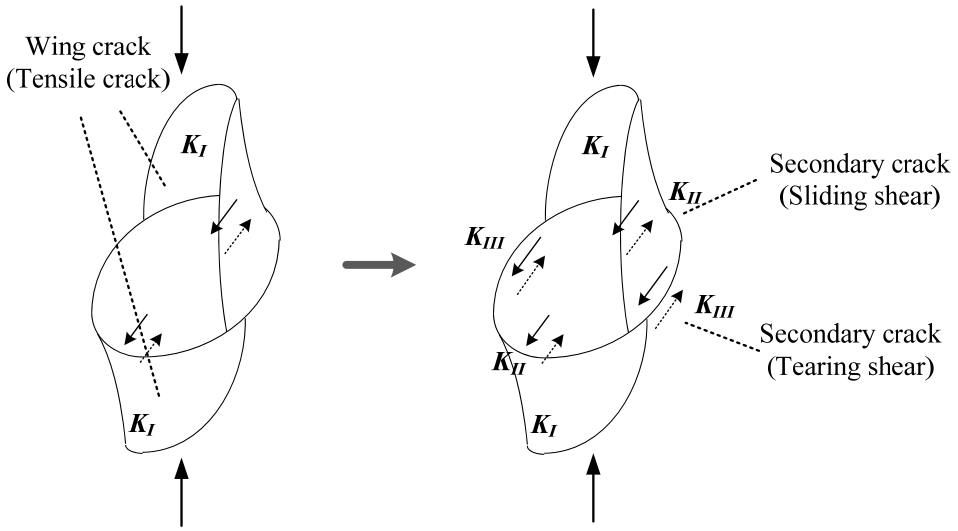

Figure 8.2 Evolution of 3D wing crack fractures from a pre-existing plane by (Mixed mode of $K_I + K_{II} + K_{III}$)

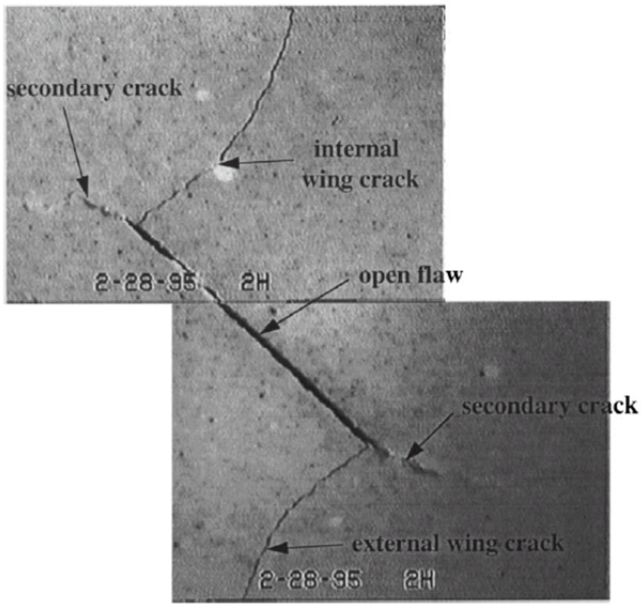

Figure 8.3 Crack growths of 2D wing-crack in uniaxial compression (Bobet and Einstein 1998).

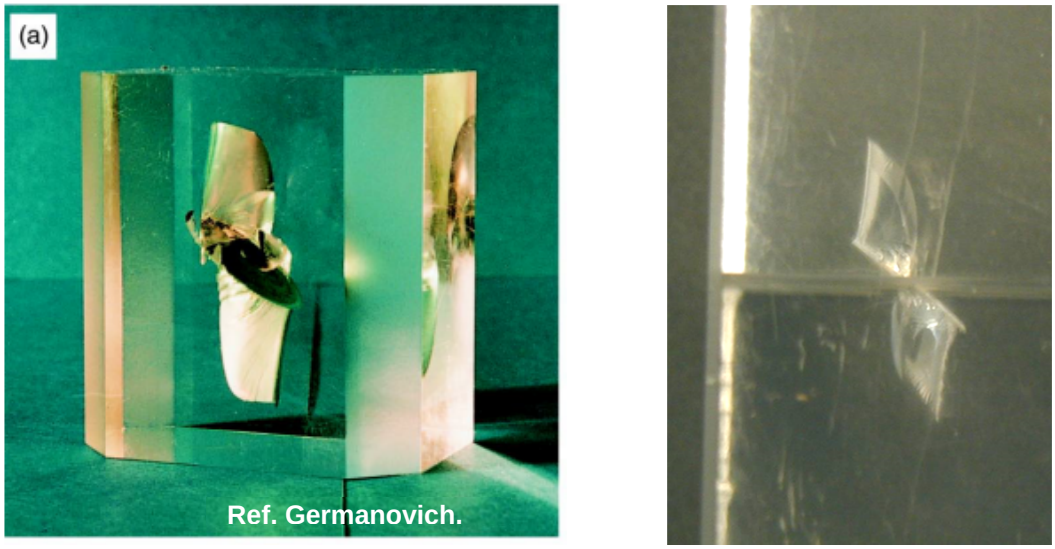

Figure 8.4 Crack growths of 3D wing-crack in uniaxial compression (Dyskin et al. 2003; Germanovich and Dyskin 2000)

8.2 Numerical results of 2D wing crack model

Two-dimensional plane strain and 40,000 uniformly meshed triangular elements were used in this simulation, described in Figure 8.5(b). Boundary conditions of the wing-crack model, described in Figure 8.5(a), were that the bottom surface of the specimen was restricted in the y-direction and the compressive force was applied on the top surface of the specimen using a displacement increment of $\Delta d=1\times10^{-3}$. Material properties and numerical input values for the 2D wing crack simulation are shown in Table 8.1. A pre-existing crack was located at center of the specimen with a 45° inclination angle [Figure 8.5(b)]. The pre-existing crack is assumed an open flaw same as the experimental test [Figure 8.3]. In order to express the open flaw in numerical domain, crack elements overlapped with the initial crack geometry are modeled by assigning high damage variable (D=0.9). In addition, same as the experiment the crack elements are assumed as frictionless. If the pre-existing flaw is rough, crack initiation and propagation from the closed flaw are much different with the open flaw propagation. The closed flaw propagation was discussed in (Bobet and Einstein 1998). Three cases are compared below: a tensile-dominated case, a shear-dominated case, and a mixed-modes case. The influence of various confinements on crack propagation and the mesh-dependency issue are discussed in this section.

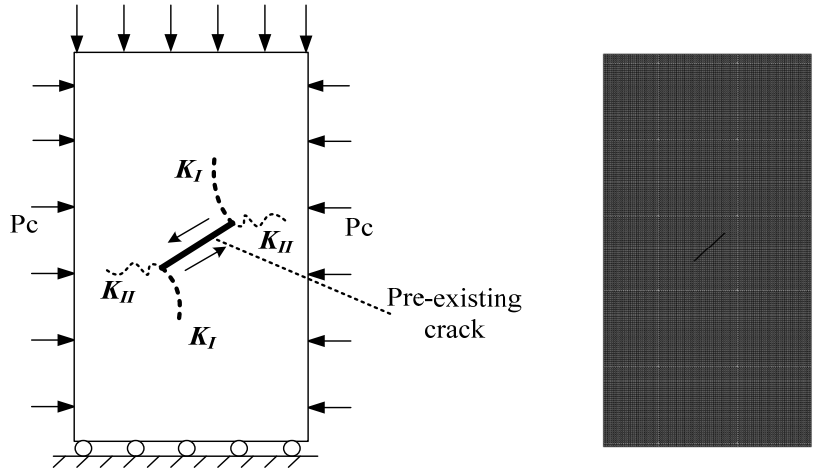

Figure 8.5 Numerical modeling of 2D wing crack model (a) Boundary condition (b) Meshed domain with inclined pre-existing crack

Table 8.1 Material properties and input parameters for 2D Wing crack

Inputs	Values
Young's Modulus, E (GPa)	37.5
Poisson ratio, υ	0.25
Number of Elements	40,000
Number of Nodes	20,301
Element type	Triangular
Ratio of specimen(D:H)	1:2

8.2.1 Tensile dominated wing crack growth (Mode I)

We assumed zero confining pressure applied on the specimen and Mohr-Coulomb parameters are assumed as shown in Table 8.2. In Figure 8.6, it was observed that tensile failure is a dominant failure mechanism under compression in the wing-crack model. In Figure 8.7, tensile stresses were concentrated at upper and lower areas of the pre-existing crack and the primary cracks (wing crack) initiated at step=25 and

propagated until step=90 with the longer primary cracks. It was also observed that the maximum tensile stress concentration was following at the tensile crack tips and high compressive stress was developed at lateral directions of the pre-existing crack [Figure 8.6(c)], but the secondary cracks (shear crack) were not developing until step=90. The compressive stress eventually leads to initiation of the secondary crack (shear crack). The shear dominating crack growth was discussed in section 8.2.2.

Table 8.2 Mohr-Coulomb parameters for tensile dominating crack (Mode I)

Inputs	Values
Mohr-Coulomb parameter, ϕ_f	10
Cohesion, c_F (MPa)	50
Tensile strength, σ_T (MPa)	10
Incremental displacement, Δd (mm)	1

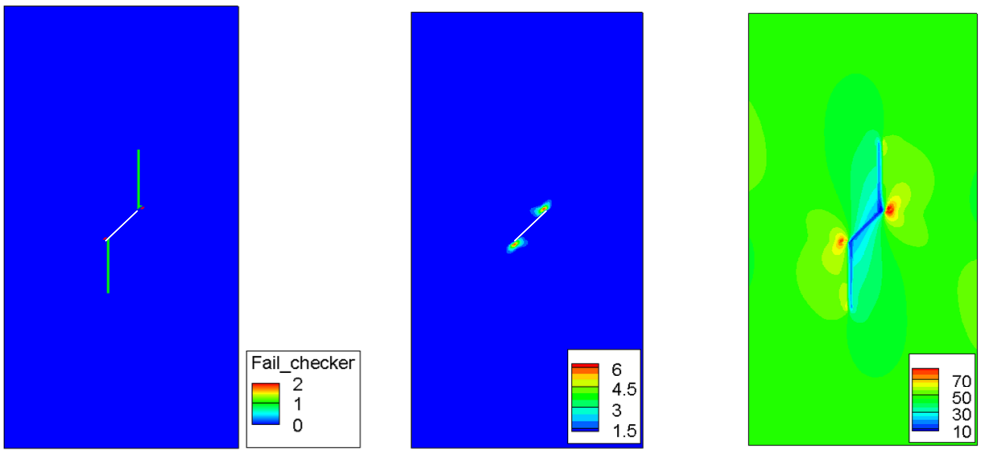

(a) step=90 (b) step=25 (c) step=90

Figure 8.6 (a) Failure type (1:tensile, 2: shear), (b) Maximum tensile stress (unit=MPa), (c) Maximum compressive stress (unit=MPa)

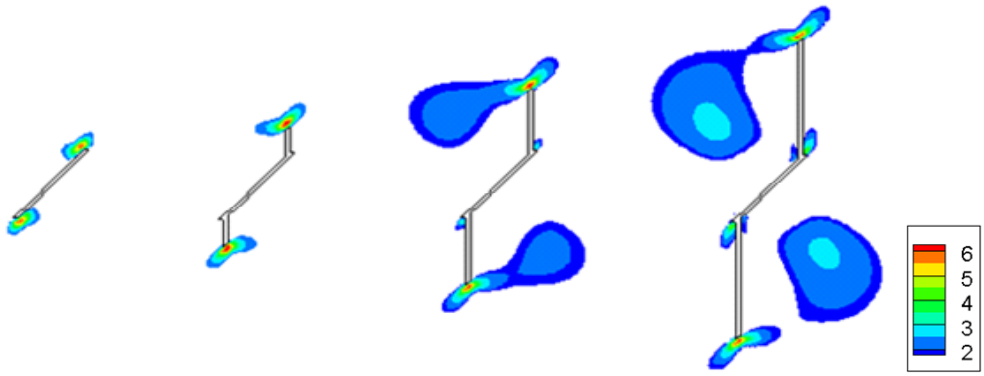

(a) step=25 (b) step=40 (c) step=60 (d) step=90

Figure 8.7 Maximum tensile stress (unit=MPa) with tensile crack growth

8.2.2 Shear dominated wing crack growth (Mode II)

For the shear dominated crack simulation, we applied a confining pressure of Pc= 20 MPa on the specimen and Mohr-Coulomb parameters are assumed as shown in Table 8.3. When a high confining pressure is applied, shear failure becomes a dominant failure mechanism in the wing crack model and the shear dominated crack propagation can be observed [Figure 8.8]. Since tensile cracks were restrained by the applied confining pressure, compressive stresses concentrated at the lateral areas exceeded shear failure criterion and led to initiation of the secondary cracks (shear crack). In Figure 8.9, the secondary cracks were initiated at the crack tips towards the lateral direction, and the shear-dominated cracks grew obliquely. The oblique shear crack growth was also observed from experiments in Figure 8.3 (Bobet and Einstein 1998). The shear failure is a dominant failure mechanism when high confining pressure was applied on the rock.

Numerical study of the transition phenomena from tensile to shear dominating failure was discussed in section 8.2.4.

Table 8.3 Mohr-Coulomb parameters for shear dominating crack (Mode II)

Inputs	Values
Mohr-Coulomb parameter, ϕ_f	10
Cohesion, c_F (MPa)	50
Tensile strength, σ_T (MPa)	15
Incremental displacement, Δd (mm)	1

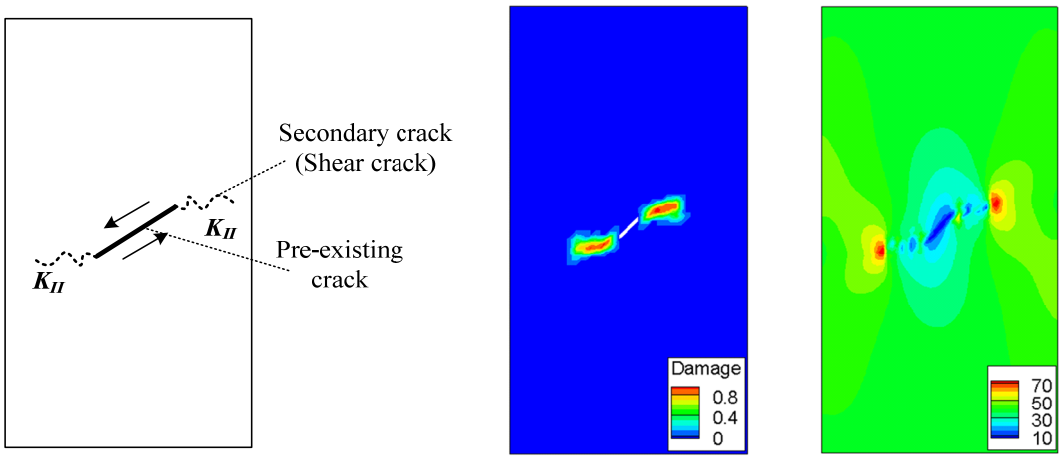

(a) (b) step=145 (c) step=145

Figure 8.8 (a) Schematic of shear dominant crack growth (b) Damage propagation (c) Maximum compressive stress (unit=MPa)

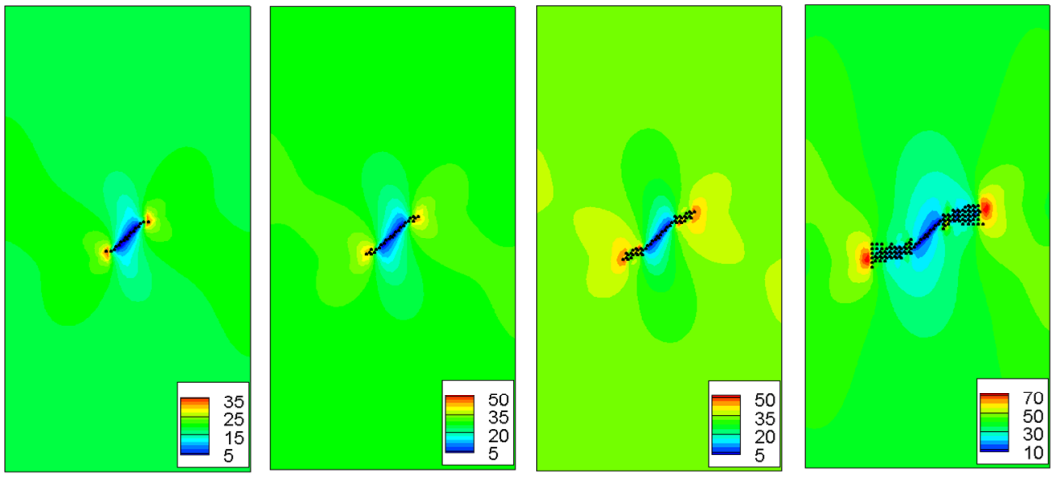

(a) step = 54 (b) step = 40 (c) step = 110 (d) step = 145

Figure 8.9 Maximum compressive stress (unit=MPa) with shear crack growth

8.2.3 Mixed modes wing crack growth (Mode I+II)

In this section, we investigated a sequential growth of the primary cracks (tensile crack) and the secondary cracks (shear crack). We assumed zero confining pressure and Mohr-Coulomb parameter, as shown in Table 8.4, are assumed for the mixed modes wing crack growth case. In Figure 8.10, it was observed that the primary cracks grew first until step=70 and the second cracks were initiated from step=80. Since a tensile strength of a rock is much lower than a compressive strength, tensile failure is dominant failure mechanism at early stages. Experimental data typically shows that the ratio of the uniaxial compressive strength/the tensile strength is much greater than 2 (Jaeger et al. 2007). So, after an amount of growth of the tensile crack, the shear-induced crack was initiated from the crack tips, and it grew laterally to the pre-existing crack. The results agree with experimental observations in Figure 8.3 (Bobet and Einstein 1998).

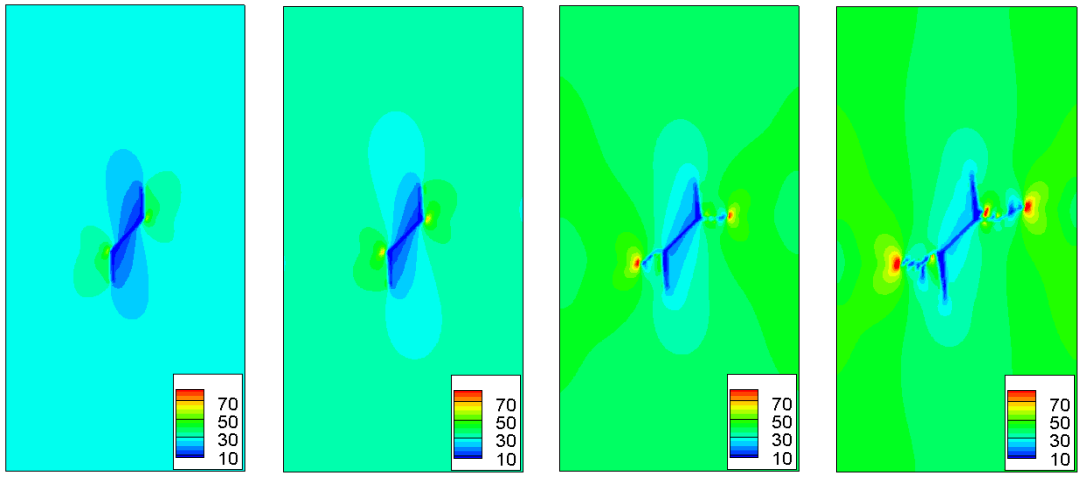

(a) step = 70 (b) step = 80 (c) step = 100 (d) step = 110

Figure 8.10 Maximum compressive stress (Unit=MPa) for mixed mode crack growth

Table 8.4 Mohr-Coulomb parameters for mixed modes 2D wing crack (Mode I+II)

Inputs	Values
Mohr-Coulomb parameter, ϕ_f	10
Cohesion, c_F (MPa)	30
Tensile strength, σ_T (MPa)	10
Incremental displacement, Δd (mm)	1

8.2.4 Influence of confining pressure

As we discussed earlier, tensile crack initiation is favored over shear crack initiation because the tensile toughness of the rock type material is lower than the shear toughness (Bieniawski 1967). However, when the confining pressure on the rock becomes higher, the confinement will constrain the tensile crack initiation; thus, the shear failure becomes dominant in failure mechanics. Especially, a rock at deep depth is

under high confining pressure, and it cannot fail by one dominant mechanism. In that case, the crack propagation is highly influenced by the confining pressure. In order to investigate the influence of the confining pressure, we simulated several numerical examples of the wing-crack model with various confining pressures. Input data and Mohr-Coulomb parameters were used as shown in Table 8.5.Table 8.4 We compared crack propagation patterns in Figure 8.11. Results of Pc=0MPa and Pc=5MPa are crack propagation at step=90, while results of Pc=10MPa and Pc=20MPa are crack propagation at step=120. The simulation results show the effect of confining pressure on a change in failure mechanism. From the simulation results, tensile cracking was dominant when the confining pressure is low, while shear cracking becomes dominant when the confining pressure is high.

Table 8.5 Mohr-Coulomb parameters for confining influence on 2D wing crack

Inputs	Values
Mohr-Coulomb parameter, ϕ_f	10
Cohesion, c_F (MPa)	35
Tensile strength, σ_T (MPa)	10
Incremental displacement, Δd (mm)	1

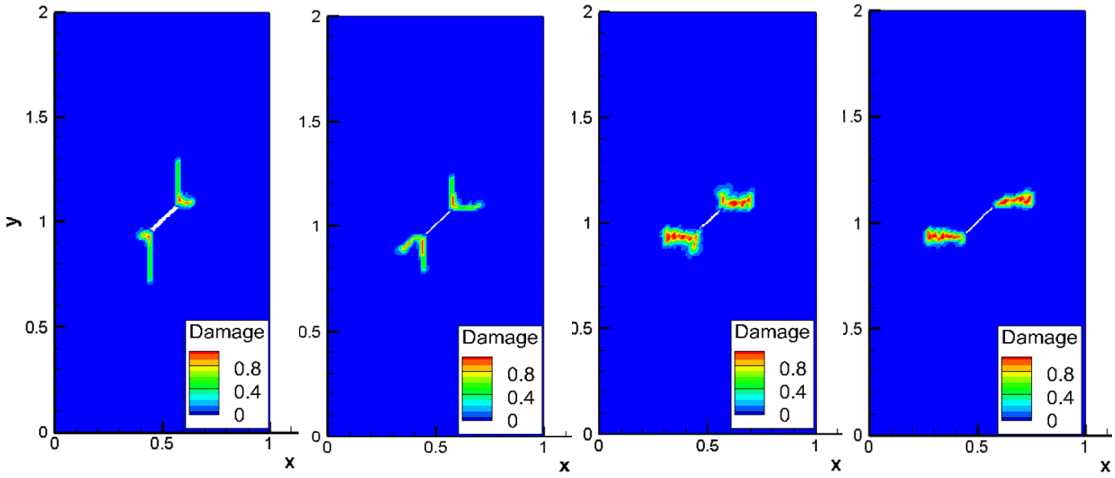

(a) Pc=0MPa (b) Pc=5MPa (c) Pc=10MPa (d) Pc=20MPa

Figure 8.11 Mixed modes crack propagation at various confining pressure

8.2.5 Mesh dependency issue for crack propagation

Similar with the previous study in Section 6.2.4, the mesh-dependency issue in crack propagation is an important issue in FEM analysis. If the mesh-dependency issue is not considered, crack growth rate could depend on the mesh size. Usually, finer mesh is preferred for use in crack propagation modeling, since the finer mesh can describe more realistic crack growth. However, the finer mesh increases computational cost exponentially. Therefore, reducing the mesh dependency is important to reduce the computational cost.

In this section, we compared three different mesh cases using a 2D wing-crack model. We assumed zero confining pressure and Mohr-Coulomb parameters are assumed as shown in Table 8.2. In Figure 8.12, three cases (size=0.04, 0.02, 0.01) are described with an inclined, pre-existing crack. Using the damage model developed using

the hypothesis of equivalent energy dissipation rate from section 3, we examined the influence of mesh size on crack growth rate. According to the simulation results in Figure 8.13, crack propagation rates at step=110 are similar in three cases. In all three cases, both tensile and shear crack growth are modeled by a similar pattern. However, larger size (size=0.04) shows much thicker damage zone than smaller size (size=0.01). This is because our crack propagation model is assumed that the crack is only propagating through elements. Thus, larger size case is only shown the thicker damage zone than other cases. But, growth rate of crack propagation is similar in all three cases, which means the mesh dependency was successfully reduced.

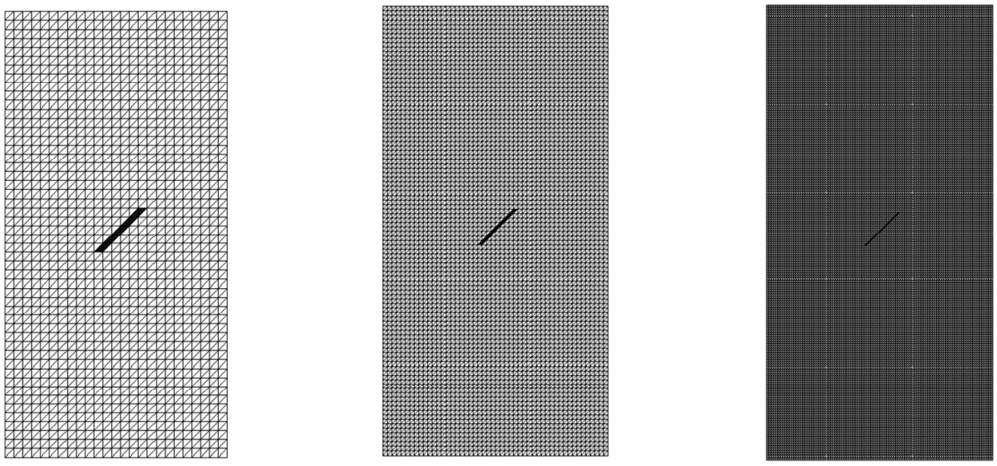

(a) size=0.04(NE=2,500) (b) size=0.02(NE=10,000) (c) size=0.01(NE=40,000)

Figure 8.12 Numerical model by different mesh size

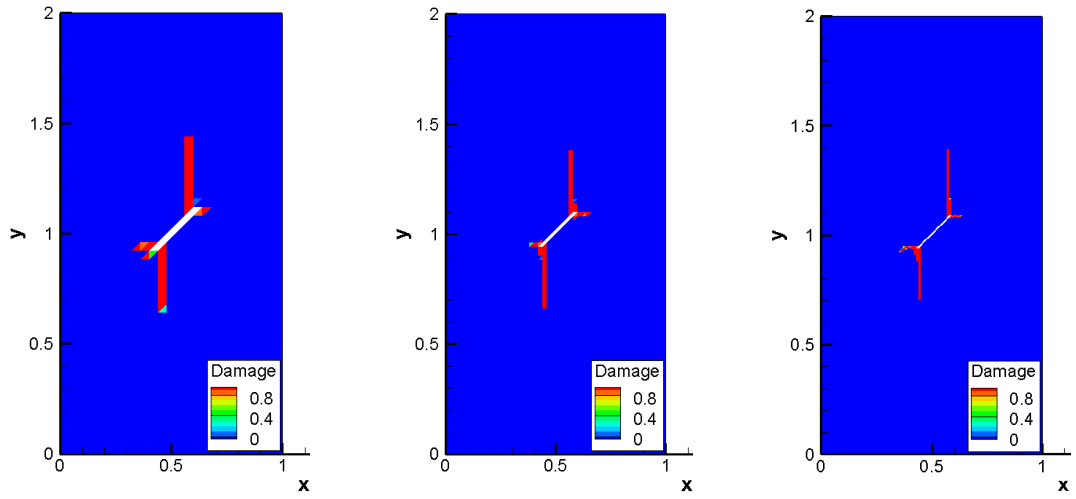

(a) size=0.04(NE=2,500) (b) size=0.02(NE=10,000) (c) size=0.01(NE=40,000)

Figure 8.13 Damage propagation (step=110) at different mesh size

8.3 Numerical results of 3D wing crack model

This section explains the development of three-dimensional wing-crack growth under uniaxial compression from an initially embedded circular crack. In addition, it examines the extension of secondary cracks in a brittle rock under uniaxial compression. The failure mechanism of the three-dimensional mixed mode crack growth is more complicated than the two-dimensional model. The tensile crack (wing crack) propagates toward the direction of maximum compression, while the secondary crack grows on the opposite side of the pre-existing crack, as observed by Mode II (sliding), or in the lateral direction due to Mode III (tearing). The numerical domain has the size of 0.1-m × 0.1-m × 0.2-m, and the radius of the pre-existing circular crack is 0.02 m; inclination angle is 45°.

8.3.1 Tensile dominated wing crack growth (Mode I)

Similar to the two-dimensional wing-crack model, when tensile failure is the dominant mechanism, wing cracks are initiated from the upper and lower crack boundaries (tip contour) toward the direction of maximum compression. In Figure 8.14, the wing-crack growth is similar to the experimental observation in Figure 8.4.

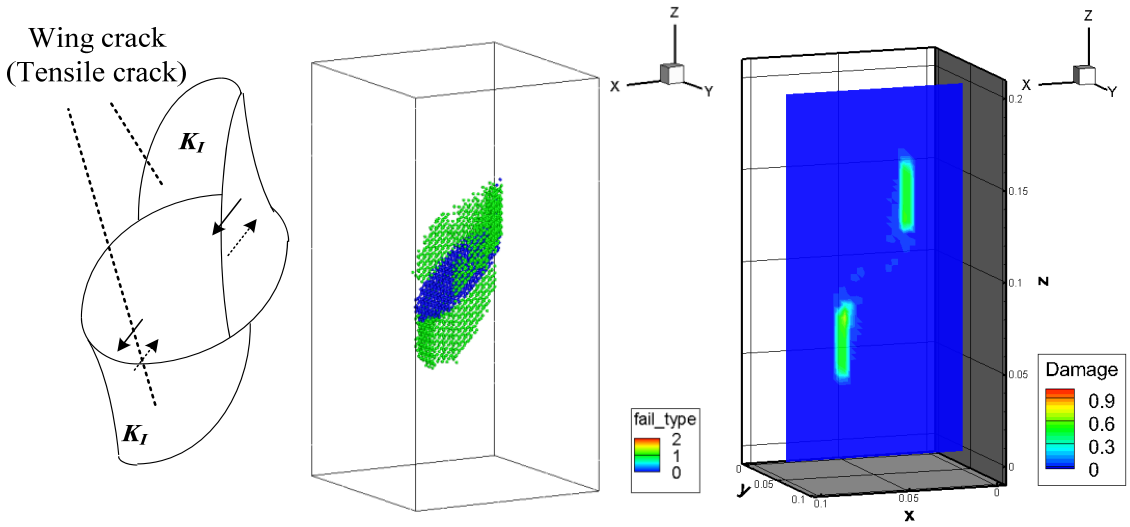

Figure 8.14 (a) Tensile dominated crack, (b) Failure type (1:tensile, 2: shear)
(c) Damage propagation

8.3.2 Shear dominated wing crack growth (Mode II+III)

When the brittle rock is highly confined, the tensile crack initiation is constrained and shear failure is dominant during crack propagation. Due to frictional forces on the pre-existing crack surface, shear cracks are initiated by the transverse shear localization. The shear friction force leads to growth of secondary cracks on the opposite side of the pre-existing crack. Figure 8.15 shows that the secondary fracture develops from the

upper and lower tips by the Mode II fracture, and the secondary fracture propagates outwardly to the lateral side of specimen by Mode III. The side fracture that initiated from the side tip rotates from the initial crack tip toward the lateral side of the specimen, which represents the Mode III response. The shear-induced fracture is oblique.

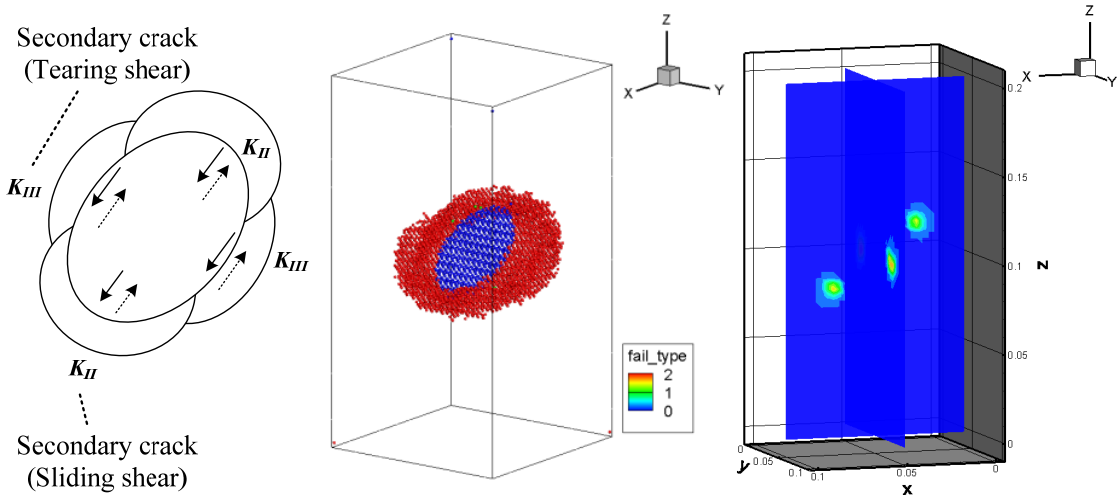

Figure 8.15 (a) Shear dominated crack, (b) Failure type (1:tensile, 2: shear)
(c) Damage propagation

8.3.3 Mixed modes dominated wing crack growth (Mode I+ II+III)

In Figure 8.16, wing cracks grow to the major compression first, and then secondary cracks grown by shear forces act on both the upper and the lower part of the pre-existing crack. However, no secondary crack appears in the lateral direction of the pre-existing crack inthis example. Because only compressive force is applied on the top, the secondary crack is hard to initiate by Mode III (tearing). If confinement is applied to sides of the specimen, the failure mechanism might transition to a shear-dominant mode

as shown in Section 8.2.4. This pattern of fracture propagation has been observed in experimental modeling of 3D crack growth from pre-existing circular cracks (Adams and Sines 1978). Also, Dyskin et al. tested the wing-crack model using a brittle material and including the presence of the contact effect.

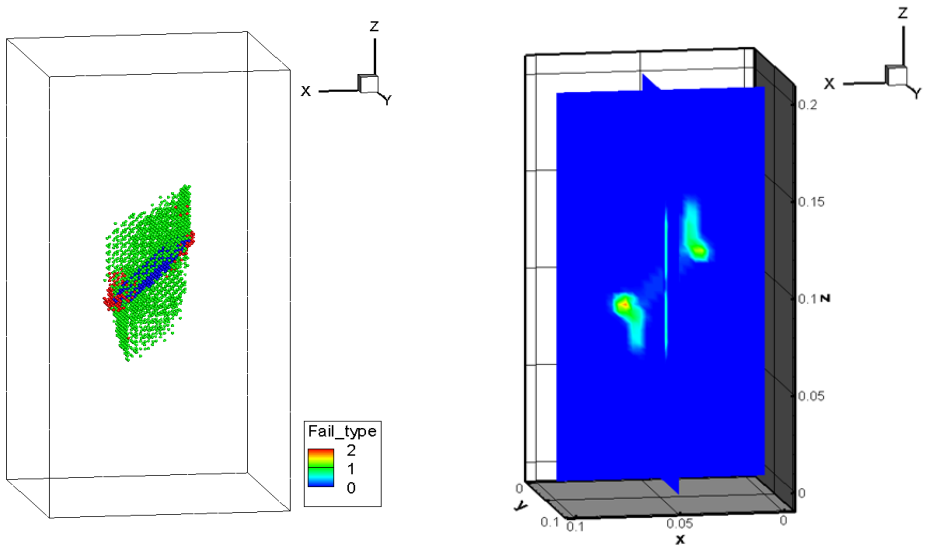

Figure 8.16 Mixed modes crack, (a) Failure type (1:tensile, 2: shear), (b) Damage propagation

8.4 Conclusions

Simulating crack propagation of an embedded fracture subjected to various stress regimes is a challenging problem because the fracture can grow simultaneously by Modes I, II and III. In this section, numerical simulation of mixed modes fracture propagation in brittle rock was studied using 2D and 3D wing-crack models. In 2D simulation, mixed modes fracture of Mode I and II and the influence of confinement on the crack growth were studied. As shown in above, the dominant failure mechanism

depends on the confinement and the local stress condition decides direction of the crack propagation. In 3D simulation, a wing crack has initially grown in the major compression direction; but its direction changes due to the presence of the free surface of the 3D specimen. In 2D case, since there is no Mode III fracture, the secondary crack could grow farther toward the compression direction, but a 3D secondary crack growth from the pre-existing circular crack involves mixed modes of II and III, so that 3D fracture propagation becomes more complicated. Since the real world is 3D, it is necessary to study 3D crack propagation. Especially, finding a failure mechanism of Mode III is extremely difficult by experimental observation. However, the numerical study could provide valuable interpretation and could improve understanding of the fracture propagation mechanism for designing multiple hydraulic fractures.

9. 2D HYDRAULIC FRACTURE PROPAGATION IN IMPERMEABLE ROCK

In unconventional reservoir development, multiply-fractured reservoirs are developed vertically or horizontally. Three areas of investigation are of special interest in the study of unconventional reservoir stimulation: the importance of mixed fracture modes and correct wellbore positioning, the estimation of crack paths from the inclined perforation, and the influence of tortuous fracture path on net injection pressure increase. In this section, these were investigated using models of fracture propagation induced by hydraulic pressure. Generally, when the perforations are misplaced within the maximum in-situ stress direction, high pumping pressure is required to open and initiate cracks.

9.1 Facture propagation from fractured wellbore

The hydraulic fracturing treatment usually starts from an initial path for the fracture, which is created by a "perforation" technique. The perforation, a finger-lke hole, is designed to give orientations. Consider a wellbore with a short initial crack on its boundary. The crack is either oriented along the maximum stress direction or is inclined as shown in Figure 9.1. Radius of the wellbore is 0.1 m, and it is situated in a 3m × 3m block [Figure 9.2]. The numerical domain is meshed by 4-node triangular element [Figure 9.2]. The initial crack is created by perforations before hydraulic fracturing stimulation. The length of the perforations is assumed as 0.1 m. The rock is subjected to anisotropic far-field stresses applied in the x- and y-directions and material properties of the rock are shown in Table 9.1. The wellbore/fracture system is pressurized

incrementally using a pressure-boundary condition. The pressure level is updated at every time step and applied on both existing and newly propagated crack elements using a moving-boundary scheme. Slow fluid injection increases the hydraulic pressure uniformly over the fracture surfaces except in the crack tip area. Due to the highest fluid loss in the fluid-lag region, the applied hydraulic pressure decreases rapidly near the fracture tip (Papanastasious 1997). Also, the low-pressure region indicates fracture-tip effects, since the fracturing fluid never quite reaches the fracture tip (Smith and Shlyapobersky 2000). So in the simulation, the fracture tip pressure is assumed to be the zero. Except the fracture tips, we apply uniform pressurization in the fracture plane and increase incrementally until the fracture tips are propagating. Once the fracture propagated, we adjust lower uniform pressurization in the fracture and increase incrementally again until the fracture tips are propagating. It is also assumed that the process is isothermal and the rock is impermeable.

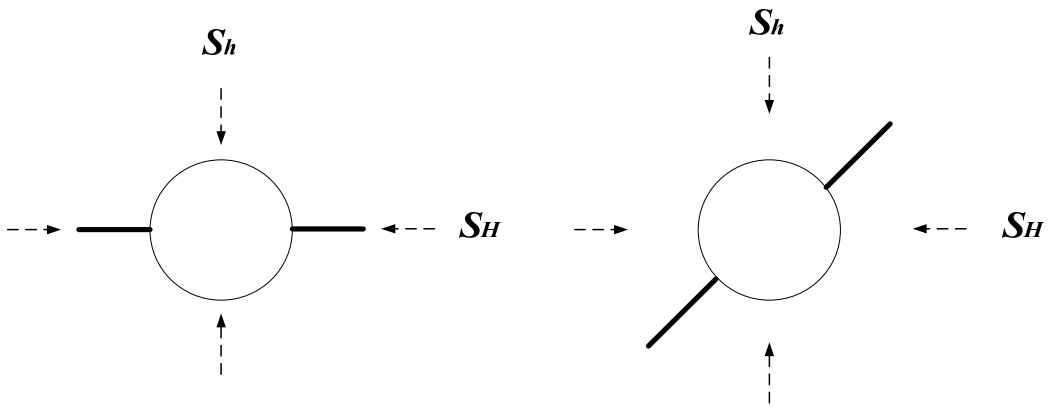

Figure 9.1 Fractured wellbore with perforations under in-situ stress

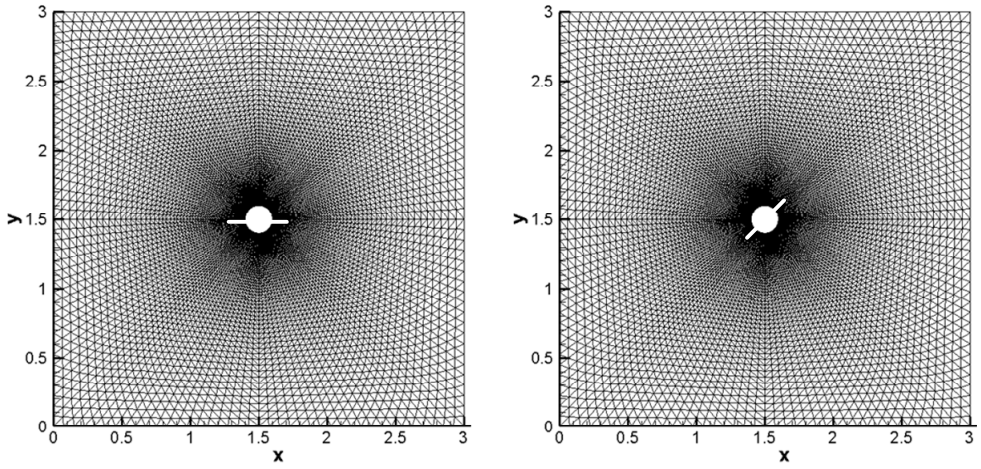

Figure 9.2 Numerical domains for the fractured wellbore

Table 9.1 Material properties and input parameters for 2D HF model

Inputs	Values
Young's Modulus, E (GPa)	37.5
Poisson ratio, υ	0.25
Number of Elements	19,200
Number of Nodes	9,760
Element type	Triangular
Mohr-Coulomb parameter, ϕ_f	10
Cohesion, c_F (MPa)	40
Tensile strength, σ_T (MPa)	25

9.1.1 Parallel perforated wellbore

As a boundary condition [Table 9.2], the far-field stresses are 4 MPa in the x-direction and 1MPa in the y-direction. As expected, the hydraulic fracture propagates toward the maximum principal stress direction [Figure 9.3]. Note that the wellbore pressure decreases during fracture propagation. Since we used uniform pressure

boundary condition (except fracture tips), required pressurization is decreasing with the growth of the fracture length. Applied total force in the fractures is increasing by multiplying the uniform pressure by the fracture length. In addition, when the injection rate remains the same during fracture propagation, the hydraulic pressure applied to the fracture surface is proportional to the fracture length. When the fracture is not propagating, the wellbore pressure increases until the fracture propagates and the wellbore pressure drops. In Figure 9.4, the wellbore pressure decreases continuously with fracture length. The rapid variations in the wellbore pressure profile are caused by propagation increments. The resulting aperture changes are smooth and continuously vary during crack propagation in Figure 9.4.

Table 9.2 Boundary conditions for parallel fractured wellbore

Inputs	Values
Max. Far-field stress, S_H (MPa)	4
Min. Far-field stress, S_h (MPa)	1
Initial hydraulic pressure (MPa)	4
Incremental hydraulic pressure (MPa)	0.2

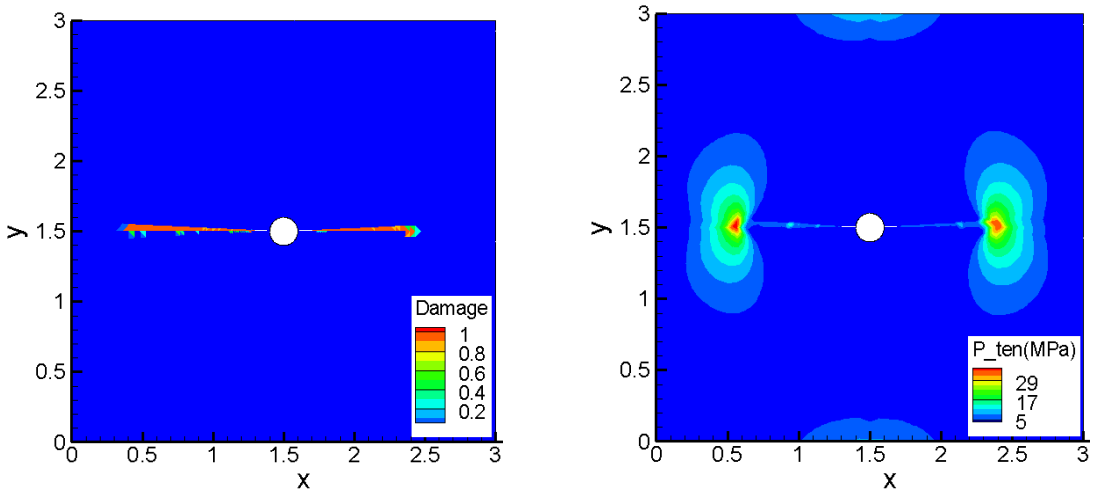

Figure 9.3 Damage propagation and maximum tensile stress distribution

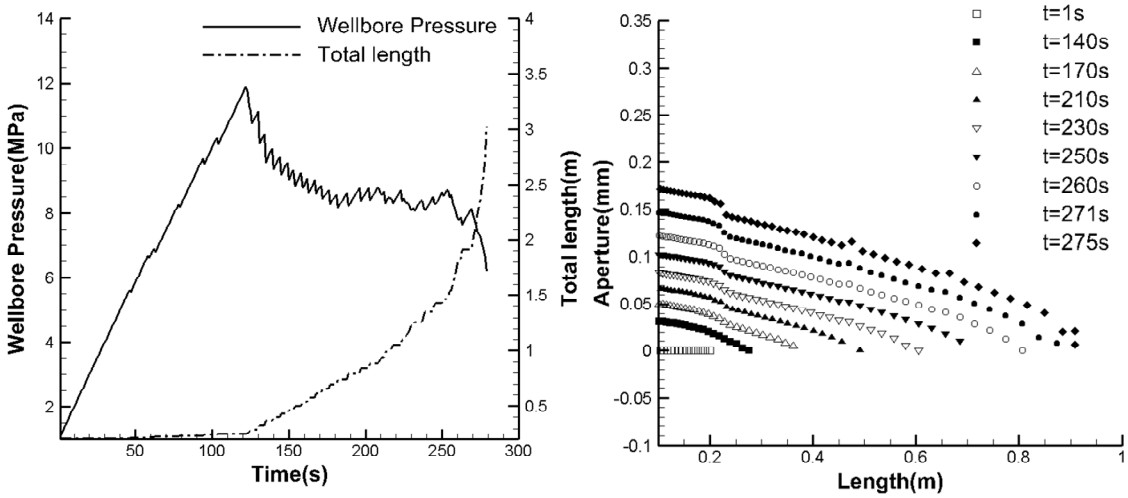

Figure 9.4 Wellbore pressure change and aperture change during hydraulic fracturing

9.1.2 Inclined perforated wellbore

The inclination angle, 45°, of the initial crack is assumed in the example. As a result, the direction of crack propagation changes with increasing length as the fracture reorients itself in the maximum far-field stress direction. At early time, the hydraulic

fracture is propagating with the same initial crack angle, and then the hydraulic fracture turns toward the maximum far-field stress direction. That is, the initial fracture is opened by the hydraulic pressure and slips under the anisotropic in-situ stress. So both tensile propagation and shear slip are detected near the turning zone of the crack path. As can be observed in Figure 9.4, the wellbore pressure is decreasing at early time when the crack propagates in its original direction, but after time steps, the wellbore pressure increases again as the crack turns, reflecting crack-path tortuosity. When the mixed mode fractures are combined during hydraulic fracturing, required wellbore pressure increases to create fracture propagation. Despite the high hydraulic pressurization, the fracture aperture change [Figure 8.6] is not larger than the aperture change for the straight propagation segment. The shear slip of the opened fracture causes highly compressive stress near the wellbore and the curved section of the fracture [Figure 9.7].

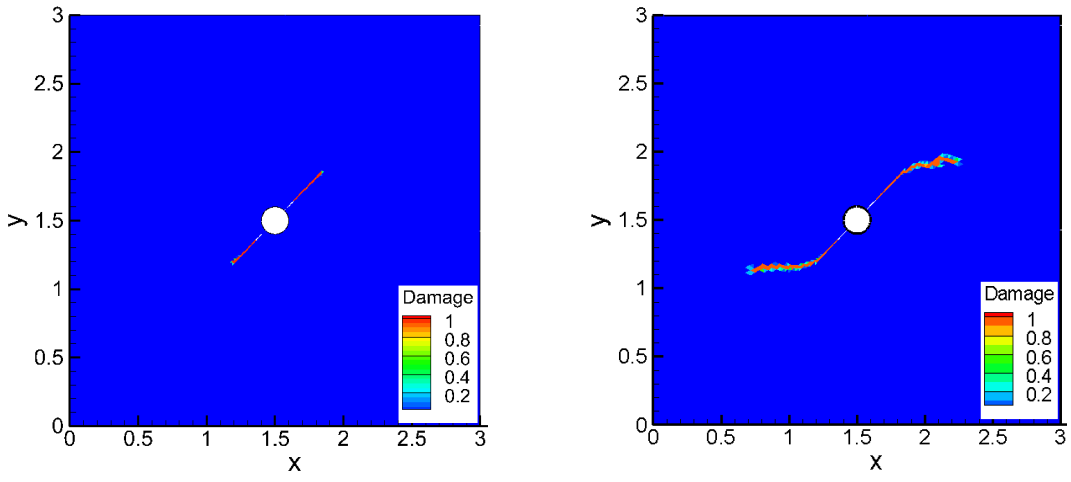

Figure 9.5 Damage propagation at early time and later time

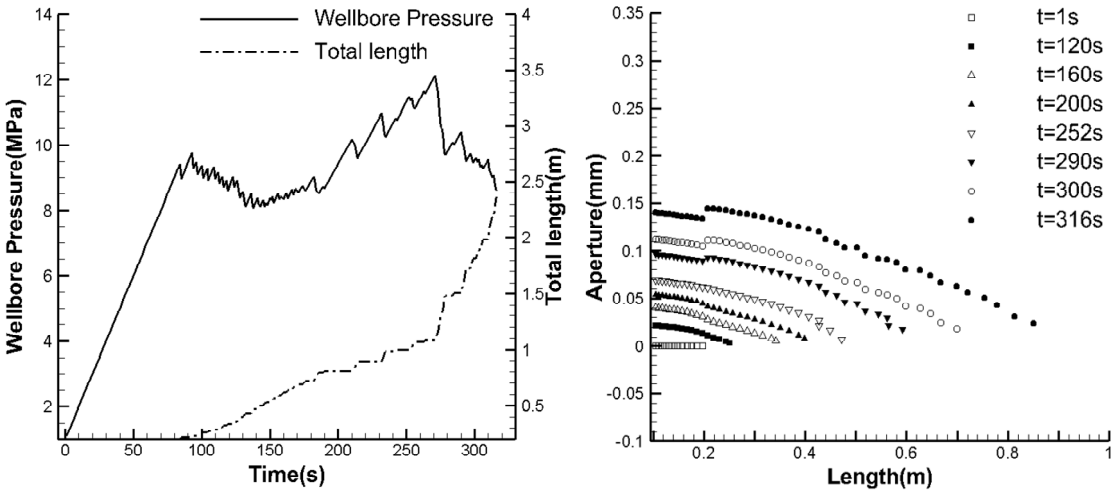

Figure 9.6 Wellbore pressure change and aperture change during hydraulic fracturing

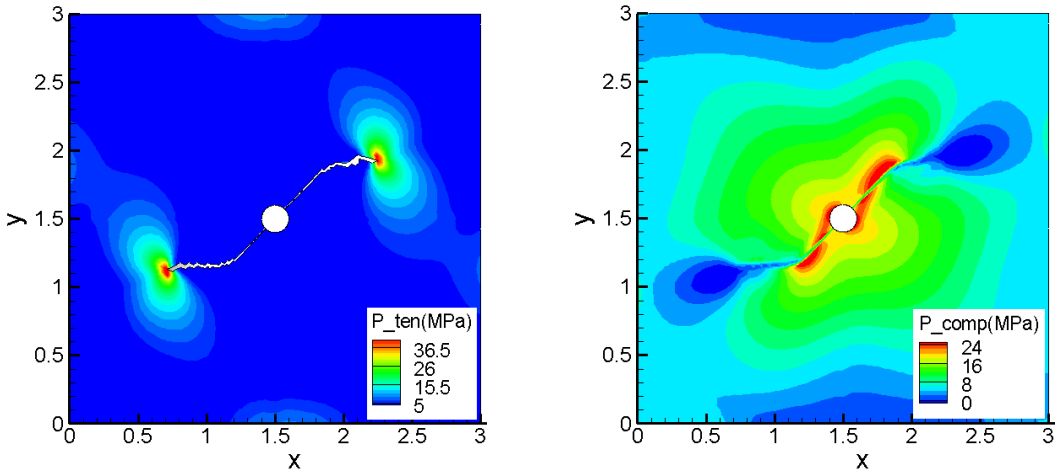

Figure 9.7 Principal tensile and compressive stress distributions

9.2 Fracture propagation from long perforation

When the initially fractured perforation is relatively large compared with the wellbore size, the influence of the wellbore could be neglected. A larger scale reservoir model with an initial fracture is modeled 10-m × 10-m block and meshed uniformly in

Figure 9.8. Material properties described in Table 9.1 and 20,000 uniform triangular elements were used in this simulation.

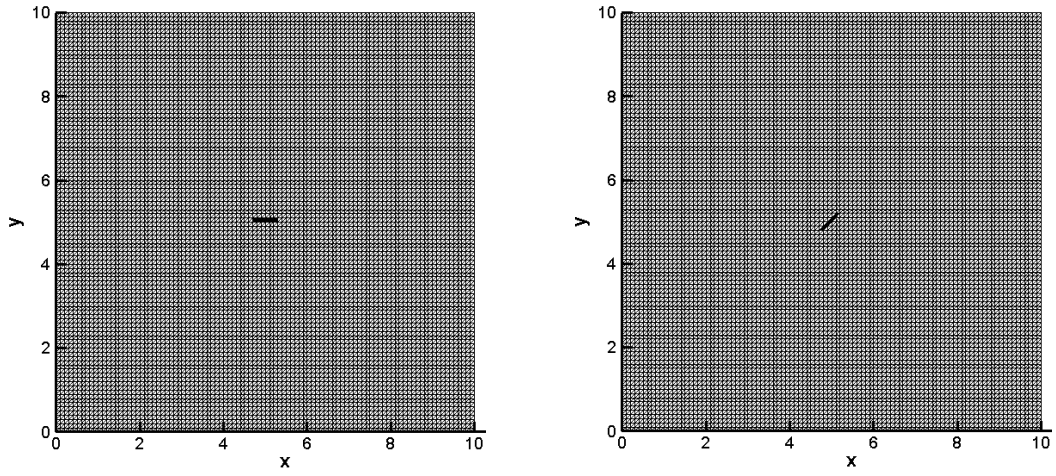

Figure 9.8 Schematic numerical domain of reservoir model w/o wellbore geometry

9.2.1 Parallel perforation

The initial fracture is assumed to be long enough to ignore the wellbore geometry effect. Initial fracture length is assumed as 0.6 m, and the far-field stresses are 10MPa and 5MPa in the x- and y- direction, as mentioned in Table 9.3. As can be observed in Figure 9.9, crack propagates straight, and the wellbore pressure profile is similar with the previous simulation with a wellbore. Trend of the wellbore pressure is decreasing with the growth of the fracture length and aperture profile is gradually increasing [Figure 9.10]. Basically, tensile failure is dominating during hydraulic fracturing, but when shear failures were combined during fracture propagation, the wellbore pressure increases to overcome the shear toughness and propagates the hydraulic fracture. Because of the mixed mode fractures, wellbore pressure is going to up and down during hydraulic

fracture propagation [Figure 9.10]. Compared with the previous parallel fractured wellbore case, the applied max/min in-situ stress ratio is changed from 3:1 to 2:1, and due to relatively higher far-field stress contrast, the crack path shows some turns but the main crack propagating direction follows the maximum far-field stress. The simulation results show that the fracture tortuosity is not severe and the crack path is relatively straight.

Table 9.3 Boundary conditions for parallel perforation

Inputs	Values
Max. Far-field stress, S_H (MPa)	10
Min. Far-field stress, S_h (MPa)	5
Initial hydraulic pressure (MPa)	7
Incremental hydraulic pressure (MPa)	0.5

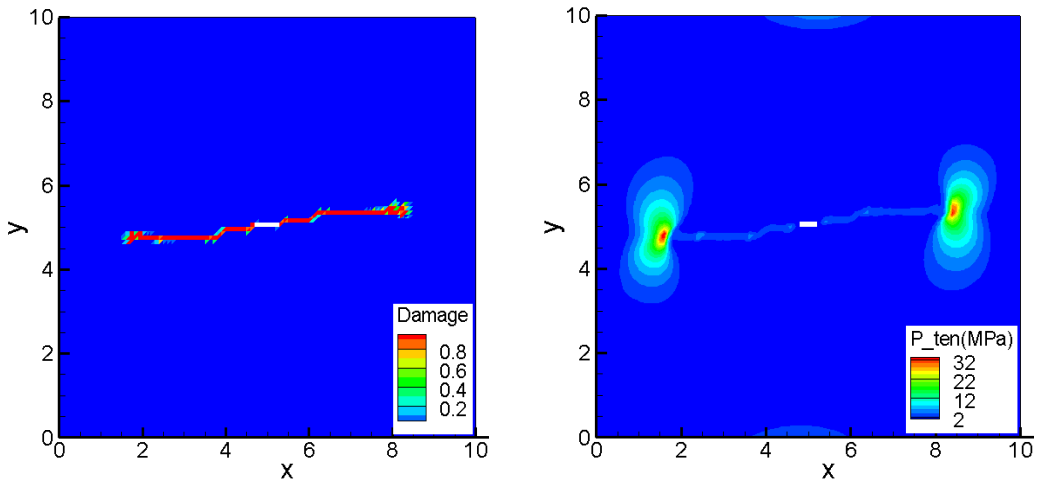

Figure 9.9 Damage propagtion and maximum tensile stress distribution

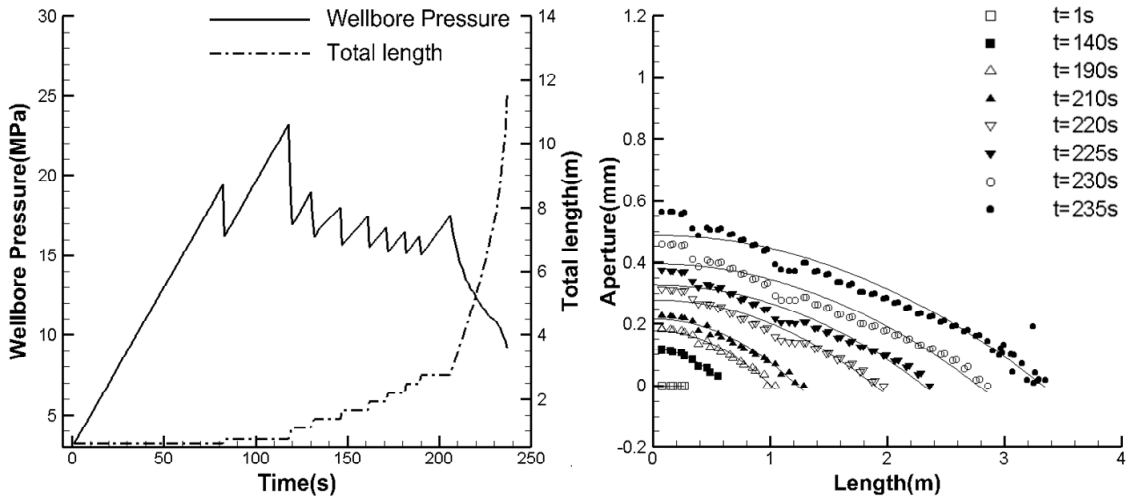

Figure 9.10 Wellbore pressure change and aperture change during hydraulic fracturing

9.2.2 Inclined perforation

The inclination angle, 45° and the fracture length of the initial crack are assumed as 0.55 m in the example. The reservoir dimensions are 10 m each. The far-field stress is given by 10MPa and 5MPa applied in the x- and y- directions, respectively. Similar with the previous simulation, the hydraulic fracture turns to the maximum far-field stress direction and shows tortuous crack propagation [Figure 9.11]. At early time, tensile propagation is dominating and the hydraulic fracture is propagating with the same initial crack angle. At later time, the hydraulic fracture turns with shear slip and lots of damages are identified near the hydraulic fracture. In Figure 9.11, higher damage zones (red) indicate the main hydraulic fracture, while the lower damaged zone indicate secondary or microscopic fractures. As explained above, the wellbore pressure drops sharply during propagation and increases again when mixed mode fractures are combined. In addition, since the initial perforation is inclined, the wellbore pressure to

overcome the anisotropic far-field stresses is higher than the parallel perforation case. In order to create tensile propagation, more pumping is required in the inclined perforation case. Therefore, it could be an indication of shear failure during hydraulic fracturing stimulation, when the wellbore pressure goes up after initial wellbore pressure drop.

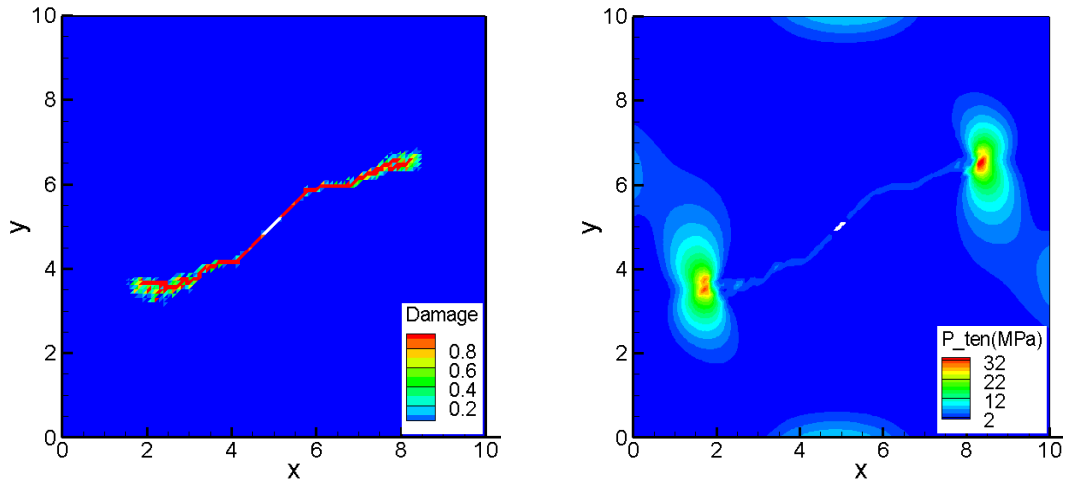

Figure 9.11 Damage propagtion and maximum tensile stress distribution

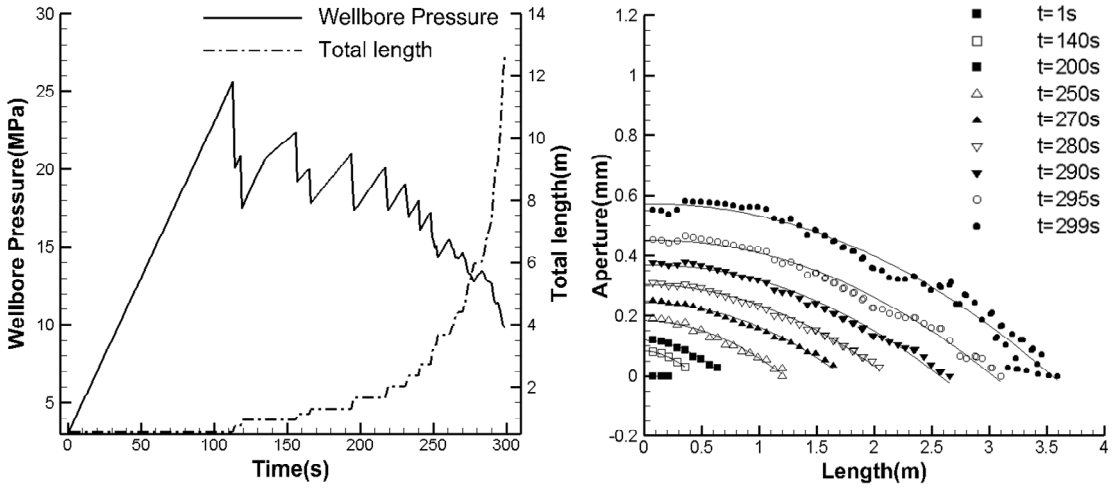

Figure 9.12 Wellbore pressure change and aperture change during hydraulic fracturing

9.3 Conclusion

In this section, hydraulic fracture propagation in impermeable rock was simulated using mechanical loadings. In this simulation, the damage variable growth was used to represent stiffness degradation and crack propagation, since the cracks are propagated through the locally damaged ruptured path. According to the simulation results, when the perforations are misplaced, mixed mode fractures are involved during propagation and high pumping pressure was required to open and initiate cracks. During the mixed-modes fracturing procedure, both tensile and shear-failure fracturing were interacted complexly during hydraulic fracturing stimulation. So, we could estimate that when mixed mode fractures are dominating and the hydraulic fracture could not propagate and the wellbore pressure might be suddenly increasing and fracture volume looks stationary.

The crack propagation study could give valuable information for the direction of the rupture path and determination of perforation placement. Fractured length is highly related with the anisotropic far-filed stresses condition and the position of preplaced cracks (perforations). In this simulation, uniform pressurization was assumed for fluid pressure inside the fracture. It could be valid for slowly injected fracturing fluid, but we should consider fluid-flow motion caused by injected fracturing fluid in order to estimate variation of the fluid pressure through propagating fracturing path. Therefore, in the next section, the numerical modeling of fluid-driven fracture propagation is developed using the coupled fluid flow and poroelastic rock deformation analysis. In this fluid-driven

fracture propagation simulation, fracture length, aperture and pressure profiles are computed as functions of time.

10. 2D HYDRAULIC FRACTURE PROPAGATION IN PERMEABLE ROCK

Hydraulic fracturing can be defined as coupled fluid-solid interaction problem. This interactive problem is very challenging to interpret via numerical methods, because of lots of numerical complexity such as the moving boundary issue, dynamic crack growth, and complex geometry. Therefore, one approach to solve the hydraulic fracture propagation problem has been quasi-static fluid-driven fracturing (Adachi et al. 2007; Boone 1989; Papanastasious 1997). Although the quasi-static assumption might be invalid for realistic crack growth behavior, it has given a reasonable solution so far.

Hydraulic fracturing can be divided into three coupled processes of fluid flow, hydromechanical deformation, and fracture propagation. The fluid flow inside fractures is modeled using the lubrication equation, and the hydromechanical deformation of rock is solved using fully coupled poroelastic analysis. Fracture propagation is modeled as quasi-static crack growth. So at each time step we solved an iterative solution for rock deformation and fluid pressure using the coupled iterative algorithm explained in section 5. In this section, we present 2D hydraulic fracture propagation simulation using the quasi-static fluid-driven fracturing model. The influence of reservoir heterogeneity on hydraulic fracturing stimulation is of special interest. The heterogeneous feature of the rock could affect multiple fracture propagation and fluid flow in the fracture by increasing leakoff volume, so that reservoir heterogeneity is an important factor to determine the hydraulic fracturing strategy. Through the numerical study of hydraulic fracturing, the numerical model could help to design an optimized hydraulic fracturing

strategy and save developing costs in was such as minimizing unnecessary experimental tests.

10.1 2D numerical modeling

Similar to a previous simulation, a 10-m × 10-m 2D reservoir model was used. The numerical domain was meshed by 20,000 uniform triangular elements [Figure 10.1]. The length of the perforation was assumed as 1.2 m, which is placed in the center of the numerical domain. Material properties of westerly granite were used [Table 10.1], and boundary conditions of the far-field stresses were 10 MPa and 5 MPa in the x- and y-directions [Table 10.2]. Water was used for fracturing fluid and was injected to the center of the numerical domain. Constant fluid injection rate of 24 L/min was used and applied as a point-fluid-source boundary condition into the numerical domain.

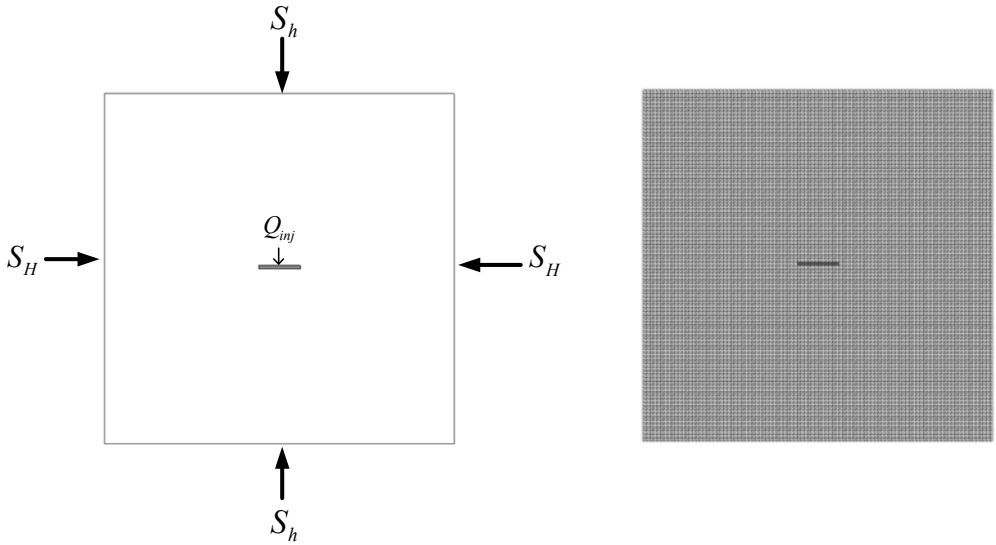

Figure 10.1 Numerical domain and boundary condition for hydraulic fracturing simulation

Table 10.1 Rock properties of Westerly granite (McTigue 1986)

Inputs	Values
Young's Modulus, E (GPa)	37.5
Shear Modulus, G	15
Drained Poisson ratio, υ	0.25
Undrained Poisson ratio, υ_u	0.33
Biot's coefficient, α	0.44
Skempton's coefficient, B	0.82
Permeability, k (md)	0.01
Porosity	0.01
Fluid mass density, ρ_f (kg/m3)	1000
Fluid viscosity, μ (Pa·s)	1.e-3
Bulk modulus for fluid	3.291e9

Table 10.2 Boundary condition and input parameters

Inputs	Values
x-dir. Far-field stress, S_H (MPa)	10
y-dir. Far-field stress, S_h (Mpa)	5
Injection rate, q_{inj} (L/min)	24
Mohr-Coulomb parameter, ϕ_f	10
Cohesion, c_F (MPa)	30
Tensile strength, σ_T (MPa)	7
Weibull distribution parameters	m_1=1, a_1=5 m_2=1.1, a_2=9 m_3=1, a_3=4

10.2 Hydraulic fracturing in homogeneous reservoir

According to the simulation results, the hydraulic fracture in homogeneous rock propagated toward the maximum far-field stress direction without branching or multiple crack growth [Figure 10.4]. The small formation damage near the fracture plane limited

the leakoff volume to a very small value. That is, most of the injected fracturing fluid remained inside the fracture volume. The remaining fracture volume was highly influenced by the fluid pressure distribution in the fractures. The injected fluid flow defined the fluid pressure distribution [Figure 10.2].

The fluid pressure induced the mechanical deformation (opening) of the fractures. The fluid pressure distribution and aperture changes varied with fracturing time and fracture propagation. We solved iteratively the aperture changes and fluid pressure distribution with the fracture growth during the hydraulic fracturing treatment [Figure 10.3]. The pore pressure at the crack tip was nearly zero due to opening modes along the fracture; while compressive fluid pressure forces pushed the pore pressure near the fracture was higher [Figure 10.4]. Because of curvature of the hydraulic fracture path, pore pressure near the curvature area shows higher distribution. This is because compressive stresses by the hydraulic pressurization are concentrated at the curvature area. Wellbore pressure decreased and stabilized near 9MPa as the hydraulic fracture propagated [Figure 10.5].

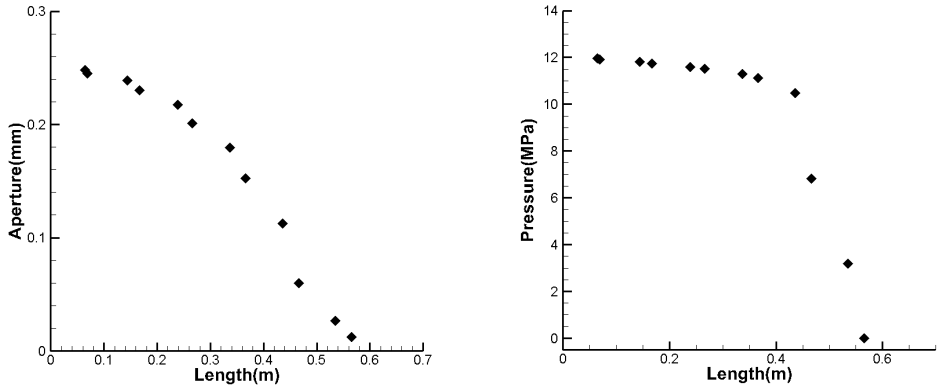

Figure 10.2 Aperture profile and fluid pressure profile at first step (t=0.6seconds)

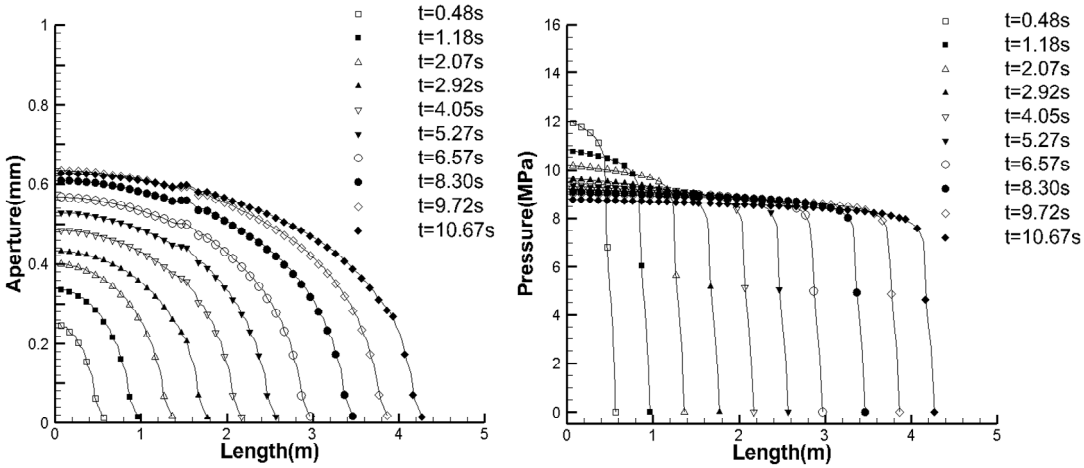

Figure 10.3 Aperture profile and fluid pressure profile during hydraulic fracturing

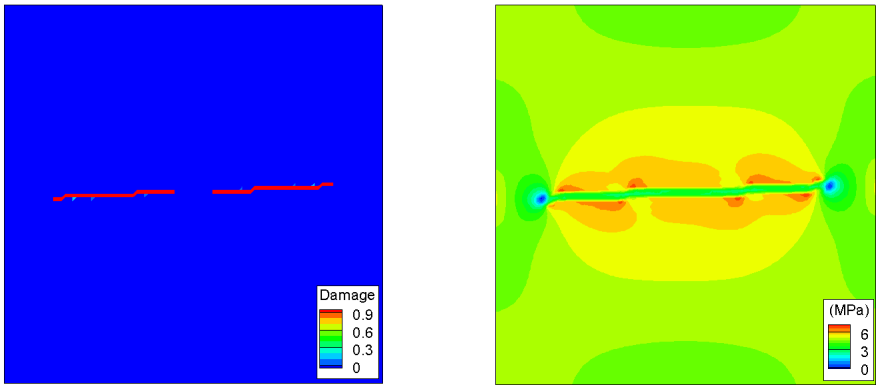

Figure 10.4 Crack propagation and pore pressure distribution during hydraulic fracturing

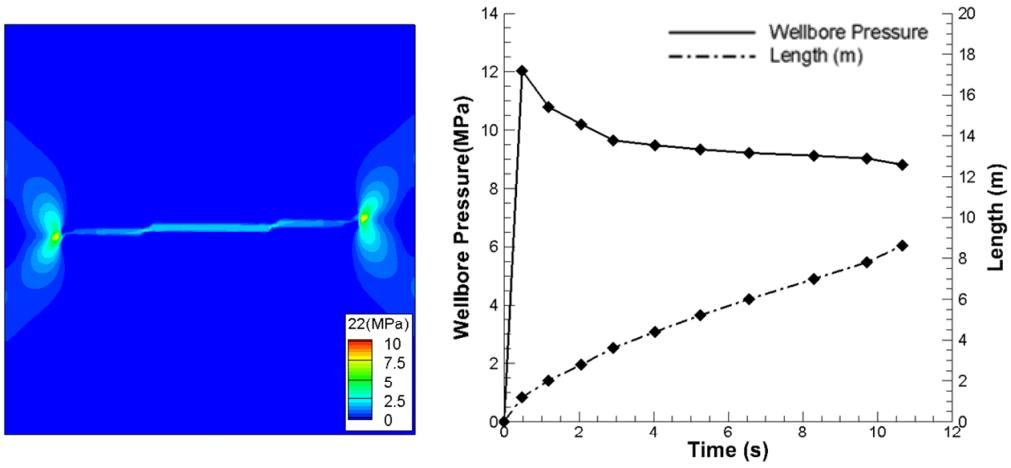

Figure 10.5 σ_{yy} distribution and wellbore pressure change during hydraulic fracturing

10.3 Hydraulic fracturing in heterogeneous reservoir

In this section, we investigated an influence of reservoir heterogeneity on the hydraulic fracturing design. In order to represent the reservoir heterogeneity, we assumed values of Weibull parameters [Table 10.2] and applied to the numerical model. The random variables generated by the Weibull function are applied to distributions of material strength, Young's modulus, and matrix permeability. If the random variables were applied to porosity or Poisson's ratio, by wide distribution of the random variables the porosity could be over 1 and the Poisson's ratio could be over 0.5. There is violation of general rules, so that it is inappropriate to apply random variables to the porosity and Poisson's ratio. The combination of the distributions represents reservoir heterogeneity [Figure 10.6]. Boundary conditions were same as in the homogeneous case. According to the simulation results, a lower wellbore pressure profile [Figure 10.7], a smaller opening, and lower fluid pressure distribution were obtained by the heterogeneous

influence [Figure 10.8]. Due to the heterogeneous feature, injected fluid volume and leakoff volume increased [Figure 10.7].

Therefore, we can conclude that the hydraulic fracturing in the heterogeneous reservoir requires more fluid injection and more time to create the same length of fracture as in the homogeneous reservoir [Figure 10.7]. In addition, breakdown pressure is lower than the homogenous case because locally distributed strength and stiffness vary randomly. The pore pressure near the fracture is varied and sparsely concentrated because of the stress heterogeneity and the pore pressure at the curvature area is higher because of compressive stress concentration [Figure 10.6].

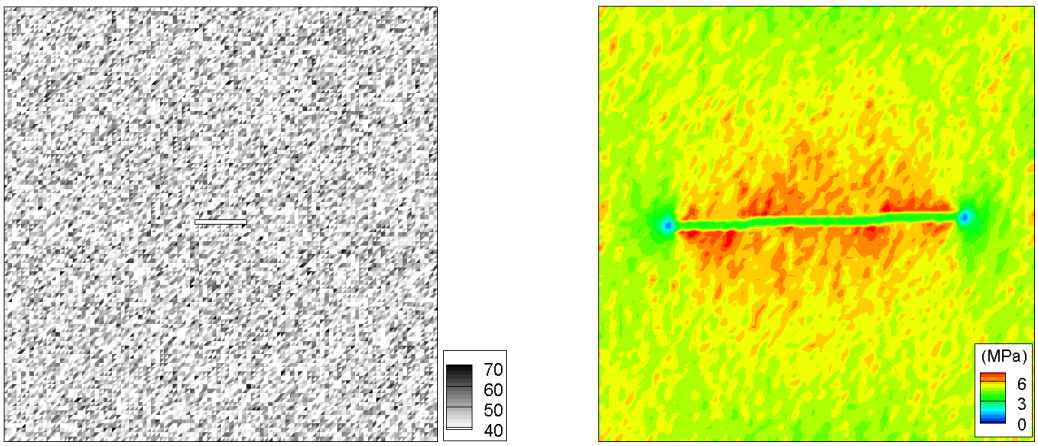

Figure 10.6 Heterogeneity distribution (Unit=GPa) and pore pressure changes after fracture propagation

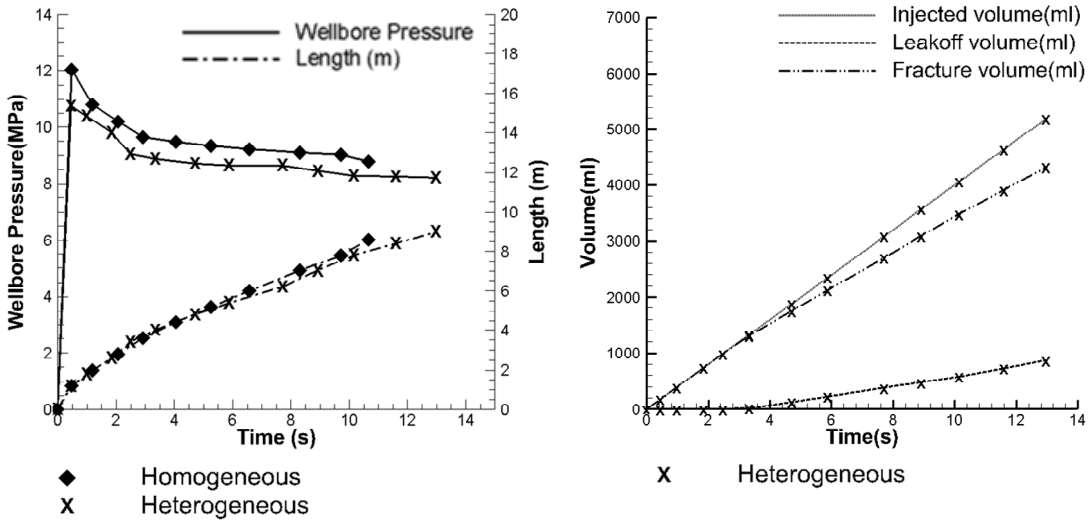

Figure 10.7 Comparison of wellbore pressure profile and injected fluid volume

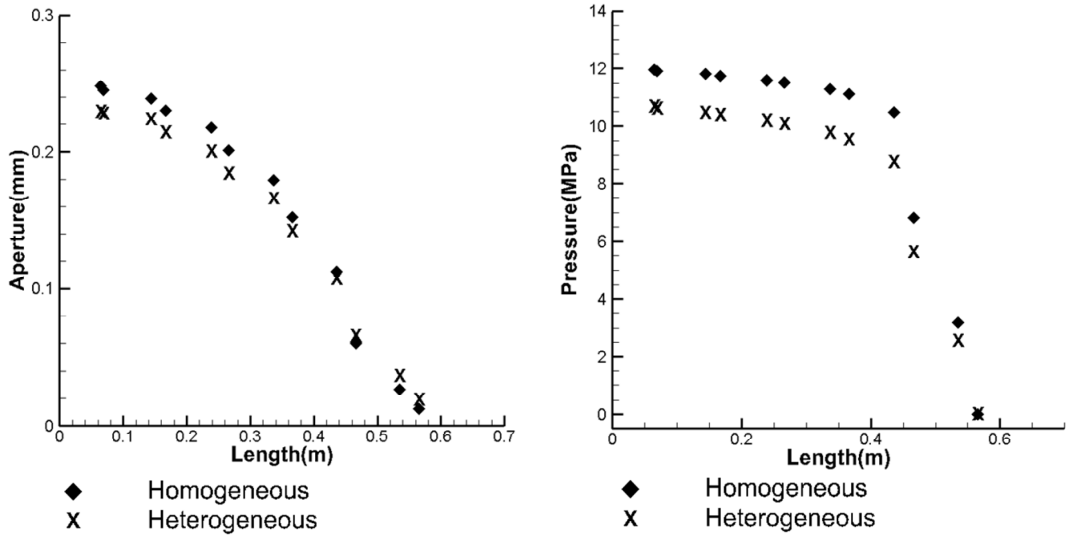

Figure 10.8 Comparison of aperture and fluid pressure profiles at first step (t=0.6seconds)

10.3.1 Hydraulic fracturing in highly heterogeneous reservoir

In this section, we examined the influence of the heterogeneity when the target reservoir had more heterogeneous geomechanical features. We increased the reservoir heterogeneity by modifying the Weibull parameters (m_1=1, a_1=4, m_2=1, a_2=3, m_3=1, a_3=3) [Figure 10.9]. Based on the simulation results, when a highly heterogeneous reservoir was assumed, the fracture length propagated slowly and leakoff volume increased greatly [Figure 10.10]. The high leakoff rate left only a small remaining fluid volume in the fracture and prevented the fluid flow from generating enough fluid pressure to create cracks. Therefore, injection efficiency also decreased and the fracture could not grow anymore. Wellbore pressure of the high-heterogenity case remained higher than the low-heterogeneity case [Figure 10.10] because the fracture length of the high-heterogeneity case did not increase as much as the low-heterogeneity case.

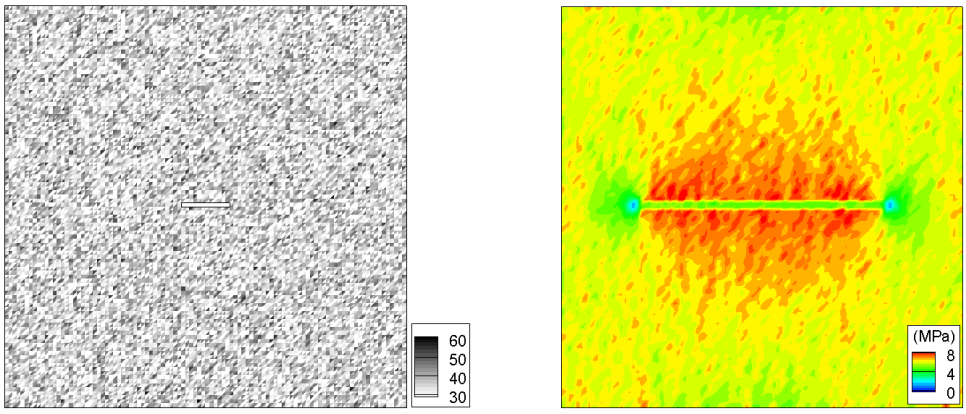

Figure 10.9 Heterogeneity distribution (Unit=GPa) and pore pressure changes after fracture propagation

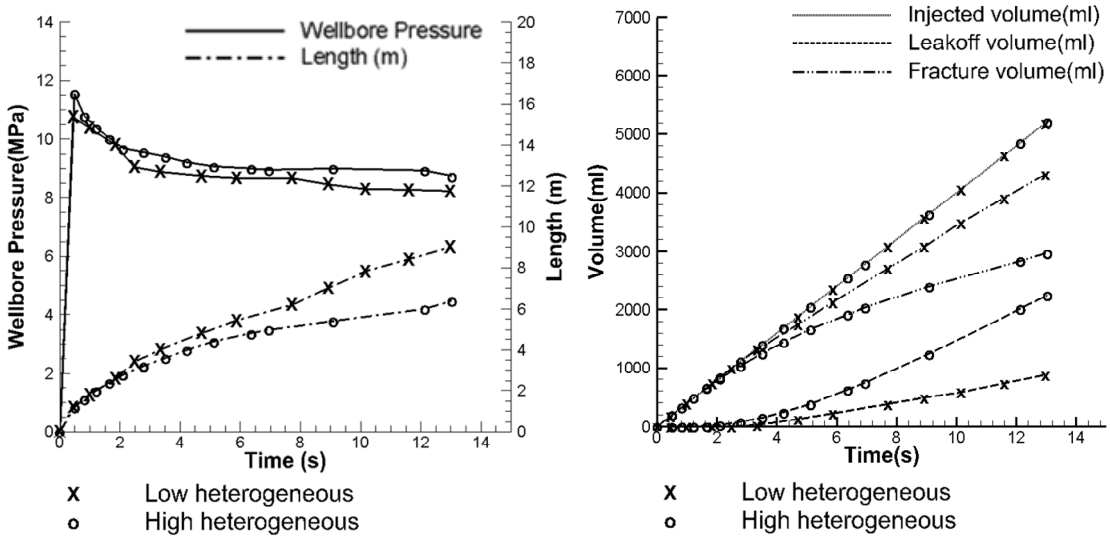

Figure 10.10 Comparison of wellbore pressure profile and fluid volume

10.3.2 Hydraulic fracturing in heterogeneous reservoir with high injection

When an injection rate of fracturing fluid is increasing, faster fracture growth is expected. According to the simulation results, the treatment time decreased from 12 seconds to 4 seconds when the injection is increased from 24 L/min to 144 L/min [Figure 10.12]. The high injection rate induced a large fluid pressure profile in the fracture, and the increased fluid pressure caused secondary fracture propagation from the primary fracture [Figure 10.11]. The secondary fractures were initiated from crack tips of the primary facture, because concentrated tensile stresses largely exceed the tensile strength. The main trend of the fracture propagation was similar in both lower and higher injection cases, but the secondary fractures grew along with the primary fracture growth in the higher injection case [Figure 10.11]. The creation of the multiple fractures increased the leakoff volume d twice much as the low injection case [Figure 10.12]. In

addition, breakdown pressure was as high as 14.5 MPa and the wellbore pressure quickly dropped with fracture propagation [Figure 10.12]. The high injection rate led to large mechanical deformation (aperture profile) and high pore pressure near the fracture tips [Figure 10.13].

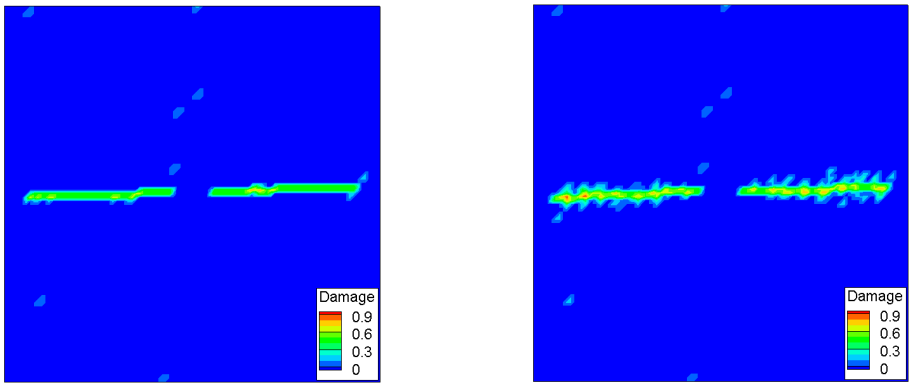

(a) q_{inj}=24L/min (b) q_{inj}=144L/min

Figure 10.11 Comparison of hydraulic fracture propagation at lower injection rate vs. higher injection rate

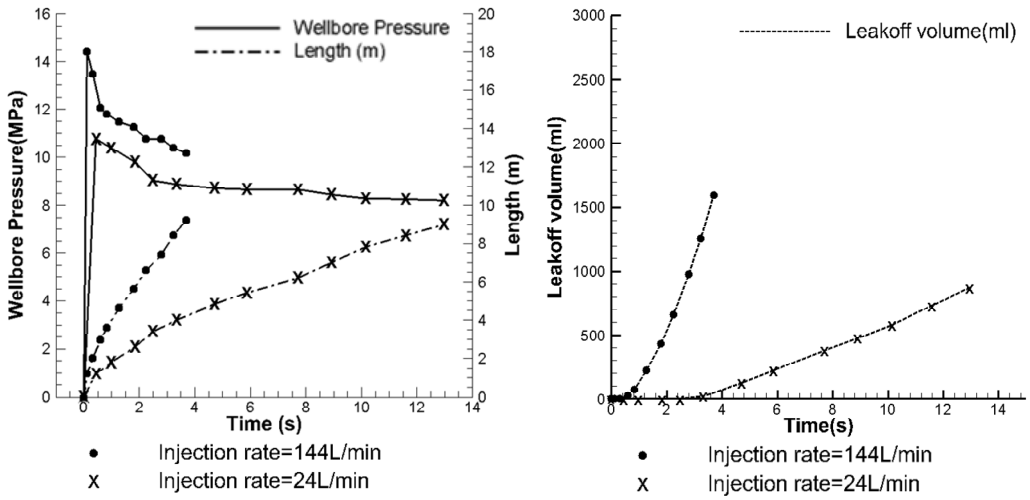

Figure 10.12 Comparison of wellbore pressure profile and leakoff volume change in lower injection vs. higher injection

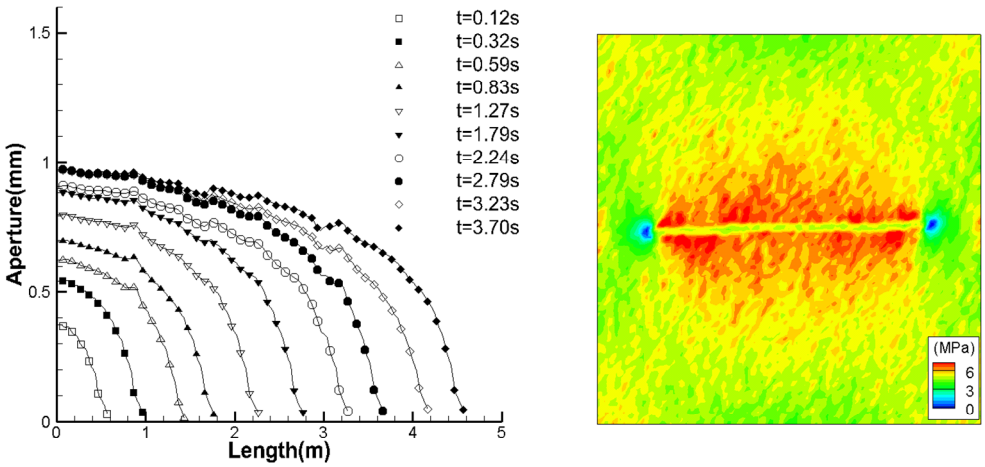

Figure 10.13 Aperture profile and pore pressure distribution during hydraulic fracturing of q_{inj}=144L/min

10.4 Conclusions

In this section, we examined 2D hydraulic fracture propagation simulations in permeable rock and investigated the influence of the reservoir heterogeneity and the injection rate. The reservoir heterogeneity is a critical factor to determine the hydraulic fracturing strategy, because both mechanical deformation and fluid flow behavior are affected by the heterogeneity factor. Especially, high heterogeneity increases leakoff volume and reduces the injectivity of fracturing fluid. When the rock was highly heterogeneous, the injection efficiency was decreased to 0.57 [Table 10.3]. When the injection rate was increased by 6 times, the injection efficiency decreased only from 0.832 to 0.82. So that means the injection efficiency is a function of the heterogeneity factor and not a function of the injection rate. Based on the simulation results, the

hydraulic fracturing strategy should carefully determine if the reservoir is highly heterogeneous.

Table 10.3 Comparison of fluid volume and injection efficiency

	Time (s)	Injected volume (ml)	Fracture volume (ml)	Leakoff volume (ml)	Injection efficiency, ε_{inj}
Homogeneous	10.67	4266.39	4258.413	7.977	0.998
Low Hetero.	12.97	5189.38	4316.84	872.54	0.832
High Hetero.	13.04	5214.275	2970.55	2243.73	0.57
High injection	3.70	8878.55	7282.33	1596.225	0.82

where, the injection efficiency is defined as;

$$\varepsilon_{\text{inj}} = \frac{V_f}{V_i} = \frac{V_i - V_l}{V_i} \tag{10.1}$$

11. 3D MODELING OF HYDRAULIC FRACTURE EXPERIMENTS

Hydraulic fracturing has continued to become more important for the oil and gas industry. Optimization of the hydraulic fracturing treatment is necessary to save developing cost. Lab experiments and numerical hydraulic fracturing models give valuable information for the optimization procedure. Laboratory-scaled hydraulic fracturing experiments have frequently been used previously. Many researchers have conducted laboratory-scaled hydraulic fracturing tests (Daneshy 1974; Lamont and Jessen 1963; Teufel and Clark 1984; Zoback et al. 1977). These laboratory experiments are useful to examine an insight into the process of hydraulic fracturing treatment, because they provide guidelines for evaluating laboratory environments and the influences of different factors (e.g., injection schedule, fracturing fluid, and confining pressures) that can be monitored in the hydraulic fracturing treatment. Compared with field tests, laboratory tests can reduce developing cost significantly.

Laboratory tests are also used to validate numerical hydraulic fracturing models (Bai et al. 2006). This section compares the fully 3D hydraulic fracturing model with the laboratory hydraulic fracturing tests of Niobrara shale that was performed by TerraTek (Ghassemi and Suárez-Rivera 2012). The numerical simulation provides a sophisticated understanding of the complex process of hydraulic fracturing. We investigated the hydraulic fracturing simulation in both homogeneous and heterogeneous blocks.

11.1 Large-scale laboratory hydraulic fracturing test

The laboratory scale hydraulic fracturing test was performed in TerraTek's large block multiaxial stress frame. Using the multiaxial stress frame [Figure 11.1], the in-situ effective stress conditions were generated in three principal directions by high pressure flatjacks. The tested Niobrara shale [Figure 11.1] was obtained from a quarry located in Colorado and prepared for 27.25-in. × 27.25-in. × 32-in. dimensions of the block. The wellbore was drilled in the middle of the testing block. Vertical completion with a cased borehole was placed, and a 7-in. long openhole section located was 15 to 22-in. from the top face of the block. Two slots of 12-mm penetration were sandblasted along the length of the openhole section to facilitate fracture initiation and breakdown. 37 acoustic sensors were installed on the faces of the block to evaluate fracture geometry and propagation during the hydraulic fracturing test. Glycerol, which has high viscosity of 1,000 cp, was used for the fracturing fluid, and a constant injection rate of 1,000 *mL*/min was pumped into the block sample subjected to anisotropic in-situ stresses.

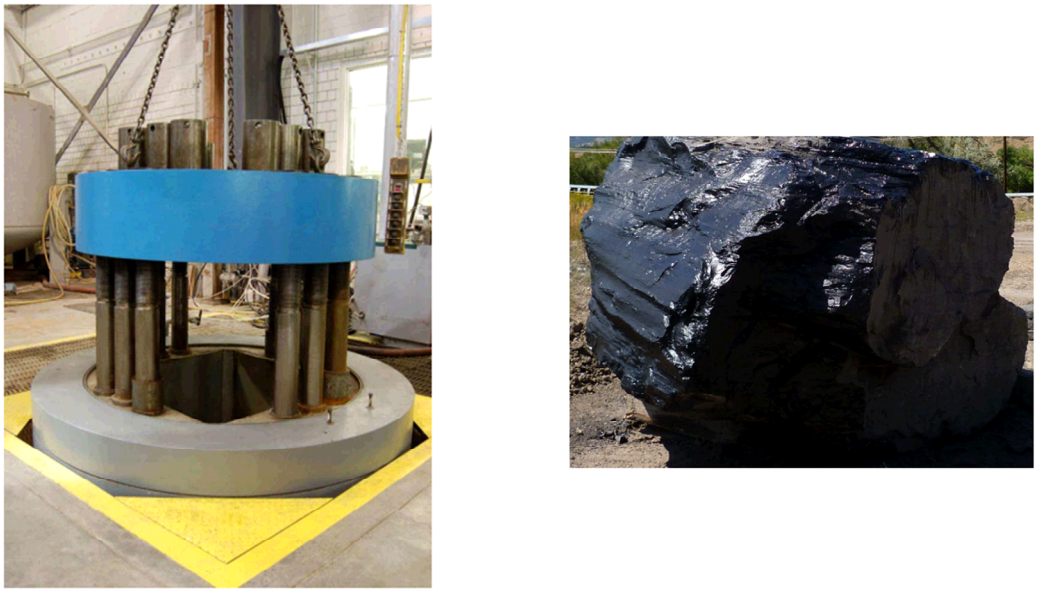

Figure 11.1 TerraTek's large multi-axial stress frame and Niobrara boulder acquired from the quarry in Colorado (Ghassemi and Suárez-Rivera 2012)

11.2 Numerical modeling for laboratory-scaled hydraulic fracturing test

As we explained earlier, the hydraulic fracturing process was modeled using the fluid-driven fracturing problem. So rock deformation was modeled for poroelastic solids, and fracture propagation was modeled by a quasi-static assumption. The fluid flow in the propagating fracture was solved by the lubrication equation. In this 3D hydraulic fracturing simulation, the fracture propagation process is more simplified because of complexity of numerical description of fracture tip contour of the non-planar fracture growth. It is assumed that the main hydraulic fracture plane was propagated constantly with given crack increment in the direction of the maximum far-field stress. That is, the crack increment law and an angle of fracture direction are not considered in the 3D simulation. In the 3D hydraulic fracturing simulation, once the fracturing tip contour met

with the maximum tensile criterion, the fracture plane is extended with the given crack increment at every time step.

The laboratory-scale large block was modeled using a 3D finite-element model and meshed using 26,400 tetrahedron elements [Figure 11.2]. Since quasi-static planar fracture propagation is assumed, our interest zone is the middle zone of the numerical domain. So, finer mesh is applied in the middle zone to capture the fracture plane propagation. The dimensions of the block were modeled as 1-m × 1.2-m × 1-m. We assumed a center-located pre-existing fracture plane of radius of 0.1-m for an open-hole perforation in the experiment. In the numerical domain [Figure 11.2(b)], elements overlapped with the initial fracture plane geometry (r=0.1m) are treated as crack elements. The crack elements are used to compute equivalent nodal forces by EPM as explained in Appendix C. For quasi-static fracture propagation modeling, the crack increment is given as Δr=0.05m. A fracturing fluid injection rate of 1,000 mL/min was applied as a point-source boundary condition at the center of the propagation fracture plane. For in-situ stress conditions, the vertical stress was applied in the y-direction and the maximum and minimum in-situ stresses were applied in the x- and z-directions respectively [Table 11.1].

Fluid properties of glycerin appear in Table 11.2. Since the material properties of the Niobrara shale were not given, we approximated the material properties from Colorado shale test data performed by (Regehr 2012). Approximate material properties of the Niobrara shale are shown in Table 11.3. Assumed Mohr-Coulomb parameters and tensile strength also appear in Table 11.1.

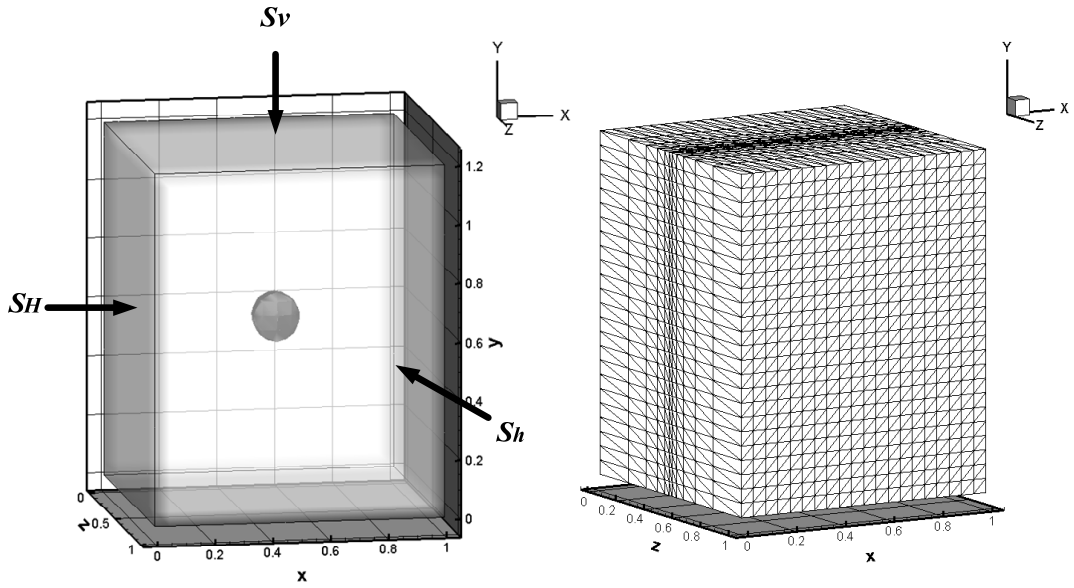

(a) Boundary conditions (b) Finite element mesh

Figure 11.2 3D numerical model and meshed finite element model for laboratory-scaled hydraulic fracturing test

Table 11.1 Boundary conditions and input parameters

Inputs	Values
Vertical in-situ stress, S_v (MPa)	31(4,500 psi)
Maximum in-situ stress, S_H (Mpa)	20.7(3,000 psi)
Minimum in-situ stress, S_h (MPa)	6.9 (1000 psi)
Injection rate, q_{inj} (mL/min)	1,000
Mohr-Coulomb parameter, ϕ_f	10
Cohesion, c_F (MPa)	30
Tensile strength, σ_T (MPa)	7
Number of elements	26,400
Number of nodes	6,300

Table 11.2 Fluid properties for Glycerin

Inputs	Values
Fluid mass density, ρ_f (kg/m3)	1261
Fluid viscosity, μ_f (Pa·s)	1 (1,000 cp)
Bulk modulus for fluid	4.35e9

Table 11.3 Rock properties of Niobrara Shale

Inputs	Values
Young's Modulus, E (GPa)	3.7
Shear Modulus, G (GPa)	1.42
Drained Poisson ratio, υ	0.3
Undrained Poisson ratio, υ_u	0.46
Biot's coefficient, α	0.866
Skempton's coefficient, B	0.949
Permeability, k (md)	0.01
Porosity, ϕ	0.1

11.3 Hydraulic fracturing in homogeneous block

In a homogeneous block, only major planar fracture growth propagated [Figure 11.7]. With the planar fracture growth, fluid pressure distributions changed with time. Figure 11.7 (a to h) captures continuous changes of the fracture plane and the fluid pressure distribution.

In Figure 11.4, the fluid pressure profile changed quickly with time and the fracture aperture opened gradually. As the fracture plane grew, the fluid pressure profile stabilized.

A viscous fracturing fluid is inducing a steep rise of wellbore pressure and eventually leads the initiation of a fracture. Wellbore pressure profile [Figure 11.3] quickly dropped with the fracture growth. Breakdown pressure in this simulation was 30.12 MPa (4368.55 psi) and wellbore pressure stabilized around 10.6 MPa (1537.4 psi). Since the block was assumed as homogeneous, the leakoff volume was small (48 ml).

In Figure 11.5 and Figure 11.6, the compressive stress increased the pore pressure near the fracture plane. Pore pressures near fracture tips were nearly zero due to the opening mode of fracture. Maximum opening stresses were concentrated in this region.

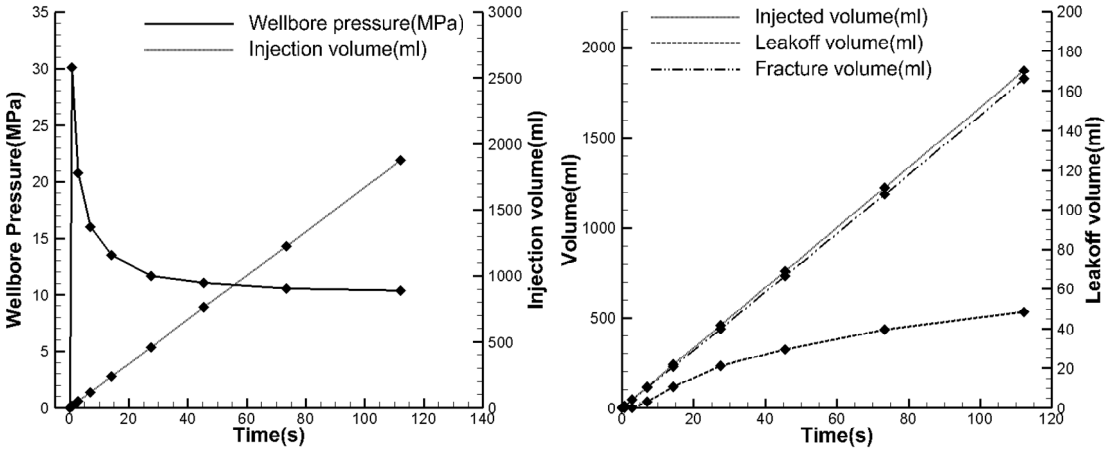

Figure 11.3 Wellbore pressure profile and injected fluid volume

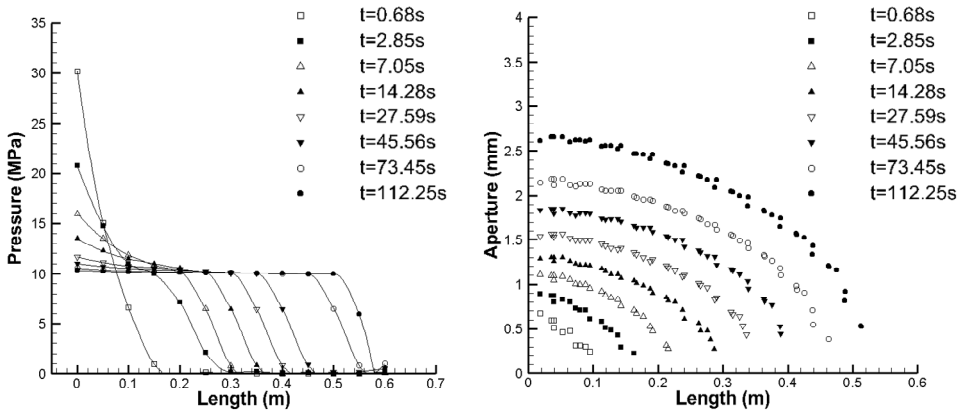

Figure 11.4 Fluid pressure change and aperture change during hydraulic fracturing

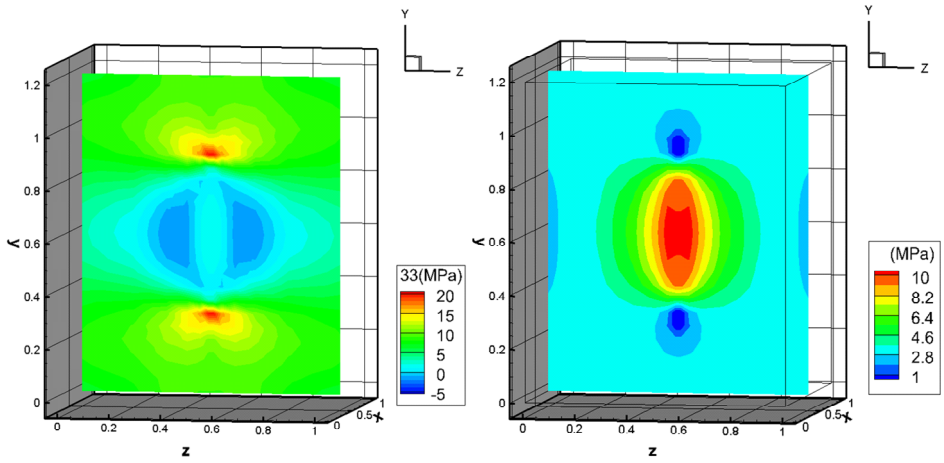

Figure 11.5 σ_{zz} distribution and pore pressure distribution at t=14.28 seconds in homogenous block

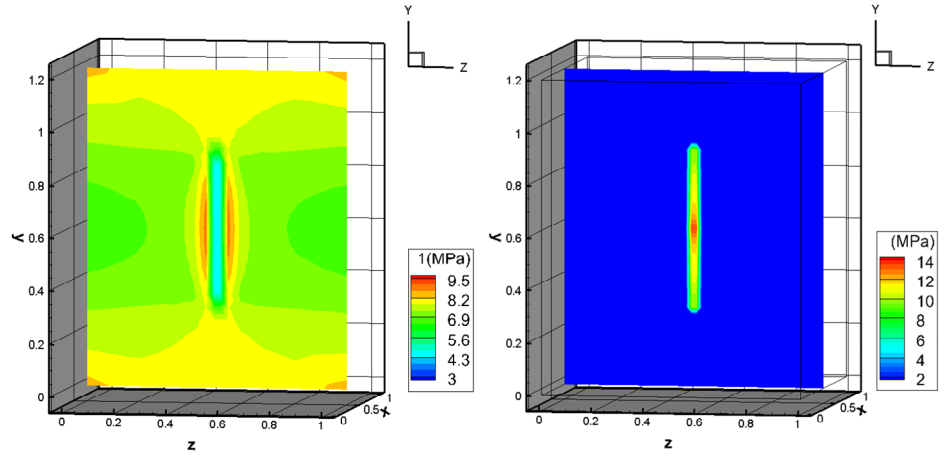

Figure 11.6 Maximum compressive stress and fluid pressure distribution (from center cut-view) at t=14.28 seconds in homogeneous block

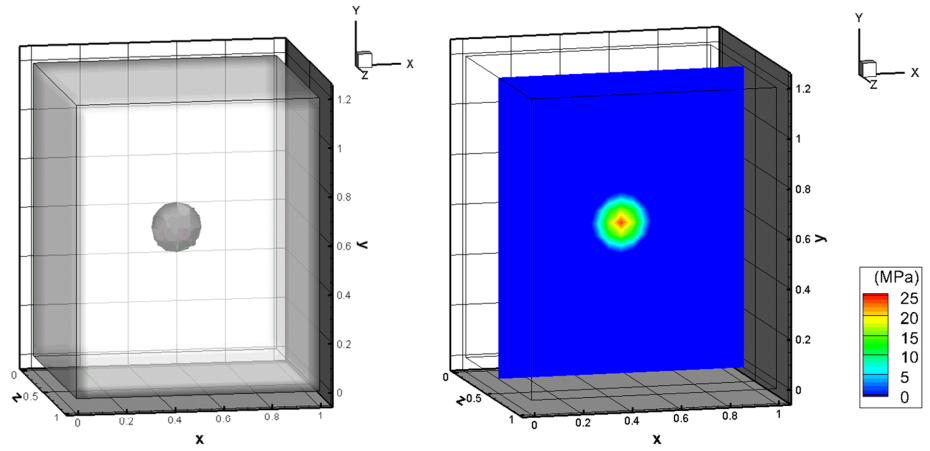

(a) t=0.68 seconds

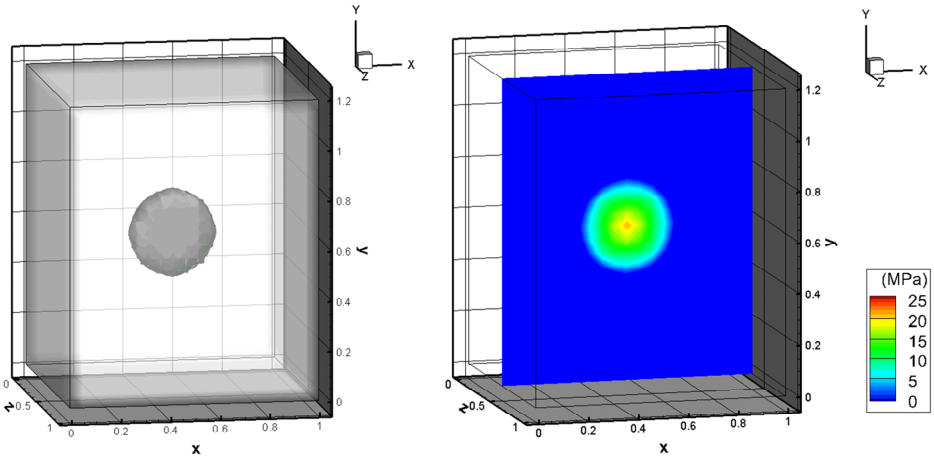

(b) t=2.85 seconds

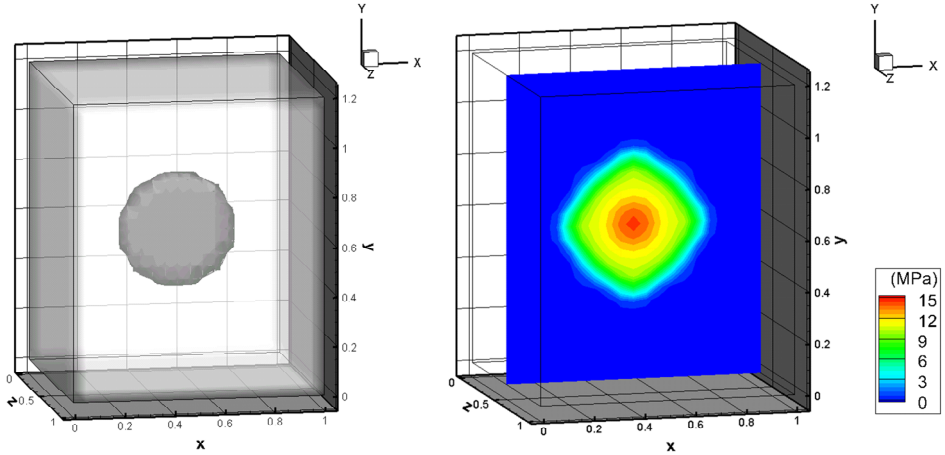

(c) t=7.05 seconds

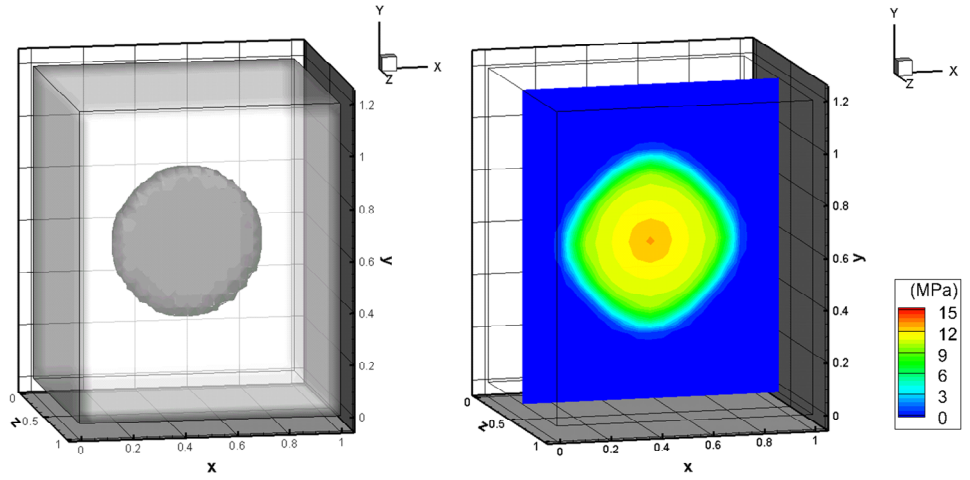

(d) t=14.28 seconds

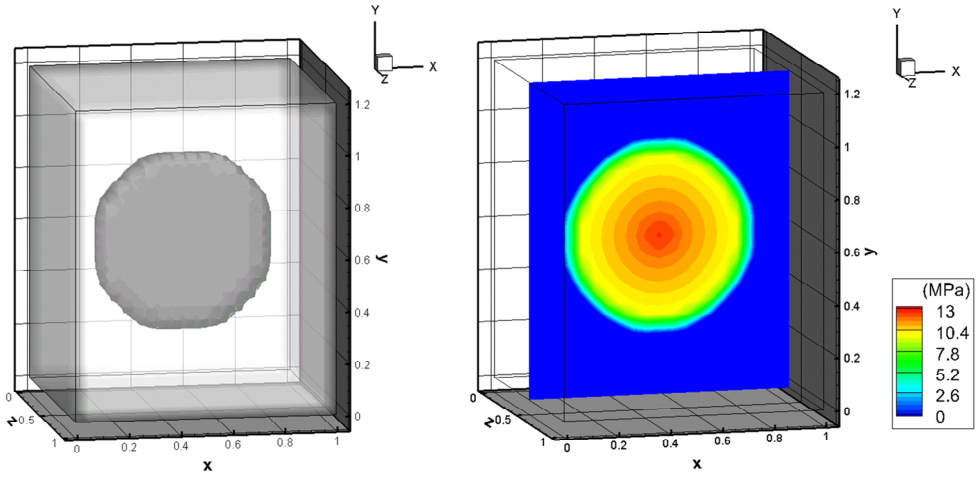

(e) t=27.59 seconds

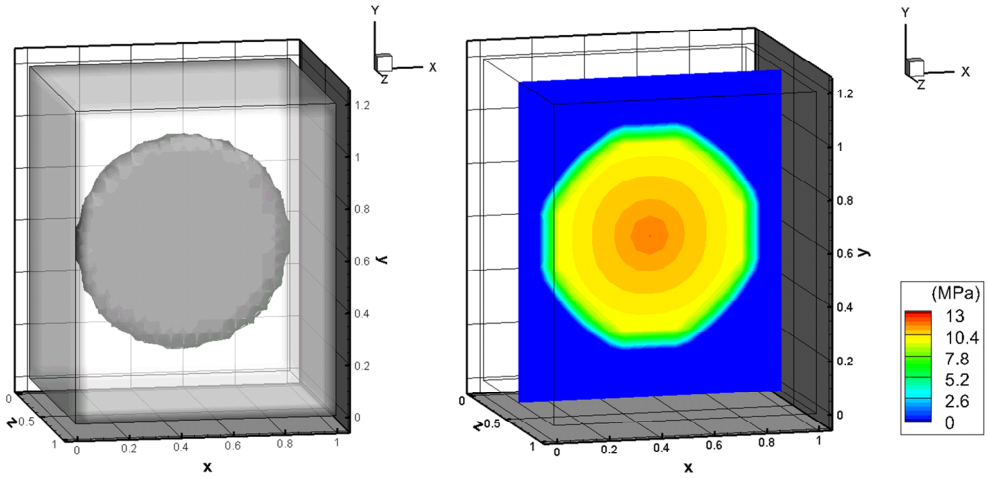

(f) t=45.56 seconds

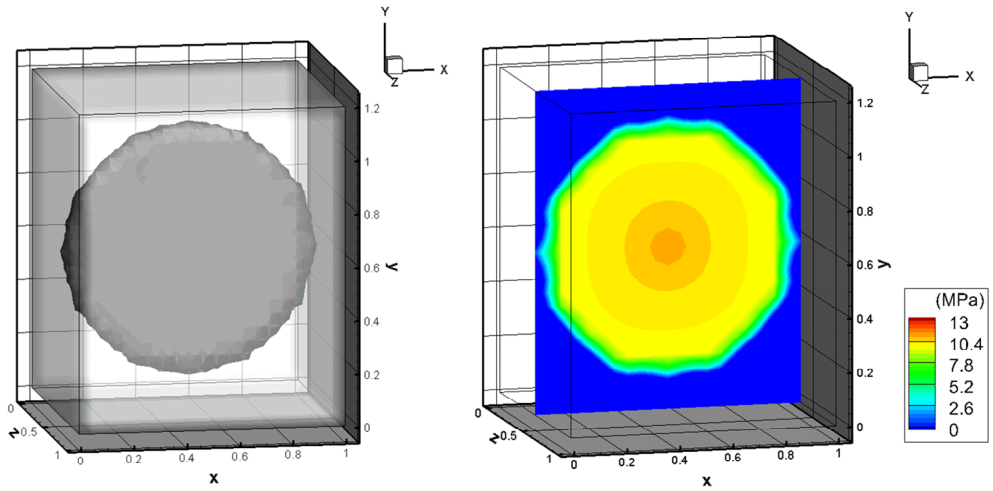

(g) t=73.45 seconds

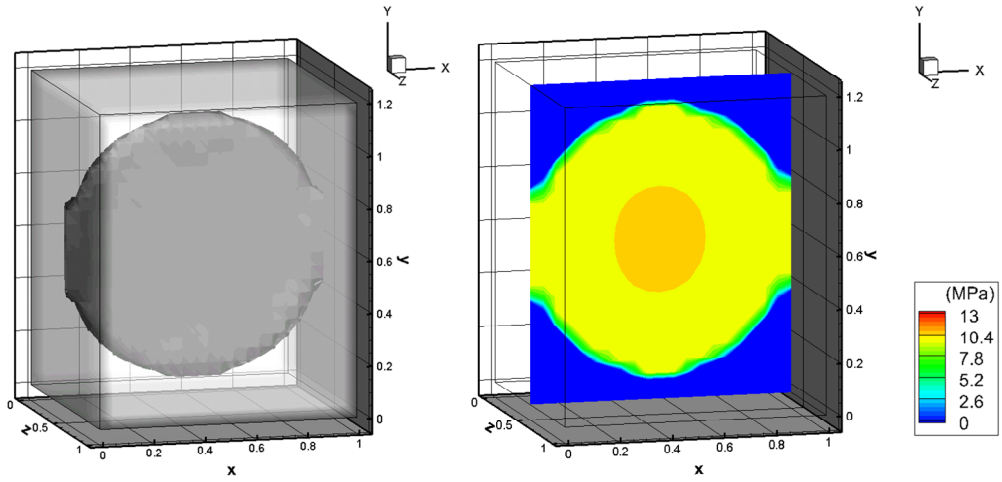

(h) t=112.25 seconds

Figure 11.7 Fracture plane growth and fluid pressure distribution with time

11.4 Hydraulic fracturing in heterogeneous block

Because the real testing block is characterized by heterogeneous fabric, we applied the heterogeneities to the numerical block using random variables generated by the Weibull distribution function. There are no initially assigned cracks in the numerical block. Generated random variables applied to stiffness, permeability, and strength of

each element for representation of the block heterogeneity. Selected Weibull parameters are shown in Table 11.4. The heterogeneity of the block is described in Figure 11.8.

During hydraulic fracturing in the heterogeneous block, lots of failures were detected with the main planar fracture growth [Figure 11.11]. The secondary failures are induced by the hydraulic pressurization in the main fracture plane. However, the spotted failures are not directly connected with the main fracture plane, so that the secondary failures could not be opened by fluid pressure. The spotted failures have been increasing with time and fracture plane growth. Figure 11.12 captured failures in orthogonal direction of the major fracture plane are captured. The lateral growth of the fracture is also observed in experiments.

The wellbore pressure profile [Figure 11.9] was similar to the homogeneous case. Breakdown pressure in this simulation was slight lower at 28.75 MPa (4169.84 psi) and wellbore pressure is stabilized around 10.6 MPa (1537.4 psi). Because of effect of the heterogeneity, leakoff volume is increasing to 385 ml [Figure 11.9].

In Figure 11.10, pore pressures near the fracture plane are high due to the compressive forces of fluid pressurization. The pore pressure is more widely distributed than the homogeneous case and the heterogeneous pore pressure increase could affect failures, because increased pore pressure moves the failure envelope left to right. The pore pressure effect triggered tensile or shear failures are. In addition, because the maximum opening stresses concentrated on the fracturing tip region, pore pressures near the fracturing tip region are nearly zero by the fracture opening.

Table 11.4 Weibull parameters for block heterogeneity

Inputs	Values
Distribution for stiffness	m_1=1, a_1=5
Distribution for permeability	m_2=1.1, a_2=10
Distribution for strength	m_3=1, a_3=6

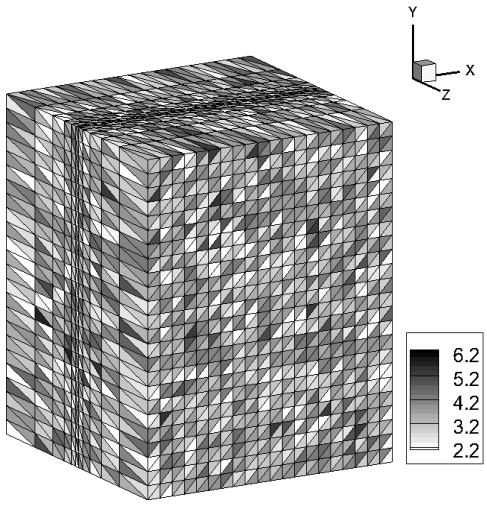

Figure 11.8 Representation of stiffness heterogeneity (unit=GPa)

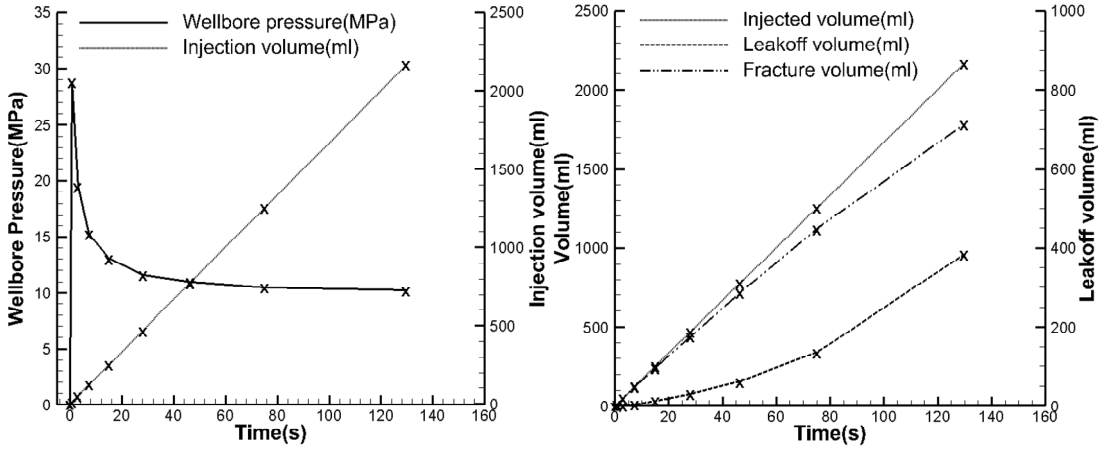

Figure 11.9 Wellbore pressure profile and injected fluid volume

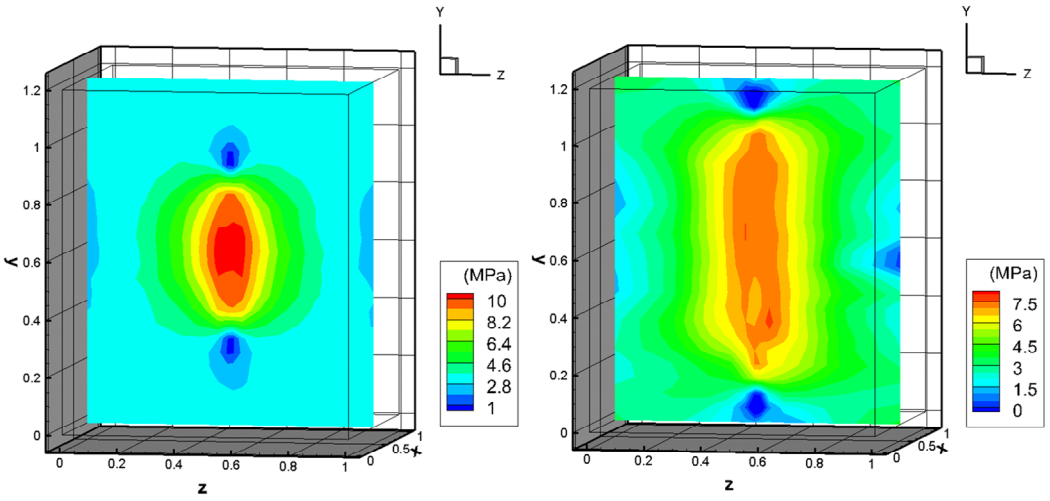

Figure 11.10 Pore pressure distribution at t=15.07 seconds and t=75.15 seconds in heterogeneous block

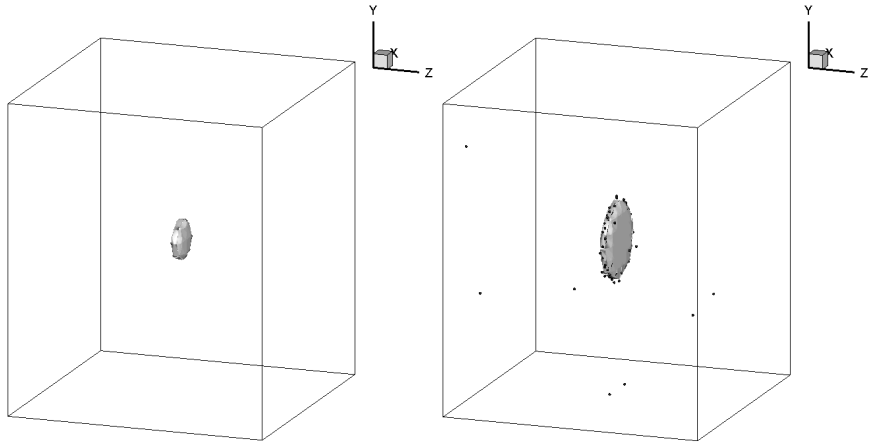

(a) t=0.73 seconds (b) t=3.02 seconds

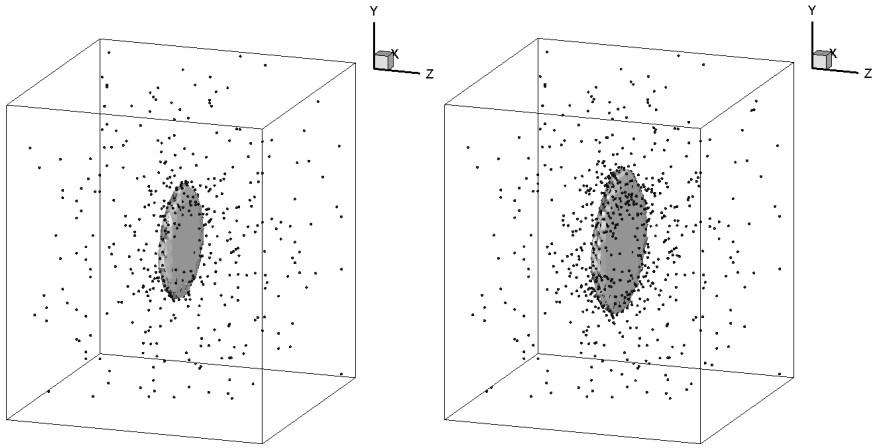

(c) t=7.48 seconds (d) t=15.07 seconds

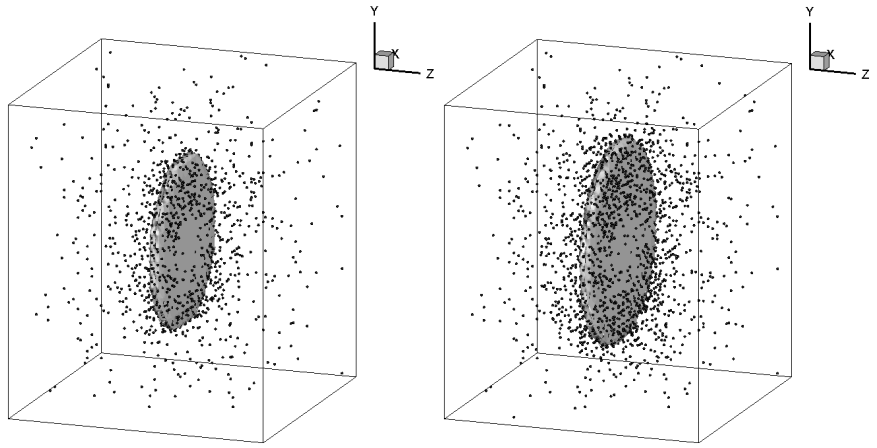

(e) t=28.10 seconds (f) t=46.48 seconds

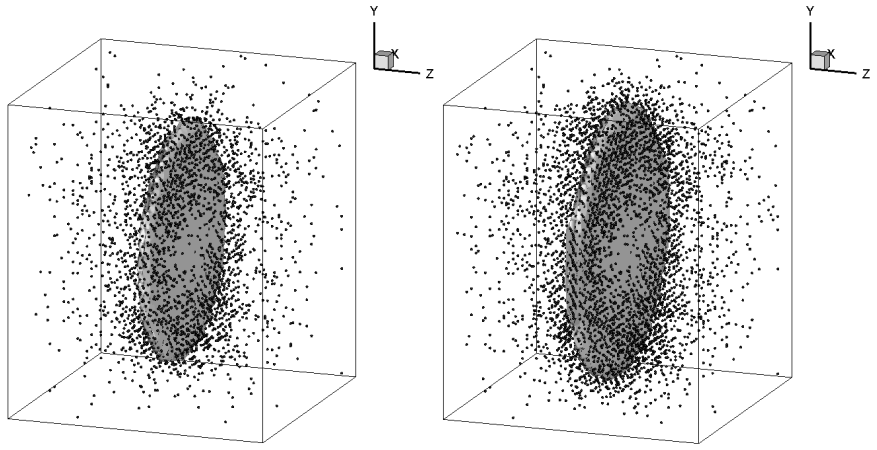

(g) t=75.15 seconds (h) t=129.8 seconds

Figure 11.11 Fracture plane growth and failure events in heterogeneous block

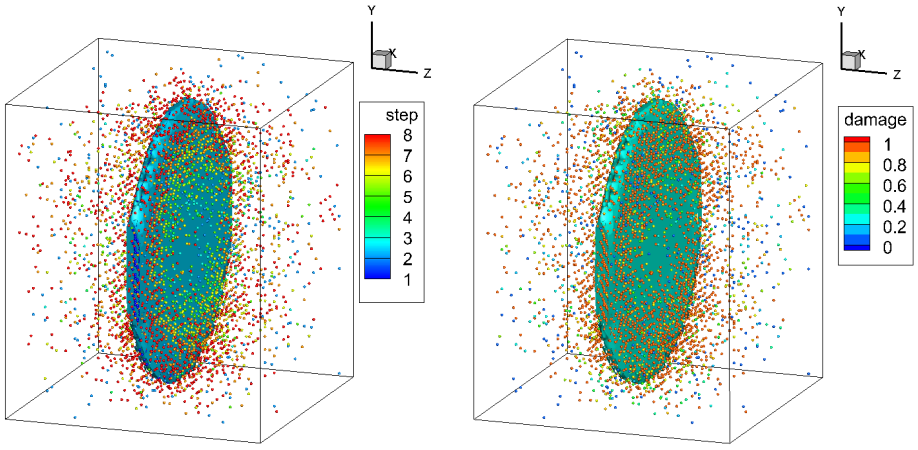

(a) Colored by step (b) Colored by damage

Figure 11.12 Failure events colored by step and damage at t=129.8 seconds

In Figure 11.11 and Figure 11.12, the main fracture plane is represented by iso-surface, while the multiple and spotted failures are indicated by points. The spotted failures have been detected by damage events during hydraulic fracturing simulation.

In Figure 11.11(a), the initial fracture plane is pressurized by fracturing fluid injection and after a short time (t=0.73 seconds), wellbore pressure reaches breakdown pressure (P_b= 28.75MPa) and the fracture plane propagates toward the maximum in-situ stress direction. We only observe a few failures in the heterogeneous block until t=3.02 seconds and then the multiple and spotted failures are detected after t=7.82 seconds [Figure 11.11(c)]. After t=28.10 seconds, the multiple failures are concentrated on near the primary fracture plane toward orthogonal direction of the primary fracture plane [Figure 11.11(e)-(h)]. These orthogonal failures are an indication of branching of the hydraulic fracture propagation. In Figure 11.11(g)-(h), the fracture plane has almost

reached the boundary of the block. The fracture plane is highly opened and leakoff volumes are also increasing [Figure 11.9].

11.5 Comparison of numerical and experimental results

In Figure 11.13, we compared the wellbore pressure profile of the numerical simulation with the experimental results. According to the comparison, the breakdown pressure of the homogeneous block is slightly higher than in the experiments, while the breakdown pressure of the heterogeneous block is almost similar with the experiments. The simulation time of the homogeneous block case is shorter than in the experiments and the heterogeneous block [Table 11.5].

A major difference between the wellbore pressure profile of the numerical simulation and the experiments appears after breakdown pressure. Wellbore pressure of the experiment is shown to drop more quickly than the numerical simulation. This is because we assumed the fracture propagation would grow in a quasi-static manner. However, practically speaking, the fracture grew dynamically and the speed of growth was faster than our simulation.

Table 11.5 Comparison of experimental results and numerical simulations

	Breakdown pressure	Stabilized pressure	Treatment time (s)
Experimental results (by TerraTek)	28.97 MPa (4202 psi)	10.93 MPa (1585 psi)	130
Num. Homogeneous block	30.12 MPa (4368.55 psi)	10.6 MPa (1537.4 psi)	112.25
Num. Heterogeneous block	28.75 MPa (4169.84 psi)	10.6 MPa (1537.4 psi)	129.8

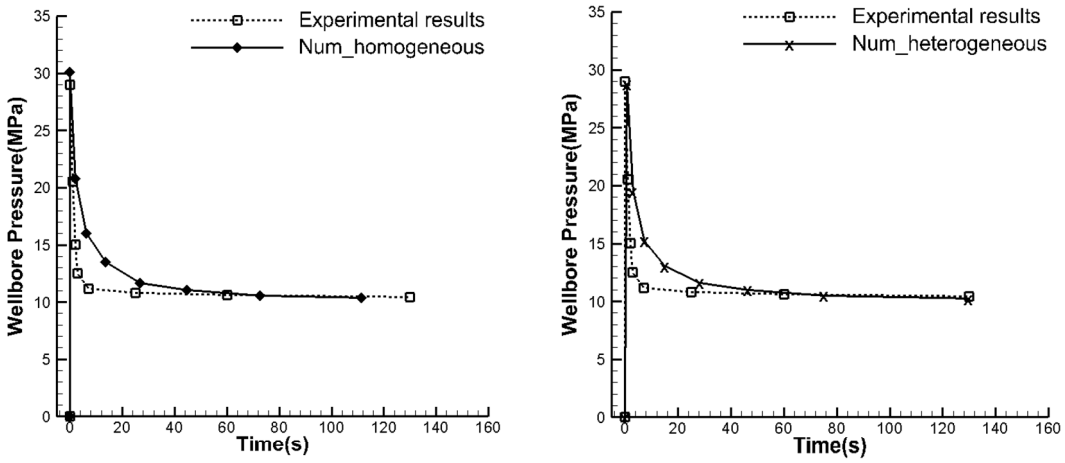

Figure 11.13 Comparison of wellbore pressure profile with experimental results

11.6 Sensitivity of numerical model by material property

In Figure 11.14, we investigated the sensitivity of the 3D hydraulic fracturing simulation against Young's modulus. Since mechanical deformation of a rock is dependent on the Young's modulus of the rock, hydraulic fracturing behaviors are also influenced by the change of the mechanical deformation. When the rock was softer

(*E*=2.7GPa), less breakdown pressure was obtained and more simulation time was required, because the fractures opened wider in the soft rock. In contrast, when the rock was harder (*E*=4.5GPa), breakdown pressure was higher and shorter simulation time was required, because the fractures opened less in the hard rock.

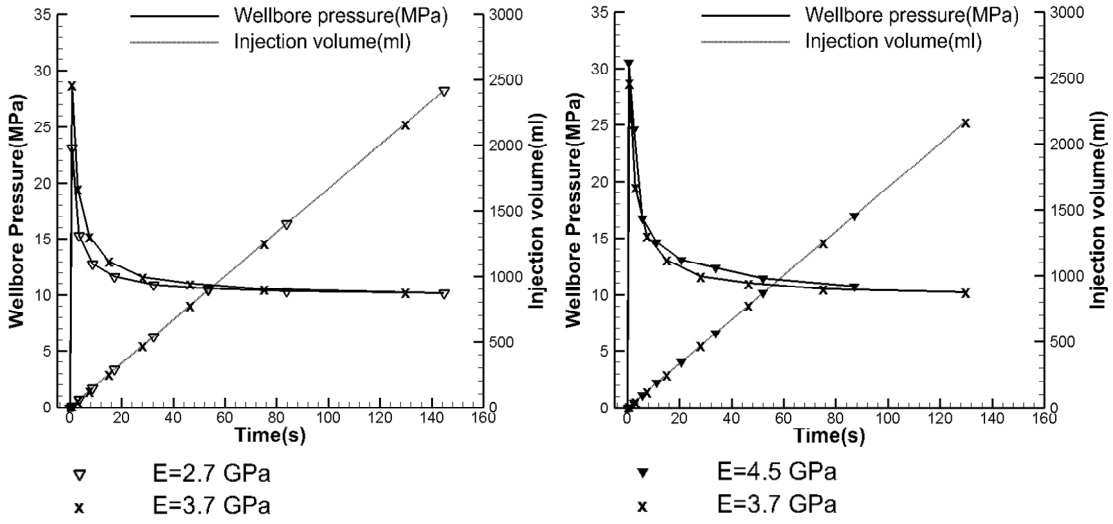

Figure 11.14 Comparison of wellbore pressure profile and injection volume by Young's modulus changes

11.7 Viscosity of fracturing fluid

In the hydraulic fracturing stimulation, choice of fracturing fluid is another important issue, because fracture opening (i.e. aperture) is highly affected by viscosity of the fracturing fluid. Generally, high viscosity fluid opens more, while low viscosity fluid opens less. Because the high viscosity fluid induces strong tensile force, higher breakdown pressure is observed than the low viscosity fluid. In this section, influence of the fluid viscosity on the hydraulic fracturing was investigated.

11.7.1 μ=1000cp vs. μ=100cp

Previously we used glycerin for the fracturing fluid, which has high fluid viscosity (μ=1000cp). Lower viscosity fluid (μ=100cp) was used instead of the glycerin. When same amount of injection rate (q_{inj}=1L/min) was used, low breakdown pressure (P_b=13MPa) was observed and the fracture plane did not propagated since the low injection rate could not induce enough tensile forces at fracturing tips [Figure 11.15]. So, when the injection rate was changed to q_{inj}=10L/min, higher breakdown pressure (P_b=28MPa) was obeserved and the fracture plane was fully propagated [Figure 11.15]. When the low viscosity result (μ=100cp, q_{inj}=10L/min) was compared with the high viscosity result (μ=1000cp, q_{inj}=1L/min) [Figure 11.15], the low viscosity case required shorter treatment time than the high viscosity case because the injection rate of the low viscosity case is ten times higher than the high viscosity case. Because of the high injection rate of the low vicosity case, amount of injected fracturing fluid (V_f=2,500mL) is higher than the high viscosity case (V_f=1,900mL).

Consequently, when the lower viscosity fluid is used, higher injection rate is required to create hydraulic fracturing. Unless the injection rate is increased, the fracture plane could not be extended. Hence, high pumping equipment is required when the fracturing fluid has low viscosity property. Because the high visous fluid lead high breakdown pressure, the high viscous fracturing fluid used for making direction at early stage and low viscous fracturing fluid is used to create wider fractures.

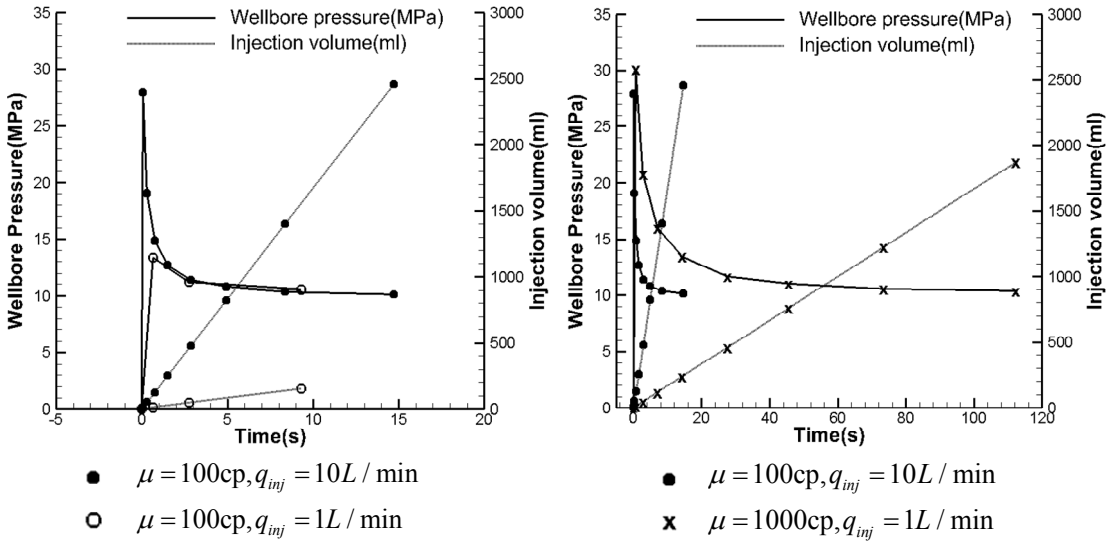

Figure 11.15 Comparison of wellbore pressure profile and injection volume by fracture fluid viscosity and injection rate

11.8 Conclusions

In this study, we developed a fully 3D hydraulic fracturing model for the large-scale laboratory hydraulic fracturing test and successfully validated it with the experiment performed by TerraTek. Planar fracture propagation was observed from the both numerical simulation and experiment, as expected. In the case of the heterogeneous block test, both main planar fracture growth and widely distributed fractures were observed.

The greatest difficulty of the 3D hydraulic fracturing model is tracking the crack tips, because the crack tip is no longer 2D and the 3D variation of the crack tips makes them difficult to identify. In our 3D hydraulic fracturing simulation, we assumed the main planar fracture plane was propagating toward the maximum in-situ stress direction.

However, the main fracture could be turned or intersected with natural fractures, so that these complex fracture interactions increased numerical difficulties. The numerical difficulties required huge numerical challenges that remain for future improvement.

12. 3D THERMAL FRACTURE PROPAGATION

In geothermal reservoir development, thermal stresses arise from conductive and convective heat transfer. These stresses become important for long injection times and may result in thermal fracturing (Min and Ghassemi 2011). Basically, three mechanisms of heat transferring—conduction, convection and radiation—could be acting on the porous rock. Conduction is transferring heat through solid material from high temperatures to low temperatures. Convection is a process of heat transfer by a flowing fluid. Radiation is a heat transfer process of electromagnetic waves moving through space, so there is negligible radiation effect through the porous rock, and usually it is not considered as an important heat transfer mechanism (Pratt 1982).

Among these three heat transfer mechanisms, heat conduction is a dominant heat transfer mechanism in porous rock (Settari 1989). Therefore, in enhanced geothermal system (EGS) design, thermally induced stresses might be used to create reservoir permeability. When cold water was injected into the geothermal reservoir, the reservoir rock gradually lost its heat and the rock shrank due to the cooling process. Eventually, the thermally induced stresses nucleate fractures when the strain energy from the thermal load is sufficient to create initial cracks in an intact rock mass (Tarasovs and Ghassemi 2010). The secondary thermally induced fractures initiate perpendicular to the preexisting major fracture (Tester et al. 1989), and the creation of thermally induced fractures could provide larger contact area by increasing fracture permeability near the preexisting fracture networks, increasing injectivity and productivity of the geothermal

reservoir. Especially, serial processes of cooling and heating in geothermal reservoirs could enhance reservoir permeability due to the secondary thermal fracture growth (Min and Ghassemi 2011). We investigated the basic fracture mechanism of the thermally induced fracture growth and the role of the heterogeneity in a geothermal reservoir. The thermal stresses were calculated using the coupled thermo-hydro-mechanical (THM) analysis, and their influence on crack propagation during reservoir stimulation was simulated using numerical simulation.

12.1 Numerical modeling

The size of the section of interest is 150-m × 100-m × 80-m [Figure 12.1] and the upper and lower zone have 20 m and 75G Pa each, while the zone of interest is 40 m thick and has a variable modulus, between 45 and ~ 55 GPa [Figure 12.2]. In the center of the zone, a preexisting fracture is assumed, and its surface is considered cooling. The closed fractured surface is simplified as an elliptical surface as in a hydraulic fracture. In the thermal coupling part, conductive heat transfer is considered between the rock matrix and the cooled fracture. In addition, the boundary conditions of the numerical model are simplified; a zero pore-pressure boundary condition is applied to top and bottom surfaces of the model. Table 12.1 shows the statistically generated heterogeneities applied to the zone of interest in the geothermal reservoir. The randomly generated variables are applied to materical stiffness, matrial strength, and permeability. Hydraulic, thermo-physical, and mechanical properties for simulation domain are described in Table 12.1.

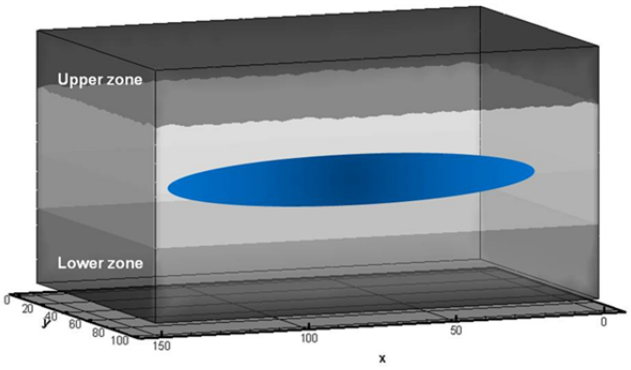

Figure 12.1 Schematic numerical modeling of a geothermal reservoir with a pre-existing cooled fracture.

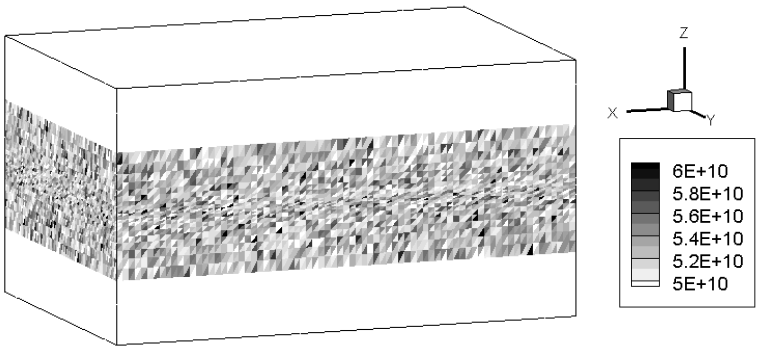

Figure 12.2 Representation of stiffness heterogeneity (unit=Pa)

Table 12.1 Material properties and input parameters for thermal fracturing

Inputs	Values
Young's Modulus	54.5 GPa
Poisson ratio	0.25
Permeability	0.001 md
Porosity	0.19
Biot coefficient	0.966
Thermal diffusivity	1.6×10^{-6} m^2/s
Thermal expansion of solid phase	1.8×10^{-5} K^{-1}
Thermal expansion of fluid phase	3.0×10^{-4} K^{-1}
Num. of element	275,556
Num. of nodes	49,019
Reservoir dimension	150-m×100-m×80-m
Thermal loading	ΔT=90°C

12.2 Numerical results of thermal fracturing

No initial cracks were applied in our FEM model. Crack initiation and propagation were detected by both the damage variable and the maximum principal strain criterion. Pore pressure changes around the fracture surface were influenced by the temperature variation through thermo-poroelastic effects.

The cooling zone was extended by the cooling injection over time [Figure 12.3], the distribution of ε_{zz} and the maximum tensile value of ε_{zz} were concentrated on the fracture surface, and the tensile-strain concentration led to crack growth perpendicular to the preexisting fracture surface [Figure 12.4]. When the heterogeneous reservoir was subjected to temperature change, the fracture volume increased; the amount of the volume change was dependent on the thermal expansion coefficient of the rock. The considerable difference of thermal expansion coefficient between damaged rock and intact rock will increase the effective volumetric stress in the heterogeneous reservoir. The volumetric stress change will initiate thermal fractures and increase a significant positive pore pressure in the thermally induced fractures. And the continuous change of volumetric expansion of the pore space will cause further propagation of the thermal fractures.

Figure 12.5 shows crack initiation at early (a) and later (b) stages of cooling. Clearly, the longer cracks grew mostly in the central area of the main fracture surface. The length of the fracture was limited by the extent of the cooled zone. Tension failure by thermal loading created several cracks perpendicular to the major fracture surface at various locations due to the heterogeneous nature of the rock matrix. . In this simulation,

we assumed that the initial pore pressure of the rock matrix was 20 MPa and the pore pressure of the fractured element was 25 MPa. However, the low matrix permeability prevented rapid communication of the hydraulic pressure with the rock matrix until the thermal fractures grew. The pore-pressure distribution at this stage is shown in Figure 12.6.

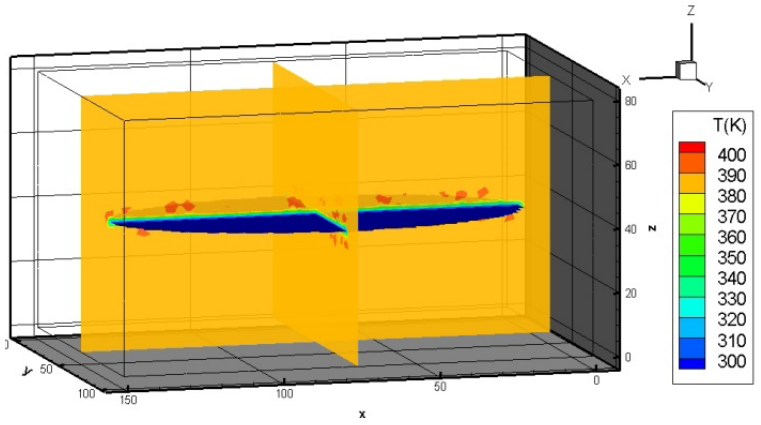

(a) Time = 2 hours

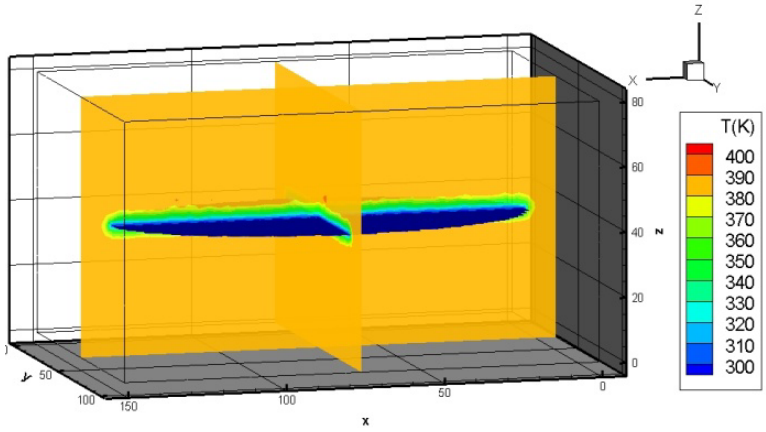

(b) Time = 173 days

Figure 12.3 Temperature distribution changes by cooling injection

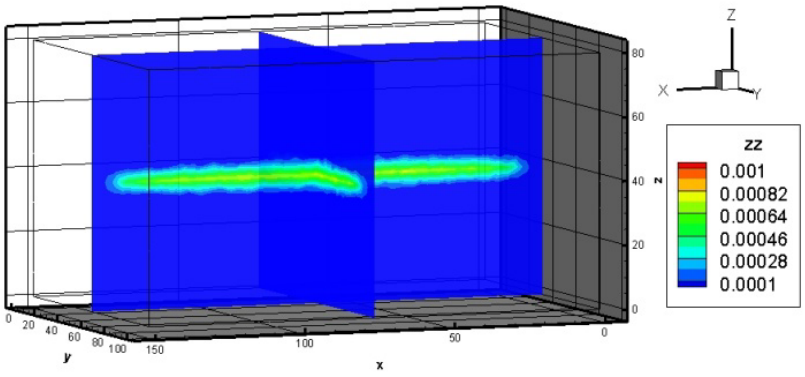

(a) Time = 2 hours

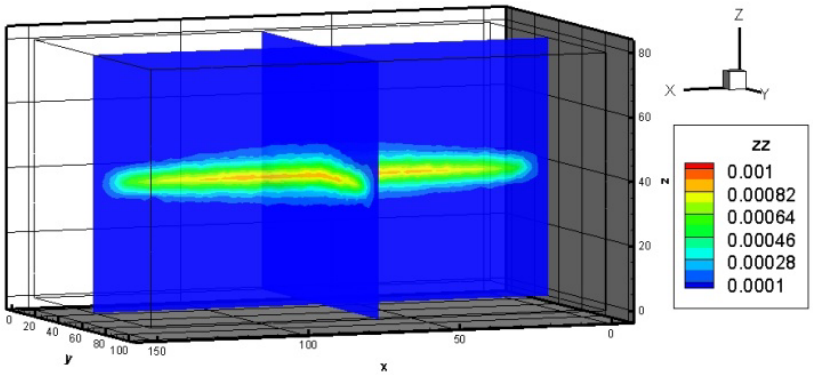

(b) Time = 173 days

Figure 12.4 Distribution of ε_{zz} changes by cooling

In this simulation, the minimum element size was about 0.2 m. This means that the minimum crack length growth at each step was at least 0.2 m, so it was difficult to see thermal fracture growth clearly in this coarse mesh. In Figure 12.7, crack propagation is scattered at early stages, while the spacing of the cracks decreases at the later stages of fracturing. Red spots indicate early crack growth and orange spots indicate later crack growth. Since tensile stresses were concentrated in the center of the fracture surface, cracks nucleated mostly from the interior regions of the fracture surface, and later cracks initiated from the outer boundary of the closed fracture as the tensile

region transferred to the edge of the cooled fracture surface. However, the fracture spacing should eventually increase as the fractures interact and some cease to propagate.

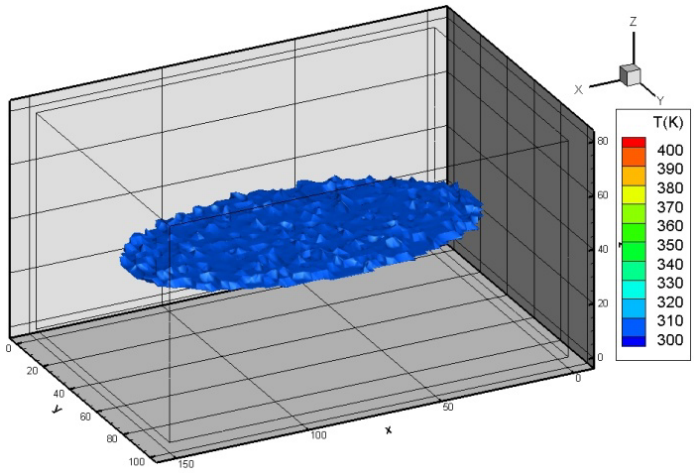

(a) Crack initiation stage

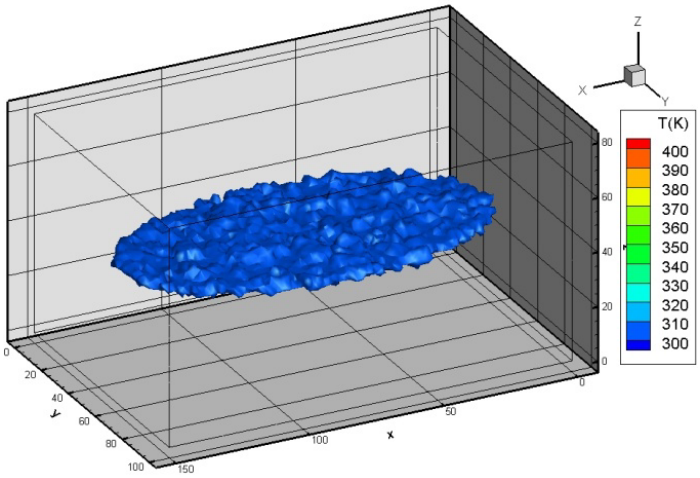

(b) Crack propagation stage

Figure 12.5 Thermal fracture growth represented by the iso-thermal surface

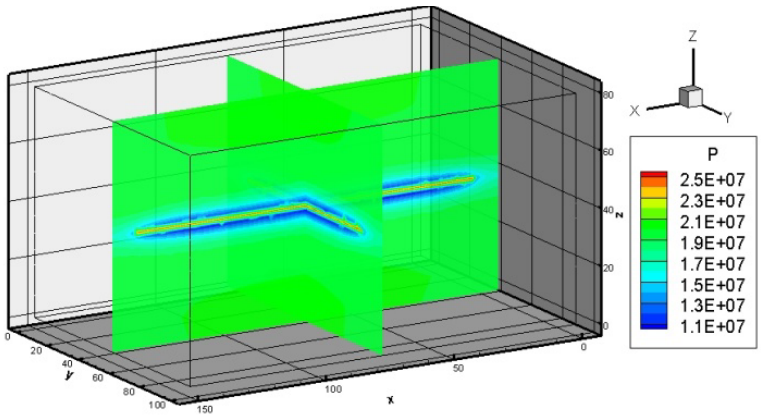

(a) Pore pressure distribution at the early stage of thermal fracturing

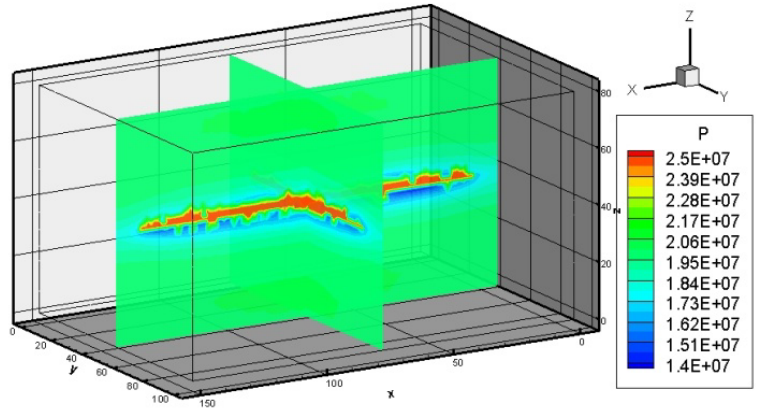

(b) Pore pressure distribution at the later stage of thermal fracturing

Figure 12.6 Pore pressure distribution during thermal fracturing

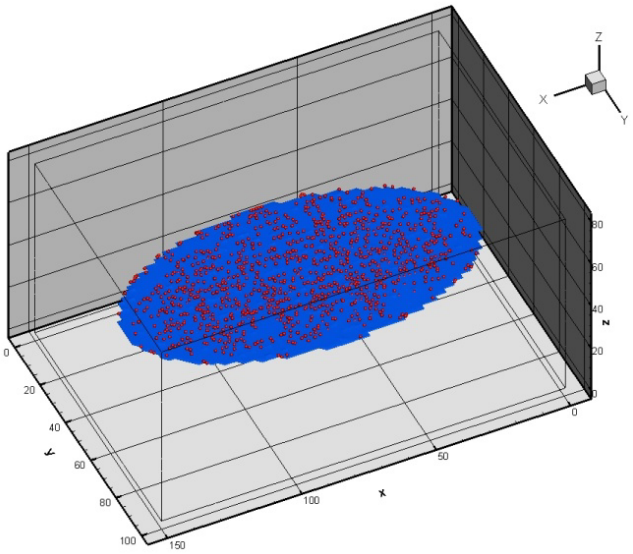

(a) Crack growth at the early stage

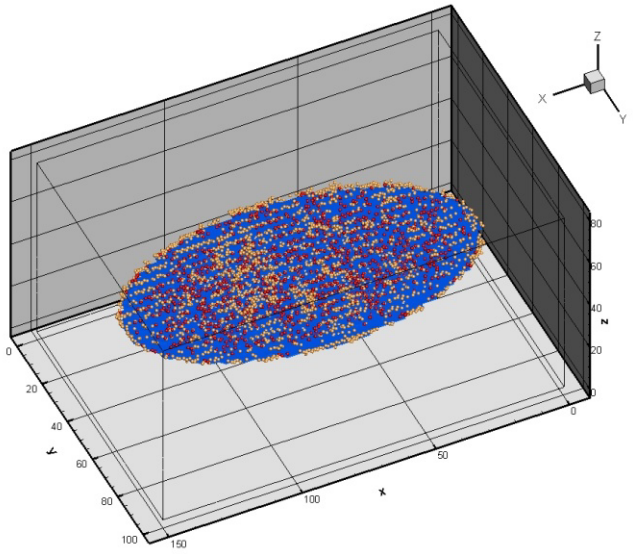

(b) Crack growth at the later stage

Figure 12.7 Thermal fracturing growth using scatter image in sequential stages

12.3 Conclusion

This evaluation showed that thermal fractures propagate perpendicular to the original natural fracture. Because of heterogeneity, some fractures align differently, but

the major trend of thermal fracturing is similar to previous work (Tarasovs and Ghassemi 2010). Characterization of the thermal fracture spacing is difficult with the current simulations. The major difficulty of thermal fracturing characterization is applying a crack-propagation and branching scheme. In many cases, simulation results produce unstable configurations when propagation is very fast. Thus, it is necessary to carefully determine the step size and the critical criterion for crack propagation and branching.

Also, to characterize very small fracture growth from a large fracture surface, a finer mesh is needed; however, a drawback of the finer mesh model is increasing computational cost. For future research, long-term thermal fracturing growth will be simulated and characterized using a finer mesh case.

13. CONCLUSIONS AND DISCUSSIONS

In this research, providing better understanding of brittle fracture process, complexity of mixed fracture propagation and hydraulic fracturing treatment is aimed. These issues are important in many rock engineering areas (eg. nuclear waste disposal, enhanced geothermal system, enhanced oil/gas reservoir recovery, deep underground injection and CO_2 storage). In addition, rock heterogeneity is a special interest in this dissertation. Since most rocks consist of crystals, grains, pores, and natural cracks, complex behavior and unpredictable fracture growth are commonly observed in both field-scale and laboratory-scale experiments, it is very difficult to resemble physically realistic fracturing in the heterogeneous reservoir. In order to study the physical complexity of rock mechanics, following objectives were addressed in this dissertation;

- Provide numerical description and interpretation of rock properties and fracture patterns, and analysis of rock experiments data for reservoir characterization
- Better understanding of critical information for complex fractures affected by brittle/ductile behavior of a rock during compaction.
- Provide 3D hydraulic fracturing model for laboratory block experiments and applicable to use in larger geological problem.
- Provide improved prediction techniques for hydraulic fracturing stimulation in heterogeneous reservoir by properly balanced model between theoretical and experimental measurements.

13.1 Conclusions

Hydraulic fracturing process was modeled using fluid-solid interaction analysis incorporating fluid flow, fracture mechanics, rock deformation and moving boundary problem. The hydraulic fracture propagation and moving boundary scheme were modeled using damage mechanics with the element splitting technique in three-node tetrahedron and four-node tetrahedron element. The 3D hydraulic fracturing model was validated with a large scale hydraulic fracture laboratory experiment.

The sequential procedure of hydraulic fracturing propagation was investigated using coupled analysis of fluid flow analysis in fracture network with the elastic-brittle analysis for mechanical local degradation behavior of rock mass. The influences of coupled processes on fracture propagation were developed using Continuum Damage Mechanics (CDM) along with the discontinuous crack propagation algorithm. Damage mechanics describes the inelastic response of micro-crack growths and the macroscopic fracture. The numerical model of passive/active crack element provides for explicit resolution of discontinuous shear fracturing behavior of fracture clusters.

During the hydraulic fracturing treatment design, several physical problems are emerged from the complex relationships among rock deformation, fluid flow, and heat transfer. In addition, correct estimate fracture conductivities and fracture geometry, and to describe reservoir heterogeneity, fracturing path and patterns are important parameters to determine. However, it is so difficult to interpret these parameters from field measurements due to unknown nature of rock properties and stress fields. Hence, an importance of developing a numerical modeling to estimate the unknown parameters and

to overcome many reservoir uncertainties is recognized in the design of the optimized hydraulic fracturing treatment.

Fracture propagation in heterogeneous reservoir is more than one mode of fracture, so that mixed-mode fracture is frequently observed. Understanding of physical behavior of the mixed mode fracture propagation is important. Damage mechanics is used to represent both micro and macro crack propagation and severely damaged zone causes macroscopic crack propagation through the damaged zone. 2D triaxial and 3D uniaxial compression test for brittle rock were simulated using the damage model. The damage variable is used to represent stiffness degradation and crack propagation. It was clearly seen that crack propagated through ruptured path of damage propagation.

Rock is heterogeneous material composed by grains, pores, crystals, minerals and various scales of natural cracks. Due to the uncertainty and complexity of rock mechanics, it is difficult to estimate fracturing phenomena of brittle heterogeneous rock. Thus, it is better to compare the numerical estimation with empirical results, but it is very difficult to sustain same heterogeneity conditions in the experiments. Consequently, in order to investigate the independence influence of the heterogeneity on rock fracture, the numerical simulation might be a better method.

In order to characterize rock heterogeneity, Weibull distribution function was used in this study, since it is widely used in several areas including survival analysis, weather forecasting, and failure analysis because of the flexibility of its variables (Weibull 1951). Random values generated by Weibull distribution function are applied to both stiffness and compressive strength to represent heterogeneous character of rock.

However, it is very difficult to resemble the realistic heterogeneous composer, fabric, and orientation of rock into numerical models using statistical methods because each differently composed material requires different type of statistical model (Wong et al. 2006).

13.2 Discussions and recommendations

In this dissertation, we simplified real behaviors of fracturing because of numerical difficulties. Single phase and Newtonian fracturing fluid flow was assumed, and simplified elastic-brittle stress-strain relations was used to describe confining dependent mechanical behaviors.

First, we assumed single phase fluid flow, but this is not true in deep reservoir subjected by high compression. Normally, liquid/gas phases exist and the phases are changed by status of temperature and pressure. Therefore, multiphase fluid flow behavior should be considered.

Second, Newtonian fluid flow was used for the fluid flow analysis in hydraulic fractures. However, the fracturing fluid is mixture of various liquids and solids. In addition, the fracturing fluid is usually blended with proppants such as sands, ceramics, or special chemicals (polymers) in order to retain fracture permeability. Thus, we should consider the mixture fluid flow in the fracture networks.

Third, as mentioned above, large part of rock properties are still unknown, especially fracture patterns are so much depends on circumstances of nature. In this dissertation, physical behavior of brittle rock is modeled using elastic and brittle

softening constitutive model. It is general agreement when reservoir formation is hard and brittle. However, when hydraulic fracturing is operated in weakly consolidated reservoir such as Gulf of Mexico, highly non-linear mechanical failures are dominant, so viscous change of the rock stress becomes important factor to determine failures in the reservoir. These complicate behaviors make numerical modeling far more challenging.

Forth, investigation of scale effect from laboratory scale to large scale geological model is an important issue in geomechanical reservoir simulation. From direct monitoring of field treatments, the fractures are grown in complicated manner by local heterogeneities, layered formation and natural fracture network in the reservoir (Adachi et al. 2007). The issue is related how the small scale of rock heterogeneity/micro-fractures represents to larger scale block. The small scale of rock heterogeneity is highly affecting on failures and tortuous/multiple fracturing growth in geomechanical analysis, however dimension of each numerical block in reservoir-scale modeling is normally 1~2km, so that the upscaling issue from small to large modeling is challenging and critical subject we should solve in the near future.

Most challenge subject in physically realistic hydraulic fracturing model is finding suitable models to express complex fracture networks in naturally fractured reservoirs. Effects of the natural fractures on hydraulic fracture propagation are a critical part for the optimization of hydraulic treatment design in the naturally fractured reservoirs. The existing joints, faults and bedding planes are significantly affected to form the hydraulic fractures networks. When hydraulic fracturing path is intersected with the geological discontinuities, the hydraulic facture can be arrested, penetrating, or

branched. By the non-planar and multiple branching growth of the hydraulic fracturing, fluid flow in the fracture networks becomes complex by increasing the amount of leakoff volume.

REFERENCES

Aboustit, B. L., Advani, S. H., and Lee, J. K. (1985). "Variational principles and Finite Element simulations for Thermo-Elastic consolidation." *International Journal for Numerical Analytical Methods in Geomechanics*, 19, 49-69.

Adachi, J., and Detournay, E. (2008). "Plain strain propagation of a hydraulic fracture in permeable rock." *Engineering Fracture Mechanics*, 75(16), 4666-4694.

Adachi, J., Siebrits, E., Perice, A., and Desroches, J. (2007). "Computer simulation of hydraulic fractues." *International Journal of Rock Mechanics and Mining Sciences*, 44, 739-757.

Adams, M., and Sines, G. (1978). "Crack extension from flaws in a brittle material subjected to compression." *Tectonophysics*, 79, 97-118.

Al-Rub, R. K. A., and Darabi, M. K. (2010). "A straightforward numerical technique for finite element implementation of non-local gradient-dependent continuum damage mechanics theories " *International Journal of Theoretical and Applied Multiscale Mechanics*, 1(4), 352-385.

Bai, M., Green, S., Casas, L. A., and Miskimins, J. L. (2006). "3-D simulation of large scale laboratory hydraulic fracturing tests", ARMA, (ed.) *41st U.S. Symposium on Rock Mechanics (USRMS)*. City: Golden, Colorado USA.

Batchelor, G. K. (1967). *An introduction to fluid mechanics*, Cambridge, UK: Cambridge University Press.

Bathe, K. J. (1982). *Finite Element procedures*, New Jersey, USA: Prentice Hall.

Bazant, Z. P. (1986). "Mechanics of distributed crackings." *Applied Mechanics Review*, 39(5), 675-705.

Bazant, Z. P., and Pijaudier-Cabot, G. (1988). "Nonlocal continuum damage, localization instability and convergence." *Journal of Applied Mechanics*, 55, 287-293.

Bazant, Z. P., and Planas, J. (1997). *Fracture and size effect in concrete and other quasibrittle material*, Boca Raton, FL: CRC Press.

Belytschko, T., and Black, T. (1999). "Elastic crack growth in finite elements with minimal re-meshing." *International Journal for Numerical Methods in Engineering*, 45, 601-620.

Belytschko, T., Moës, N., Usui, S., and Parimi, C. (2001). "Arbitrary discontinuities in finite elements." *International Journal for Numerical Methods in Engineering*, 50, 993-1013.

Bieniawski, Z. (1967). "Mechanism of brittle fracture of rock part II—experimental studies." *International Journal of Rock Mechanics and Mining Sciences*, 4, 407-423.

Biot, M. A. (1941). "General theory of three-dimensional consolidation." *Journal of Applied Physics*, 12, 155-164.

Bobet, A., and Einstein, H. H. (1998). "Fracture coalescence in rock-type materials under uniaxial and biaxial compression." *International Journal of Rock Mechanics and Mining Sciences*, 35(7), 863-888.

Boone, T. J. (1989). *Simulation and visualization of hydraulic fracture propagation in poroelastic rock*, Cornell University, Ithaca, NY.

Boone, T. J., and Ingraffea, A. R. (1989). "An investigation of poroelastic effects related to hydraulic fracture propagation in rock and stress measurement techniques", in A.W.Khair, (ed.), *Rock Mechanics as a Guide for Efficienct Untilization of Natural Resources*. Rotterdam, The Netherlands: Balkema.

Boone, T. J., and Ingraffea, A. R. (1990). "A numerical procedure for simulation of hydraullcally-driven fracture propagation in poroelastic media." *International Journal for Numerical Analytical Methods in Geomechanics*, 14, 27-47.

Boone, T. J., Ingraffea, A. R., and Roegiers, J. C. (1991). "Simulation of hydraulic fracture propagation in poroelastic rock with application to stress measurement techniques." *International Journal of Rock Mechanics and Mining Sciences*, 28(1), 1-14.

Börgesson, L., Chijimatsu, M., Fujita, T., Nguyen, T. S., Rutqvist, J., and Jing, L. (2001). "Thermo-hydro-mechanical characterization of a bentonite-based buffer material by laboratory tests and numerical back analysis." *International Journal of Rock Mechanics and Mining Sciences*, 38(1), 95-104.

Brace, W. F. "Dependence of fracture strength of rocks on grain size." *Presented at the 4th Symposium on Rock Mechanics*, University Park, PA.

Budiansky, B., and O'Connell, R. J. (1976). "Elastic moduli of a cracked Solid." *International Journal of Solids and Structures*, 12(2), 81-97.

Camacho, G., and Ortiz, M. (1996). "Computational modeling of impact damage in brittle materials." *International Journal of Solids and Structures*, 33, 2899-2938.

Carrier, B., and Granet, S. (2012). "Numerical modeling of hydraulic fracture problem in permeable medium using cohesive zone model." *Engineering Fracture Mechanics*, 79, 312-328.

Christian, J. T. (1977). "Two- and three dimensional consolidation", in C. S. Desai and J. T. Christian, (eds.), *Numerical Methods In Geomechanical Engineering*. London, UK: McGraw-Hill, pp. 399-426.

Cleary, M. P. (1976). *Fundamental solutions for fluid-saturated porous media and application to localized rupture phenomena*, Brown University, Providence, RI.

Cleary, M. P. (1977). "Fundamental solutions for a fluid-saturated porous solid." *International Journal of Solids and Structures*, 13(785).

Combarnous, N. A., and Bories, S. A. (1975). "Hydrothermal convection in saturated porous media." *Advances in Hydroscience*, 10, 231-307.

Courant, R. (1943). "Variational methods for the solution of problems of equilibrium and vibration." *Bulletin of the American Mathematical Society*, 49, 1-43.

Daneshy, A. A. (1974). "Hydraulic fracture propagation in the presence of planes of weakness"*SPE-European Meeting*. City: Amsterdam, The Netherlands, pp. 1-5.

Detournay, E. (2004). "Propagation regimes of fluid-driven fractures in impermeable rocks." *International Journal of Geomechanics*, 4(1), 35-45.

Devloo, P. R. B., Rylo, E. C., and Demkowicz, L. (2002). "An HP-adaptive refinement strategy for the finite element method", H. A. Mang, F. G. Rammerstorfer, and J. Eberhardsteiner, (eds.), *Fifth World Congress on Computational Mechanics*. City: Viena, Austria.

Dyskin, A. V., Sahouryeh, E., Jewell, R. J., Joer, H., and Ustinov, K. B. (2003). " Influence of shape and locations of initial 3-D cracks on their growth in uniaxial compression." *Engineering Fracture Mechanics*, 70(15), 2115-2136.

Dyskin AV, S. E., Jewell RJ, Joer H, Ustinov KB. (2003). " Influence of shape and locations of initial 3-D cracks on their growth in uniaxial compression." *Engineering Fracture Mechanics*, 70(15), 2115-2136.

Economides, M. J., and Nolte, K. G. (2000). *Reservoir stimulation*, Chichester, NY: Wiley.

Erigen, A. C., and Edelen, D. G. B. (1972). "On nonlocal elasticity." *International Journal for Engineering Science*, 10, 233-248.

Fang, Z., and Harrison, J. P. (2002a). "Application of a local degradation model to the analysis of brittle fracture of laboratory scale rock specimens under triaxial conditions." *International Journal of Rock Mechanics and Mining Sciences*, 39, 459-476.

Fang, Z., and Harrison, J. P. (2002b). "Development of a local degradation approach to the modeling of brittle fracture in heterogeneous rocks." *International Journal of Rock Mechanics and Mining Sciences*, 39, 443-457.

Fjær, E., Holt, R. M., Horsrud, P., Raaen, A. M., and Risnes, R. (2008). *Petroleum Related Rock Mechanics 2nd Edition*: Elsevier.

Fredrich, J., Evans, B., and Wong, T. F. (1990). "Effects of grain size on brittle and semi-brittle strength, implications for micromechanical modelling of failure in compression." *Journal of Geophysical Research*, 95(B7), 10907-10920.

Garagash, D. I., and Detournay, E. (2000). "Near tip processes of a fluid-driven fracture." *Journal of Applied Mechanics*, 67, 183-192.

Geertsma, J., and Klerk, F. d. (1969). "A rapid method of predicting width and extent of hydraulic induced fractures." *Journal of Petroleum Technology*, 246, 1571-2581.

Germanovich, L. N., and Dyskin, A. V. (2000). "Fracture mechanisms and instability of openings in compression " *International Journal of Rock Mechanics and Mining Sciences*, 37(1-2), 263-284.

Ghassemi, A., Cheng, A., Diek, A., and Roegiers, J. C. (2001). "A complete plane strain fictitious stress boundary element method for poroelastic media." *Engineering Analysis with Boundary Elements*, 25, 41-48.

Ghassemi, A., and Diek, A. (2003). "Linear chemo-poroelasticity for swelling shales: theory and application." *Journal of Petroluem Science Engineering*, 38, 199-212.

Ghassemi, A., and Suárez-Rivera, R. (2012). *Sustaining fracture area and conductivity of gas shale reservoirs for enhancing long-term production and recovery*. Final Report to RPSEA Unconventional Onshore Program Under Contract 08122-48.

Ghassemi, A., Tao, Q., and Diek, A. (2009). "Influence of coupled chemo-poro-thermoelastic processes on pore pressure and stress distribution around a wellbore in swelling shale." *Journal of Petroluem Science Engineering*, 67, 57-64.

Graham, S., and Yang, N. (2003). "Representative volumes of materials based on microstructural statistics." *Scripta Materialia*, 48, 269-274.

Grebe, J., and Stoesser, M. (1935). "Increasing crude production 20,000,000 bbl from established fields." *World Petroleum J*, August(473-82).

Hallquist, J. O. (1998). "LS-DYNA theory manual". City: Livemore software technology corporation: Livermore, CA.

Harrison, J. P., and Hudson, J. A. (2000). *Engineering rock mechanics. Part 2 Illustrative workable examples*, Oxford, UK: Pergamon.

Hoek, E., and Brown, E. T. (1990). *Underground excavations in rock*, London, UK: Inst of Min and Metall, Tayor & Francis.

Huang, K., and Zhang, Z. N. (2010). "Three dimensional element partition method and numerical simulation for fracture subjected to compressive and shear stress." *Engineering Mechanics*, 27(12), 51-58.

Hughes, J. R. (1987). *The Finite Element Method - Linear Static and Dynamic FEA*, New Jersey, USA: Prentice-hall.

Irwin, G. (1958). *Fracture. in Handbuch der Physik*, Berlin - Heidelberg, Germany: Springer-Verlag.

Jaeger, J. C., Cook, N. G. W., and Zimmermann, R. W. (2007). *Fundamentals of Rock Mechanics*, London, UK: Blackwell Publishing Ltd.

Jing, L. (2003). "A review of techniques, advances and outstanding issues in numerical modelling for rock mechanics and rock engineering." *International Journal of Rock Mechanics and Mining Sciences*, 40, 283-353.

Jing, L., and Hudson, J. A. (2002). "Numerical methods in rock mechanics." *International Journal of Rock Mechanics and Mining Sciences*, 39, 409-427.

Jing, L., Stephansson, O., Rutqvist, J., Tsang, C. F., and Kautsky, F. (1993). *DECOVALEX-Mathematical models of coupled T-H-M processes for nuclear waste repositories, Phase I report*. Stockholm, Sweden.

Jing, L., Stephansson, O., Rutqvist, J., Tsang, C. F., and Kautsky, F. (1995). *DECOVALEX-Mathematical models of coupled T-H-M processes for nuclear waste repositories, Phase II report*. Stockholm, Sweden.

Jing, L., Stephansson, O., Rutqvist, J., Tsang, C. F., and Kautsky, F. (1996). *DECOVALEX-Mathematical models of coupled T-H-M processes for nuclear waste repositories, Phase III report*. Stockholm, Sweden.

Jirasek, M. (2004). "Non-local damage mechanics with application to concrete." *Revue Française de Génie Civil*, 8(5-6), 683-707.

Jirasek, M., and Zimmermann, T. (1998). "Rotating crack model with transition to scalar damage." *Journal of Engineering Mechanics*, 124(3), 277-284.

Kachanov, L. M. (1986). *Introduction to continuum damage mechanics*, Hingham, MA: Martinus Nijhoff Publishers.

Khoei, A. R., Azadi, H., and Moslemi, H. (2008). "Modeling of crack propagation via an automatic adaptive mesh refinement based on modified superconvergent patch recovery technique." *Engineering Fracture Mechanics*, 75, 2921-2945.

Khristianovic, S., and Zheltov, Y. (1955). "Formation of vertical fractures by means of highly viscous fluids"*4th World Petroleum Congress*. City: Rome, Italy, pp. 579-586.

Krajcinovic, D. (1989). "Damage Mechanics." *Mechanics of Materials*, 8, 117-197.

Krajcinovic, D. (2000). "Damage mechanics: accomplishments, trends and needs." *International Journal of Solids and Structures*, 37, 267-277.

Krajcinovic, D., and Fonseka, G. V. (1981). "The continuous damage theory of brittle material." *Journal of Applied Mechanics*, 48, 809-815.

Kunin, I. A. (1968). "The Theory of Elastic Media with Microstructure and the Theory of Dislocations", in E. Kroger, (ed.), *Mechanics of General Continua*. Heidelberg, Germany: Springer-Verlag, pp. 321-328.

Kurashige, M. (1989). "A thermoelastic theory of fluid-filled porous materials." *International Journal of Solids and Structures*, 25(9), 1039-1052.

Lajtai, E. Z. (1973). "Brittle fracture in compression." *International journal of Fracture*, 10, 525-536.

Lamont, N., and Jessen, F. W. (1963). "The effects of existing fractures in rocks on the extension of hydraulic fractures." *SPE*, 419, 203-209.

Lee, S. H. (2011). *Thermo-Poroelastic Modeling of Reservoir Stimulation and Microseismicity using Finite Element Method with Damage Mechanics* Ph.D dissertation, Texas A&M University, College Station, TX.

Lee, S. H., and Ghassemi, A. (2010). " Themo-poroelastic analysis of injection-induced rock deformation and damage evolution"*Stanford Geothermal Workshop*. City: Stanford University, CA.

Lemaitre, J. (1984). "How to use Damage Mechanics." *Nuclear Engineering and Design*, 80(2), 233-245.

Li, X. (1998). *Thermoporomechanical Modelling of Inclined Boreholes*, University of Oklahoma, Norman, OK.

Liu, H. Y., Roquete, M., Kou, S. Q., and Lindqvist, P. A. (2004). "Characterization of rock heterogeneity and numerical verification." *Engineering Geology*, 72, 89-119.

Loehner, R. (2001). *Applied CFD techniques: an introduction based on finite element methods*, New York: Wiley.

Lubarda, V., and Krajcinovic, D. (1993). "Damage tensors and the crack density distribution." *International Journal of Solids and Structures*, 30(20), 2859-2877.

Mahabadi, O. K., Randall, N. X., Zong, Z., and Grasselli, G. (2012). "A novel approach for micro-scale characterization and modeling of geomaterials incorporating actual material heterogeneity." *Geophysical Research Letters*, 39(L01303).

Mazars, J., and Pijaudier-Cabot, G. (1989). "Continuum damage theory: application to concrete." *Journal of Engineering Mechanics*, 115(2), 345-365.

McTigue. (1986). "Thermoelastic response of fluid-saturated porous rock." *Journal of Geophysical Research*, 91, 9533-9542.

Millard, A. (1996). "Short description of CASTEM 2000 and TRIO-EF." *Developments in Geotechnical Engineering*, 79, 559-564.

Min, K. S., and Ghassemi, A. (2011). "A three-dimensional numerical analysis of thermal fracturing in rock "*45th US Rock Mechanics / Geomechanics Symposium* City: San Francisco, CA.

Min, K. S., Huang, K., and Ghassemi, A. (2011). "A study of numerical simulations of mixed-mode fracture propagation in rock "*Thirty-Sixth Workshop on Geothermal Reservoir Engineering*. City: Stanford University, CA.

Mogi, K. (2007). *Experimental Rock Mechanics*, London, UK: Taylor & Francis.

Nguyen, V. P., Rabczuk, T., Bordas, S., and Duflot, M. (2008). "Meshless methods: A review and computer implementation aspects." *Mathematics and Computers in Simulation*, 79, 763-813.

Noorishad, J., and Tsang, C. F. (1996). "Coupled thermohydroelasticity phenomena in variably saturated fractured porous rock - formation and numerical solution", in O. Stephansson, L. Jing, and C. F. Tsang, (eds.), *Coupled Thermo-Hydro-Mechanical processes of Fractured Media*. Amsterdam, The Netherlands: Elsevier Science.

Noorishad, J., Tsang, C. F., and Witherspoon, P. A. (1992). "Theoretical and field studies of coupled hydromechanical behaviour of fractured rocks—1. Development and verification of a numerical simulator." *International Journal of Rock Mechanics and Mining Sciences*, 29(4), 401-409.

Nordgren, R. (1972). "Propagation of vertical hydraulic fractures." *Journal of Petroleum Technology*, 253(306-314).

Palciauskas, V. V., and Domenico, P. A. (1982). "Characterization of drained and undrained response of thermally loaded respository rocks." *Water Resources Research*, 18, 281-290.

Pan, E., and Maier, G. (1997). "A symmetric integral approach to transient poroelastic analysis." *Computation Mechanics*, 19, 169-178.

Pande, G. N., Beer, G., and Williams, J. R. (1990). *Numerical methods in rock mechanics*, Chichester, UK: Wiley.

Pandolfi, A., Guduru, P. R., Ortiz, M., and Rosakis, A. J. (2000). "Three dimensional cohesive-element analysis and experiments of dynamic fracture in C300 steel." *International Journal of Solids and Structures*, 37, 3733-3760.

Papanastasious, P. (1997). "The influence of plasticity in hydraulic fracturing." *International Journal of Fracture*, 84, 61-79.

Paris, P., and Erdogan, F. (1963). " A critical analysis of crack propagation laws." *Journal of Basic Engineering*, 85, 528-534.

Park, K., Pereira, J. P., Duarte, C. A., and Paulino, G. H. (2009). "Integration of singular enrichment functions in the generalized/extended finite element method for three-dimensional problem." *International Journal for Numerical Methods in Engineering*, 78, 1220-1257.

Perkins, T., and Kern, L. (1961). "Widths of hydraulic fractures." *Journal of Petroleum Technology*, 222(937-949).

Picard, E. (1890). *Jour. de Math*, 4(6), 145-210.

Pijaudier-Cabot, G., and Bazant, Z. P. (1987). "Nonlocal damage theory." *Journal of Engineering Mechanics*, 113(10).

Pratt, M. (1982). *Thermal Recovery*: Society of Petroleum Engineers.

Rabczuk, T., Bordas, S., and Zi, G. (2007). "A three-dimensional meshfree method for continuous multiple-crack initiation, propagation and junction in statics and dynamics." *Computation Mechanics*, 40, 473-495.

Rabczuk, T., Bordas, S., and Zi, G. (2008). "A three-dimensional modelling of crack growth using partition of unity methods." *Computers and Structures*.

Regehr, M. (2012). "A reservoir and geomechanical model of the Colorado Shale, Western Canadian sedimentary basin"*SPWLA topical conference*. City: Houston, TX.

Renshaw, C. E., and Pollard, D. D. (1994). "Numerical simulation of fracture set formation: a fracture mechanics model consistent with experimental observations." *Journal of Geophysical Research*, 99, 9359-9372.

Rice, J. R., and Cleary, M. P. (1976). "Some basic stress-diffusion solutions for fluid saturated elastic porous media with compressible constituents." *Reviews of Geophysics*, 14, 227-241.

Rutqvist, J., Börgesson, L., Chijimatsu, M., Kobayashi, A., Jing, L., Nguyen, T. S., Noorishad, J., and Tsang, C. F. (2001). "Thermohydro-mechanics of partially saturated geological media: governing equations and formulation of four finite element models." *International Journal of Rock Mechanics and Mining Sciences*, 38(1), 105-127.

Sagong, M. (2001). *The study on the fracture of multiple flaw specimens*, Purdue University, West Lafayette, IN USA.

Samieh, A., and Wong, R. (1997). "Deformation of Athabasca oil sand at low elective stresses under varying boundary conditions." *Canadian Geotechnical Journal*, 34, 985-990.

Sarris, E., and Papanastasiou, P. (2012). "Modeling of hydraulic fracturing in a poroelastic cohesive formation." *International Journal of Geomechanics*, 12, 160-167.

Sarris, E., and Papanastasious, P. (2011). "The influence of the cohesive process zone in hydraulic fracturing modelling." *International Journal of Fracture*, 167, 33-45.

Schrefler, B. A. (2001). "Computer modelling in environmental geomechanics." *Computers and Structures*, 79, 2209-2223.

Settari, A. (1989). "Physics and modeling of thermal flow and solid mechanics in unconsolidated porous media" *SPE Symposium On Reservoir Simulation*. City: SPE: Houston, TX, pp. 155-166.

Skempton, A. W. (1954). "The pore pressure coefficients a and b." *Geotechnique*, 4, 143-147.

Smith, M. B., and Shlyapobersky, J. W. (2000). "Basics of hydraulic fracturing", in M. J. Economides and K. G. Nolte, (eds.), *Reservoir Stimulation*. Chichester, UK: John Wiley & Sons Ltd, pp. 5-1,5-29.

Sneddon, I. N. (1946). "The distribution of stress in the neighbourhood of a crack in an elastic solid." *Proceedings of the Royal Society of London. Series A, Mathematical and Physical*, 187(1009), 229-260.

Sneddon, I. N., and Elliott, H. A. (1946). "The opening of a Griffith crack under internal pressure." *Applied Mechanics Review*, 4, 262-268.

Song, J.-H., Wang, H., and Belytschko, T. (2008). "A comparative study on finite element methods for dynamic fracture." *Computation Mechanics*, 42, 239-250.

Stephansson, O., Jing, L., and Tsang, C. F. (1996). *Coupled Thermo-Hydro-Mechanical Processes of Fractured Media*: Elsevier Science.

Taleghani, A. D. (2009). *Analysis of hydraulic fracture propagation in fractured reservoirs: an improved model for the interaction between induced and natural fractures*, University of Texas at Austin, Austin, TX.

Tang, C. A., and Hudson, J. A. (2011). *Rock Failure Mechanism*, London, UK: Tayler & Francis.

Tang, C. A., Jiu, H., Lee, P. K. K., Tsui, Y., and Tham, L. G. (2000). "Numerical studies of the influence of microstructure on rock failure in uniaxial compression—part I: effect of heterogeneity." *International Journal of Rock Mechanics and Mining Sciences*, 37, 555-569.

Tang, C. A., Tham, L. G., Lee, P. K. K., Yang, T. H., and Li, L. C. (2002). "Coupled Analysis of flow, stress and damage (FSD) in rock failure." *International Journal of Rock Mechanics and Mining Sciences*, 39, 1231-47.

Tarasovs, S., and Ghassemi, A. (2010). "A study of propagation of cooled cracks in a geothermal reservoir"*Geothermal Resources Council Annual Meeting*. City: Sacramento, CA.

Terzaghi, K. (1923). "Die berechnug der Durchlässigkeitsziffer des Tones aus dem Verlauf der hydrodynamischen Spannungserscheinungen." *Sitzungsber Akad Wiss Math-Naturwiss Section IIa*, 132(3/4), 125-138.

Tester, J. W., Murphy, H. D., Grlgsby, C. O., Potter, R. M., and Robinson, B. A. (1989). "Fractured geothermal reservoir growth Induced by heat extraction." *SPE Reservoir Engineering*, 4(1), 97-104.

Teufel, L. W., and Clark, J. A. (1984). "Hydraulic fracture propagation in layered rock: experimental studies of fracture containment." *SPE* (9878), 19-32.

Tsang, C. F. (1987). *Coupled processes associated with nuclear waste repositories*, New York, USA: Academic Press.

Tsang, C. F. (1991). "Coupled hydromechanical-thermochemical processes in rock fractures." *Reviews of Geophysics*, 29(4), 537-551.

Tsang, C. F., Stephansson, O., Kautsky, F., and Jing, L. (2004). "Coupled THM processes in geological systems and the DECOVALEX project", in O. Stephansson, J. A. Hudson, and L. Jing, (eds.), *Coupled Thermo-Hydro-Mechanical-Chemical Processes in Geo-systems*. Oxford, UK: Elsevier.

Voyiadjis, G. Z., and Kattan, P. I. (2009). "A comparative study of damage variables in continuum damage mechanics." *International Journal of Damage Mechanics*, 18(315).

Wang, J., Jung, W., and Ghassemi, A. (2012a). "Deformation and failure properties of Newberry welded Tuff"*46th US Rock Mechanics / Geomechanics Symposium*. City: Chicago, IL.

Wang, J., Jung, W., and Ghassemi, A. (2012b). *Petrophysical and rock mechanical properties of rock from Newberry. DOE Annual report*. Department of Petroleum Engineering at Texas A&M University College Station, TX.

Wang, J. S. Y., and Narasimhan, T. N. (1985). "Hydrologic mechanisms governing fluid flow in a partially saturated, fractured, porous medium." *Water Resources Research*, 21, 1861-1874.

Wang, Y., Yin, X., Ke, F., Xia, M., and Peng, K. (2000). "Numerical simulation of rock failure and earthquake process on mesoscopic scale." *Pure Appl Geophys*, 157, 1905-1928.

Weibull, W. (1939). "A statistical theory of the strength of materials." *Ing Vetenskaps Akad Handl*, 151, 5-44.

Weibull, W. (1951). "A statistical distribution function of wide applicability." *Journal of Applied Mechanics*, 18, 293-7.

Witherspoon, P. A., Wang, J. S. Y., Iwai, K., and Gale, J. E. (1980). "Validity of cubic law for fluid flow in a deformable rock fracture." *Water Resources Research*, 16(6), 1016-1024.

Wong, L. N. Y., and Einstein, H. H. (2009). "Systematic evaluation of cracking behavior in specimens containing single flaws under uniaxial compression." *International Journal of Rock Mechanics and Mining Sciences*, 46, 239-249.

Wong, T., H., R., Wong, C., Chau, K. T., and Tang, C. A. (2006). "Microcrack statistics, Weibull distribution and micromechanical modeling of compressive failure in rock." *Mechanics of Materials*, 38, 664-681.

Wulf, J., Schamuder, S., and Fishmeister, H. F. (1993). "Finite element modelling of crack propagation in ductile fracture." *Computational Materical Science*, 1, 297-301.

Xu, X.-P., and Needleman. (2006). "Numerical simulation of fast crack growth in brittle solids." *Journal of Mechanics, Physics, Solids*, 42, 1397-1434.

Yamamoto, K., Gutierrez, M., Shimamoto, T., and Maezumi, S. (2000). "Verification of a 3D hydraulic fracturing model against a field case"*SPE/DOE Improved Oil Recovery Symposium*. City: Tulsa, OK, pp. SPE 59373.

Yuan, S. C., and Harrison, J. P. (2005). "Development of a hydro-mechanical local degradation approach and its application to modelling fluid flow during progressive fracturing of heterogeneous rocks." *International Journal of Rock Mechanics and Mining Sciences*, 42, 961-984.

Zhang, Z. N., and Chen, Y. (2008). "Simulation of fracture propagation subjected to compressive and shear stress field using virtual multidimensional internal bonds." *International Journal of Rock Mechanics and Mining Sciences*, 46, 1010-1022.

Zhou, X., and Ghassemi, A. (2009). "Finite Element analysis of coupled chemo-poro-thermo-mechanical effects around a wellbore in swelling shale." *International Journal of Rock Mechanics and Mining Sciences*, 46, 769-778.

Zi, G., and Belytschko, T. (2003). "New crack-tip elements for XFEM and applications to cohesive cracks." *International Journal for Numerical Method in Engineering*, 57, 2221-2240.

Zienkiewicz, O. C., and Taylor, R. L. (1967). *The Finite Element Method for Solid and Structural Mechanics*, London, UK: McGraw-Hill.

Zoback, M. D., Rummel, F., Jung, R., and Raleigh, C. B. (1977). "Laboratory hydraulic fracturing experiments in Intact and pre-fractured rock." *International Journal of Rock Mechanics*, 14, 49-58.

APPENDIX A

FINITE ELEMENT FORMULATION FOR THE COUPLED T-H-M EQUATIONS

A.1 Basic of Finite Element Method

The finite element method has been developed and remarkably advanced by several researchers (Bathe 1982; Courant 1943; Hughes 1987; Zienkiewicz and Taylor 1967), so that it has become the most popular method in engineering fields. In FEM analysis, three steps are required: domain discretization, local approximation, and assembly in the global matrix equation.

In this section, the procedure of FEM analysis is briefly reviewed using a quadrilateral element. A domain in equilibrium state is discretized by a four-node quadrilateral finite-element mesh, as depicted in Figure A.1. Nodal values can be approximated through a trial function in a polynomial form:

$$u_i^e = \sum_{j=1}^{4} \mathbf{N}_j \overline{u}_j \tag{A.1}$$

where $\mathbf{N}_j$ is the matrix of finite-element shape functions defined in intrinsic coordinates to use Gaussian quadrature integration.

$$\mathbf{N}_j = \begin{bmatrix} N_j & 0 \\ 0 & N_j \end{bmatrix} \tag{A.2}$$

Also, the strain field can be calculated as:

$$\varepsilon = \sum_{j=1}^{4} \mathbf{B}_j \overline{u}_j \tag{A.3}$$

where the geometry matrix $\mathbf{B}_j$ is defined in terms of derivatives of the shape functions N_j:

$$\mathbf{B}_j = \begin{bmatrix} \dfrac{\partial N_j}{\partial x} \\ 0? \dfrac{\partial N_j}{\partial y} \\ \dfrac{\partial N_j}{\partial y} \dfrac{\partial N_j}{\partial x} \end{bmatrix} \tag{A.4}$$

Using the chain rule, the coefficients of B_j are approximated as:

$$\begin{Bmatrix} \dfrac{\partial N}{\partial x} \\ \dfrac{\partial N}{\partial y} \end{Bmatrix} = \mathbf{J}^{-1} \begin{Bmatrix} \dfrac{\partial N}{\partial \xi} \\ \dfrac{\partial N}{\partial \eta} \end{Bmatrix} \tag{A.5}$$

where $\mathbf{J}$ is the Jacobian matrix.

$$\mathbf{J} = \begin{bmatrix} \dfrac{\partial x}{\partial \xi} & \dfrac{\partial y}{\partial \xi} \\ \dfrac{\partial x}{\partial \eta} & \dfrac{\partial y}{\partial \eta} \end{bmatrix} \qquad \mathbf{J}^{-1} = \frac{1}{\det \mathbf{J}} \begin{bmatrix} \dfrac{\partial x}{\partial \xi} & \dfrac{\partial y}{\partial \xi} \\ -\dfrac{\partial x}{\partial \eta} & \dfrac{\partial y}{\partial \eta} \end{bmatrix} \tag{A.6}$$

The element stiffness matrix, $\mathbf{K}_e$ of an element can be determined:

$$\mathbf{K}_e = \int_{V_e} \mathbf{B}^{\mathbf{T}} \mathbf{D}_m \mathbf{B} dV \tag{A.7}$$

where $\mathbf{D}_m$ is the material stiffness matrix, which can be rewritten in local curvilinear coordinate ξ, η:

$$\mathbf{K} = \int_{-1}^{1} \int_{-1}^{1} \mathbf{B}(\xi,\eta)^T \mathbf{D}_m \mathbf{B}(\xi,\eta) (\det \mathbf{J}) d\xi d\eta \tag{A.8}$$

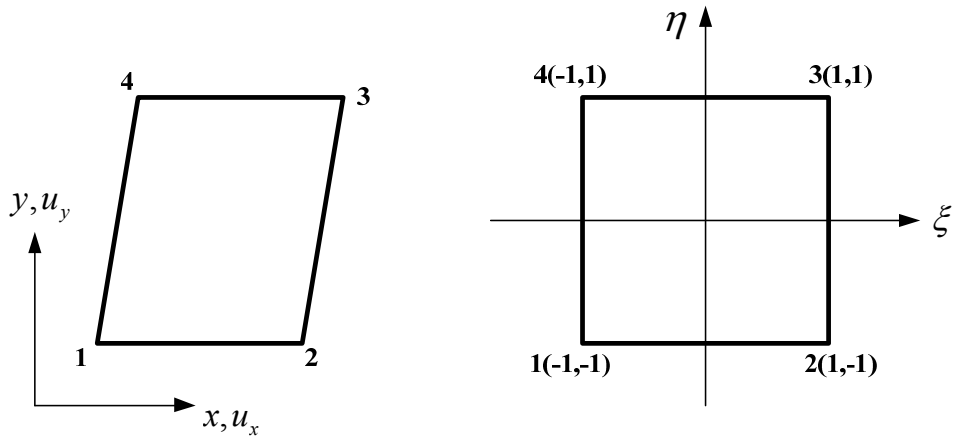

Figure A.1 Four nodes quadrilateral element in global and local curvilinear coordinates.

A.2 FEM Implementation for Thermo-Hydro-Mechanical processes

For the fully coupled Thermo-Hydro-Mechanical model, following field equations could be written;

$$\left(K+\frac{G}{3}\right)\nabla\left(\nabla\cdot\mathbf{u}\right)+G\nabla^2\mathbf{u}+\mathbf{m}\left(\alpha\nabla p+\gamma_1\nabla T\right)=0 \tag{A.9}$$

$$\alpha\left(\nabla\cdot\dot{\mathbf{u}}\right)+\beta_p\dot{p}-\frac{k}{\mu}\nabla^2 p-\gamma_2\nabla\dot{T}=0 \tag{A.10}$$

$$\dot{T}-c^2\nabla^2 T=0 \tag{A.11}$$

where **u** is displacement vector and **m**=$[1,1,1,0,0,0]^{\mathrm{T}}$ for 3D problems. The coefficients in Eqn. (A.9) and (A.10) are defined as following;

$$\beta_p=\frac{\alpha-\phi}{K_s}+\frac{\phi}{K_f} \tag{A.12}$$

$$\gamma_1=K\alpha_m \tag{A.13}$$

$$\gamma_2 = \alpha\alpha_m + \left(\alpha_f - \alpha_m\right)\phi \tag{A.14}$$

A.2.1 Spatial discretization

The field equations (A.7), (A.8) and (A.9) can be discretized in the solution domain into an assembly of elements, approximate the displacements, pore pressure, and temperature within each element from nodal values via spatial interpolation functions. Field variables could be described as:

$$\mathbf{u} = \mathbf{N}_u \bar{\mathbf{u}} \tag{A.15}$$

$$\mathbf{p} = \mathbf{N}_p \bar{\mathbf{p}} \tag{A.16}$$

$$\mathbf{T} = \mathbf{N}_T \bar{T} \tag{A.17}$$

Then nodal values of displacement, pore pressure, and temperature are expressed as:

$$\bar{\mathbf{u}} = \left[\begin{array}{cccccc} \bar{u}_x^1 & \bar{u}_y^1 & \bar{u}_z^1 & \ldots & \bar{u}_x^n & \bar{u}_y^n & \bar{u}_z^n \end{array}\right]^T \tag{A.18}$$

$$\bar{\mathbf{p}} = \left[\begin{array}{ccc} \bar{p}^1 & \ldots & \bar{p}^n \end{array}\right]^T \tag{A.19}$$

$$\bar{\mathbf{T}} = \left[\begin{array}{ccc} \bar{T}^1 & \ldots & \bar{T}^n \end{array}\right]^T \tag{A.20}$$

And shape function matrices are represented as:

$$\mathbf{N}_u = \left[\begin{array}{cccccc} N_u^1 & 0 & 0 & \ldots N_u^n & 0 & 0 \\ 0 & N_u^1 & 0 & \ldots 0 & N_u^n & 0 \\ 0 & 0 & N_u^1 & \ldots 0 & 0 & N_u^n \end{array}\right] \tag{A.21}$$

$$\mathbf{N}_p = \left[\begin{array}{ccc} N_p^1 & \ldots & N_p^n \end{array}\right] \tag{A.22}$$

$$\mathbf{N}_T = \left[\begin{array}{ccc} N_T^1 & \ldots & N_T^n \end{array}\right] \tag{A.23}$$

So, the gradient relationships can be expressed as:

$$\varepsilon = \mathbf{B}_u \left\{ \overline{\mathbf{u}} \right\} \tag{A.24}$$

$$\nabla p = \mathbf{B}_p \left\{ \overline{\mathbf{p}} \right\} \tag{A.25}$$

$$\nabla T = \mathbf{B}_T \left\{ \overline{\mathbf{T}} \right\} \tag{A.26}$$

The gradients matrices, $\mathbf{B}_u$, $\mathbf{B}_p$, and $\mathbf{B}_T$ are expressed as:

$$\mathbf{B}_u = \begin{bmatrix} \frac{\partial N_u^1}{\partial x} & 0 & 0 & \cdots & \frac{\partial N_u^n}{\partial x} & 0 & 0 \\ 0 & \frac{\partial N_u^1}{\partial y} & 0 & \cdots & 0 & \frac{\partial N_u^n}{\partial y} & 0 \\ 0 & 0 & \frac{\partial N_u^1}{\partial z} & \cdots & 0 & 0 & \frac{\partial N_u^n}{\partial z} \\ \frac{\partial N_u^1}{\partial y} & \frac{\partial N_u^1}{\partial x} & 0 & \cdots & \frac{\partial N_u^n}{\partial y} & \frac{\partial N_u^n}{\partial x} & 0 \\ 0 & \frac{\partial N_u^1}{\partial z} & \frac{\partial N_u^1}{\partial y} & \cdots & 0 & \frac{\partial N_u^n}{\partial z} & \frac{\partial N_u^n}{\partial y} \\ \frac{\partial N_u^1}{\partial z} & 0 & \frac{\partial N_u^1}{\partial z} & \cdots & \frac{\partial N_u^n}{\partial z} & 0 & \frac{\partial N_u^n}{\partial z} \end{bmatrix} \tag{A.27}$$

$$\mathbf{B}_p = \begin{bmatrix} \frac{\partial N_p^1}{\partial x} & \cdots & \frac{\partial N_p^n}{\partial x} \\ \frac{\partial N_p^1}{\partial y} & \cdots & \frac{\partial N_p^n}{\partial y} \\ \frac{\partial N_p^1}{\partial z} & \cdots & \frac{\partial N_p^n}{\partial z} \end{bmatrix} \tag{A.28}$$

$$\mathbf{B}_T = \begin{bmatrix} \dfrac{\partial N_T^1}{\partial x} & \cdots & \dfrac{\partial N_T^n}{\partial x} \\ \dfrac{\partial N_T^1}{\partial y} & \cdots & \dfrac{\partial N_T^n}{\partial y} \\ \dfrac{\partial N_T^1}{\partial z} & \cdots & \dfrac{\partial N_T^n}{\partial z} \end{bmatrix} \tag{A.29}$$

Substituting Eqn. (A.22), (A.23), (A.24) into the above field equations (A.7), (A.8), (A.9), and then using Galerkin's method the FEM for the fully coupled thermo-hydro-mechanical (THM) model can be written as:

$$\mathbf{K}\dot{\mathbf{u}} + \mathbf{A}\dot{\mathbf{p}} + \mathbf{V}\dot{\mathbf{T}} = \dot{\mathbf{F}}_u \tag{A.30}$$

$$\mathbf{A}^{\mathbf{T}}\dot{\mathbf{u}} + \mathbf{S}\dot{\mathbf{p}} + \mathbf{H}_{\mathbf{H}}\mathbf{p} + \mathbf{N}\dot{\mathbf{T}} = \mathbf{F}_q \tag{A.31}$$

$$\mathbf{R}\dot{\mathbf{T}} + \mathbf{U}\mathbf{T} = \mathbf{F}_h \tag{A.32}$$

where,

$$\mathbf{K} = \int_{V_e} \mathbf{B}_u^{\mathbf{T}} \mathbf{D}_m \mathbf{B}_u dV \tag{A.33}$$

$$\mathbf{A} = \int_{V_e} \mathbf{B}_u^{\mathbf{T}} \alpha \mathbf{m} \mathbf{N}_{\mathbf{p}} dV \tag{A.34}$$

$$\mathbf{V} = \int_{V_e} \mathbf{B}_u^{\mathbf{T}} \gamma_1 \mathbf{m} \mathbf{N}_{\mathbf{T}} dV \tag{A.35}$$

$$\mathbf{S} = \int_{V_e} \mathbf{N}_p^T \beta_p \mathbf{N}_p dV \tag{A.36}$$

$$\mathbf{N} = \int_{V_e} \mathbf{N}_p^T \gamma_2 \mathbf{N}_T dV \tag{A.37}$$

$$\mathbf{H}_{\mathbf{H}} = \int_{V_e} \left(\nabla \mathbf{N}_p\right)^T \left(k/\eta\right) \left(\nabla \mathbf{N}_p\right) dV \tag{A.38}$$

$$\mathbf{R} = \int_{V_e} \mathbf{N}_T^T \mathbf{N}_T dV \tag{A.39}$$

$$\mathbf{U} = \int_{V_e} \left(\nabla \mathbf{N}_T\right)^T c^T \left(\nabla \mathbf{N}_T\right) dV \tag{A.40}$$

where V_e is the spatial area of an element, $\mathbf{F}_u$ is the external applied loads, and $\mathbf{B}_u$ is the strain-displacement matrix. Since the coupled nonlinear non-symmetric equations are time dependent, they need to be integrated in time to make them ready for linear factorization in matrix form. Also, proper incremental matrix formations are required for the strongly nonlinear problem, because previous matrix equations can only produce one increment of change from equilibrium. Therefore, based on the solution of the first-order time-dependent, integrating process is performed between t_1 and $t_2=t_1+dt$.

A.2.2 Temporal discretization

Adopting the first-order temporal discretization, the filed variables can be expressed as:

$$\bar{\mathbf{u}} = \theta_t \mathbf{u}_2 + \left(1-\theta_t\right)\mathbf{u}_1 \tag{A.41}$$

$$\bar{\mathbf{p}} = \theta_t \mathbf{p}_2 + \left(1-\theta_t\right)\mathbf{p}_1 \tag{A.42}$$

$$\bar{\mathbf{T}} = \theta_t \mathbf{T}_2 + \left(1-\theta_t\right)\mathbf{T}_1 \tag{A.43}$$

where $\theta_t=(t_2-t_1)/\Delta t$, when $\theta_t=0$, 1/2, 2/3, and 1 the corresponding schemes are an explicit, Crank-Nicolson, Galerkin or an implicit schemes respectively.

$$\mathbf{K}\left(\mathbf{u}_2-\mathbf{u}_1\right)+\mathbf{A}\left(\mathbf{p}_2-\mathbf{p}_1\right)+\mathbf{V}\left(\mathbf{T}_2-\mathbf{T}_1\right)=\mathbf{F}_2-\mathbf{F}_1 \tag{A.44}$$

$$\mathbf{A}^{\mathbf{T}}\left(\mathbf{u}_2-\mathbf{u}_1\right)+\mathbf{S}\left(\mathbf{p}_2-\mathbf{p}_1\right)+\Delta t\mathbf{H}_{\mathbf{H}}\bar{\mathbf{p}}+\mathbf{N}\left(\mathbf{T}_2-\mathbf{T}_1\right)=\Delta t\mathbf{F}_q \tag{A.45}$$

$$\mathbf{R}\left(\mathbf{T}_2-\mathbf{T}_1\right)+\Delta t\mathbf{U}\bar{\mathbf{T}}=\Delta t\mathbf{F}_h \tag{A.46}$$

Then, all average nodal values over integration time are marked as $\bar{\mathbf{u}}$, $\bar{\mathbf{p}}$, $\bar{\mathbf{T}}$, In their final form, the equations above are represented as:

$$\mathbf{K}\Delta\mathbf{u}+\mathbf{A}\Delta\mathbf{p}+\mathbf{V}\Delta\mathbf{T}=\Delta\mathbf{F} \tag{A.47}$$

$$\mathbf{A}^{\mathbf{T}}\Delta\mathbf{u}+\mathbf{S}\Delta\mathbf{p}+\theta_t\mathbf{H}_{\mathbf{H}}\Delta\mathbf{p}+\mathbf{N}\Delta\mathbf{T}=-\Delta t\mathbf{H}_{\mathbf{H}}\mathbf{p}_1 \tag{A.48}$$

$$\mathbf{R}\Delta\mathbf{T}+\theta_t\Delta t\mathbf{U}\Delta\mathbf{T}=-\Delta t\mathbf{U}\mathbf{T}_1 \tag{A.49}$$

Finally, the finite element formulation is obtained by temporal discretization considering the total stress, σ_{ij} for tensile positive, pore pressure, p, for compressive positive, and temperature, T, as the coupled variables.

$$\begin{bmatrix} \mathbf{K} & -\mathbf{A} & \mathbf{V} \\ -\mathbf{A}^{T} & -\left(\mathbf{S}+\theta_t\Delta t\mathbf{H}_{\mathbf{H}}\right) & \mathbf{N} \\ \mathbf{0} & \mathbf{0} & -\left(\mathbf{R}+\theta_t\Delta t\mathbf{U}\right) \end{bmatrix} \begin{Bmatrix} \Delta\mathbf{u} \\ \Delta\mathbf{p} \\ \Delta\mathbf{T} \end{Bmatrix} = \begin{Bmatrix} \Delta\mathbf{f} \\ \Delta t\mathbf{H}_{\mathbf{H}}\mathbf{p}\left(t_{n-1}\right) \\ \Delta t\mathbf{U}\mathbf{T}\left(t_{n-1}\right) \end{Bmatrix} \tag{A.50}$$

Now, we can solve these equations directly in incremental solution forms using linearization schemes. However, the coupled, nonlinear, and non-symmetric nature of the equations might be necessarily required iterative solution at each time-matching step to get the solution to convergence.

The fully coupled Thermo-Hydro-Mechanical processes by three partial differential equations of equilibrium, fluid flow and heat transfer are solved simultaneously through the general matrix form. Since the problem is time dependent, state variables are incremental values. Stiffness matrix is controlled by 'damage parameter' for each of the elements individually. The finite element formulations and the hydraulic fracturing modeling were coded in a computer program using FORTRAN language.

APPENDIX B

2D EQUIVALENT NODAL FORCES INDUCED BY HYDRAULIC PRESSURE

Element Partition Methodology (EPM) is used to calculate a hydraulic fracturing path inside elements and evaluate equivalent nodal forces induced by hydraulic pressurization. In this method, the hydraulic fracturing path can be described by splitting of the crack elements using given fracturing path in Finite Element Method (FEM). For numerical simplification, linear triangular element is used for 2D EPM and few assumptions are made. First, there is only one fracture plane available in each crack element. Second, the fracture plane inside the crack element is linear. Third, the fracturing path is propagated through surface (not through nodes) of the crack element. So, there are two basic processes necessary to describe the equivalent nodal forces. Identifying process for the fracture plane inside the crack element and computing process for the equivalent nodal forces at nodes of the crack element.

B.1 Identifying fracture plane inside element

In Figure B.1, coordinates of 2D line crack path were given in $C_1\left(x_{c1}, y_{c1}\right)$ and $C_2\left(x_{c2}, y_{c2}\right)$. Then, intersection points $\left(P_{x1}, P_{y1}\right)$ and $\left(P_{x2}, P_{y2}\right)$ can be calculated by following relations:

$$P_{x1} = \left(\frac{\left(x_{c1}y_{c2} - y_{c1}x_{c2}\right)\left(x_i - x_k\right) - \left(x_{c1} - x_{c2}\right)\left(x_i y_k - y_i x_k\right)}{\left(x_{c1} - x_{c2}\right)\left(y_i - y_k\right) - \left(y_{c1} - y_{c2}\right)\left(x_i - x_k\right)} \right) \tag{B.1}$$

$$P_{y1}=\left(\frac{\left(x_{c1}y_{c2}-y_{c1}x_{c2}\right)\left(y_i-y_k\right)-\left(y_{c1}-y_{c2}\right)\left(x_iy_k-y_ix_k\right)}{\left(x_{c1}-x_{c2}\right)\left(y_i-y_k\right)-\left(y_{c1}-y_{c2}\right)\left(x_i-x_k\right)}\right) \tag{B.2}$$

$$P_{x2}=\left(\frac{\left(x_{c1}y_{c2}-y_{c1}x_{c2}\right)\left(x_j-x_k\right)-\left(x_{c1}-x_{c2}\right)\left(x_jy_k-y_jx_k\right)}{\left(x_{c1}-x_{c2}\right)\left(y_j-y_k\right)-\left(y_{c1}-y_{c2}\right)\left(x_j-x_k\right)}\right) \tag{B.3}$$

$$P_{y2}=\left(\frac{\left(x_{c1}y_{c2}-y_{c1}x_{c2}\right)\left(y_j-y_k\right)-\left(y_{c1}-y_{c2}\right)\left(x_jy_k-y_jx_k\right)}{\left(x_{c1}-x_{c2}\right)\left(y_j-y_k\right)-\left(y_{c1}-y_{c2}\right)\left(x_j-x_k\right)}\right) \tag{B.4}$$

After calculating the intersection points, a fracture length can be described as:

$$C_L^{\,e}=\sqrt{\left(P_{x2}-P_{x1}\right)^2+\left(P_{y2}-P_{y1}\right)^2} \tag{B.5}$$

where $C_L^{\,e}$ is the fracture length inside an element.

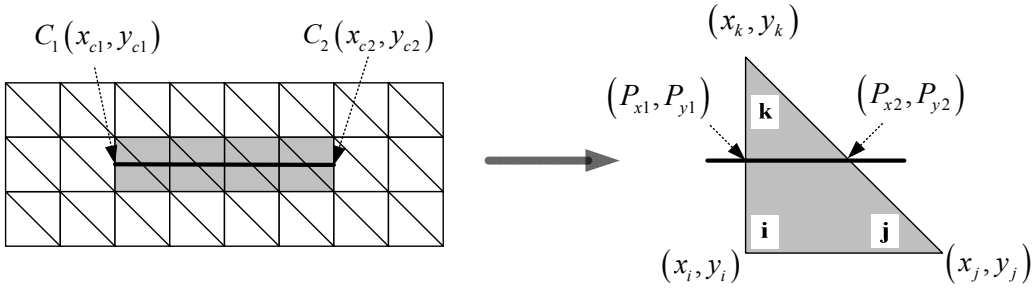

Identifying crack elements Calculating fracture plane

Figure B.1 Schematic of identifying process for fracture plane inside element

B.2 Computing process for equivalent nodal forces by hydraulic pressurization

In Figure B.2, average fluid pressure acting inside the crack element can be defined as:

$$p_f{}^e = \frac{p_f{}^i + p_f{}^j + p_f{}^k}{3} \tag{B.6}$$

where $p_f{}^i, p_f{}^j, p_f{}^k$ are fluid pressure at each node of the crack element. Then, the equivalent nodal forces are computed using the average fluid pressure and following equations:

$$F_x^i = p_f{}^e \left[\frac{(y_j - y_k)}{3} + \frac{(y_j - y_x)}{6} + \frac{(y_i - y_k)}{6} \right] \tag{B.7}$$

$$F_y^i = p_f{}^e \left[\frac{(x_k - x_j)}{3} + \frac{(x_i - x_j)}{6} + \frac{(x_k - x_i)}{6} \right] \tag{B.8}$$

$$F_x^j = p_f{}^e \left[\frac{(y_k - y_i)}{3} + \frac{(y_k - y_j)}{6} + \frac{(y_j - y_i)}{6} \right] \tag{B.9}$$

$$F_y^j = p_f{}^e \left[\frac{(x_i - x_k)}{3} + \frac{(x_j - x_k)}{6} + \frac{(x_i - x_j)}{6} \right] \tag{B.10}$$

$$F_x^k = p_f{}^e \left[\frac{(y_i - y_j)}{3} + \frac{(y_i - y_k)}{6} + \frac{(y_k - y_j)}{6} \right] \tag{B.11}$$

$$F_y^k = p_f{}^e \left[\frac{(x_j - x_i)}{3} + \frac{(x_k - x_i)}{6} + \frac{(x_j - x_k)}{6} \right] \tag{B.12}$$

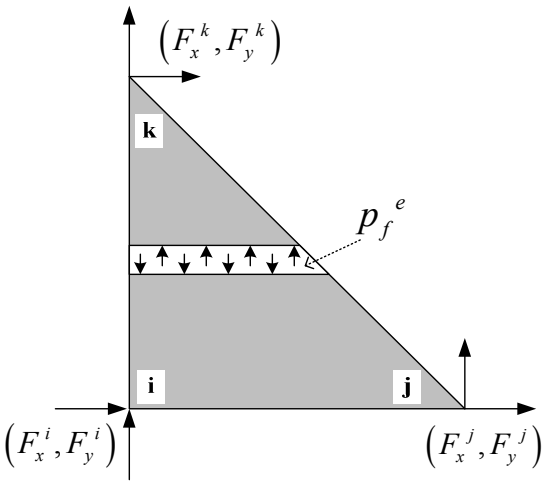

Figure B.2 Schematic of computing process for the equivalent nodal forces

APPENDIX C

3D EQUIVALENT NODAL FORCES INDUCED BY HYDRAULIC PRESSURE

Element partitioning algorithm in 3D hydraulic fracturing simulation is more complex than 2D simulation. In this dissertation, four-node tetrahedron element was used and the fracture plane is expressed as an elliptical surface. Because of geometrical complexity of the 3D crack propagation, few numerical simplifications were made. There is no intersection considered in a crack element. That is, only one fracture plane can be placed in each crack element. The fracture plane taken placed in the crack element is assumed as linear without curvatures. Also, the fracturing path only can be propagating through inside of the crack element. Identifying process for the fracture plane inside the crack element and computing process for the equivalent nodal forces at nodes of the crack element are described in this appendix.

C.1 Identifying fracture plane inside element

There are two types of splitting scheme possible when the linear fracture plane is cutting a tetrahedron element. In Figure C.1, triangular and quadrilateral splitting schemes are described. In this dissertation, the fracture plane is assumed as an elliptical plane, so the plane can be expressed as a following function:

$$A_e x + B_e y + C_e z + D_e = 0 \tag{C.1}$$

where A_e, B_e, C_e are the normal vector from the fracture plane in x-, y-, and z-direction. D_e is a constant value described as $D_e = A_e \cdot c(x) + B_e \cdot c(y) + C_e \cdot c(z)$, where c(x, y, z) is

a center coordinate of the elliptical plane. Then, distance from the elliptical plane to each nodes (***i, j, k, l***) can be calculated as;

$$d_e(i) = \mathrm{A}_e x_i + \mathrm{B}_e y_i + \mathrm{C}_e z_i + \mathrm{D}_e \tag{C.2}$$

where, x_i, y_i, z_i are coordinate of node ***i***. Using same equation, distances for other nodes ***j, k, l*** can be calculated respectively. If only one node is indicated as positive distance, the crack element is identified as a triangular splitting element, while if two nodes are indicated as positive distance, the crack element is identified as the quadrilateral splitting element.

Then, we need to compute a fracture area taken placed inside the crack element to calculate equivalent hydraulic force. This is a line-plane intersection problem. Coordinate of point **1** (x_1, y_1, z_1) between node ***i*** and ***l*** can be calculated by following procedure [Figure C.1]:

$$s_I = \frac{-\left(\mathrm{A}_e x_i + \mathrm{B}_e y_i + \mathrm{C}_e z_i + \mathrm{D}_e\right)}{\mathrm{A}_e\left(x_l - x_i\right) + \mathrm{B}_e\left(y_l - y_i\right) + \mathrm{C}_e\left(z_l - z_i\right)} \tag{C.3}$$

$$x_1 = s_I\left(x_l - x_i\right) + x_i \tag{C.4}$$

$$y_1 = s_I\left(y_l - y_i\right) + y_i \tag{C.5}$$

$$z_1 = s_I\left(z_l - z_i\right) + z_i \tag{C.6}$$

where (x_i, y_i, z_i) and (x_l, y_l, z_l) are coordinates of node ***i*** and ***l***. Similarly, coordinates of points (**2**, **3**, **4**) [Figure C.1] can be calculated respectively. Once the intersected coordinates are calculated, area of the triangular splitting fracture plane and the

quadrilateral splitting fracture plane can be computed. The triangular fracture area can be described as:

$$A_c = \frac{1}{2}\sqrt{\left(x_2 \cdot x_3 - x_3 \cdot x_2\right)^2 + \left(x_3 \cdot x_1 - x_1 \cdot x_3\right)^2 + \left(x_1 \cdot x_2 - x_2 \cdot x_1\right)^2} \qquad \text{(C.7)}$$

where A_c is an cross-section area of the splitting element.

The quadrilateral fracture area can be calculated by summation of two triangular fracture surfaces of points (**1**, **2**, **3**) and points (**2**, **3**, **4**) using Eqn. (C.7).

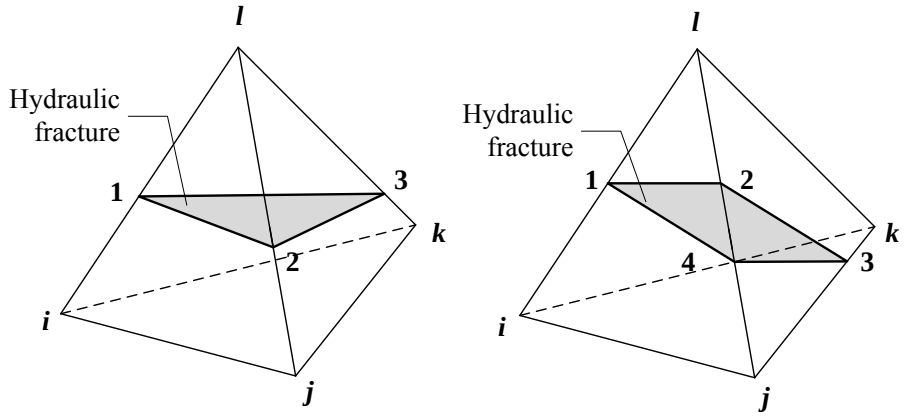

(a) Triangular splitting scheme (b) Quadrilateral splitting scheme

Figure C.1 Types of splitting scheme by fracturing direction

C.2 Computing process for equivalent nodal forces by hydraulic pressurization

In the 3D hydraulic fracturing simulation, planar fracture plane growth is assumed, so that the computing process for the equivalent nodal forces is simplified to two types of splitting schemes [Figure C.2].

Average fluid pressure acting inside the tetrahedron crack element can be defined as:

$$p_f{}^e = \frac{p_f{}^i + p_f{}^j + p_f{}^k + p_f{}^l}{4} \tag{C.8}$$

where $p_f{}^i, p_f{}^j, p_f{}^k, p_f{}^l$ are fluid pressure at each node (***i***, ***j***, ***k***, ***l***) of the crack element. Then, the equivalent nodal forces are computed using the average fluid pressure by the type of splitting scheme. For the triangular splitting element [Figure C.2 (a)], when F_l is acting to positive direction, the equivalent nodal forces are described as:

$$F_l = \frac{1}{2}\left(p_f{}^e \cdot A_c\right) \tag{C.9}$$

$$F_i = F_j = F_k = -\frac{1}{3}\left(\frac{1}{2}\left(p_f{}^e \cdot A_c\right)\right) \tag{C.10}$$

For the quadrilateral splitting element [Figure C.2 (b)], when F_k, F_l are acting to positive direction, the equivalent nodal forces are described as:

$$F_i = F_j = -\frac{1}{4}\left(p_f{}^e \cdot A_c\right) \tag{C.11}$$

$$F_k = F_l = \frac{1}{4}\left(p_f{}^e \cdot A_c\right) \tag{C.12}$$

where A_c is the cross-sectional fracture surface partitioned by fracturing path. So, a total force, F_f, applied on the splitting fracture surface can be expressed as $F_f = p_f{}^e \cdot A_c$.

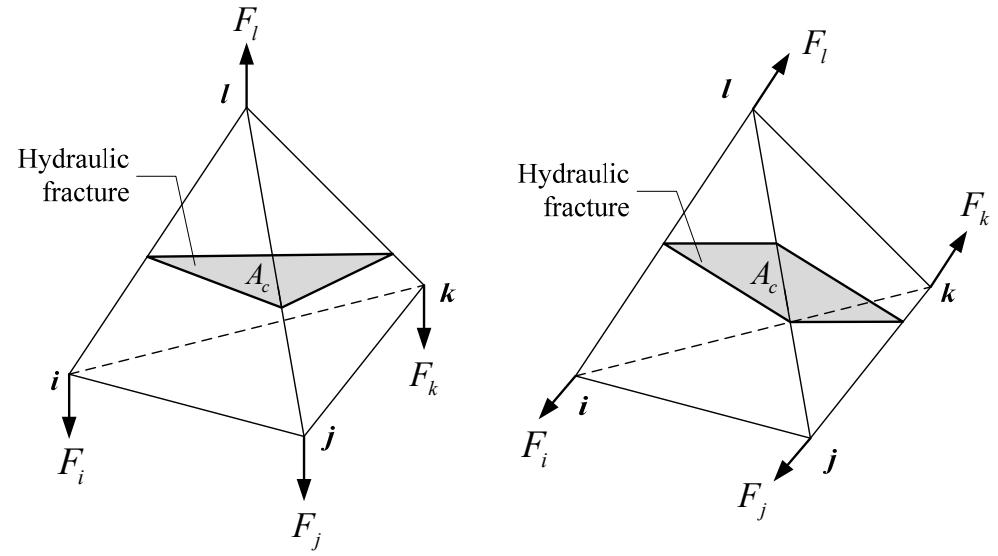

(a) Triangular splitting scheme (b) Quadrilateral splitting scheme

Figure C.2 Schematic of equivalent nodal forces by different splitting scheme